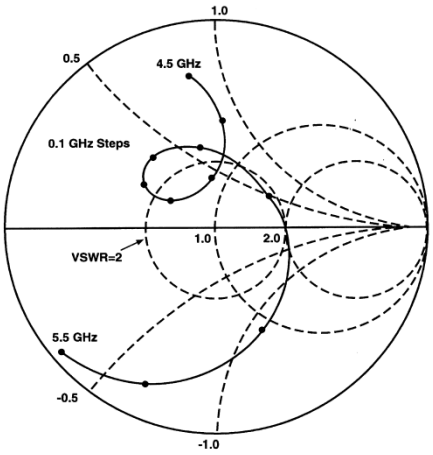

Applied Computational Electromagnetics Society Journal

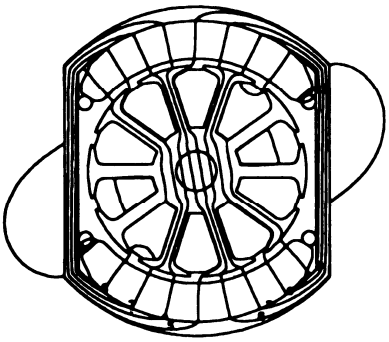

Editor-in-Chief
Atef Z. Elsherbeni

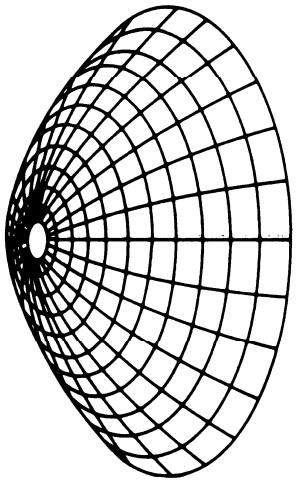

May 2010
Vol. 25 No. 5
ISSN 1054-4887

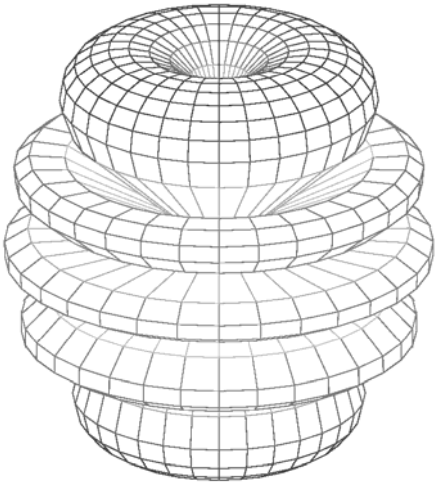

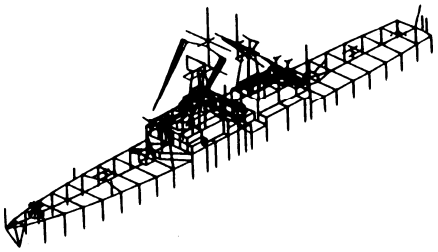

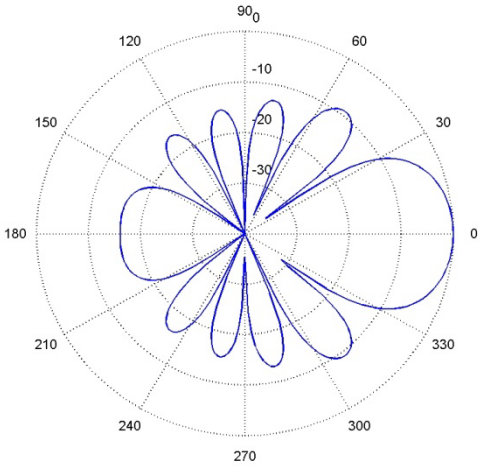

GENERAL PURPOSE AND SCOPE: The Applied Computational Electromagnetics Society ***(ACES)*** Journal hereinafter known as the ***ACES Journal*** is devoted to the exchange of information in computational electromagnetics, to the advancement of the state-of-the art, and the promotion of related technical activities. A primary objective of the information exchange is the elimination of the need to "re-invent the wheel" to solve a previously-solved computational problem in electrical engineering, physics, or related fields of study. The technical activities promoted by this publication include code validation, performance analysis, and input/output standardization; code or technique optimization and error minimization; innovations in solution technique or in data input/output; identification of new applications for electromagnetics modeling codes and techniques; integration of computational electromagnetics techniques with new computer architectures; and correlation of computational parameters with physical mechanisms.

SUBMISSIONS: The ***ACES Journal*** welcomes original papers relating to applied computational electromagnetics. Typical papers will represent the computational electromagnetics aspects of research in electrical engineering, physics, or related disciplines. However, papers which represent research in applied computational electromagnetics itself are equally acceptable.

Manuscripts are to be submitted through the upload system of ***ACES*** web site http://aces.ee.olemiss.edu See "Information for Authors" on inside of back cover and at ***ACES*** web site. For additional information contact the Editor-in-Chief:

Dr. Atef Elsherbeni
Department of Electrical Engineering
The University of Mississippi
University, MS 386377 USA
Phone: 662-915-5382 Fax: 662-915-7231
Email: atef@olemiss.edu

SUBSCRIPTIONS: Members of the Applied Computational Electromagnetics Society who have paid their subscription fees are entitled to download any published journal article available at http://aces.ee.olemiss.edu, and have the option to receive the ***ACES Journal*** with a minimum of three issues per calendar year.

Back issues, when available, are $15 each. Subscriptions to ***ACES*** is available through the web site. Orders for back issues of the ***ACES Journal*** and changes of addresses should be sent directly to ***ACES***:

Dr. Allen W. Glisson
302 Anderson Hall
Dept. of Electrical Engineering
Fax: 662-915-7231
Email: aglisson@olemiss.edu

Allow four week's advance notice for change of address. Claims for missing issues will not be honored because of insufficient notice or address change or loss in mail unless the ACES Treasurer is notified within 60 days for USA and Canadian subscribers or 90 days for subscribers in other countries, from the last day of the month of publication. For information regarding reprints of individual papers or other materials, see "Information for Authors".

LIABILITY. Neither ***ACES***, nor the ***ACES Journal*** editors, are responsible for any consequence of misinformation or claims, express or implied, in any published material in an ***ACES Journal*** issue. This also applies to advertising, for which only camera-ready copies are accepted. Authors are responsible for information contained in their papers. If any material submitted for publication includes material which has already been published elsewhere, it is the author's responsibility to obtain written permission to reproduce such material.

APPLIED COMPUTATIONAL ELECTROMAGNETICS SOCIETY JOURNAL

Editor-in-Chief
Atef Z. Elsherbeni

May 2010
Vol. 25 No.5
ISSN 1054-4887

The ACES Journal is abstracted in INSPEC, in Engineering Index, DTIC, Science Citation Index Expanded, the Research Alert, and to Current Contents/Engineering, Computing & Technology.

The first, fourth, and sixth illustrations on the front cover have been obtained from the Department of Electrical Engineering at the University of Mississippi.

The third and fifth illustrations on the front cover have been obtained from Lawrence Livermore National Laboratory.

The second illustration on the front cover has been obtained from FLUX2D software, CEDRAT S.S. France, MAGSOFT Corporation, New York.

THE APPLIED COMPUTATIONAL ELECTROMAGNETICS SOCIETY

JOURNAL

Vol. 25 No. 5 May 2010

TABLE OF CONTENTS

Effect of Numerical Dispersion in FDTD Simulations of Light Scattering from Photoreceptors

Samer S. Abdallah[1], Alexandre Iolov[2,1], Kostadinka Bizheva[2] and Omar M. Ramahi[1,2]

[1] Department of Electrical and Computer Engineering
[2] Department of Physics and Astronomy
University of Waterloo
Waterloo, ON, N2L3G1, Canada
oramahi@ece.uwaterloo.ca

Abstract ─ Recently, the FDTD method was used to investigate the optical functional response of retinal photoreceptors. Light scattering patterns of the cells were simulated under various hypothetical states to determine the physiological processes that are most likely responsible for the experimentally observed signals. An FDTD model of a photoreceptor cell spans several wavelengths, therefore, the numerical dispersion, inherent in FDTD algorithms, will introduce significant phase errors in the simulation results. These phase errors can lead to erroneous predictions, especially for narrow band light stimulus. Currently, the qualitative and quantitive effects of numerical dispersion on light scattering computations are still unknown. In this paper, an analysis of the numerical dispersion errors in the near and far scattered fields is performed. The analysis provides decision guidelines for selecting enough computational resources to obtain the light scattering patterns with acceptable margin of errors.

Index Terms ─ Finite-difference time-domain, biomedical applications, scattering, numerical simulation, time-domain analysis.

I. INTRODUCTION

A large number of diseases can cause various changes in the structural and physiological properties of biological tissues. Previous research studies [1-2] have shown that such changes can affect light scattering patterns of the infected cells. Therefore, the interest in numerical simulations of light scattering from biological tissue has increased significantly in the past years [3-5], especially with the advent of parallel processing and the increase in available computational resources. In most cases, the finite-difference time-domain (FDTD) method was the preferred numerical technique due to its simplicity in modeling large and complex structures such as the biological cells. Recently, we have used the FDTD method in investigating the causes of the optical functional response of retinal photoreceptors cells [6, 7]. The goal was to understand which of the physiological processes that can affect the power of the backscattered light.

When compared to the exact analytical solution, the FDTD results suffer from phase errors that originate from the discrete nature of the FDTD algorithms. For second-order accurate finite-difference algoirthms, the phase errors strongly depend on the ratio of wavelength to the grid meshing size [8]. Therefore, the effect of the errors on a propagating signal is similar to the effect of propagation in a dispersive material, and consequently, the term ``numerical dispersion'' was coined for this class of errors. In general, reducing the effect of numerical dispersion is constrained by the computational resources and the size of the problem since halving the phase errors requires the doubling of the resolution (i.e., doubling the mesh size in all directions). The main trade-off is between computational resources and accuracy. Moreover, numerical dispersion is more severe in electrically large structures which spans

several wavelengths since the error in phase can accumulate up to a 180° phase reversal during the propagation in the space-time coordinate system. Currently, there are no studies that quantify the error introduced by the numerical dispersion in the scattering profiles. Therefore, the meshing step is usually set to the minimum possible value. This approach consumes large computational resources in terms of memory, processing units, storage and it will increase the waiting time for simple profiling first round simulations.

In this paper, in light of the increasing interest in the use of the FDTD method to simulate wave interaction with biological media, we study the critical effect of numerical dispersion in light scattering simulations. The nature and magnitude of errors introduced in the scattering profiles for a given mesh size are investigated while making a distinction between results calculated for the near field vs. those calculated for the far field. While the focus here is related to our work on light scattering from retinal photoreceptors, the results obtained have direct implication to the general problem of scattering from electrically-long biological tissues. The results and conclusions reached here will help to optimize computational resources when applying FDTD for scattering related problems.

II. PHYSICAL VS. NUMERICAL DISPERSION

Numerical dispersion is manifested by the modification of the real wavenumber k to a numerical wavenumber $\tilde{k}$. Eq. 1 shows how the wave dispersion equation in FDTD depends on the time step Δt and the mesh step Δz [8]. The stability of the FDTD algorithm constrains the Courant factor $C=v\Delta t/\Delta z$ to be less than $1/dim^{1/2}$ (less than $1/3^{1/2}$ for 3D simulations). Setting the Courant factor to 0.5, $\tilde{k}$ can be simply expressed as a function of the relative mesh size $\Delta z/\lambda$ (eq. 2) and the solution will be stable up to the coarse meshing of $\lambda/\Delta z=10$. In the case of sinusoidal waves, the numerical phase velocity can be calculated using eq. 3 [8]. Figure 1 presents a plot of the ratio of the numerical phase velocity to theoretical one versus the relative mesh size. The maximum phase error introduced in a structure spanning m number of wavelengths can be calculated using eq. 4 [8]. Fig. 2 shows the phase error introduced in a sinusoidal wave after propagating a distance of 10λ (i.e. m=10). From these results we observe that for a structure of several wavelengths, a small change in the relative mesh size can lead to a phase error of several degrees (see Fig. 2).

$$\tilde{k}=\frac{1}{\Delta Z}\arccos\left\{1+\left(\frac{\Delta Z}{c\Delta t}\right)^2[\cos(\omega\Delta t)-1]\right\} \quad (1)$$

$$\tilde{k}=\frac{1}{\Delta Z}\mathbf{arccos}\left\{1+4[\mathbf{cos}(2\frac{\Delta Z}{\lambda})-1]\right\} \quad (2)$$

$$\tilde{v}_p=\frac{\omega}{\tilde{k}}=\frac{2\pi f}{\frac{1}{\Delta Z}\arccos\left\{1+4[\cos(2\frac{\Delta Z}{\lambda})-1]\right\}} \quad (3)$$

$$=\left\{\frac{\frac{\Delta Z}{\lambda}}{\arccos\left\{1+4[\cos(2\frac{\Delta Z}{\lambda})-1]\right\}}\right\}v_p$$

$$\Delta\phi=m\lambda\frac{\Delta Z}{\lambda}\left(1-\frac{\tilde{v}_p}{v_p}\right)\times 360^{\circ}. \quad (4)$$

In an ideal world where computational resources are infinite, one would like to have the lowest relative mesh size ratio as it yields the lowest phase error. The FDTD method, while extremely robust, flexible and having the ability to model a wide range of problems, demands excessive computational resources. In the coming sections, we show that optimal simulation does not necessarily imply lower relative mesh size. The reason is that not only the computational efficiency of the simulation has to be taken into account but also the target of the simulation (viz., fixed field point, distributed field, near-field monitor point vs. far-field monitor point, etc.).

III. NUMERICAL METHODS

A. Overview

In light scattering computations using the FDTD method, there are two processing steps: The first step consists of the FDTD solution of the interaction of an incident wave with a scattering object. At the end of the first step, the near-fields over a surface enclosing the object are stored. The second step consists of the near-to-far field transformation which integrates the contribution of all near-fields at the far zone. Numerical

dispersion is introduced in the first step and it has been suggested in [9] that the integration aspect of the near-to-far field transform can mitigate the phase errors, therefore, reducing the weight of the numerical dispersion on the scattering profiles. In investigating the effect of numerical dispersion on light scattering, separate analyses were made for the near- and far-fields results.

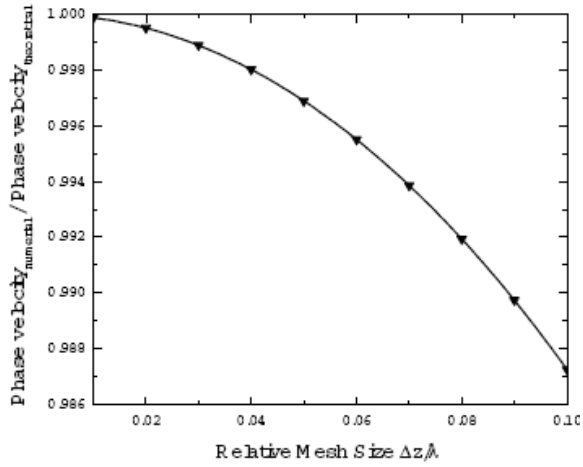

Fig. 1. Relative numerical phase velocity vs. relative mesh size. The numerical phase velocity is taken relative to the theoretical one.

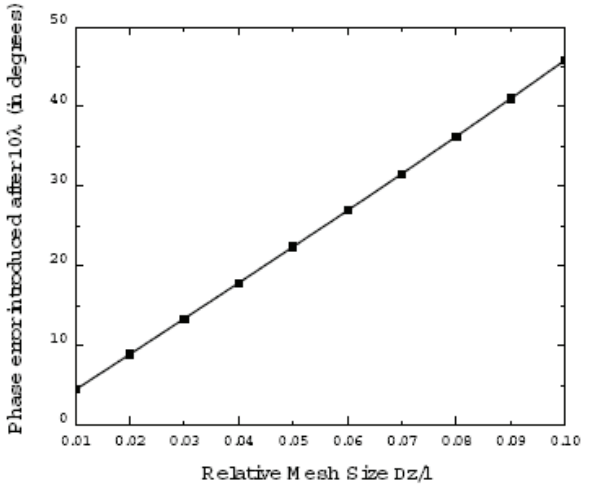

Fig. 2. Numerical phase error (in degrees) vs. relative mesh size. The error is introduced in the phase of a sinusoidal signal which propagated a distance of 10λ.

B. Model

Since we are interested in quantifying the errors in the simulations of light scattering patterns of the photoreceptors, the scattering object was selected to match the basic photoreceptor model, shown by the solid cylinder in fig. 3. The refractive index for the host medium is n_0=1.34 and for the cylinder is n_1=1.41. The effect of numerical dispersion on the model was simulated by increasing progressively the mesh size in the axial direction since the incident wave travels for the longest distance and duration in this direction. The incident plane wave pulse has 100nm bandwidth around a central wavelength of λ_{cen} = 1μm. The simulations were performed for three cylinders of different diameters (0.1μm, 1μm and 5μm. These different apertures are meant to be representative of the three distinct scattering regimes: In the first regime, λ, the wavelength of the excitation is greater than $\sigma^{1/2}$ where $\sigma = \pi d^2/4$ is the scattering cross section area and d the diameter of the cylinder. In the second regime, λ is comparable to $\sigma^{1/2}$and in the third regime, λ is smaller than $\sigma^{1/2}$.

C. Near-Fields Analysis Method

The analysis of the near-fields consists of determining the error in phase introduced during the propagation of the plane wave from its insertion point at the Total-Field Scattered-Field (TF-SF) boundary to the opposite boundary, going through the solid cylinder representing the photorecyptor. Two time-domain point monitors were positioned along the main axis of the cylinder to record the time signals that will be used in the processing (see Fig. 3). The first time-monitor records the incident plane wave entering the TF region whereas the second time-monitor records the signals reaching the other end of the TF region. The incident signal recorded by the first time-domain monitor was used to create the propagated incident signal as it should be theoretically at the location of the second time-domain monitor.

Figure 4 presents the processing flow used to implement the ideal propagation of the incident signal. A Discrete-Fourier-Transform (DFT) transforms the incident pulse into the frequency

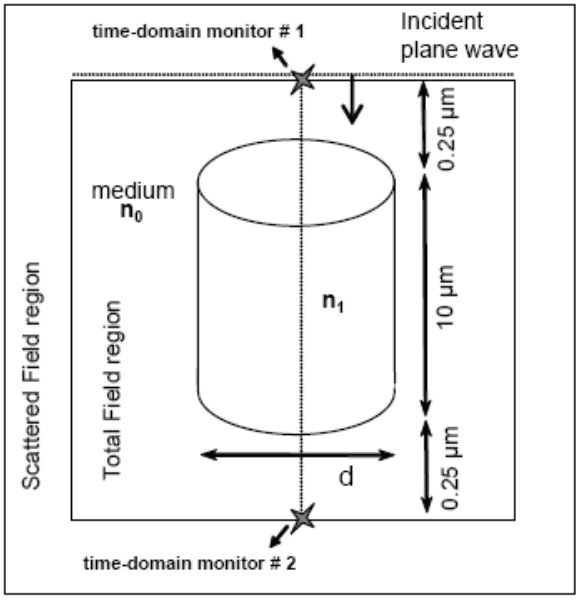

Fig. 3. The setup of the FDTD simulations for numerical dispersion. The stars show the locations of the time-domain monitors used. The refractive index for the host medium is n_0=1.34 and for the cylinder is n_1=1.41.

domain, then each frequency component is selected and inverse transformed back to the time-domain using Inverse-Discrete-Fourier-Transform (IDFT). The harmonical signal obtained in the previous step is multiplied by the phase factor e^{-kx} where k is the wavenumber corresponding to the frequency f and to the medium of propagation with length ΔL and refractive index n (c is light celerity). Finally, all time sub-signals are integrated to generate the ideally propagated signal $S_{theoretical}$. Ideally, $S_{theoretical}$ has zero phase error and therefore, the difference in phase when compared to the FDTD signals recorded by the second time-domain monitor approximates the phase error introduced by the numerical dispersion. It is important to note that the wave number k used in the phase translation e^{-kx} takes into account the different media encountered along the path of propagation (*viz*., the media n_0 and n_1, see Fig. 3.)

Figure 5 presents the processing diagram for the computation of phase errors in the near fields point signals. First, the DFT signals of both reference (i.e. theoretical) and target (i.e. simulated) signals were computed to determine the spectrum of interest. Then each frequency component is selected and inverse transformed back to the time-domain using IDFT. The time-domain sub-signals are inputted to the hilbert analyzer which computes the phase difference. The phase difference are reported per each frequency of the source signal spectrum.

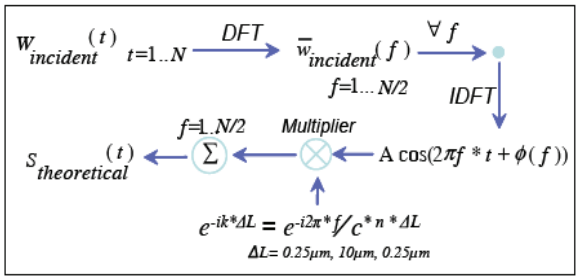

Fig. 4. Processing flow showing the generation of the theoretical signal $S_{theoretical}$ with ideally zero phase error. $S_{theoretical}$ was obtained from an ideal propagation of the incident signal recorded by the first time-domain monitor toward the location of the second time-domain monitor.

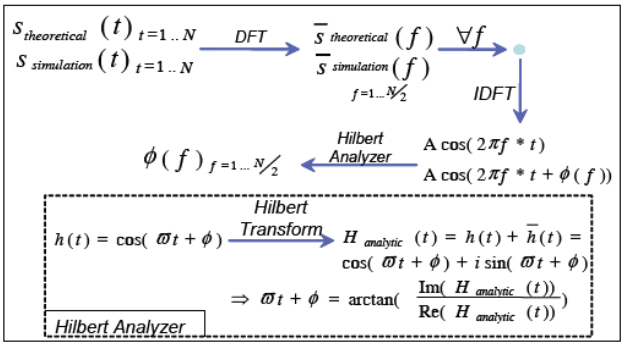

Fig. 5. Diagram of processing to determine numerical dispersion.

IV. NUMERICAL SIMULATION RESULTS

A. Near-Fields Results

Figure 6 shows the phase error introduced in the near-fields data after propagating through the TF region. The figure shows that, as the mesh size increases, the phase error at the smaller wavelengths starts to increase at a faster rate compared with the errors at the longer wavelengths. For relative mesh sizes $\lambda/\Delta z > 0.02$, this difference in phase error can pass the 200%. Fig. 7 presents the phase error occurring at the

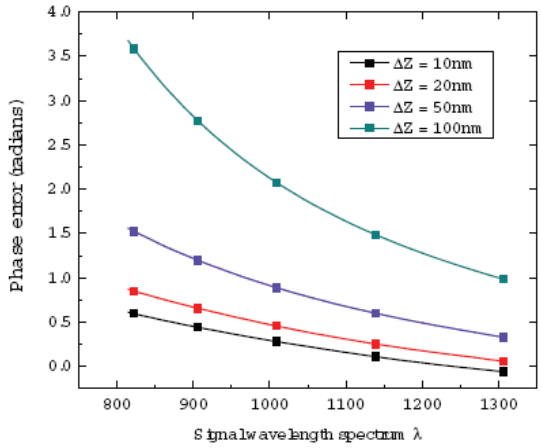

Fig. 6. Phase error plotted vs. signal wavelength spectrum for various mesh sizes ($\lambda/\Delta z$=0.01, 0.02, 0.05 and 0.1).

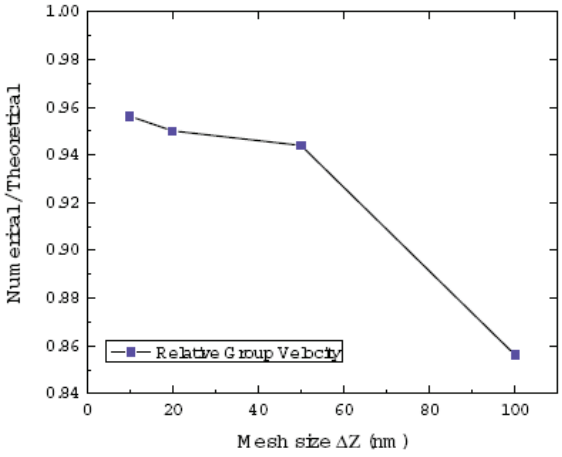

Fig. 8. Ratio of average phase velocity to the theoretical phase velocity plotted vs. mesh sizes ($\lambda/\Delta z$ =0.01, 0.02, 0.05 and 0.1).

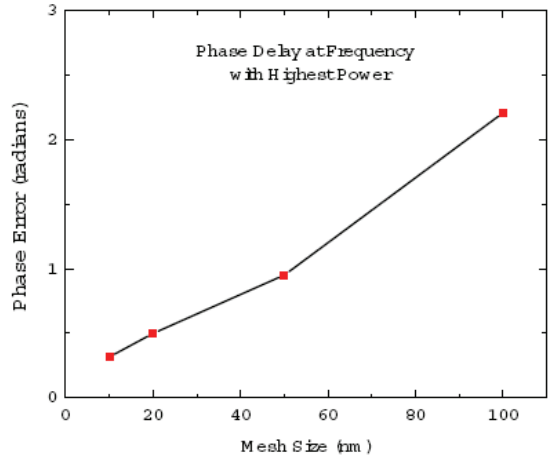

Fig. 7. Phase error at median spectrum wavelength (with highest power) plotted vs. mesh sizes ($\Delta z/\lambda$=0.01, 0.02, 0.05 and 0.1).

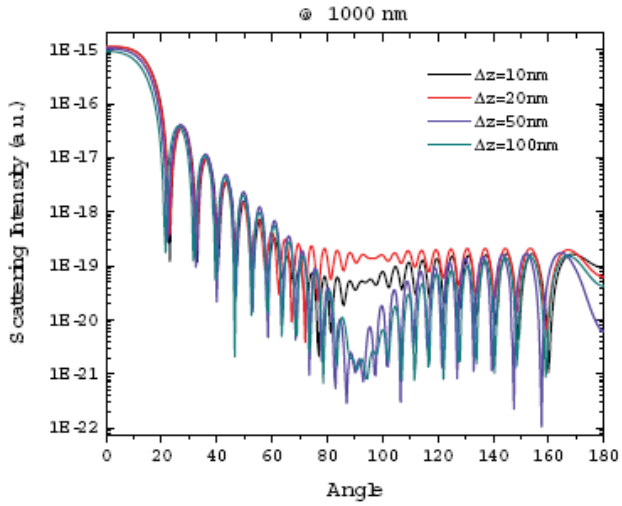

Fig. 9. Effect of numerical dispersion on light scattering in the case of small scattering cross section as compared to the wavelength (case 1).

median wavelength with peak power λ=100nm. The result compares well with the theoretical phase error calculated for the same wavelength and presented in fig. 1. Also, it shows that for a structure of 10λ, the error in phase in the near-fields is less than 180° for most practical meshing sizes and less than 90° for mesh size satisfying $\Delta z/\lambda < 0.06$.

Figure 8 presents the ratio of the average phase velocity of the propagated signal. The results show significant deviations and faster decrease as a function of the mesh size when compared with phase velocity values reported by the theoretical analysis done in Fig. 1.

The analysis of the effect of numerical dispersion on near-fields showed that the phase error will not exceed 90° for mesh size satisfying $\lambda/\Delta z>0.05$. Also, over a spectrum of 100nm=$\lambda_{central}/10$, the variation in phase error will not exceed 60°, again for mesh sizes $\Delta z/\lambda < 0.05$. Above these thresholds, the variations show a deviation from the linear behavior where the phase error can change by values up to 180°. In terms of phase velocity, the change is less or equal to 5° for mesh size satisfying $\Delta z/\lambda < 0.05$ and can reach 15°

for mesh size satisfying $\Delta z/\lambda < 0.1$.

B. Far-Fields Results

The far-fields results consist of scattering profiles computed for each mesh size. The errors can only be reported relative to the case of finest grid since there is no analytical solution for light scattering from a finite cylinder where the incident wave propagates along the axial direction.

The far-fields results are reported for the three regimes of scattering as explained earlier. Fig. 9 shows the light scattering profile for the first regime, where the wavelengths of the signal are much greater than the diameter of the cylinder. In this case, numerical dispersion has the greater effect around the normal scattering directions where the sidelobes experience large fluctuations in their magnitude. The sidelobes in the forward and backscattering directions show a slight shift towards lower angles.

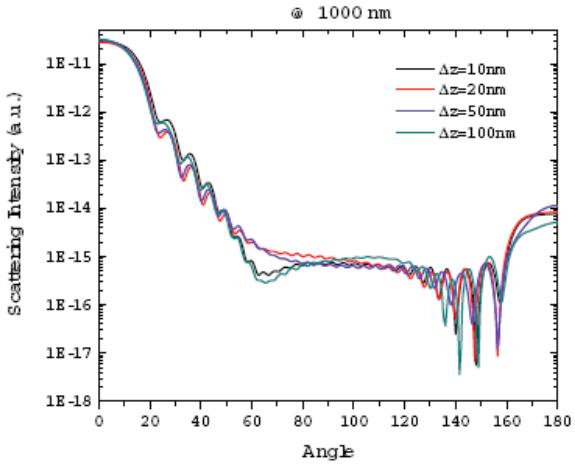

Fig. 10. Effect of numerical dispersion on light scattering in the case of medium scattering cross section as compared to the wavelength (case 2).

Fig. 10 presents the light scattering profile for the second regime of scattering where the diameter of the cylinder is comparable to the wavelengths of the signal. In this regime, the sidelobes around the normal directions start to show less magnitude fluctuations and more positional fluctuations whereas the opposite happens in the normal and backscattered directions. Fig. 11 presents the light scattering profile for the third regime of scattering where the diameter of the cylinder is larger than the wavelengths of the signal. In this regime, the sidelobes around the normal directions show slight variations in magnitude whereas the sidelobes of the backscattered and forward regions show a mix of large magnitude and positional changes.

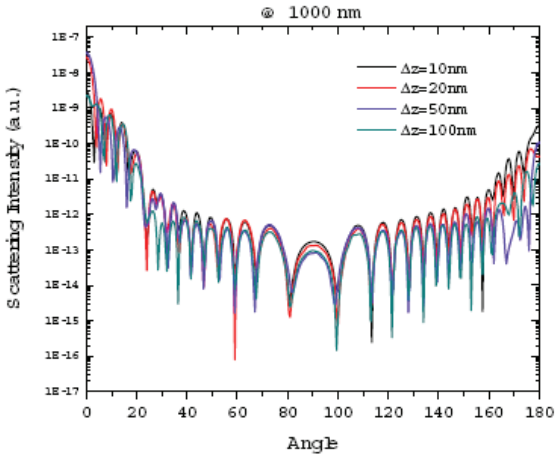

Fig. 11. Effect of numerical dispersion on light scattering in the case of large scattering cross section as compared to the wavelength (case 3).

V. CONCLUSION

We have investigated the effect of numerical dispersion on light scattering profiles obtained from simulations of retinal photoreceptors models. The near-fields results quantified the maximum phase error and the relative phase velocity observed versus the meshing size. Far-fields results show that the numerical dispersion either affects the sidelobes in forward and backscattering regions or the sidelobes in the normal scattering directions. The normal direction sidelobes are less affected as the aperture increases whereas the opposite happens for the sidelobes of the forward and backscattering regions. The results presented show that, depending on the simulation objectives, the relative mesh size ratio can be optimally selected to achieve sufficient accuracy while minimizing the computational requirements of the FDTD method.

VI. ACKNOWLEDGMENTS

The authors acknowledge the financial support from NSERC, ORDCF and the University of Waterloo that made this research possible.

REFERENCES

[1] M. J. Piket-May, A. Taflove, and J. B. Troy, "Electrodynamics of visible light interactions with the vertebrate retinal rod," *Optics Letters*, vol. 18, pp. 568-570, 1993.

[2] A. K. Dunn, *Light Scattering Properties of Cells,* Phd, Univ. Texas at Austin, 1997)

[3] A. Dunn, C. Smithpeter, A. J. Welch, and R. Richards-Kortum, "Finite-difference time-domain simulation of light scattering from single cells," *J. Biomed. Opt*., vol. 2, no. 3, pp. 262—266, 1997.

[4] R. Drezek, A. Dunn, and R. Richards-Kortum, "A pulsed finite-difference time-domain (FDTD) method for calculating light scattering from biological cells over broad wavelength ranges", *J. Opt. Express,* vol. 6, no. 7, pp. 147-157, 2000.

[5] R. Drezek, M. Guillaud, T. Collier, I. Boiko, A. Malpica, C. Macaulay, M. Follen, and R.Richards-Kortum, "Light scattering from cervical cells throughout neoplastic progression: influence of nuclear morphology, DNA content, and chromatin texture", *J. Biomed. Opt.,* vol. 8, no. 1, pp. 7-16, 2003.

[6] S. S. Abdallah, *Finite-Difference Time-Domain Simulations of Light Scattering from Retinal Photoreceptors,* Electrical Eng., Univ. of Waterloo, 2007.

[7] S. S. Abdallah, O. M. Ramahi, and K. Bizheva, "FDTD Simulation of Electromagnetic Wave Scattering from Retina Cells", *The 29th Annual International Conference of IEEE Engineering in Medicine and Biology Society*, pp. 1639-1642, 2007.

[8] T. Taflove, and S. C. Hagness, *Computational Electrodynamics: The Finite-Difference Time-Domain Method*, 2nd ed. Norwood, MA: Artech House, 2000.

[9] F. D. Hastings, J. B. Schneider, and S. L. Broschatc, "A finite-difference time-domain solution to scattering from a rough pressure-release surface," *J. Acoust. Soc. Am.,* vol. 102, no. 6, pp. 3394-3400, 1997.

Efficient Techniques for Accelerating the Ray-Tracing for Computing the Multiple Bounce Scattering of Complex Bodies Modeled by Flat Facets

Felipe Cátedra[1], Lorena Lozano[1], Iván González[1], Eliseo García[2], and Mª Jesús Algar[1]

[1] Computer Sciences Department
University of Alcalá, 28871 Alcalá de Henares (MADRID), SPAIN
felipe.catedra@uah.es, lorena.lozano@uah.es, ivan.gonzalez@uah.es, chus.algar@uah.es

[2] Department of Automática
University of Alcalá, 28871 Alcalá de Henares (MADRID), SPAIN
eliseo.garcia@uah.es

***Abstract*—** A new algorithm to accelerate the ray-tracing for computing the radar cross section (RCS) of complex targets is presented. The algorithm is based on a combination of the angular Z-buffer (AZB), the volumetric space partitioning (SVP) and the depth-limited search method. The algorithm is very useful for RCS computing techniques based on geometrical optics (GO) and physical optics (PO). The targets are represented geometrically by a collection of flat patches. The approach is extremely efficient for computations of the RCS of large and complex bodies modeled by a high number of flat surfaces taking into account ray paths with multiple bounces. Results for representative targets are shown.

***Index Terms*—**Radar cross section, physical optics, geometrical optics, ray-tracing.

I. INTRODUCTION

Computer tools for analyzing the RCS of complex objects are very useful for designing platforms with a limited radar echo. In addition, being capable of analyzing the RCS of an object in a particular environment, taking into account the mutual interaction between object and environment, is crucial for the identification of objects on the ground or in the sea. Traditionally, complex targets and their surrounding environments have been modeled with facets; this requires a very large number of facets (tens or hundreds of thousands) for a realistic model. A suitable method for performing the electromagnetic analysis of the reflection of a facet is PO, [1-2] with additional calculations based on equivalent currents method (ECM) [3] to correct the edge effects of the facets. The PO integrals are computed using Gordon's Method for planar surfaces [4] and the stationary phase method (SPM) [5] for curved surfaces. Fresnel´s reflection coefficients are included in the PO approach to take into account radar absorbing materials (RAM) and other materials [6]. Contributions to the RCS from double, triple and higher order reflections between flat facets can be computed assuming that after any reflection the field is collimated in a cylindrical tube and it conserves its plane wave nature in the tube [7-8]. The boundary of the cylindrical tube is defined by projecting the reflection of the silhouette of the facets that have experienced the reflection. In this way, a multiple bounce contribution to the RCS can be computed by a hybrid method that uses GO-GO-….-GO-PO, where GO is used for all reflections except the last, which is evaluated using PO in a similar way. After any bounce the collimated tube is trimmed by the silhouette of the corresponding facet.

Using this approach for RCS analysis with complex targets/environments, most of the CPU-time is spent on determining the facets of the environment that either produce reflection or diffraction— either event will obstruct a ray path. If we consider the problem of finding the RCS of a body modeled by N facets from rays that suffer K bounces, for the incident and observation directions we must identify the sets of K facets that can form ray-paths with K bounces. An exhaustive way to obtain these sets is by forming a search tree [9] (see Fig. 1). In the search tree N branches leave from the node-root (R) to the N

nodes of the first tree level. Each one of the nodes of the first level corresponds to the simple reflection contribution of a facet of the target. (N-1) branches leave from a given node of the first level that correspond with all the double reflection contributions that have the first reflection in that first level node. The third level of the tree has N(N-1)(N-2) nodes, each one of them representing a triple reflection. The subsequent tree levels are formed similarly so that the K^{th} level has N(N-1)(N-2)...(N-K+1) nodes (approximately N^K nodes if N is much greater than K, as usual), where each node of the K^{th} level corresponds to a set of K facets that contribute K reflections. The complexity of the search tree for realistic targets and high order reflection RCS analyses is very high. For instance, a target with 10,000 facets has a tree search with about 10^{16} nodes in the fourth level of the tree— this is unmanageable even for large computers. Of course, not all of the N^K nodes need to be stored or tested for several reasons: the facets of many sets corresponding to the nodes of the K^{th} level are not properly oriented, the ray paths between a pair of facets are obstructed, etc. Thus, as only a very small fraction of the nodes of that level can potentially contribute to the RCS, many tree branches can be pruned at that level or at previous levels. It is numerically very expensive to rigorously check whether or not a facet will suffer a reflection/diffraction. In order to be efficient one should avoid such rigorous checking, discarding facets as early as possible using a fast check.

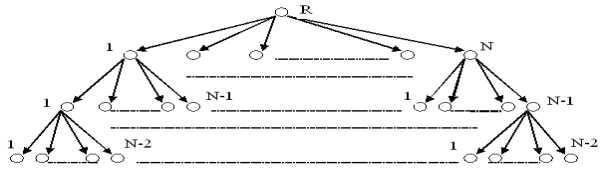

Fig. 1. Search tree for the RCS computation of a given direction considering up to three bounces of a target modeled by N facets.

Recently, in order to speed up the RCS calculation, several ray-tracing acceleration techniques— such as space volumetric partitioning (SVP), binary space partitioning (BSP), angular Z-buffers (AZB), and shooting and bouncing Rays (SBR)—have been developed and applied [10-13]. The underlying philosophy in these algorithms is a fast exploration of the search tree nodes combined with an early pruning of the tree branches: as soon as a node in a given level of the tree search is found to not contribute to the RCS, the node and all its successor nodes are discarded from the RCS analysis. The differences in the performances of the previously mentioned algorithms are due to their different capabilities to quickly explore the tree nodes and pruning the non-contributing tree branches early in the computation. These algorithms have increased the computational capacity: complete RCS processing, including a detailed RCS for images of targets with 50,000 facets and three reflections. The analysis of targets with a larger number of facets and higher orders of reflection is not affordable with the computers available today.

Most of the algorithms mentioned above are based on a non-informed exploration of the search tree, which usually follows a "breadth-first search" strategy [9-14]. In this strategy, to obtain the RCS considering contributions with K bounces, first all the nodes of the first tree level are explored, then all the nodes of the second level and so on until the K^{th} level of the tree is explored (while performing appropriate pruning of the tree branches as early as possible). The complexity of this strategy is proportional to N^K for both the CPU-time and memory. The bottleneck of this strategy is the memory needed because in order to explore the i^{th} level, the information of all the nodes of the previous level needs to be stored. It is hard to explore more than 3 levels in a complex tree search using the "breadth-first search" strategy (e.g. the tree of a target with 50,000 facets). A better way to explore the tree search of Fig. 1 is using the "depth-limited-search" method [9, 14]. As explained in detail later in this paper, this method avoids storing the information of all the nodes of the previous level. In this way, the memory needed is proportional to only KN, which means that in the practice all problems can be analyzed using an affordable amount of computer memory. The CPU-time required by the "depth-limited-search" is still proportional to N^K. Using efficient ray-tracing techniques— such as SVP, BSP, and AZB— the branches of the search-tree can be pruned early in such a way that the effective branching factor N_e of the tree search is quite less than the branching factor N of the tree. This reduction of the branching factor allows for analyses that include high order reflections.

Here we propose a new ray-tracing accelerating technique. For that the AZB algorithm is applied in a different way than in [13]. In this reference, the geometrical model was assumed to be composed of only flat facets and the reflections are treated using images: an image of the source (the primary image) for each visible facet, a secondary image for each pair of visible facets for treating double reflections, etc. This AZB application is source dependent: the images (primary and secondary) and their AZB matrices are built and stored for a particular source. This approach is efficient for treating first and second reflections, but efficiency is lost when we need to treat higher order reflections for complex models because the number of second or higher order images depends on N^K. In addition, the AZB matrices of the algorithm in [13] are source dependent. The new AZB algorithm that we propose here is not source dependent and the number of AZB matrices is limited to the number of facets in the model, N. In the new algorithm one AZB matrix is associated with each facet of the model. These matrices are not source dependent and are used in a recursive algorithm to find all the ray-paths independently of the number of reflections.

The new AZB algorithm that we propose here has some resemblance to the SBR technique, but it is fundamentally different. In SBR, rays are shot in each direction of a prefixed set of scanning directions. The rays are re-addressed after each reflection impact. No new rays are generated on any point of the ray paths. This usually implies that near the source the space is over-sampled with lots of very close rays, but far from the source or after several reflections the rays are very scarce and the space is sub-sampled. Using the SBR technique, the field at a point is computed considering some of the rays in close proximity. The AZB algorithm that we propose here defines an AZB matrix for each facet of the model and considers the possible reflections from all of the facets visible from the source. For an n-order reflection, the algorithm considers all the facets visible from the facets that have suffered the n-1 order reflection. In this way the resolution of the technique is maintained for higher order reflections. The AZB technique computes the field at a point by accurately considering all of the ray paths that left the source and suffered a specified-order reflection; there is no loss in accuracy when the reflection order increases.

The proposed ray-tracing approach has been developed in the last years to improve FASCRO, a computer code to compute the RCS based on GO-PO [6] that was not able to analyze the RCS of complex bodies considering more than two bounces with affordable computational resources. First efforts in this improvement were addressed to reduce the need of large amount of computer memory required by previous versions of the AZB algorithm. For that, the AZB was combined with the Space Volumetric Partitioning (SVP) algorithm for the analysis considering simple reflections [15] and diffraction, [16], of the RCS of electrically large and complex targets using a reduced computer memory. A very efficient approach based on the AZB and SVP algorithms combined with the A* heuristic search method, [9], was developed to consider multiple iterations between different flat surfaces, [17]. However this approach presented some fail due to the difficulty of finding a reliable way to compute the heuristic value for the RCS computations which the A* algorithm requires. In order to avoid this problem the depth-limited search strategy was proposed in [18]. A new code, called POGCROS, for an efficient computation of RCS of complex targets was implemented with all these improved algorithms and presented in [19]. In this paper we present in details the approach outlined in [18-19] together with a new version of the AZB-SVP algorithm which gives a further reduction of the CPU-time and memory resources required for analyzing large and complex problems.

This paper is organized as follows. Section II describes the AZB and SVP matrices and gives a procedure for obtaining them efficiently. The scheme proposed for speeding up the tree exploration, using a combination of AZB+SVP and the "depth-first search" algorithm is shown in Section III. This approach permits the treatment of complex targets, even for high order RCS contributions, while keeping the memory requirement affordable. The AZB+SVP scheme involves a very early pruning of the search tree, thereby reducing the search complexity. In Section IV, a detailed description of the exploration of the tree-search using the depth-limited algorithm is included. Finally, Section V presents some cases

showing the robust performance of these new ray-tracing approaches.

II. DEFINITION OF AZB AND SVP MATRICES

First, let us consider multiple reflections in a flat faceted body. We will assume a complex body modeled by many flat facets, say thousands of facets or even more. Each facet is identified by a facet number. In a pre-process we compute the AZB matrix associated with each facet. The AZB matrix of the facet with number X informs us about the visibility of the rest of facets of the model from the point of view of the X facet. To explain how this matrix is formed, let us start reviewing the AZB matrix associated with a point [6, 13].

The space viewed from a reference point can be split in angular regions that we will call anxels (an analogy with pixels). Figures 2 and 3 show an example of an anxel and space split by anxels, respectively. For simplicity, we consider angular space division for a 2D case, as shown in Fig. 4; the facets of the model are located in the 2D anxels space. Sometimes a facet extends over only one anxel, but in other cases a facet can span several anxels. The AZB technique associates a sub-matrix to each of the anxels [13]. The sub matrix of an anxel includes a list with the facet numbers of all the facets completely or partially contained in that anxel. The facet numbers in the list are ordered following the painting algorithm in an increasing order with the distance of the facet from the reference point [13]. The lists do not include the facets of the anxel that are not visible from the reference point. For example, the list for anxel 8 in Fig. 4 is: 10, 3.

As explained in [13], the AZB matrix reduces the order of complexity by searching only the facets that can reflect a ray that leaves the reference point. This search, with the help of the AZB, is performed as follows: we start by identifying the anxel corresponding with the ray direction, we check the facets whose facet numbers appear in the anxel list, and then we begin checking where the first facets on the list presumably have a high probability of being impacted by the ray.

The AZB matrix of a facet is formed combining the AZB matrices of its vertices. An anxel of the AZB of facet X contains the list of all the facets

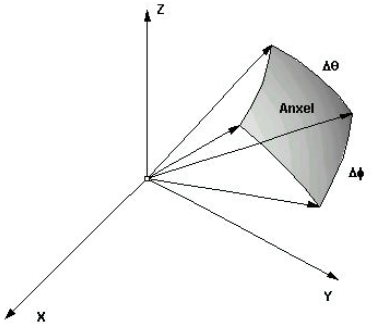

Fig. 2. Example of angular region, or "anxel" as seen from a reference point.

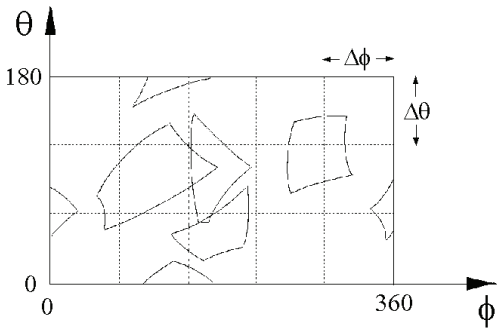

Fig. 3. The complete space seen from a point is split in anxels. The facets of the models extend over one or more anxels.

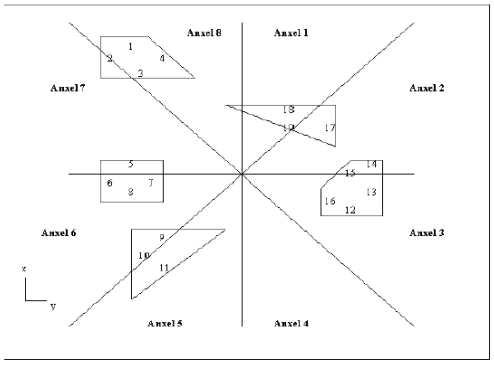

Fig. 4. Example of AZB as seen from a reference point for a 2D case.

that are seen (fully or partially) in this anxel from all the vertices of facet X. In other words, the AZB matrix of facet X is built by considering, in each anxel, the list resulting of the Boolean union of the lists in this anxel of the AZB buffers of all the vertices of facet X. The AZB of facet X contains information on how the rest of the visible facets are seen from facet X.

In addition to the AZB matrices of each facet, a particular AZB is associated with the whole structure. We call this matrix the "normal AZB matrix," which stores all the facets of the structure in accordance with the directions of the facets' normal vectors. Every facet has associated a normal vector pointing outward from the structure. The angular space of the normal AZB matrix extends over the complete angular space: 4π steroradians. In each anxel of this space we store the facets whose normal vectors are oriented into the angular range of the anxel. Only the facets that are visible from the infinite surface are considered for the normal AZB matrix.

In order to efficiently obtain the AZB matrices of the facets of a complex structure we use an adaptive version of SVP [20]. In this technique, the space containing the structure is divided into small sub-volumes called "voxels." Figure 5 shows a parallelogram containing the structure. The parallelogram is divided into smaller parallelograms or voxels. This is a first level division of the SVP. We obtain the second level division of the SVP by subdividing the small parallelograms in Fig. 5 into smaller voxels and by successively subdividing these voxels for the higher subdivision levels of the SVP. Figure 6 shows a two-level subdivision for a 2D problem, while Fig. 7 shows a three-level subdivision for the same case. In this last figure, the subdivisions are made adaptively, meaning that not all of the voxels are subdivided for a given level because if a voxel is empty or does not have small geometrical features, a subdivision is not required.

The information on the facets contained in the voxels of the lowest level of subdivision together with the relation between the voxels in an adaptive SVP subdivision is stored in a relational database of matrices. We use Fig. 7 to explain how we can take advantage of the SVP method. For instance, if we want to know if there is any facet obstructing the segment which joins the centers of facets 16 and 31 in Fig. 7, we only need to check for a possible obstruction to the facets contained in voxels: (1)-(a)/(1)-(a); (1)-(b)/(1)-(a); (1)-(b)/(1)-(b); (2)-(a)-(i)/(1)-(b)-(j); and (2)-(2). To obtain the AZB matrix of facet 31, we shall explore for each of the vertices of facet 31 in which angular region are the rest of facets of Fig. 7—if they are visible from these vertices.

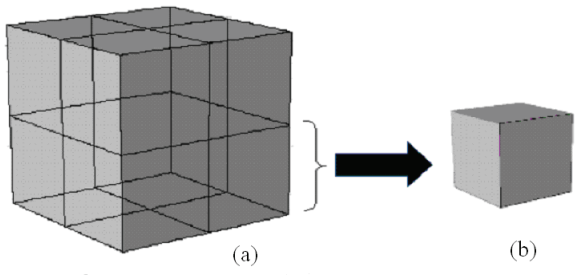

Fig. 5. Example of a first level division of a volume into 8 sub-volumes or voxels.

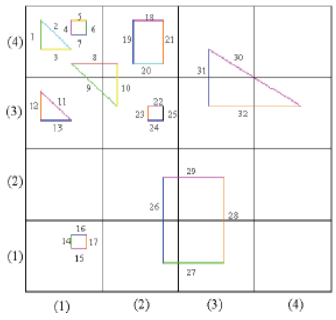

Fig. 6. Example of a two level, uniform SVP for a 2D case.

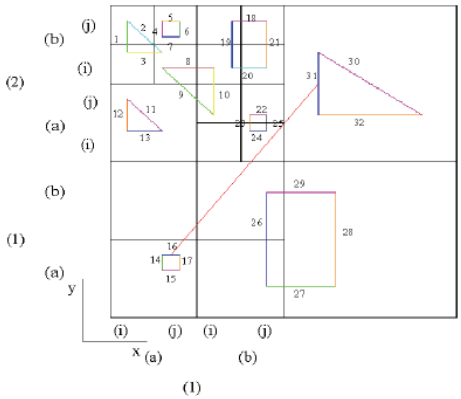

Fig. 7. Application of the adaptive SVP to find the facets in the line joining the centers of facets 16 and 31. Three non uniform levels are considered.

III. APPLICATION OF THE RECURSIVE AZB+SVP ALGORITHMS FOR RCS COMPUTATIONS

AZB+SVP can be applied recursively to compute the RCS of a complex structure composed of flat facets. We assume that the total number of facets N is very large. This approach is applicable to monostatic or bistatic RCS computations. The directions of incidence and

observation are defined by the unit vectors $\hat{k}_i$ and $\hat{k}_o$, respectively (where $\hat{k}_i = \hat{k}_o$ for monostatic RCS)

A. Computation of the RCS Due to Simple Reflections

The contribution to the RCS from each illuminated facet for simple reflection is computed using Gordon´s expressions for the evaluation of the PO integral that gives the far field radiated by currents of constant amplitude and phase with a lineal variation [4]. A very rough way to select the facets that can potentially be illuminated is by applying the Culling's criterion for the incidence and observation directions (the facets of the structure that are simultaneously seen in the incidence and observation directions) [13]. A facet with normal unit vector $\hat{n}$ is classified as potentially illuminated applying this criterion if the following expressions of scalar vector products are simultaneously satisfied:

$$\hat{n} \circ \hat{k}_i \le 0 \qquad (1)$$

$$\hat{n} \circ \hat{k}_o \ge 0. \qquad (2)$$

The application of the Culling's criterion reduces the complexity of the problem from order N to order N/2. However, we can furthermore reduce the complexity of the problem by taking into account that the contribution to the bistatic RCS of a flat facet vanishes when the directions of incidence and observation are far away, following Snell's law for the reflection off this facet (see Fig. 8):

$$\left|\hat{n} \circ \hat{k}_i\right| = \left|\hat{n} \circ \hat{k}_o\right|. \qquad (3)$$

We shall consider facets that are finite in size; the PO solution gives a scattered field in a narrow beam of width $\Delta\Phi$ around the Snell direction of reflection. Therefore, given the directions of incidence and observation, we shall consider facets as potential RCS contributors only if their normal vectors follow this relation:

$$\hat{n} \circ \left(\frac{\hat{k}_i + \hat{k}_o}{\left|\hat{k}_i + \hat{k}_o\right|} \right) \ge cos(\ \Delta\Phi\ ). \qquad (4)$$

We can select all the facets that follow (4) very efficiently by considering all of the facets in the anxel of the "*normal AZB matrix*" that include into their angular window the direction:

$$\hat{n}_s = \frac{\hat{k}_i + \hat{k}_o}{\left|\hat{k}_i + \hat{k}_o\right|}. \qquad (5)$$

When only the facets in the anxel of $\hat{n}_s$ are taken as potential contributors, the complexity of the problem is reduced to $N/(N_\theta N_\varphi)$, where N_θ and N_φ are the divisions on the entire angular space considered in the "*normal AZB matrix*" for the θ and φ spherical coordinates, respectively. Typically, the factor $N_\theta N_\varphi$ is about 400 and, therefore, using the "*normal AZB matrix*" reduces much of the complexity for problems involving simple reflections. In the case where $\hat{n}_s$ is close to the boundaries of its anxel in the "*normal AZB matrix*," or when the angular range of this anxel is less than the width $\Delta\Phi$ of the PO reflected beam, we select the facets located in this anxel and on its neighboring anxels (typically the 8 surrounding anxels); we notice that the complexity of this problem is also largely reduced.

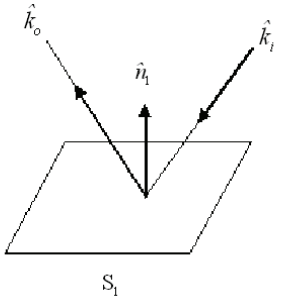

Fig. 8. Visualization the a case where the incidence direction vector $\hat{k}_i$, observation direction vector $\hat{k}_o$ and normal vector $\hat{n}_1$ follow or are close to Snell's law at surface S_1.

Once we have selected the set of facets that potentially contribute to the RCS using the fast procedure described above, we will determine if each facet contributes to the RCS and if we should trim its surface before applying Gordon's law to take into account partial occultation to correctly compute the PO integral. Some of the facets of this set cannot contribute to the RCS because they are shadowed by other facets that can occlude the

incident ray or the reflected ray in the observation direction. To determine which facets shadow the incident ray that illuminates facet *f*, we only consider the facets in the anxel that contains the incident direction $\hat{k}_i$ of the AZB of facet *f*. We apply rigorous algorithms to these facets [13]; the algorithms allow us to discover if facet *f* is completely or partially occluded by other facets when it is illuminated in the incident direction $\hat{k}_i$. In the case that facet *f* is partially occluded, its surface S_f shall be trimmed, saving for PO evaluation only the illuminated surface area S_f^i. Figure 9 shows an example of a facet trimming.

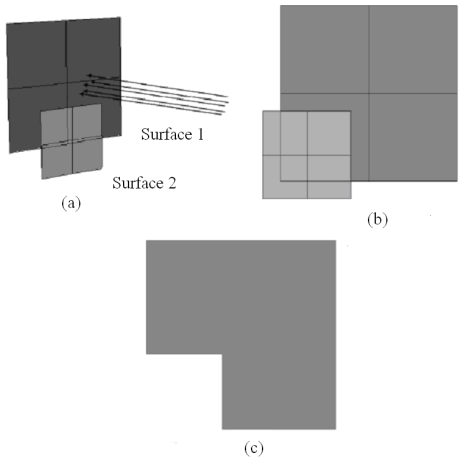

Fig. 9. An example of trimming the surface of a facet when it is partially occluded by another facet that intersects the incident rays.

After reflection on facet *f* we can assume that the reflected fields are located in a cylindrical tube of collimated rays parallel to the direction of reflection. This tube can suffer a total or partial occlusion from some of the facets of the structure. In the case of a total occlusion, we can state that facet *f* is shadowed in the observation direction $\hat{k}_o$ and therefore does not contribute to the RCS. In the case of partial occlusion, we will compute the trimming of the reflected tube section; after trimming the tube will have a surface S_f^{io}. We only employ rigorous algorithms for facet occlusion computations to the facets in the anxel of the AZB of facet *f* that contains the observation direction $\hat{k}_o$ in order to only select the facets that can potentially occlude the tube of rays reflected by facet *f*, as shown in Fig. 10 [13].

We note that applying the rigorous algorithms for determining if a facet is shadowed completely or partially in either the incidence or observation directions by other facets, and in this case the corresponding trimming, is time consuming and shall be applied only to the facets that have a chance to occlude facet *f*. The AZB of facet *f* permits us to select the facets that can potentially occlude facet *f*, lowering the complexity of the problem by a factor of $N/(N_1N_2)$, where N_1N_2 is the number of anxels considered in the AZB of the facets.

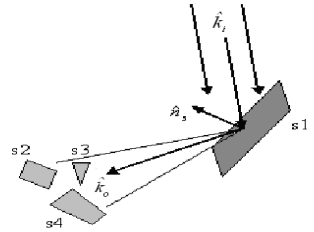

Fig. 10. Only the facets included in the anxel AZB of facet S1 that contain the direction $\hat{k}_o$ are considered for studying of the occultation of the tube of rays reflected in S1.

B. Computation of the RCS Due to Double Reflections

The contribution to the RCS by double reflection between pairs of facets is computed using GO+PO. GO is applied to study the reflection on the first facet, while Gordon's expression is used to evaluate the PO integral of the current induced in the second facet. The ray-tracing approach starts by selecting the facets that can suffer the first reflection, following the procedure described above: facets not visible in the incident direction are discarded using the Culling's criterion; the surfaces that shadow a potentially illuminated facet are those located in the anxel of the AZB of the facet that contains the direction of incidence $\hat{k}_i$; rigorous checking algorithms for shadowing are applied only to the facets located in this anxel and the surface of the illuminated facets partially occluded is trimmed.

A reflected cylindrical tube of rays is formed for each facet that suffer the first reflection. The tube of rays follows the direction given by the Snell's law after the reflection in the illuminated facets. The tubes can bounce on some of the facets of the structure, and these secondary facets give the double reflection. These facets are located in

the anxels that contain the direction of reflection of the AZB of the facets from which the tube of rays emanates. The rigorous checking algorithms for shadowing are only applied to the facets of these anxels. The facets of these anxels that are partially illuminated by the tube of rays are trimmed.

The last step in the computation of double reflection is applied only to the set of facets completely or partially illuminated by the tubes of rays formed after the first reflection. When the tubes from this set suffer a second reflection, they change their direction of propagation following Snell's law. We note that due to its finite section, the tube of rays redirected by a facet becomes a narrow beam of width $\Delta\Phi$ around the direction of reflection in the far field. Therefore, if the direction of observation $\hat{k}_o$ is outside this beam, this facet does not contribute to the RCS in that direction of observation. Elsewhere, the facet can potentially contribute to the RCS due to double reflection. We shall check if the redirected tube is partially or totally occluded by the other facets of the structure. To efficiently treat this new occlusion study, we apply the rigorous checking algorithms only to the facets located in the anxel that contains the $\hat{k}_o$ direction of the AZB of the facet that suffers the second reflection. If the tube is partially occluded, we shall trim again the section of the tube in the surface of the facet that suffers the second reflection. The computation of the PO integral is performed only over the surfaces of the facets whose redirected tubes of rays have not been completely occluded.

We notice that when using only the Culing's criterion without the AZB algorithm, the complexity of the problem for a given incidence and reflection directions is proportional to $N^2/4$ for finding the pairs of facets that can contribute to the double reflection and the complexity is proportional to $3N^3/4$ for finding the potential occlusions by other facets in each one of the three segments of a ray path that underwent double reflection (from the source to the first facet of the pair, between the facets of the pair and from the second facet of the couple and the observation point). Using the AZB algorithm and the Culling's criterion the complexity is reduced to $N^2/(2(N_1N_2))$ for finding the pair of facets that can give a double reflection, and the complexity is reduced to $3N^3/(2(N_1N)^2)$ for finding the facets that can potentially occlude any one of the three segments of a double reflection ray-path.

C. Computation of the RCS Due to Triple and Higher Order Reflections

The contribution to RCS due to m-order reflections is related to sets of m-facets. In each set the field incident in the $\hat{k}_i$ direction is reflected by the first facet and its direction of propagation is redirected following Snell's law. The reflected field suffers consecutive reflections until it reaches the last facet of the set where the field is radiated in a beam that contains the direction of observation $\hat{k}_o$. The tube of rays that bounces the first facet will likely suffer successive trimming due to partial occlusions during its propagation along the ray path connecting the facets of the set. Finding the sets of m-facets that give m-order reflections and computing trimming for the tubes of rays after successive occlusions is undoubtedly a hard and cumbersome process. Without using a ray-tracing algorithm (except for Culing's criterion), the complexity of the problem for finding the contributing sets of m-facets is proportional to $(N/2)^m$ and the complexity of finding the occlusion of the tubes of rays proportional to $(m+1)\ (N/2)^{m+1}$. Using the AZB algorithm, the complexity of the problem is reduced to $(N^m/2)/(N_1N_2)^{m-1}$ for finding the groups of m-facets and to $(m+1)(N^{m+1}/2)(N_1N)^m)$ for finding the occlusions in the (m+1) segments of the ray paths.

Applying AZB for the first and last reflections is similar to the case of double reflection. The treatment of the reflection i^{th} is as follows:

- First, we study the facets potentially illuminated by the tube of rays reflected by the facet *i-1*. To do so, we consider all the facets in the anxel of the AZB of facet *i-1* that contains the direction of propagation of the tube. We apply rigorous algorithms to the facets of this anxel to accurately check if the illumination is total or partial. The tube of rays is trimmed after the occlusion in every facet that suffers total or partial occultation in the trajectory from the $(i\text{-}1)^{th}$ reflection to the i^{th} reflection.

- A new tube of rays is formed in every facet that undergoes the i^{th} reflection. The directions of these tubes are given by Snell´s law and their

section is formed by trimming the surfaces of every one of these facets with the incident tubes of rays in order to maintain only the illuminated parts. This trimming is performed using rigorous algorithms. Using these tubes of rays we can proceed to study the $(i+1)^{th}$ reflection.

IV. COMBINING AZB+SVP WITH THE DEPTH-LIMITED-SEARCH METHOD

A procedure for implementing the depth-limited-search method for exploring the search tree in Fig. 1 is summarized in the following paragraphs. The scheme permits the computation the RCS of a complex-faceted geometry. The maximum order or reflection is limited to N_{order}, the number of levels to be considered in the search tree.

Figure 11 is a flow chart of the new algorithm based on the combination of SVP+AZB with the depth-limited-search method.

1. The nodes of the first level in the search tree of Fig. 1 correspond to those facets that can be the first in the pair of facets that gives an n-order contribution to the RCS for prefixed incident and observation directions and any value of n. The facets of the first level are selected among all of the facets of the geometry considering back-face culling: the facets of the structure that are seen in the incidence direction (see appendix 3.b of [13]). These facets are considered as "active" surfaces and are stored in a list called OPENLIST. The facets are sorted in this list in an increasing order following the facet index, which is a number in the geometry database used for identifying the facets. Account number I_{level} is made equal to one and it is associated with each of the facets stored in OPENLIST.

2. The surface with the smallest facet order in OPENLIST, which is the first facet in that list, is selected. This surface is moved to the file ACTUAL and then removed from OPENLIST. The contribution to the RCS for the first reflection in the observation direction is computed using the algorithms described above in Section III.

3. If the I_{level} count of facets in ACTUAL is less than N_{order}, then next step is to update OPENLIST by inserting a new set of active surfaces into the list, or else the procedure skips to step 4. They are selected from the anxel of the AZB matrix of the surface in ACTUAL that contains the Snell reflection direction of that facet. The surfaces in

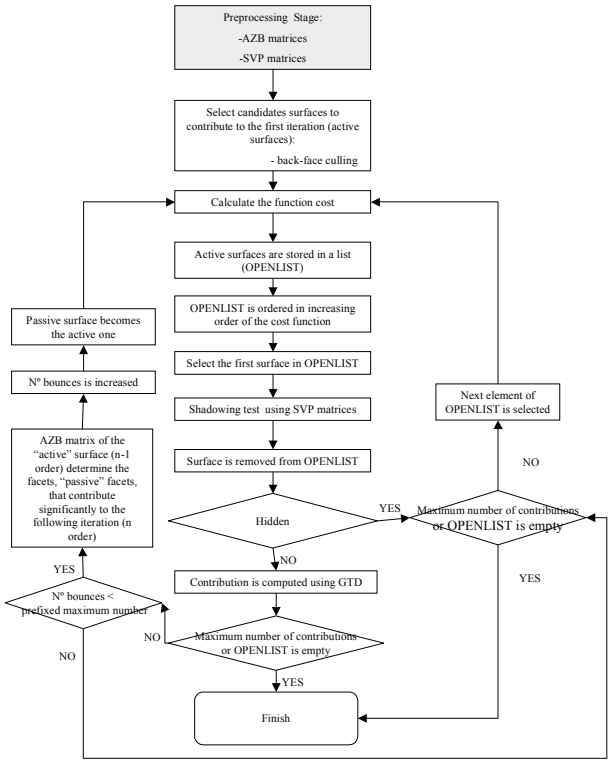

Fig. 11. Flow chart of AZB+SVP combined with the depth-limited-search method.

that anxel are inserted into the first spots in OPENLIST in increasing order of their facet index. The account number I_{level} associated with the new facets inserted in OPENLIST is the account number of ACTUAL plus one. We note that the new facets inserted in OPENLIST are placed in front of all of the facets previously stored in OPENLIST, and therefore the list can be classified as LIFO (last input-first input). The facet is then removed from ACTUAL.

4. The first facet in OPENLIST is removed and inserted in ACTUAL; the RCS contribution of this facet is computed following the procedure indicated in part 3 for a second or higher order reflection. Steps 3 and 4 are repeated.

The process is completed when all of the elements have been analyzed (OPENLIST is empty).

V. RESULTS

To show the performance of the new algorithm, several results are presented with an increasing difficulty. In all the cases presented the targets are

perfect electric conductors. The first case is the set defined by the dihedral and trihedral pictured in Fig. 12. The sides of both entities (dihedral and trihedral) are formed by flat 1.0m x 1.0m squares. The trihedral has its vertex at the origin of a Cartesian coordinate system with its sides parallel to the coordinate planes. The dihedral has one side parallel to the z=0 plane and the other parallel to the x = -y plane, as shown in Fig. 12. The coordinates of the mid-point of the edge of the dihedral are (2, 2, 1). The geometry of the case has been designed to show scattering with a large and rich number of interactions between the sides of the two entities of the figure when the set is illuminated by incident waves in the plane ϕ=45° (of the associated cylindrical coordinates). The structure undergoes multiple reflections/ diffractions. Until fifth order reflections are generated. Figures 13-14 show a comparison between RCS values for the geometrical approach using MONURBS [21], a moment method (MM) code, and POGCROS a computer code implemented using the present approach. In order to obtain reliable results, POGCROS was run computing until sixth order reflections. The results were stable if the effects order was increased until ten—in other words, for the incidence direction considered, sixth or higher order reflections are negligible. From the comparison between the MM results and the present approach we notice good agreement, considering the limitations of a GO-PO approach and the rich of mutual iterations of the test case in Fig. 12. The CPU-times using POGCROS (run in a Pentium Dual Core (2.5 GHz) using only one processor) have been of 50 s and 52 s for the cases with a maximum of 6 and 10 bounces, respectively.

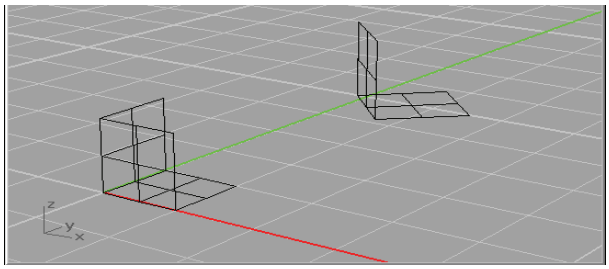

Fig. 12. Geometrical set defined by a dihedral and a trihedral designed in order to maximize the number of multiple reflections between the sides of the set.

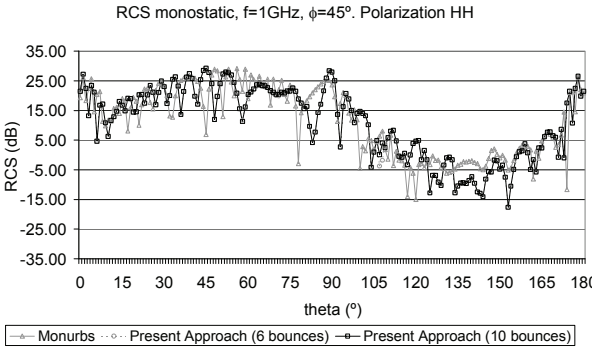

(a)

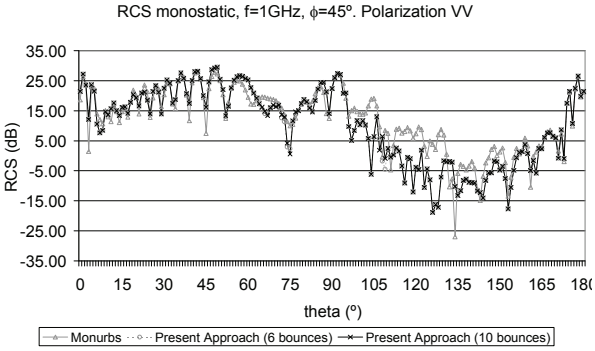

(b)

Fig. 13. Comparison between the values of the monostatic RCS for the geometrical structure in Fig. 12 obtained using MONURBS and the present approach for Φ =45°, for HH (a) and VV (b) polarizations and a frequency of 1 GHz.

Previous cases are suitable for analyzing the reliability of our proposed approach for simple problems with multiple reflections. We present here two examples to show the improvement in computational efficiency in terms of memory and CPU-time of our approach when complex problems are analyzed. The first case, called Placyl, is a hemisphere-cylinder above a flat plate as shown in Fig. 15. The radius of the hemisphere and of the cylinder is 0.2 m, the length of the cylinder is 1 m and the dimensions of the plate are 1.8 m and 1.2 m. The axis of the cylinder is parallel to the longer side of the plate and there is a gap between the cylinder and the plate of height 0.02 m. The Placyl case has been modeled by 1038 flat surfaces. Figure 16 shows the monostatic results obtained for HH and VV polarizations for a θ =45º cut and a sweeping from Φ =0º to Φ =180º

running POGCROS with a maximum of six bounces.

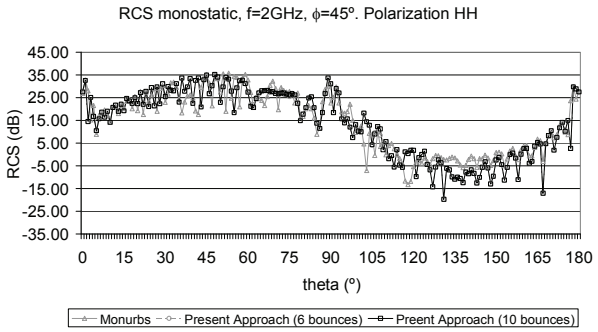

(a)

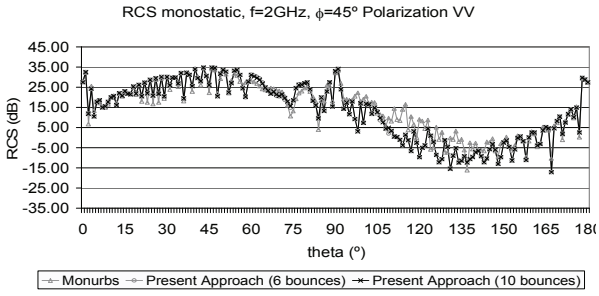

(b)

Fig. 14. Comparison between the values of the monostatic RCS for the geometrical structure in Fig. 12 obtained using MONURBS and the present approach for Φ =45°, HH (a) and VV (b) polarizations and a frequency of 2 GHz.

The comparison between the results obtained with MONURBS and POGCROS show a reasonably good agreement between MM and GO+GO...+PO approaches. The results of POGCROS have been run in a Pentium Dual Core, 2.5 GHz, using only 56 MB of RAM and a CPU-time of 5 min 21 sec.

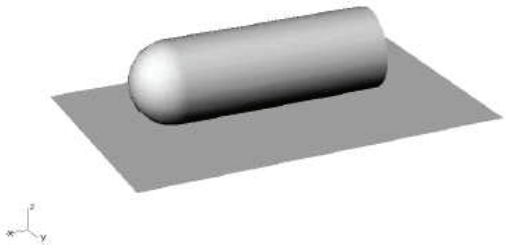

Fig. 15. Geometric model and coordinates system of the "placyl" case.

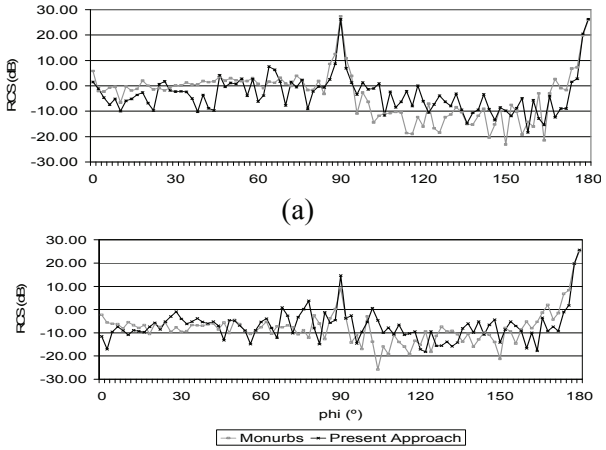

(a) (b)

Fig. 16. Comparison between the values of the monostatic RCS for the plane-cylinder geometrical structure shown in Fig. 15 obtained using MONURBS and the present approach for Φ =45°, HH (a) and VV (b) polarizations and a frequency of 10 GHz.

Fig. 17 . Flat faceted model of T72 tank.

The last and more complex example presented here is a geometrical model of a T72 tank composed of 22,225 flat facets, as shown in Fig. 17. First, we study the reliability of the results obtained using present approach (POGCROS) for this complex target. To do so, in Fig. 18 we compare RCS results for the T72 tank obtained using POGCROS and FASCRO. This last code is a well tested computer tool that can be considered as a previous version of POGCROS. The FASCRO code is based on an electromagnetic approach kernel similar to that used by POCROS to compute the RCS [6], but with a less efficient ray-tracing engine that is not able to treat more than two bounces with affordable computational resources. Due to this limitation of FASCRO, the comparison in Fig. 18 considers a maximum of two bounces. We note that the results obtained with both codes agree very well. However, the

computational resources required for obtaining the RCS values for the 360 directions in Fig. 18 are very different, as can be seen in table 1 where the superior efficiency of POGCROS is quite clear (a SUN V40Z computer has been used for all the T72 calculations in this paper).

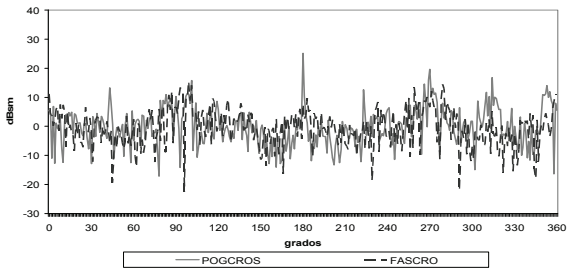

Fig. 18. Comparison between monostatic RCS results obtained using FASCRO and POGCROS for the cut θ = 72º, from Φ = 0º to Φ = 360º at 10 GHz and vertical polarization.

The POGCROS code has been used to study the impact on the RCS values from the maximum number of bounces in the ray-tracing. The RCS of a large and complex target, as it is the case for the T72, fluctuates very fast when we consider a step of a degree in a given cut, as for example the θ=72º cut. Due to these fast fluctuations it is difficult to obtain conclusions from RCS diagrams obtained when considering different values for the maximum number of bounces when they are drawn together. To avoid these problems, we consider windowed values of the RCS for each direction in the cut. Figure 19 show the averaged RCS values for each direction considering a 5 degree width flat window (the value shown for a given direction Φ_a is the average of the RCS in dBm considering the five directions contained in angular sector of 5 degrees centered at Φ_a). Figure 19 show results obtained considering 2, 3 and 6 bounces. The convergence is obtained considering 6 or more bounces. It can be noticed that the results obtained considering a maximum of only 2 bounces are not accurate enough compared with the results with a maximum of 6 bounces. Therefore, for the complex T72 target, it is evident that one needs to have available computer tools that are able to analyze the RCS considering 3 or more bounces with affordable computational resources. Table 2 shows the CPU-time and computer memory required for obtaining the RCS of the T72 for the 360 possible directions and a given maximum number of bounces. A SUN V40Z computer was used for all of the simulations

Table 1: Comparison between the CPU-time and computer memory required by FASCRO and POGCROS for obtaining the results of Fig. 21.

Code	CPU-time	Memory
POGCROS	1h, 45m, 33s	200 MB
FASCROS	8h, 52m, 32s	2 GB

Table 2: CPU-time and memory required by both polarizations considering several values of the maximum number of bounces in the RCS analysis.

Maximum number of bounces	Polarization vv	Polarization hh	Memory
2	1h, 45m, 33s	1h, 44m, 40s	200 MB
4	1h, 56m, 22s	1h, 54m, 23s	200 MB
6	2h, 00m, 15s	1h, 59m, 29s	200 MB
10	2h, 02m, 40s	2h, 01m, 56s	200 MB

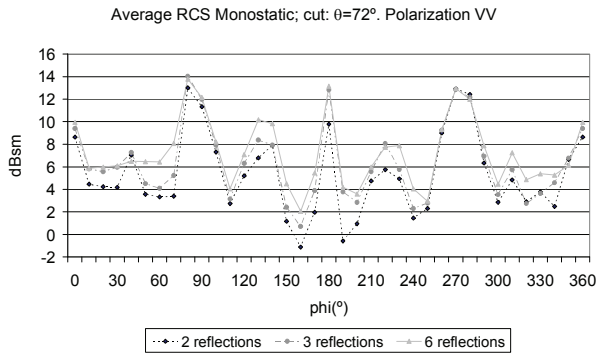

(a)

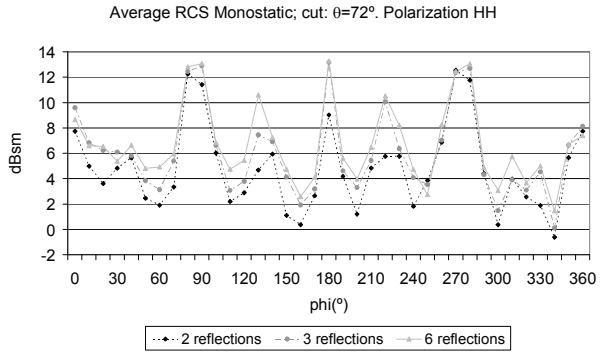

(b)

Fig. 19. Convergence study of the averaged monostatic RCS at 10GHz for VV and HH polarizations changing the maximum number of bounces considered.

in table 2. We note that the increase in computer resources to consider 3 or more bounces is negligible.

VI. CONCLUSIONS

An approach that combines an electromagnetic model based on GO and PO and a new ray-tracing scheme for the analysis of the Radar Cross Section (RCS) of complex structures that considers any number of bounces is presented. The structures are modeled by flat surfaces. The new ray-tracing scheme presented is based on a combination of the angular Z-buffer (AZB), volumetric space partitioning (SVP) and depth-limited-search methods and it is very efficient for computing the RCS of large and complex bodies. Several results have been presented for simple targets to show the accuracy of the approach. When analyzing large and complex targets, where one needs to take into account 3 or more bounces, we prove that the approach needs a very small amount of computer memory and affordable CPU-times.

Currently the authors are extending this approach to find the RCS of bodies modeled by curves surfaces. The approach has recently been implemented for analysis of radiating sources near complex bodies [22]. In a preprocessing stage of the approach, the curved surfaces are converted into small facets according to the curvature of the surface. Thus, the reflection points are calculated on the facets by applying image theory and the Z-buffer algorithm. This ray-tracing algorithm is able of computing n-order bounces. Once the *n* points of reflection are calculated they are used as a point seed in a conjugate gradient algorithm that is used to accurately compute the real reflection points on the curved surface.

ACKNOWLEDGMENTS

This work has been supported, in part by the Comunidad de Madrid and S-0505/TIC/0255 and by the Spanish Department of Science, and Technology Projects TEC 2007-66164 and CONSOLIDER-INGENIO Nº CSD-2008-0068.

REFERENCES

[1] N. N. Youssef, "Radar Cross Section of Complex Targets", *Proceedings of the IEEE,* vol. 77, no. 5, May 1989, pp. 722-734.

[2] E. F. Knott, "A Progression of High Frequency RCS Prediction Techniques", *Proceedings of the IEEE,* vol. 73, no. 2, pp. 252-264, February 1985.

[3] A. Michaeli, "Equivalent edge currents for arbitrary aspects of observation", *IEEE Transactions on Antennas and Propagaion.,* vol. AP-32, pp. 252-258, Mar. 1984.

[4] W. B. Gordon, "Far-Field Approximation to the Kirchoff-Helmhotz Representations of Scattered Field", *IEEE Transactions on Antennas and Propagation,* vol. AP-23, pp. 864-876, July 1975.

[5] D. S. Jones and M. Kline, "Asymptotic expansions of multiple integrals and the method of the stationary phase", *J. Math. Phys.,* vol. 37, pp. 1-28, 1957.

[6] F. Saez de Adana, I. González, O. Gutiérrez, P. Lozano, and M.F. Cátedra, "Method Based on Physical Optics for the Computation Radar Cross Section Including Diffraction and Double Effects of Metallic and Absorbing Bodies Modeled With Parameter surfaces", *IEEE Trans. on Antennas and Propagation,* vol. AP-53, pp. 3295-3303, Dec. 2005.

[7] T. Griesser and C. A Balanis, "Backscatter Analysis of Dihedral Corner Reflectors Using Physical Optics and Physical Theory of Diffraction", *IEEE Transactions on Antennas and Propagation,* vol. AP-35, pp. 1137-1147, Oct. 1989.

[8] J. Baldauf, S. W. Lee, L. Lin, S. K. Jeng, S. M. Scarborough, and C. L. Yu, "High Frequency Scattering From Trihedral Corner Reflectors and Other Benchmark Targets: SBR Versus Experiment", *IEEE Transactions on Antennas and Propagation,* vol. AP-39, pp. 1345-1351, Sept. 1991.

[9] S. Russel and P. Norvig, *Artificial Intelligence: a Modern Approach,* Prentice Hall, 2003.

[10] H. Ling, R. Chou, and S. W. Lee, "Shooting and Bouncing Rays: Calculating the RCS of an Arbitrarily Shaped Cavity," *IEEE Transactions on Antennas and Propagation,* vol. AP-37, pp. 194-205, Feb. 1989.

[11] D. J. Andersh, M. Hazlett, S. W. Lee, D. D. Reeves, D. P. Sullivan and *Y.* Chu, "Xpatch: A High Frequency Electromagnetic Scattering Prediction Code and environment for Complex Three-Dimensional Objects," *IEEE Antennas and Propagation Magazine,* vol. 36, pp. 65-69, Feb. 1994.

[12] J. Perez, F. Saez de Adana, O. Gutierrez, I. Gonzalez, M. F Cátedra, I. Montiel, and J. Guzman, "FASANT: Fast Computer Tool for the Analysis of on board Antennas", *IEEE Magazine on Antennas & Propagation,* pp. 15-28, Apr. 1999.

[13] M. F. Cátedra and J. Pérez-Arriaga, *Cell Planning for Wireless Communications,* Artech House Publishers, 1999.

[14] G. F. Luger, *Artificial Intelligenc. Sructures and Strategies for Complex Solving,* Addisson Wesley, 2005.

[15] L. Lozano, M. I. Hernández, C. Romera, I. González, F. Saez de Adana, and M. F. Cátedra, "Ray-Tracing acceleration techniques to compute RCS of complex targets", *IEEE Antennas and Propagation Society Symposium,* pp. 4495-4498, June 2004.

[16] L. Lozano, E. Ortega, F.Saez de Adana, and F, Catedra, "Improvements in ray-tracing acceleration techniques to compute diffraction effect and doubles and triples effects in the RCS prediction of complex targets", *IEEE Antennas and Propagation Society International Symposium,* vol. 3A, pp. 93- 96, July 2005.

[17] L. Lozano, I. Gonzalez, O. Gutierrez, J.M. Gomez, and F. Catedra, "Iterative method for computing N - reflections between flat surfaces in the RCS prediction of complex targets", *IEEE Antennas and Propagation Society International Symposium,* pp. 2502-2505, June 2007.

[18] L. Lozano, M.J. Algar, M. Blanco, I. Gonzalez, and F. Catedra, "Depth limited search applied to compute N-order reflections in the analysis of the RCS in large and complex targets", *IEEE Antennas and Propagation Society International Symposium,* vol. AP-S, pp. 1-4, July 2008.

[19] M. J. Algar, L. Lozano, I. Gonzalez, F. Catedra, "An efficient approach to compute the RCS of complex targets consideringmultiple bounces", *Antennas and Propagation, (EuCAP),* pp. 3703-3707, March 2009.

[20] V. Havran, *Heuristic Ray Shooting Algorithms*, Dissertation Thesis, November 2000.

[21] I. González, E. Garcia, F. Saez de Adana, and M. F. Cátedra, "MONURBS: A Parallelized Multipole Multilevel Code for Analyzing Complex Bodies Modeled by NURBS Surfaces", *Applied Computational Electromagnetics Society Journal,* vol. 23, no. 2, pp. 134-14, June 2008.

[22] F. Cátedra, L. Lozano, and I. Gonzalez, "New Algorithm for Computing Antenna Iterations with flat/curved Structures considering any Number of Bounces**"**, *30th ESA Antenna Workshop on Antennas,* pp. 551-554, May 2008.

Manuel F. Catedra received his M.S. and Ph. D. degrees in Telecommunications Engineering from the Polytechnic University of Madrid (UPM) in 1977 and 1982 respectively. From 1976 to 1989 he was with the Radiocommunication and Signal Processing Department of the UPM. He has been Professor at the University of Cantabria from 1989 to 1998. He is currently Professor at the University of Alcalá, in Madrid, Spain. He is a Fellow of the IEEE.

He has worked on about 90 research projects solving problems of Electromagnetic Compatibility in Radio and Telecommunication Equipment, Antennas, Microwave Components and Radar Cross Section and Mobile Communications. He has developed and applied CAD tools for radio-equipment systems such as Navy-ships, aircraft, helicopters, satellites, the main contractors being Spanish or European Institutions such as EADS, ALCATEL, CNES, ALENIA, ESA, DASA, SAAB, INTA, BAZAN, INDRA, the Spanish Defence Department.

He has directed about 15 Ph D. dissertations, has published about 60 papers (IEEE, Electronic Letters, etc), and two books.

Lorena Lozano Plata was born in Madrid, Spain in 1978. She received the BS, MS and PhD. Degrees in Telecommunications Engineering from the University of Alcalá, Spain, in 2000, 2002 and 2006, respectively. Since 2005 she works at the University of Alcalá, fist as Faculty Research

and since 2007 as Professor. She has worked as Faculty Research at Arizona State University from May 2004 to November 2004.
Her areas of interest are on-board antennas analysis, radio propagation on mobile communications, ray-tracing techniques and high frequency techniques, where she has worked on about forty research projects solving problems of Radar Cross Section computation, analysis of on board antennas, Mobile Communications, radio propagation, etc.
She has given short courses and has given about twenty presentations in International Symposium. She has authored four papers in referred journals and in chapters in a book.

Iván González Diego was born in Torrelavega, Spain in 1971. He received the B.S. and M.S. degrees in telecommunications engineering from the University of Cantabria, Spain, in 1994 and 1997 respectively, and the Ph.D degree in telecommunications engineering from the Univeristy of Alcalá , Madrid, Spain in 2004.

He worked in the Detectability Laboratory of the National Institute of Technical Aerospace (INTA), Madrid, Spain in RCS prediction and measurements and as Assistant Researcher at the University of Alcalá. Since 2004, he works as Assistant Professor in the University of Alcalá in the Computation Science Department teaching concepts about Data Base Systems. He has participated in several research projects with Spanish and European companies, related with analysis of on board antennas, radio propagation in mobile communications, RCS computation, etc. His research interests are in numerical methods applied to the electromagnetic problems, rigorous and asymptotic techniques like Method of Moments, GTD/UTD, PO, etc. He is also interested in the numerical methods to represent complex bodies for the electromagnetic techniques and compuer graphics is one of his research area.

Eliseo Garcia was born in Madrid, Spain, in 1977. He received the B.S., M.S. and Ph.D. degrees in telecommunication engineering from the University of Alcalá, Spain, in 1999, 2001 and 2005, respectively.
Since 2005, he worked at the University of Alcalá, first as Assistant Professor and since 2006 as Associated Professor in the Automatic Department. His research interests include numerical methods applied to scattering and radiation problems, parallel computing and fast computational techniques applied to electromagnetics.

María Jesus Algar Díaz was born in Madrid, Spain in 1984. She received a MS (2007) in Telecommunications Engineering from Alfonso X El Sabio University, Spain. She is currently pursuing a PhD. in Tlecommunications from University of Alcalá, where she works as Research. Her current research interests include analysis of on-board antennas, radio propagation on mobile communications, ray-tracing techniques and high frequency techniques.

Parallel Implementations of the PEEC Method

Danesh Daroui and Jonas Ekman

Department of Computer Science and Electrical Engineering
Luleå University of Technology, 971 87 Luleå, Sweden
danesh.daroui@ltu.se, jonas.ekman@ltu.se

Abstract ─ This paper presents the first parallel implementation of a partial element equivalent circuit (PEEC) based electromagnetic modelling code suitable for solving general electromagnetic problems. The parallelization is based on the GMM++ and ScaLAPACK packages which are cross-platform libraries available for major operating systems. The parallel PEEC solver has been tested on several high performance computer systems. Large structures containing over 250 000 unknown current and voltage basis functions were successfully analyzed for the first time with a general PEEC-solver. The numerical examples are of orthogonal type, studied both in the time and frequency domain, for which memory, performance, and speed-up results are presented.

Index Terms ─ PEEC, parallel computing, integral equation.

I. INTRODUCTION

As for all the methods within computational electromagnetics, the problem system size that can be solved increases with more efficient computer implementations and more powerful computer systems. However, the desired problem sizes to be solved also increase and there is a clear gap between desired and possible problem size to be solved. Fast solutions for EM problems have been treated for a long time, i.e. [1] where both differential and integral equation solvers were discussed. For the integral equation based solvers, fast Krylov subspace approaches are available, for example, the fast-multipole method (FMM) [2] and QR-based algorithms [3]. The next step, after faster implementations, is to improve the computing power running the algorithms. One solution is to use grid computing on different levels. For example, using a local area network of interconnected computers to speed-up calculations or by porting the code to parallel architectures. Recent publications on the extension to parallel implementations are for example [4] where a nesting combination of the finite element domain decomposition method and the algebraic multigrid method is presented, [5] on the implicit FDTD method, and [6] for a parallel version of the numerical electromagnetics code (NEC).

The partial element equivalent circuit (PEEC) method [7] is widely used for solving mixed circuit and electromagnetic (EM) problems. The method gives a framework for creating electric equivalent circuit representations for three-dimensional electromagnetic problems and calculating self and mutual partial inductances [8] and capacitances (coefficients of potential) [9]. The resulting equivalent circuits can be solved in SPICE-like solvers or, for the full-wave case, by creating and solving the fully coupled circuit equations [10]. Until now, no parallel implementation on the PEEC method has been reported except for in [11] where a sequential code was parallelized for LANs using a freeware. In this paper, the first parallel implementation of a non-accelerated, e.g. FMM, PEEC method [12] is presented for high performance computing using the ScaLAPACK package [13].

Other approaches for accelerating PEEC-based computations are for example FMM-based approaches as detailed in [14, 15], wavelet-based PEEC analysis as in [16-18], and QR-decomposition as shown in [19]. The goal with this work has been to accelerate the general PEEC method which allows for both time and frequency domain solution from DC to the highest frequency of interest (given by the mesh) and not to be restricted by the above mentioned acceleration techniques impacting, for example, on the low frequency behaviour. The paper is organized in the following way. Section II presents a summary of

the PEEC method and the developed computer program while Section III presents the parallelization of the same using the ScaLAPACK package. Then, Section IV and V show the applicability of the solver for two numerical examples, a free-space reactor and a shielding study. Finally conclusions and further work are detailed in Section VI. It is shown that with this type of parallel PEEC solvers the problem size can be increased considerably and new application areas arise.

II. SUMMARY OF PEEC THEORY

This section gives a brief summary of the classical, orthogonal PEEC formulation. For further information, see [7-9].

A. Extraction of Equivalent Circuit

The classical PEEC method is derived from the equation for the total electric field at a point [20] written as

$$\boldsymbol{E}^i(\boldsymbol{r},t)=\frac{\boldsymbol{J}(\boldsymbol{r},t)}{\sigma}+\frac{\partial \boldsymbol{A}(\boldsymbol{r},t)}{\partial t}+\nabla\varphi(\boldsymbol{r},t)\,, \qquad (1)$$

where E^i is an incident electric field, J is a current density, A is the magnetic vector potential, ϕ is the scalar electric potential, and σ the electrical conductivity all at observation point $\boldsymbol{r}$. By using the definitions of the scalar and vector potentials, the current- and charge-densities are discretized by defining pulse basis functions for the conductors and dielectric materials. Pulse functions are also used for the weighting functions resulting in a Galerkin type solution. By defining a suitable inner product, a weighted volume integral over the cells, the field equation (1) can be interpreted as Kirchhoff's voltage law over a PEEC cell consisting of partial self inductances between the nodes and partial mutual inductances representing the magnetic field coupling in the equivalent circuit. The partial inductances shown as L_{p11} and L_{p22} in Fig. 1 are defined as

$$L_{p\alpha\beta}=\frac{\mu}{4\pi}\frac{1}{a_\alpha a_\beta}\int_{v_\alpha}\int_{v_\beta}\frac{1}{|r_\alpha-r_\beta|}dv_\alpha dv_\beta\,, \qquad (2)$$

for volume cell α and β. Figure 1 also shows the node capacitances which are related to the coefficients of potential p_{ii} while ratios consisting of p_{ij}/p_{ii} are leading to the current sources in the PEEC circuit. The coefficients of potentials are computed as

$$p_{ij}=\frac{1}{S_iS_j}\frac{1}{4\pi\varepsilon_0}\int_{S_i}\int_{S_j}\frac{1}{|r_i-r_j|}dS_j dS_i\,, \qquad (3)$$

and a resistive term between the nodes, defined as

$$R_\gamma=\frac{l_\gamma}{a_\gamma\sigma_\gamma}\,. \qquad (4)$$

In (2) and (4), a represents the cross section of the rectangular volume cell normal to the current direction γ, and l is the length in the current direction. Further, v represents the current volume cells and S the charge surface cells. For a detailed derivation of the method, including the nonorthogonal formulation, see [21].

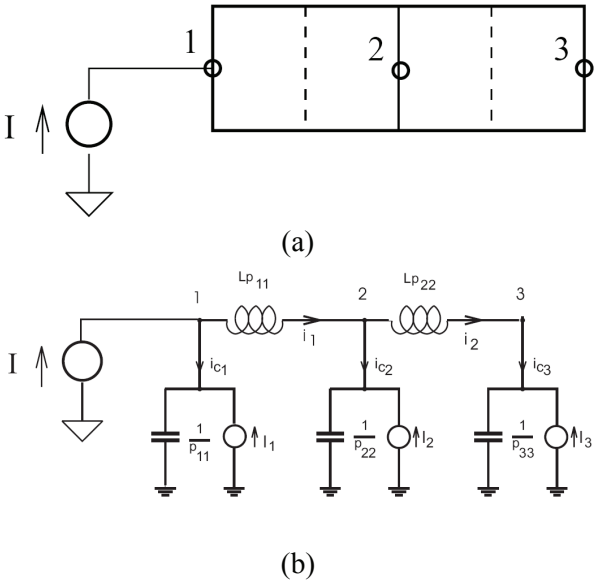

Fig. 1. Metal strip with 3 nodes and 2 cells (a) and corresponding PEEC circuit (b).

B. Solution of Equation of Circuit

The discretization process of the EFIE in (1) and the successive Galerkin's weighting leads to an equivalent circuit formulation. When Kirchhoff's voltage and current laws are enforced

to the N_i independent loops and N_ϕ independent nodes of the PEEC equivalent circuit we obtain:

$$\begin{aligned} &- A\Phi(t) - Ri_L(t) - L_p i_L^{\bullet}(t) = v_s(t), \\ &P^{-1}\Phi(t) - A^T i_L(t) = i_s(t), \end{aligned} \tag{5}$$

where

- $\Phi(t) \in \Re^{N_\phi}$ is the vector of node potentials to infinity; $\Re^{N_\phi}$ is the node space of the equivalent network;
- $i_L(t) \in \Re^{N_i}$ is the vector of currents including both conduction and displacement currents; $\Re^{N_i}$ is the current space of the equivalent network;
- L_P is the matrix of partial inductances describing the magnetic field coupling;
- P is the matrix of coefficients of potential describing the electric field couplings;
- R is the matrix of resistances;
- A is the connectivity matrix;
- $v_s(t)$ is the vector of distributed voltage sources due to external electromagnetic fields or lumped voltage sources;
- $i_s(t)$ is the vector of lumped current sources.

The equation system in (5) is equivalent to the circuit equations formulated in SPICE-type of solvers for obtaining the solution in node voltages and branch currents. However, for PEECs the equation system in (5) contain more dense matrices (L_P and P) compared to a pure electric network system solution due to the large number of mutually coupled inductors and mutual capacitances. Therefore, the solution of PEECs requires linear algebra packages suitable for dense matrices. The exception is the full-wave, time domain case where retarded magnetic and electric field couplings are treated as known sources and the L_p and P matrices are more sparse [10].

The equation system in (5) is often entitled a Modified Nodal Analysis (MNA) formulation [22] and can be modified to suit the solution of PEECs [10]. From the MNA formulation, the Nodal Analysis (NA) formulation can be derived which only solves for the node potentials by a reduced equation system while the branch currents are calculated in a second step. In the frequency domain the NA system can be written as

$$\Phi(\omega) = \left[- A^T (R + j\omega L_p(\omega))^{-1} A + j\omega P(\omega)^{-1} \right]^{-1} I_S . \tag{6}$$

to solve for the node potentials Φ at a specific frequency for the excitation specified by I_S. Both formulations are tested in this paper and results are presented in Sec. IV and V.

C. Sequential Code for EM Analysis Using PEEC Theory

A program for EM analysis, based on the theory and references outlined above, has been developed [23]. The solver can handle both the traditional orthogonal PEEC model and the newly introduced nonorthogonal formulation [21]. In this paper, only orthogonal models are considered while nonorthogonal results will be presented in a future paper since different issues arise when working with nonorthogonal PEEC models [24], [25]. The program creates an equivalent circuit and calculates the corresponding resistances, partial inductances, capacitances, and coupled voltage and current sources (to account for electromagnetic couplings) for the given geometrical layout (CAD-data as specified in an input file). The user adds external electronic (sub-) systems and analysis mode as described by the SPICE syntax. The actual solution of the resulting circuit equations (5) in either the time or frequency domain is performed in the solver and results are given as current- and voltage distributions in the geometrical layout. Post-processing routines are implemented for calculating field quantities at specified locations. The workflow in the program is shown in Fig. 2.

The sequential implementation utilizes the GMM++ linear algebra package and the Intel C++ Compiler with pragmas for compiler optimization to be performed. This allows, for example, for the use of multiple processors in calculating partial elements and other trivial pipelining, loop unrolling/distribution, data prefetching, and loop-carried dependencies occurring in the original, sequential implementation.

It is the presented sequential code that has been

parallelized and for which results are presented in this paper.

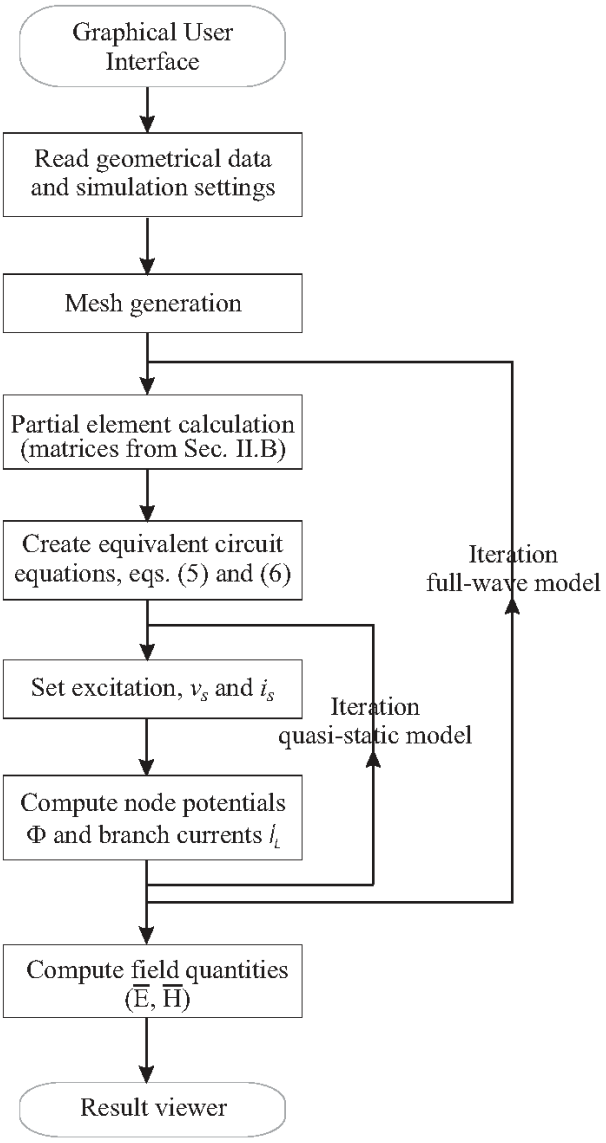

Fig. 2. Flow diagram for the PEEC solver.

III. PARALLELIZATION OF THE PEEC SOLVER

A. Introduction

The development platform was a Linux cluster consists of nodes equipped with two Intel Xeon quad-core 2.5 GHz CPUs and 16 GB of RAM memory. The code has been written in C++ under Linux and is compatible with parallel computer systems with distributed memory architecture using ScaLAPACK as computational library. ScaLAPACK (Scalable LAPACK) is a library of LAPACK routines, revised for parallel computer systems with distributed memory architecture. The package enables the use of high performance computing clusters in a simple fashion and allows for a considerable acceleration of the developed PEEC-based program. Like LAPACK, ScaLAPACK offers a set of highly optimized routines to solve systems of linear equations, which consists of matrices distributed among a bunch of processors. The library performs basic linear algebra operations such as product between matrices and vectors using PBLAS. PBLAS is parallel version of a rich library of computational routines called BLAS which is included in LAPACK. Finally a set of routines called BLACS is used to manage communication between nodes running ScaLAPACK. These routines use algorithms called block-partitioned algorithms to minimize movement of data between nodes by load balancing between computational elements. ScaLAPACK has been written in FORTRAN and developed for parallel computer systems. The choice to use this library was based on optimized and efficient message passing methods have been used in it, speed and scalability and good interface for C++ programmers. In addition it is a stable, well tested, and efficient library and provides access to a very large collection of useful, powerful and flexible functions in BLAS and LAPACK which have been parallelized efficiently. Using ScaLAPACK we were assured that a good load balancing is achieved by distributing input data on a bunch of processing nodes using block cyclic data distribution algorithms which speeds up the operations by minimizing data transfer between processing units.

The parallel solver performs these four steps to solve a problem:

1. The discretization process is entirely serial and duplicated on all processors.
2. The partial element calculations are easily parallelized as no communication is required between nodes while each node calculates assigned part of basic matrices in parallel with other nodes. The main difficulty lies in the mapping between global and local matrix coordinates [6].

3. The matrix formulation, (5) or (6), and solution parts are implemented using ScaLAPACK routines.
4. At the end when all processes have reached final synchronization point, the results will be gathered on the root processing unit and will be saved in appropriate format.

B. Parallelization of Partial Element Computations

The partial element calculations are easily parallelized using parallel processors which fill a large matrix, distributed by ScaLAPACK data management algorithms, completely in parallel and independent of each other. For the time domain problems these are L_P and P matrices which are symmetric and have entries of type double precision floating-point. Hence the fill-in times for the time domain solver is decreased linearly as number of allocated processors grows. Since these two matrices are symmetric, Cholesky factorization routines in ScaLAPACK package can be used to factorize them. Due to the properties of the entries of L_P and P matrices which has the type complex with double precision floating point for problems in frequency domain and because these matrices do not fulfill Hermitian properties, only LU factorization is possible and therefore the need to fill in the whole matrix. The process of placing element from one part of a distributed matrix to the other part is computationally expensive and complicated in parallel programs and especially for the MNA-approach seen in (5). But this was overcome by a special Transpose-And-Add method as detailed in [26].

C. Parallelization of Matrix Solutions

After filling-in the matrices, the solution of the time or frequency domain versions of the circuit equations in (5) and (6) has to be performed. This is done using the ScaLAPACK library of high-performance linear algebra routines for distributed memory message-passing MIMD (multiple instruction stream, multiple data stream) computers and networks of workstations supporting parallel virtual machine (PVM) and/or message passing interface (MPI). ScaLAPACK uses block cyclic data distribution [27] to achieving good load balancing. This means that matrices are divided into blocks in two dimensions and these blocks are assigned to a set of processors. This is further detailed in [6] when using the numerical electromagnetic code (NEC) to solve electromagnetic problems using ScaLAPACK.

IV. NUMERICAL TEST (I) - AIR-CORE REACTOR

To present the speed-up of the parallel PEEC implementation, an air-core reactor structure is utilized since measurement results have been collected and the cell count is easily increased. In previous papers, i.e. [28], the reactor have been studied in the time and frequency domain with regular (L_P, R, P, τ) PEEC models. However, the inclusion of Skin and proximity effects have not been possible in earlier works through the volume filament approach, (VFI)PEEC, due to the excessive number of unknowns. Here, the air-core reactor is analyzed with both the original serial PEEC solver, when possible and the new parallel PEEC solver in the time and frequency domain.

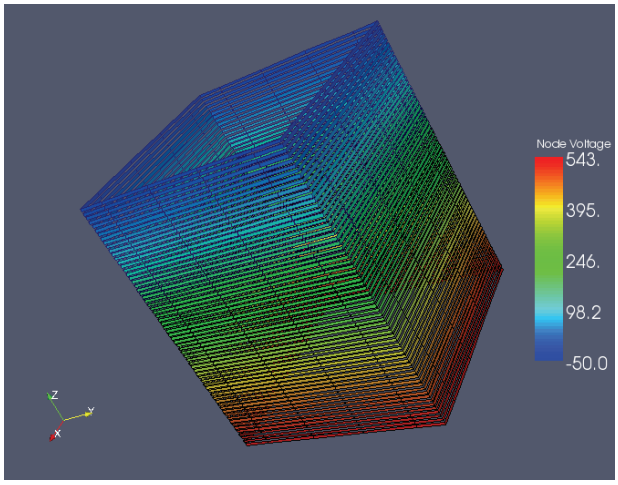

Fig. 3. Reactor voltage simulation result at 4 μs after impulse test.

The test structure, seen in Fig. 3, is of rectangular type with four sides equal in length = 0.5 m. The windings (turns) are totally 65 and consist of copper tape with dimension 0.076 mm x 6.35 mm. The center to center spacing between the turns is 10 mm. The parallel implementation of the solver can now treat this type of problem and give a more correct model for the current distribution in

the conductors. Figure 3 shows an example of the voltage distribution in the reactor windings for a, time domain, impulse test.

A. Partial Element Calculation Speed-Up

To test the speed-up, five different meshes for the reactor are utilized as seen in Table 1. For example, the first test, T1-400, has 1300 surface cells, 1040 volume cells, resulting in 2340 unknowns, and 1 105 nodes. The last test, T5-609, has 50180 unknowns since it uses the volume filament approach to model Skin effect in the windings. The naming conventions used for these test cases is in the format of T[*n*]-[*abc*], where n is the test case number and *a*, *b* and *c* represent the discretization level in the directions *x*, *y* and *z* respectively.

The partial element calculations are efficiently parallelized as seen in Table 2. The table is collected from time domain simulations. To be noted is that the test case is an orthogonal PEEC model utilizing analytical routines to evaluate partial inductances (< 5μs/element in sequential solver). The performance gain for the parallel implementation, as shown in Table 2, can be displayed by using a speed-up factor

$$S(n) = \frac{t_{p_1}}{t_{p_n}} \quad , \tag{7}$$

where t_{p_1} is the time taken by the parallel code using one processor and t_{p_n} is the time taken by the parallel code using n processors. This is shown in Fig. 4 where results from Table 2 are used together with results from the frequency domain solver by running the same test cases in the frequency domain.

From the figure it is clear that the time domain fill-in time is better than the frequency domain fill-in. This is because the time domain solvers use symmetric matrices with the data type of double precision floating point, so they can use symmetric compatible functions in ScaLAPACK which employ Cholesky factorization. But in the frequency domain, since non-Hermitian matrices with the data type of complex with double precision floating point are used, ScaLAPACK does not offer any symmetric compatible function. Therefore for frequency domain solvers the calculated part of matrix needs to be copied to the other part to form the complete matrix and this process will affect the speed-up factor as is shown in Fig. 4.

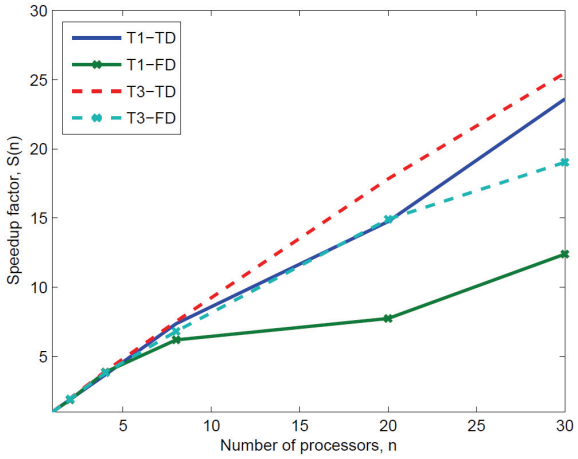

Fig. 4. Speed-up factor for partial element calculation and fill-in for air-core reactor example.

B. Solution Method - MNA or NA

From the calculated matrices, as briefly detailed in Sec. II-B, two popular methods are used to formulate the circuit equations for the PEEC model. First, the MNA formulation as shown in (5) and second the NA formulation as shown in (6). The MNA formulation is the more general of the two and preferred mainly due to its ability to handle general circuit element inclusion with the PEEC model [22] and a stable low frequency behavior. Table 3 gives details on the formulations of the different systems of circuit equations from a performance point of view.

The table gives details for three of the problems, T1, T3, and T5, when formulating the circuit equations using the Nodal Analysis (NA) or Modified Nodal Analysis (MNA) formulation in the time or the frequency domain. The table also shows several interesting results. For example, the formulations of the circuit equations are more time consuming in the frequency domain. This is expected since the equations involve complex numbers. Further, we see that the MNA formulation is always faster than the NA formulation even if the equation systems are larger in size. This is mainly due to an efficient formulation of (5) for which the inversion of the coefficient of potential matrix P is avoided [10].

Table 1: Reactor characteristics.

Test	surface cells (N_ϕ) (charge basis function)	Number of volume cells (N_i) (current basis function)	unknowns ($N_\phi + N_i$) (total)	nodes
T1-400	1 300	1 040	2 340	1 105
T2-900	2 600	2 340	4 940	2 405
T3-601	3 640	4 940	8 580	3 250
T4-605	10 920	18 460	29 380	9 750
T5-609	18 200	31 980	50 180	16 250

Table 2: Partial element calculations times for NA-implementation.

Number of processors	Time for TD-tests [s]				
	T1	T2	T3	T4	T5
Serial	9.0	35.0	81.0	-*	-
1	6.0	23.4	53.5	590.2	-
2	3.1	12.0	27.0	291.6	-
4	1.6	6.1	13.6	144.2	476.5
8	0.8	3.1	7.1	78.2	229.6
20	0.4	1.3	3.0	33.2	91.3
30	0.3	0.8	2.1	22.3	71.2

C. Total PEEC-Model Solution Time

To conclude the two previous subsections, speed-up factors for total PEEC-model solutions are given. This is shown in Fig. 5 for the time domain implementation of the NA and MNA methods and in Fig. 6 for the frequency domain implementation of the NA and MNA methods.

Since the speed-up factors, as presented in Figs. 5 and 6, are based on results for one processor, as seen in (7), it is not possible to show results for all test cases. However, using 30 processors, the only tests that could not be carried out with the current implementation are T4 and T5 in the frequency domain using the MNA method.

From the figures, several conclusions can be drawn:

- For small problems in the time domain, i.e. T1, and T2, increasing the number of processors does not improve the overall solution time since the communication

(a)

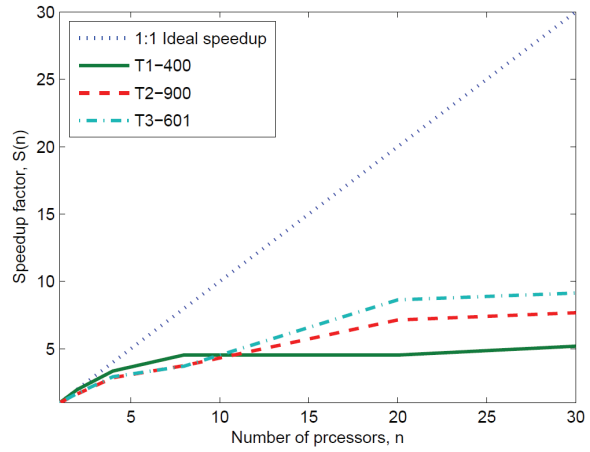

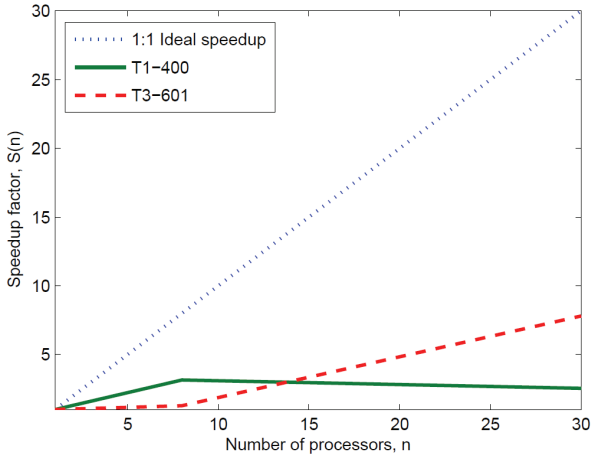

(b)

Fig. 6. Total PEEC-model solution time for frequency domain simulations using Nodal Analysis (a) and Modified Nodal Analysis (b).

Table 3: Time for formulation of circuit equations.

	Time in TD / FD [s]					
	T1-400		T3-601		T5-609	
	NA	MNA	NA	MNA	NA	MNA
Coefficient matrix size	1 300 × 1 300	2 340 × 2 340	2 640 × 2 640	8 580 × 8 580	18 200 × 18 200	50 180 × 50 180
Number of processors						
1	1.0 / 3.1	0.93 / 2.7	51.1 / 182.7	26.8 / 35	- / -	- / -
8	0.25 / 0.58	0.22 / 0.35	11.75 / 27.7	4.5 / 9.0	1 434 / 5 400	473 / -
30	0.26 / 0.32	0.14 / 0.26	4.11 / 9.7	2.0 / 3.0	634 / 2 300	138 / 380

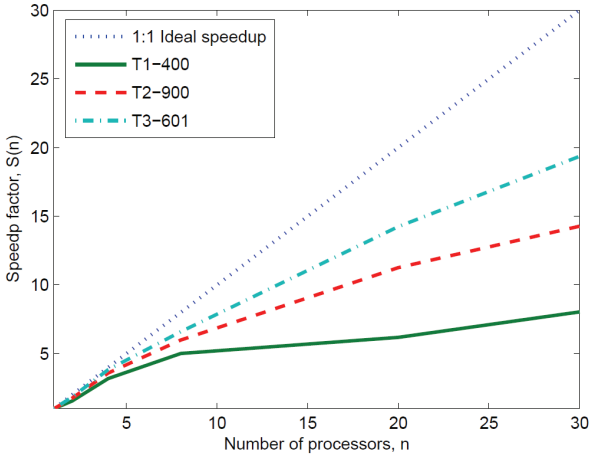

(a)

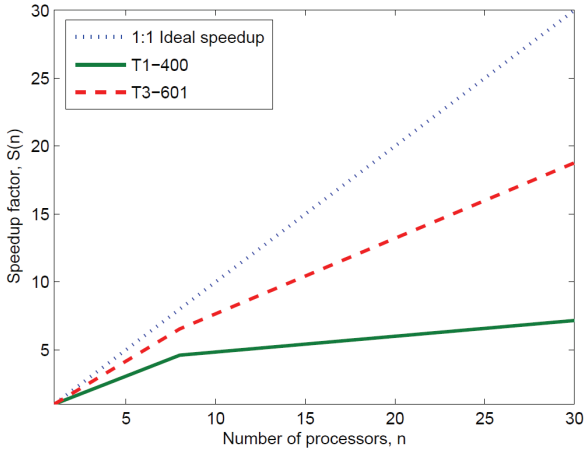

(b)

Fig. 6. Total PEEC-model solution time for frequency domain simulations using Nodal Analysis (a) and Modified Nodal Analysis (b).

time between the processors increases and exceed the total solution time. For example in Fig. 5 (a) and (b), problem T1 saturates at 8 processors. Hence, using a bunch of processors for a small problem will not necessarily improve the performance.

- Frequency domain problems experience a larger speed-up factor compared to time domain problem. However, in general frequency domain problems are more time consuming in absolute numbers.
- In both domains, the MNA-based solver shows better speed-up factor compared to the NA counterpart. This means that in both NA figures, the problem is already saturated or the speed-up factor grows very slowly when more processors are allocated. Thus, the MNA-formulation is more suited for parallelization using ScaLAPACK.

The figures presented in this section do not reveal the absolute solution time of the problems. It might seem that the MNA formulation is the fastest. However, in fact, the NA formulation is the fastest solution method for all tests. The MNA formulation is preferred for reasons given in Sec. IV-B.

D. Memory Usage

In this section, the memory usage of the parallel solver is presented based on the following aspects:

- memory usage as a function of number of processors;

- memory usage as a function of problem size.

1) *Memory usage as a function of the number of processors*: The total memory usage M should be a function of the number of processors, n, and the problem size. This can be expressed as

$$M = an + b, \tag{8}$$

where *a* and *b* are constants. Figure 7 shows the total memory usage *M* as a function of processors. The increase is clearly linear and eq. (8) is verified.

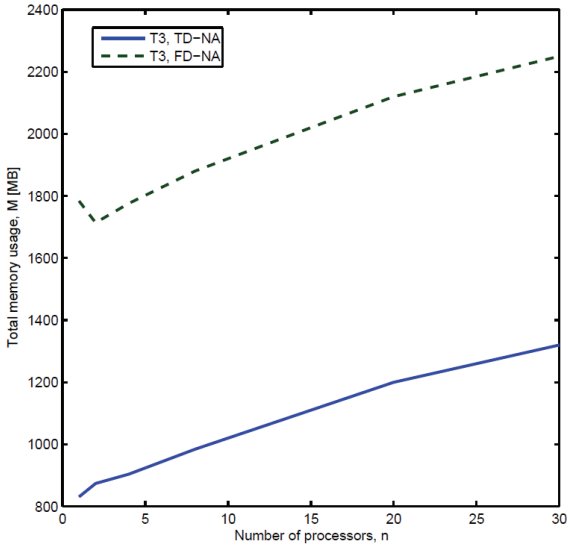

Fig. 7. Total memory usage as a function of processors.

Another way of expressing this is as average memory usage per processor *m* as

$$m = b/n + c. \tag{9}$$

This behavior for the parallel PEEC solver is verified by Table 4.

2) *Memory usage as a function of problem size*: The expected memory usage is

$$M = bn_u^2 + cn_u + d. \tag{10}$$

This is a simplification as in reality the actual increase is not as straightforward. This is due to the number of surface cells, volume cells, and nodes vary and the memory usage will be a more complicated function of these variables. The validity of (10) is exemplified in Fig. 8 for the parallel implementation using the NA approach in both the time and frequency domain on all the test cases from Table 1. Studying Fig. 8 when letting M be total memory usage and $(n_u = N_\phi + N_i)$ be the number of unknowns in eq. (10), the assumption is valid.

Table 4: Average memory usage for varying number of processors. Simulation of reactor.

Number of processors	Average memory usage/proc. [MB] T2-900		T5-609	
	TD	FD	TD	FD
1	281	643	-	-
2	160	303	-	-
4	86	159	7 472	-
8	51	88	3 815	-
20	28	44	1 543	3 545
30	24	34	1 049	2 395

V. NUMERICAL TEST (II) – SURGE TEST

In order to test the parallel solver and to find out how large problems can be solved, a second numerical example is presented. The setup is a surge pulse that is applied to a 100_100_150 cm enclosure. This is a problem that requires a fine mesh for a large structure and a long simulation time for the pulse to decay. In this test, the enclosure is excited on the top surface with a surge pulse given by

$$i(t) = I_0(e^{-\alpha t} - e^{-\beta t}), \tag{11}$$

Where

$I_0 = 218810$, $\alpha = 11354$ and $\beta = 647265$.

The enclosure is grounded using 1Ω resistor at the bottom surface. For comparison, CST software has been used to study the same problem. Figure 9 (a) shows voltage distribution in the enclosure due to the surge test and Fig. 9 (b) a comparison of CST and PEEC results for the resistor current/voltage (due to 1Ω resistor). As can be seen, the results are close to overlapping.

The simulation time was the main advantage of the PEEC simulations for this case. It was about 31 hours with the CST (note that the CST has more number of points than PEEC simulation).

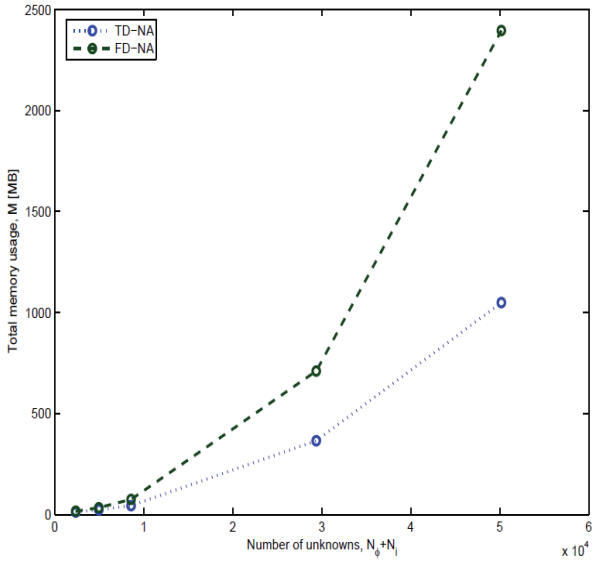

Fig. 8. Total memory usage for the Nodal Analysis implementation when increasing the problem size for a fixed number of processors (30).

The corresponding time with PEEC was about ten minutes using a sequential code (not the parallel implementation) for a mesh corresponding to ten cells per wavelength. The comparison can seem unfair, as often when comparing different basic formulations in computational electromagnetics. This example is an optimal PEEC-type of problem due to the thin, metallic walls of the enclosure located in free space. However, CST was used to validate the results and not to benchmark the implementation.

To test the parallel implementation, three cases with different discretization level were tested using the NA, time domain solver. Table 5 describes each test case and the corresponding number of unknowns. As can be seen, Surge3 contains more than a quarter of a million of unknowns and is the largest PEEC problem that has been solved using a general PEEC implementation capable of handling time and frequency domain analysis from DC to a maximum frequency given by the mesh. These problems have been designed to be large enough to stress the solver in both memory and computational complexity sense.

During these tests, it was always considered to choose an optimum number of processors, while using many processors for a small problem is not efficient and can even degrade the performance if the solver reaches or even pass saturation point. By optimum, it is meant smallest number of processors which can provide enough memory for a problem and solve the problem as fast as possible. Table 6 shows the simulation time, number of unknowns (repeated for convenience), memory consumption, and number of allocated processors for each test case.

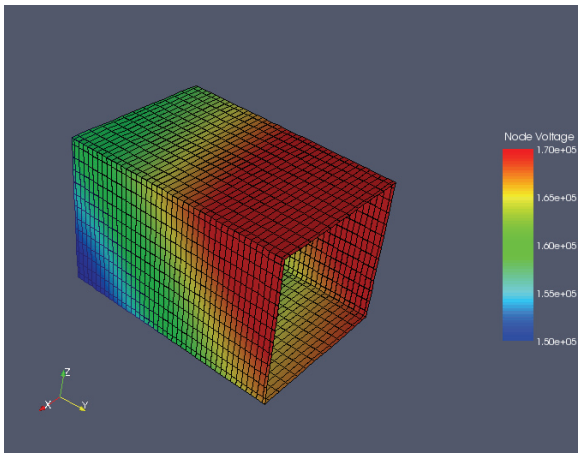

(a)

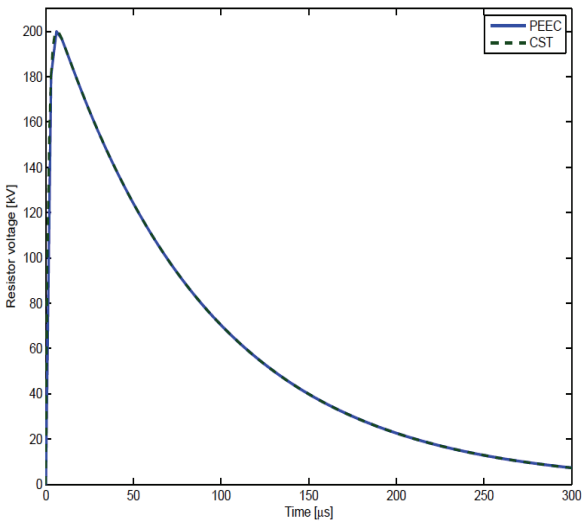

(b)

Fig. 9. Surge voltage simulation result at 1.8µs after impulse test (a) and comparison of PEEC and CST resistor current (b).

Table 5: Surge test characteristics.

Test	Number of surface cells (charge basis function)	volume cells (current basis function)	unknowns (total)	nodes
Surge 1	10 404	20 400	30 804	10 200
Surge 2	48 884	96 880	145 764	48 400
Surge 3	89 244	177 240	266 484	88 800

Table 6: Total solution times and memory for NA-implementation.

Test	Time [s]	Memory [GB]	Unknowns	Processors
Surge 1	45	16	30 804	80
Surge 2	677	278	145 764	120
Surge 3	8 700	931	266 484	440

With the number of unknowns handled in the largest test case, > 250 000, many complex problems can be studied using the PEEC method. For example, pure inductance and capacitance calculations for geometrically complex geometries, R-L-C equivalent circuit extraction, shielding and radiation problems of new computational complexity. However, with more complex models, new challenges arise in order to ensure correct simulation results [29], optimal mesh generation, and optimal usage of computational resources.

VI. CONCLUSION

In this paper the first parallel PEEC-based solver was presented which is applicable to problems formulated in both the time and frequency domain solving problems from DC to the highest frequency given by the appropriate mesh. The parallel PEEC-based solver is a ported version of the original sequential PEEC-based solver which uses GMM++ linear algebra package and is suitable for systems with shared memory structure such as multi-core machines. The parallel solver is designed to run on clusters with distributed memory architecture by using ScaLAPACK package to take advantage of any number of processors allocated in a parallel computer system.

The presented implementation opens up new doors for the solution of large problems formulates using the PEEC approach. In order to understand how parallel PEEC-based solver can improve solving problems, several tests were done. The results of these tests conclude that:

- Using a number of processors for small problems will not improve the solution time and even can degrade the performance, due to saturation.
- In general, frequency domain problems need more memory and are more time consuming, compared to time domain problems, but experienced larger speed-up factors when the number of processors was increased.
- MNA-based solver in both time and frequency domain resulted better in speed-up factor than NA-based.

By using 440 processors, problems with over quarter of a million unknowns could be studied using the nodal analysis formulation in the time domain. The next step for the presented parallel implementation is to apply acceleration algorithms, e.g. FMM, MLFMM, QR and using other LAPACK-based computational libraries, making the program suitable for solving different classes of EM problems on desktop machines.

REFERENCES

[1] W. C. Chew, J. M. Jin, C. C. Lu, E. Michielssen, and J. M. Song “Fast solution methods in electromagnetics”, *IEEE Transactions on Antennas and Propagation*, vol. 45, no. 3, pp. 533–543, 1997.

[2] N. Engheta, W. D. Murphy, V. Rokhlin, and M. S. Vassilou, “The fast multipole method (FMM)”, *PIERS*, July 1991.

[3] S. Kapur and D. Long., "IES: A fast integral equation equation solver for efficient 3-dimensional extraction," *Int. Conf. on Computer Aided Design*, pp. 448–455, November 1997.

[4] Y. Liu and J. Yuan, "A finite element domain decomposition combined with algebraic multigrid method for largescale electromagnetic field computation", *IEEE Transactions on Magnetics*, vol. 42, no. 4, pp. 655– 658, April 2006.

[5] T. Hanawa, M. Kurosawa, and S. Ikuno, "Investigation on 3-D implicit FDTD method for parallel processing", *IEEE Transactions on Magnetics*, vol. 41, no. 5, pp. 1696– 1699, May 2005.

[6] A. Rubinstein, F. Rachidi, M. Rubinstein, and B. Reusser, "A parallel implementation of NEC for the analysis of large structures", *IEEE Transactions on Electromagnetic Compatibility*, vol. 45, no. 2, pp. 177–188, May 2003.

[7] A. E. Ruehli, "Equivalent circuit models for three dimensional multiconductor systems", *IEEE Transactions on Microwave Theory and Techniques*, vol. MTT-22, no. 3, pp. 216–221, March 1974.

[8] A. E. Ruehli, "Inductance calculations in a complex integrated circuit environment". *IBM Journal of Research and Development*, vol. 16, no. 5, pp. 470–481, September 1972.

[9] A. E. Ruehli and P. A. Brennan, "Efficient capacitance calculations for three-dimensional multiconductor systems", *IEEE Transactions on Microwave Theory and Techniques*, vol. MTT-21, no. 2, pp. 76–82, February 1973.

[10] G. Antonini, J. Ekman, and A. Orlandi, "Full wave time domain PEEC formulation using a modified nodal analysis approach", *Proc. of EMC Europe*, 2004.

[11] F. Monsefi and J. Ekman, "Optimization of PEEC based electromagnetic modeling code using grid computing", *Proc. of EMC Europe*, 2006.

[12] J. Ekman and P. Anttu, "Parallel implementation of the PEEC method", *Proc. of Special Session at the IEEE Int. Symp. On EMC*, 2007.

[13] J. Choi, J. J. Dongarra, R. Pozo, and D. Walker. "ScaLAPACK: A scalable linear algebra library for distributed memory concurrent computers", *Proceedings of the Fourth Symposium on the Frontiers of Massively Parallel Computation, IEEE Computer Society Press*, 1992.

[14] G. Antonini, "Fast Multipole Formulation for PEEC Frequency Domain Modeling", *Journal of Applied Computational Electromag Society,* vol. 17, no. 3, November 2002.

[15] G. Antonini, J. Ekman, A. Ciccomancini Scogna, and A. E. Ruehli, "A comparative study of PEEC circuit elements computation", *Proc. of the IEEE International Symposium on EMC*, 2003.

[16] G. Antonini, A. Orlandi, and A. Ruehli, "Speed-up of PEEC method by using wavelet transform", *Proc. of the IEEE Int. Electromagnetic Compatibility*, August 2000.

[17] G. Antonini, A. Orlandi, and A. Ruehli, "Fast Iterative Solution for the Wavelet-PEEC Method", *Proc. of the International Zurich Symposium on Electromagnetic Compatibility*, February 2001.

[18] G. Antonini and A. Orlandi, "Computational properties of wavelet based PEEC analysis in time domain", *Proc. of Applied Computational Electromagnetics Society Conference*, March 2000.

[19] A. Ruehli, D. Gope, and V. Jandhyala, "Block partitioned gaussseidel PEEC solver accelerated by QR-based coupling matrix compression techniques", *Digest of Electr. Perf. Electronic Packaging*, vol. 13, pp. 325–328, October, 2004.

[20] S. Ramo, J. R. Whinnery, and T. Van Duzer, *Fields and Waves in Communication Electronics,* John Wiley and Sons, 1994.

[21] A. E. Ruehli, G. Antonini, J. Esch, A. Mayo J. Ekman, and A. Orlandi, "Non-orthogonal PEEC formulation for time and frequency domain EM and circuit modeling", *IEEE Transactions on Electromagnetic Compatibility*, vol. 45, no. 2, pp. 167–176, May 2003.

[22] C. Ho, A. Ruehli, and P. Brennan, "The modified nodal approach to network analysis", *IEEE Transactions on Circuits and Systems*, pp. 504–509, June 1975.

[23] LTU/UAq PEEC solver. Available. Online: http://www.csee.ltu.se/peec.

[24] A. Musing, J. Ekman, and J. W. Kollar, "Efficient calculation of non-orthogonal partial elements for the PEEC method". *IEEE Transactions on Magnetics*, 45(3), March 2009.

[25] J. Ekman, G. Antonini, G. Miscione, and P. Anttu, "Electromagnetic modeling of automotive platforms based on the PEEC method". *Proc. of Applied Computational Electromagnetics Society Conference*, Verona, IT, March 2007.

[26] D. Daroui. "Performance of integral equation based electromagnetic analysis software on parallel computer systems", Master's thesis, University of Gothenburg, February 2007.

[27] J. J. Dongarra and D. W. Walker. "The design of linear algebra libraries for high performance computers", Technical Report ORNL/TM-12404, University of Tennessee, Knoxville, TN, USA, 1993.

[28] M. Enohnyaket and J. Ekman. "Analysis of air-core reactors from dc to very high frequencies using PEEC models", *IEEE Transactions on Power Delivery*, vol. 24, no. 2, April 2009.

[29] J. Ekman, G. Antonini, A. Orlandi, and A. E. Ruehli, "The impact of partial element accuracy on PEEC model stability", *IEEE Transactions on Electromagnetic Compatibility*, vol. 48, no. 1, pp. 19–32, March 2006.

Advances of Neural Network Modeling Methods for RF/Microwave Applications

Humayun Kabir, Yi Cao, Yazi Cao, and Qi-Jun Zhang
Department of Electronics
Carleton University, Ottawa, ON K2C3L5, Canada
hkabir@doe.carleton.ca, ycao@doe.carleton.ca, yacao@doe.carleton.ca, qjz@doe.carleton.ca

***Abstract*—** This paper provides an overview of recent advances of neural network modeling techniques which are very useful for RF/microwave modeling and design. First, we review neural network inverse modeling method for fast microwave design. Conventionally, design parameters are obtained using optimization techniques by multiple evaluations of EM-based models, which take a long time. To avoid this problem, neural network inverse models are developed in a special way, such that they provide design parameters quickly for a given specification. The method is used to design complex waveguide dual mode filters and design parameters are obtained faster than the conventional EM-based technique while retaining comparable accuracy. We also review recurrent neural network (RNN) and dynamic neural network (DNN) methods. Both RNN and DNN structures have the dynamic modeling capabilities and can be trained to learn the analog nonlinear behaviors of the original microwave circuits from input-output dynamic signals. The trained neural networks become fast and accurate behavioral models that can be subsequently used in system-level simulation and design replacing the CPU-intensive detailed representations. Examples of amplifier and mixer behavioral modeling using the neural-network-based approach are also presented.

***Index Terms*—** Behavioral modeling, computer aided design, neural network.

I. INTRODUCTION

Neural network is an information processing system, which can learn from observation and generalize any arbitrary input-output relationship similar to human brain function. It has been used in many modeling and design applications [1], [2] such as vias [3], transistor [4], amplifier [5], filters [6–9], etc. Neural network can capture multidimensional non-linear device behavior accurately. The evaluation of a neural network model is also fast. These unique qualities make neural network a useful alternative of EM-based modeling.

Models developed in the conventional approach are termed as forward model where the inputs are the physical or geometrical parameters such as dielectric, length, width etc. and the outputs are electrical parameters such as S-parameters. For design purpose, the EM simulator or the forward model is evaluated repetitively in order to find the optimal solutions of the geometrical parameters that can lead to a good match between modeled and specified electrical parameters. An example of such an approach is [10]. Conversely, an inverse model is defined as the opposite to the forward model such that the geometrical or physical parameters become the outputs and electrical parameters become the inputs of the inverse model. The inverse model provides the required geometrical solution for a given electrical specification. This avoids repetitive model evaluation.

Recently an inverse modeling methodology using neural network technique has been presented [8]. The training data for the inverse model is generated using a forward EM model or from device measurement. The training data is reorganized such that the geometrical parameters become outputs and the electrical parameters become inputs. A neural network model trained using this reorganized model becomes the inverse model of the original EM-model or device. However, this process of reorganizing data may lead to a non-uniqueness problem where multiple solutions may exist for a single input value. We call it a multi-valued problem. If two or more different input values lead to a single value in the forward model, then contradiction arises in the training data of the inverse model. As a result, neural network faces hard time to provide accurate

solution at those points. To avoid these situations the data is first checked for contradictions. If contradiction exists, the inverse data is divided into sub-groups such that each sub-group does not contain any contradictory data. Multiple sub-models are then developed using the divided data. The sub-models are then combined using a special technique to form the overall inverse model. The description of various techniques is provided in the Section 2.

We also review the recent advances of neural network approaches for behavioral modeling of nonlinear microwave circuits. We focus on the specific artificial neural network (ANN) structures that are capable of learning and representing dynamic behaviors of nonlinear circuit blocks. Two ANN-based techniques, i.e., recurrent neural networks (RNN) [11–13] and dynamic neural networks (DNN) [14] techniques, are described from the perspective of nonlinear behavioral modeling. Numerical examples of modeling RF amplifiers and mixers are included.

II. INVERSE MODELING METHODS

A. Formulation of Inverse Model

Let $\boldsymbol{x}$ be an n-vector containing the inputs and $\boldsymbol{y}$ be an m-vector containing the outputs of the forward model. Then the forward modeling problem can be expressed as

$$\boldsymbol{y} = \boldsymbol{f}(\boldsymbol{x}), \tag{1}$$

where $\boldsymbol{f}$ defines input-output relationship, $\boldsymbol{x} = [x_1\ x_2\ x_3\ \ldots\ x_n]^T$, and $\boldsymbol{y} = [y_1\ y_2\ y_3\ \ldots\ y_m]^T$. Then the inverse model can be defined as

$$\overline{\boldsymbol{y}} = \overline{\boldsymbol{f}}(\overline{\boldsymbol{x}}), \tag{2}$$

where $\overline{\boldsymbol{f}}$ defines the inverse input-output relationship, $\overline{\boldsymbol{y}}$ and $\overline{\boldsymbol{x}}$ contains outputs and inputs of the inverse model respectively. As an example, if a device contain four inputs and three outputs then $\boldsymbol{x} = [x_1\ x_2\ x_3\ x_4]^T$ and $\boldsymbol{y} = [y_1\ y_2\ y_3]^T$. If input parameters x_3 and x_4 are design parameters, e.g., iris length and width of a waveguide filter and y_2 and y_3 are electrical parameters, e.g., couplings of the filter, then inputs of the inverse model become $\overline{\boldsymbol{x}} = [x_1\ x_2\ y_2\ y_3]^T$ and output vector becomes $\overline{\boldsymbol{y}} = [y_1\ x_3\ x_4]^T$. Figure 1 shows the diagrams of a neural network forward model and an inverse model. The inverse model of Fig. 1(b) is formulated by swapping partial inputs and outputs of the forward model of Fig. 1(a). Note that two input parameters and two output parameters are swapped.

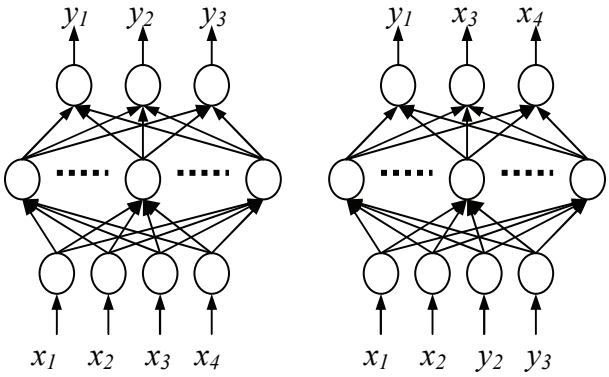

Fig. 1. Example illustrating neural network forward and inverse models, (a) forward model (b) inverse model. The inputs x_3 and x_4 (output y_2 and y_3) of the forward model are swapped to the outputs (inputs) of the inverse model respectively [8].

B. Non-Uniqueness in Inverse Training Data

If two different input values in forward model lead to the same value of output then a contradiction arises in the training data of the inverse model, because the single input value in the inverse model has two different output values (therefore contradictory data). Since we cannot train the neural network inverse model to match two contradictory data simultaneously, it is important to detect the existence of contradictions.

Detection of contradiction would have been straightforward if the training data were generated by deliberately choosing different geometrical dimensions such that they lead to the same electrical value. However in practice, the training data are not sampled at exactly those locations. Therefore, we develop numerical criteria to detect the existence of contradictions. We calculate the slope between samples within a specific neighborhood. A slope between two samples was calculated by dividing the normalized difference

of the *y*-values of the two samples with the normalized difference of the *x*-values of the two samples. If any of the slopes becomes larger than some user defined threshold value, then the data may contain contradictory samples. In that case we need to divide the data into groups such that the individual groups do not contain any contradiction. In this way we solve the problem of non-uniqueness of input-output relationship and thus contradictory sample in the inverse training data.

C. Method to Divide Inverse Training Data

If existence of contradictions is detected in training data, we perform data preprocessing. All the data samples, even though contradictory, are useful information and should not be deleted from the training data. In our method, we divide the data into groups so that contradictory samples are separated into different groups and the data in each group becomes free of contradiction. We divide the overall training data into groups based on derivatives of outputs vs. inputs of the forward model. Because variations in the output response changes directions with the change of input variables and multivalued problems occur when the response changes to a reverse direction. Thus derivative information is a logical criterion to detect such reverse phenomena. Let us define the derivatives of inputs and outputs that have been exchanged to formulate the inverse model, evaluated at each sample, as,

$$\left.\frac{\partial y_i}{\partial x_j}\right|_{\boldsymbol{x}=\boldsymbol{x}^{(k)}},\ i \in I_y \text{ and } j \in I_x, \tag{3}$$

where, $k = 1,2,3,...,N_S$, N_S is the total number of training samples, I_x is an index set containing the indices of inputs of forward model that are moved to the output of inverse model, and I_y is the index set containing the indices of outputs of forward model that are moved to the input of inverse model. The entire training data should be divided based on the derivative criteria such that training samples satisfying

$$\left.\frac{\partial y_i}{\partial x_j}\right|_{\boldsymbol{x}=\boldsymbol{x}^{(k)}} < \delta, \tag{4}$$

belong to one group and training samples satisfying

$$\left.\frac{\partial y_i}{\partial x_j}\right|_{\boldsymbol{x}=\boldsymbol{x}^{(k)}} > -\delta, \tag{5}$$

belong to a different group, where δ is zero or a small positive number. This method exploits derivative information to divide the training data into groups. We compute the derivatives by exploiting adjoint neural network technique [15]. Multiple neural networks are then trained with the divided data. Each neural network represents a sub-model of the overall inverse model.

D. Method to Combine Inverse Sub-Models

We need to combine the multiple inverse sub-models to reproduce the overall inverse model. For this purpose a mechanism is needed to select the right one among multiple inverse sub-models for a given input $\bar{\boldsymbol{x}}$. For convenience of explanation, suppose $\bar{\boldsymbol{x}}$ is a randomly selected sample of training data. Ideally if $\bar{\boldsymbol{x}}$ belongs to a particular inverse sub-model then the output from it should be the most accurate one among various inverse sub-models. Conversely the outputs from the other inverse sub-models should be less accurate if $\bar{\boldsymbol{x}}$ does not belong to them. However, when using the inverse sub-models with general input $\bar{\boldsymbol{x}}$ whose values are not necessarily equal to that of any training samples, the value from the sub-models is the unknown parameter to be solved. So we still do not know which inverse sub-model is the most accurate one. To address this dilemma, we use the forward model to help deciding which inverse sub-model should be selected. If we supply an output from the correct inverse sub-model to an accurate forward model we should be able to obtain the original data input to the inverse sub-model.

In our method input $\bar{\boldsymbol{x}}$ is supplied to each inverse sub-model and output from them is fed to the accurately trained forward model respectively, which generate different $\boldsymbol{y}$. These outputs are then compared with the input data $\bar{\boldsymbol{x}}$. The inverse sub-model that produces least error between $\boldsymbol{y}$ and $\bar{\boldsymbol{x}}$ is selected and the output from corresponding inverse sub-model is chosen as the final output of the overall inverse modeling problem.

We include another constraint to the inverse sub-model selection criteria. This constraint checks for the training range. If an inverse sub-model produces an output that is located outside its training range, then the corresponding output is

not selected. If the outputs of other inverse sub-models are also found outside their training range then we compare their magnitude of distances from the boundary of training range. An inverse sub-model producing the lowest distance is selected in this case.

III. ANN-BASED DYNAMIC BEHAVIORAL MODELING OF MICROWAVE CIRCUITS

A. Recurrent Neural Networks (RNN) for Time Domain Modeling

Conventional feed-forward neural networks (FFNN) [1] are well known for their learning and generalization capabilities. However, they are only suitable for mapping static input-output relationships. To model nonlinear circuit responses in time-domain, a neural network that can include temporal information is necessary. RNNs have been found to be a suitable candidate to accomplish this task. In the past, RNNs were successfully used in various engineering applications such as system control, speech recognition, etc [16]. For microwave dynamic modeling, the structure of a typical RNN is shown

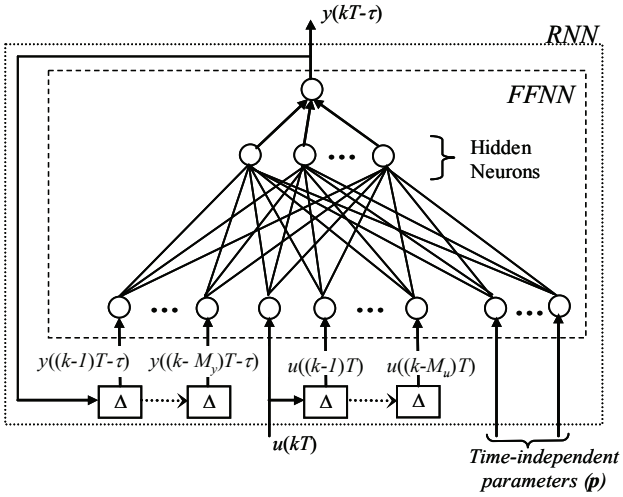

Fig. 2. RNN structure with output feedback (M_y). The RNN is a discrete time structure trained with sampled input-output data [12].

in Fig. 2 [12]. The RNN inputs include time-varying inputs $\boldsymbol{u}$ and time-independent inputs $\boldsymbol{p}$. The RNN outputs are the time varying signal $\boldsymbol{y}$. The input layer of the FFNN contains buffered (time-delayed) history of $\boldsymbol{y}$ fed back from the output layer, buffered history of $\boldsymbol{u}$, and $\boldsymbol{p}$. The hidden layer contains neurons with sigmoid activation functions. The FFNN outputs are linear functions of the responses of hidden neurons in the hidden layer. Let the trainable parameters of the RNN be denoted as $\boldsymbol{w}$. As can be observed from Fig. 2, the overall RNN structure, including both the FFNN part and feedback connections, realizes the following nonlinear dynamic relationship [12]

$$\begin{aligned}&\boldsymbol{y}(kT-\tau)\\&=\mathrm{f}_{\mathrm{FFNN}}(\boldsymbol{y}((k-1)T-\tau),...,\boldsymbol{y}((k-M_y)T-\tau),\\&\quad\boldsymbol{u}(kT),\boldsymbol{u}((k-1)T),...,\boldsymbol{u}((k-M_u)T),\boldsymbol{w},\boldsymbol{p})\end{aligned}\quad(6)$$

where k is the index for time step, T is the time step size, and τ is a delay element. The number of delayed time steps M_y and M_u, of $\boldsymbol{y}$ and $\boldsymbol{u}$ respectively, represent the effective order of original nonlinear circuit as seen from input-output data. $\mathrm{f}_{\mathrm{FFNN}}$ represents a static mapping function that could be any of the standard FFNN structures, e.g., a multilayer perceptron (MLP) neural network [1]. The formulation (6) is a generalization over the conventional RNN structure [13] by introducing the extra delay τ, which represents the delay between the input and output signals [12]. It has been found that this modified structure could help simplify the overall training of the model.

B. Dynamic Neural Networks (DNN) for Nonlinear Behavioral Modeling

For the purpose of circuit simulation, the most ideal format to describe nonlinear dynamics is the continuous-time domain formulation. In theory, this format best describes the fundamental essence of nonlinear behavior and in practice it is flexible to fit most or all the needs for nonlinear circuit simulation. On the other hand, for large-scale nonlinear microwave circuits, the detailed state equations [14] could be too complicated, computationally expensive, and sometimes even unavailable at system level. Therefore, a simplified (reduced order) model approximating the same dynamic input-output relationships is highly required. With these motivations, DNN technique [14] was presented for large-signal modeling of nonlinear microwave circuits and systems. Let N_d be the order of DNN representing the reduced order for original nonlinear circuit. Let

$\boldsymbol{v}_i$ be a N_y-vector, $i = 1,2,\ldots,N_d$. Let g_{ANN} represent an MLP neural network [1], where input neurons contain $\boldsymbol{y}$, $\boldsymbol{u}$, their derivatives $d^i\boldsymbol{y}/dt^i$, $i=1, 2, \ldots, N_d-1$, and $d^k\boldsymbol{u}/dt^k$, $k=1,2, \ldots, N_d$, and the output neuron represents $\mathrm{d}^{N_d}\boldsymbol{y}/\mathrm{dt}^{N_d}$. In [14], the DNN model was formulated as

$$\begin{aligned}
\dot{\boldsymbol{v}}_1(t) &= \boldsymbol{v}_2(t) \\
&\vdots \\
\dot{\boldsymbol{v}}_{N_d\text{-}1}(t) &= \boldsymbol{v}_{N_d}(t) \\
\dot{\boldsymbol{v}}_{N_d}(t) &= \mathrm{g}_{\mathrm{ANN}}(\boldsymbol{v}_{N_d}(t), \boldsymbol{v}_{N_d-1}(t), \cdots, \\
&\qquad \boldsymbol{v}_1(t), \boldsymbol{u}^{(N_d)}(t), \boldsymbol{u}^{(N_d-1)}(t), \cdots, \boldsymbol{u}(t))
\end{aligned} \tag{7}$$

where inputs and outputs of the DNN model are $\boldsymbol{u}(t)$ and $\boldsymbol{y}(t) = \boldsymbol{v}_1(t)$, respectively. The overall DNN model is in a standardized format for typical nonlinear circuit simulators. For example, the left-hand-side of the equation provides the charge or the capacitor part, and the right-hand-side provides the current part. This format is the standard representation of nonlinear components in many harmonic balance (HB) simulators. In this way, DNN can provide dynamic current-charge parameters for general nonlinear circuits with any number of internal nodes in original microwave circuit [14]. The DNN technique has been successfully used in modeling of nonlinear microwave circuits such as mixers and amplifiers. The trained DNN behavioral models were also used to facilitate fast high-level HB simulations of circuits and systems. As a recent advance, the work in [17] introduced a mathematical way to determine the order of the DNN formulation from the training data. A further enhancement is made in [18] where a modified HB formulation incorporating constraint functions was presented to improve the robustness and efficiency of DNN-based HB simulation of high-level nonlinear microwave circuits.

IV. EXAMPLES

A. Development of Inverse Models for Waveguide Filter

Inverse models of a dual mode waveguide filter are developed. According to [8], the filter is decomposed into three different modules each representing a separate filter junction. Neural network inverse models of these junctions were developed separately using the proposed methodology.

The first neural network inverse model of the filter structure is developed for the internal coupling iris. The inverse model is formulated as

$$\bar{\boldsymbol{y}} = [x_3 \;\; x_4 \;\; y_3 \;\; y_4]^T = [L_v \;\; L_h \;\; P_v \;\; P_h]^T \tag{8}$$

$$\bar{\boldsymbol{x}} = [x_1 \;\; x_2 \;\; y_1 \;\; y_2]^T = [D \;\; fo \;\; M_{23} \;\; M_{14}]^T. \tag{9}$$

where D is the circular cavity diameter, fo is the center frequency, M_{23} and M_{14} are coupling values, L_v and L_h are the vertical and horizontal coupling slot lengths and P_v and P_h are the loading effect of the coupling iris on the two orthogonal modes, respectively. After formulating the inverse model training data were generated and the entire data was used to train the inverse model. Direct training produced good accuracy in terms of least square (L2) errors. However the worst-case error was large. Therefore in the next step the data was segmented into four sections. Models for these sections were trained separately, which reduced the worst-case error. The final model accuracy of the two methods is shown in Table 1. We can improve the accuracy further by splitting the data set into more sections and achieve as accurate result as required.

The second inverse model of the filter is the IO iris model. The input parameters of IO iris inverse model are circular cavity diameter D, center frequency fo, and the coupling value R. The output parameters of the model are the iris length L, the loading effect of the coupling iris on the two orthogonal modes P_v and P_h, and the phase loading on the input rectangular waveguide P_{in}. The inverse model is defined as

$$\bar{\boldsymbol{y}} = [x_3 \;\; y_2 \;\; y_3 \;\; y_4]^T = [L \;\; P_v \;\; P_h \;\; P_{in}]^T \tag{10}$$

$$\bar{\boldsymbol{x}} = [x_1 \;\; x_2 \;\; y_1]^T = [D \;\; fo \;\; R]^T. \tag{11}$$

Four different sets of training data were generated according to the width of iris using mode-matching method. Each set was trained and tested separately using the direct inverse modeling method. The result of these direct inverse modeling is listed in Table 1. In the conventional direct method, L2 errors are acceptable but the

worst-case error is high. To reduce the worst-case error we split the first set of data into several segments and trained separately. These models produced acceptable accuracy. Same method was applied to the rest of the three models. The result is presented in Table 1, which shows that the proposed methodology produce more accurate result than the direct modeling method.

The last neural network inverse model of the filter is developed for tuning screw model. The input parameters of this model are circular cavity diameter D, center frequency fo, the coupling between the two orthogonal modes in one cavity M_{12}, and the difference between the phase shift of the vertical mode and that of the horizontal mode across the tuning screw P. The model outputs are the phase shift of the horizontal mode across the tuning screw P_h, coupling screw length L_c, and the horizontal tuning screw length L_h. The inverse model is formulated as

$$\bar{\boldsymbol{y}} = [y_3 \;\; x_3 \;\; x_4]^T = [P_h \;\; L_h \;\; L_C]^T \quad (12)$$

$$\bar{\boldsymbol{x}} = [x_1 \;\; x_2 \;\; y_1 \;\; y_2]^T = [D \;\; fo \;\; M_{12} \;\; P]^T . \quad (13)$$

All four techniques in Section II were applied to develop this model. The final model result is presented in Table 1, which shows that the accuracy of the tuning screw model is improved drastically using the proposed method. Minor improvement is realized for the coupling iris model in terms of L2 error (the improvement is mostly realized in terms of worst-case error), because the input-output relationship of this model is relatively simpler than that of the tuning screw model. The proposed method becomes more efficient and effective for complex devices.

Three-layer multilayer perceptron neural network structure was used for each neural network model and quasi-Newton training algorithm was used to train the neural network models. Testing data were used after training the model to verify the generalization ability of these models. Automatic model generation algorithm of NeuroModelerPlus [19] was used to develop these models, which automatically train the model until model training, and testing accuracy was satisfied. The training error and test errors were generally similar because sufficient training data was used in the examples.

Table 1: Comparison of error between conventional and proposed method for waveguide filter model [8].

Waveguide junctions	Inverse modeling methods	Model error (%)	
		L2	Worst case
Coupling iris	Conventional	0.46	14.2
	Proposed	0.32	7.20
IO iris	Conventional	1.30	54.0
	Proposed	0.45	18.4
Tuning screw	Conventional	7.51	94.25
	Proposed	0.59	8.10

B. Dual Mode 6-pole Waveguide Filter Design Using the Developed Neural Network Inverse Models

In this example we design a 6-pole waveguide filer using the proposed methodology [8]. The filter center frequency is 12.155 GHz, bandwidth is 64 MHz and cavity diameter is chosen to be 1.072". In addition to the three inverse models that were developed in Example A, we developed another inverse model for slot iris. The inputs of the slot iris model are cavity diameter D, center frequency fo and coupling M and the outputs are iris length L, vertical phase P_v and horizontal phase P_h. The normalized ideal coupling values are

$$R_1 = R_2 = 1.077$$

$$\boldsymbol{M} = \begin{bmatrix} 0 & 0.855 & 0 & -0.16 & 0 & 0 \\ 0.855 & 0 & 0.719 & 0 & 0 & 0 \\ 0 & 0.719 & 0 & 0.558 & 0 & 0 \\ -0.16 & 0 & 0.558 & 0 & 0.614 & 0 \\ 0 & 0 & 0 & 0.614 & 0 & 0.87 \\ 0 & 0 & 0 & 0 & 0.87 & 0 \end{bmatrix} . \quad (14)$$

Irises and tuning screw dimensions are calculated by the trained neural network inverse models developed in Example A. The filter is manufactured and tuned by adjusting irises and tuning screws to match the ideal response and the dimensions are listed in Table 2. Very good correlation can be seen between the initial dimensions provided by the neural network inverse models and the measured final dimensions of the fine tuned filter. Figure 3 presents the

response of the tuned filter and compares with the ideal one showing a perfect match between each other.

Table 2: Comparison of dimensions obtained from EM model, neural network inverse models and measurement of the tuned 6-pole filter [8].

Filter Dimensions	EM Model (inch)	Neural Model (inch)	Measurement (inch)
IO irises	0.352	0.351	0.358
M23 iris	0.273	0.274	0.277
M14 iris	0.167	0.170	0.187
M45 iris	0.261	0.261	0.262
Cavity 1 length	1.690	1.691	1.690
Tuning screw	0.079	0.076	0.085
Coupling screw	0.097	0.097	0.104
Cavity 2 length	1.709	1.709	1.706
Tuning screw	0.055	0.045	0.109
Coupling screw	0.083	0.082	0.085
Cavity 3 length	1.692	1.692	1.692
Tuning screw	0.067	0.076	0.078
Coupling screw	0.098	0.097	0.120

The advantage of using the trained neural network inverse models is also realized in terms of CPU time compared to EM models. An EM simulator can be used for synthesis, which requires typically 10 to 15 iterations to generate inverse model dimensions. The time to obtain the dimensions using EM method is approximately 6.25 minutes compared to 1.5 milliseconds for the neural network inverse method.

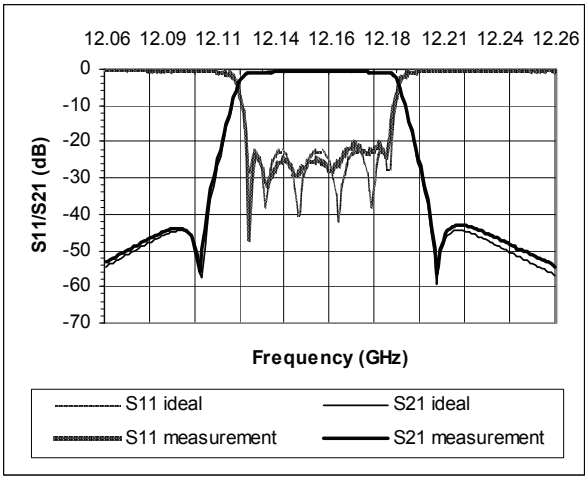

Fig. 3. Comparison of the 6-pole filter response with ideal filter response. The filter was designed, fabricated, tuned and then measured to obtain the dimensions [8].

C. Development of Behavioral Models for a Power Amplifier Using RNN Technique

Here we present an example of ANN-based behavioral modeling where the RNN is used for modeling AM/AM and AM/PM distortions of a power amplifier [12]. The circuit to be modeled is an RFIC power amplifier in Agilent ADS [20], which is represented by a detailed transistor-level description. The training data are generated using a 3G WCDMA input signal with average power (P_{av}) of 1 dBm and center frequency of 980 MHz. The channel bandwidth (chip rate) is 3.84 MHz. Two RNN models, namely the In-phase RNN (K_1) and the Quadrature-phase RNN (K_2), are individually developed using 1025 input-output samples representing 256 symbols from ADS. The RNN models are trained in a step-wise manner using the automatic model generation algorithm [12], where the size (number of hidden neurons) and the order of the RNNs are automatically adjusted depending on the training status. After the RNN models achieve a good learning, for testing signals not considered in training, the AM/AM and AM/PM distortions can be faithfully modeled by the RNNs, as shown in Fig. 4(a) and Fig. 4(b), respectively. An additional benefit of using RNN behavioral models is the improved speed over conventional circuit simulators. For the RFIC amplifier example, ADS takes

approximately 100 seconds to run the entire envelope simulation for the 3G WCDMA input whereas each RNN only takes 0.16 seconds to reproduce accurately the output for the same 3G WCDMA input.

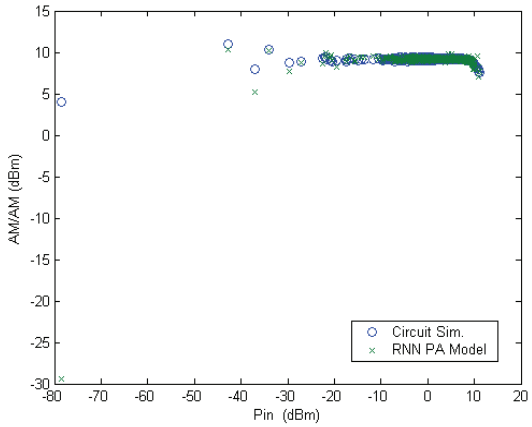

(a)

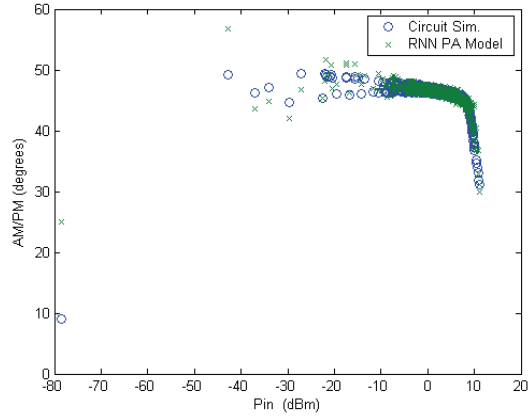

(b)

Fig. 4. (a) AM/AM distortion between ADS and RNN power amplifier (PA) behavioral model. (b) AM/PM distortion between ADS and RNN PA behavioral model [12].

D. Development of Behavioral Models for a Mixer Using DNN Technique

This example, based on [14], illustrates DNN modeling of a mixer. The circuit internally is a Gilbert cell with 14 NPN transistors in ADS [20]. The dynamic input and output of the model was defined in hybrid form as $\boldsymbol{u} = [v_{RF}, v_{LO}, i_{IF}]^T$ and $\boldsymbol{y} = [i_{RF}, v_{IF}]^T$, where v_{RF}, v_{LO}, and v_{IF} are the voltage values of radio frequency, local oscillator (LO), and inter-mediate frequency, i_{IF} and i_{RF} are the current values of intermediate frequency and radio frequency, respectively. The DNN model includes,

$$i_{RF}^{(n)}(t) = \boldsymbol{f}_{ANN1}[i_{RF}^{(n-1)}(t), i_{RF}^{(n-2)}(t), \cdots, i_{RF}(t), v_{RF}^{(n)}(t), v_{RF}^{(n-1)}(t), \cdots, v_{RF}(t)] \tag{15}$$

and

$$v_{IF}^{(n)}(t) = \boldsymbol{f}_{ANN2}[v_{IF}^{(n-1)}(t), v_{IF}^{(n-2)}(t), \cdots, v_{IF}(t), v_{RF}^{(n)}(t), v_{RF}^{(n-1)}(t), \cdots, v_{RF}(t), v_{LO}^{(n)}(t), v_{LO}^{(n-1)}(t), \cdots, v_{LO}(t), i_{IF}^{(n)}(t), i_{IF}^{(n-1)}(t), \cdots, i_{IF}(t)] \tag{16}$$

where n is the order of the DNN.

The training data were generated by varying the RF input frequency and power level from 11.7 GHz to 12.1 GHz with a step-size of 0.05 GHz and from -45 dBm to -35 dBm with a step-size of 2 dBm respectively. Local oscillator signal was fixed at 10.75 GHz and 10 dBm. Load was perturbed by 10% at every harmonic in order to allow the model learn the loading effects. The DNN was trained with different number of hidden neurons as shown in Table 3. Testing was done in ADS [20] using input frequencies from 11.725 GHz to 12.075 GHz with a step-size of 0.05 GHz and power levels at -44 dBm, -42 dBm, -40 dBm, -38 dBm, -36dBm. The agreement between model and ADS was achieved in time and frequency domains even though those test information was never seen in training. Figure 5 illustrates a comparison between the output of the DNN model and the ADS solution in time-domain.

Table 3: DNN accuracy from different training for the mixer example [14].

No. of Hidden Neurons in Training (n=4)	Testing Error for Time Domain Data	Testing Error for Spectrum Domain Data
45	8.7E-4	6.7E-4
55	4.6E-4	2.0E-4
65	6.5E-4	4.6E-4

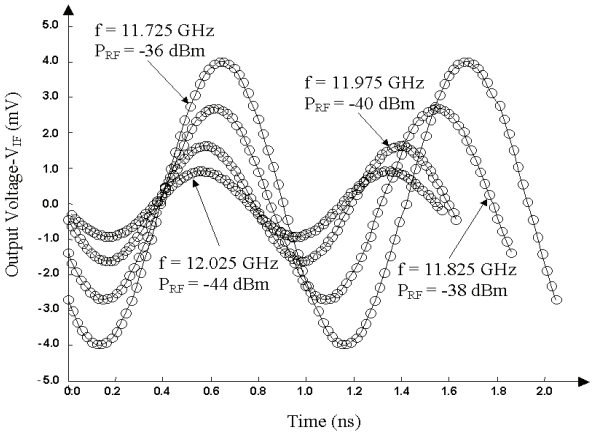

Fig. 5 Mixer v_{IF} output: time-domain comparison between DNN (—) and ADS solution of original circuit (o). Good agreement is achieved even though such data were never used in training [14].

V. CONCLUSION

We have reviewed recent advances of neural network modeling techniques for fast modeling and design of RF/microwave circuits. Inverse modeling technique is formulated and non-uniqueness of input-output relationship has been addressed. A method to identify and divide contradictory data has been proposed. Inverse models are divided based on derivatives of forward model and then trained separately to produce more accurate inverse sub-models. A method to correctly combine the inverse sub-models is presented. The proposed methodology has been applied to waveguide filter modeling and design. Very good correlation was found between neural networks predicted dimensions and that of a perfectly tuned filter following the EM method. We have also reviewed recurrent neural network and dynamic neural network modeling techniques. These time-domain neural networks are trained to learn the nonlinear dynamic input-output relationship based on the external circuit signals. The resulting neural network models are fast and accurate to predict the behavior of RF and microwave circuits.

ACKNOWLEDGMENT

Authors would like to thank Dr. Ming Yu of COMDEV for his support and collaboration in the inverse modeling project. Also thanks to Dr. Ying Wang for her technical expertise on this work.

REFERENCES

[1] Q. J. Zhang, K. C. Gupta, and V. K. Devabhaktuni, "Artificial neural networks for RF and microwave design-from theory to practice," *IEEE Trans. Microwave Theory and Tech.,* vol. 51, pp. 1339–1350, Apr. 2003.

[2] Q. J. Zhang and K. C. Gupta, *Neural Networks for RF and Microwave Design,* Artech House, Boston, 2000.

[3] P. M. Watson and K. C. Gupta, "EM-ANN models for microstrip vias and interconnects in dataset circuits," *IEEE Trans. Microwave Theory and Tech.,* vol. 44, pp. 2495–2503, Dec. 1996.

[4] B. Davis, C. White, M. A. Reece, M. E. Jr. Bayne, W. L. Thompson, II, N. L. Richardson, and L. Jr. Walker, "Dynamically configurable pHEMT model using neural networks for CAD," *IEEE MTT-S Int. Microwave Symp. Dig.,* vol. 1, pp. 177–180, June 2003.

[5] M. Isaksson, D. Wisell, and D. Ronnow, "Wide-band dynamic modeling of power amplifiers using radial-basis function neural networks," *IEEE Trans. Microwave Theory and Tech.,* vol. 53, no. 11, pp. 3422–3428, Nov. 2005.

[6] H. Kabir, Y. Wang, M. Yu, and Q. J. Zhang, "Applications of artificial neural network techniques in microwave filter modeling, optimization and design," *Progress In Electromagnetic Research Symposium,* Beijing, China, pp. 1972–1976, March 2007.

[7] P. Burrascano, M. Dionigi, C. Fancelli, and M. Mongiardo, "A neural network model for CAD and optimization of microwave filters," *IEEE MTT-S Int. Microwave Symp. Dig.,* Baltimore, MD, vol. 1, pp. 13–16, June 1998.

[8] H. Kabir, Y. Wang, M. Yu and Q. J. Zhang, "Neural network inverse modeling and applications to microwave filter design" *IEEE Trans. Microwave Theory and Tech.,* vol. 56, no. 4, pp. 867–879, Apr. 2008.

[9] Y. Wang, M. Yu, H. Kabir, and Q. J. Zhang, "Effective design of cross-coupled filter using neural networks ad coupling matrix*," IEEE MTT-S Int. Microwave Symp. Dig.,* pp. 1431–1434, June 2006.

[10] M. M. Vai, S. Wu, B. Li, and S. Prasad, "Reverse modeling of microwave circuits with bidirectional neural network models," *IEEE Trans. Microwave Theory and Tech.,* vol. 46, pp. 1492–1494, Oct. 1998.

[11] Q. J. Zhang and Y. Cao, "Time-domain neural network approaches to EM modeling of microwave components," *Springer Proceedings in Physics: Time Domain Methods in Electrodynamics*, pp. 41–53, Oct. 2008.

[12] H. Sharma and Q. J. Zhang, "Automated time domain modeling of linear and nonlinear microwave circuits using recurrent neural networks," *Int. J. RF Microwave Comput.-Aided Eng.*, vol.18, no. 3, pp. 195–208, May 2008.

[13] Y. H. Fang, M. C. E. Yagoub, F. Wang, and Q. J. Zhang, "A new macromodeling approach for nonlinear microwave circuits based on recurrent neural network," *IEEE Trans. Microwave Theory Tech.,* vol. 48, no. 12, pp. 2335–2344, Dec. 2000.

[14] J. J. Xu, M. Yagoub, R. T. Ding, and Q. J. Zhang, "Neural based dynamic modeling of nonlinear microwave circuits," *IEEE Trans. Microwave Theory Tech.*, vol. 50, pp. 2769–2780, Dec. 2002.

[15] J. Xu, M. C. E. Yagoub, R. Ding, and Q. J. Zhang, "Exact adjoint sensitivity analysis for neural-based microwave modeling and design," *IEEE Trans. Microwave Theory and Tech.*, vol. 51, pp. 226–237, Jan. 2003.

[16] S. Haykin, *Neural Networks: A Comprehensive Foundation,* 2nd ed., Prentice-Hall, pp. 751–756, 1999.

[17] J. Wood, D. E. Root, and N. B. Tufillaro, "A behavioral modeling approach to nonlinear model-order reduction for RF/microwave ICs and systems," *IEEE Trans. Microwave Theory Tech.*, vol. 52, no. 9, pp. 2274–2284, Sep. 2004.

[18] Y. Cao, L. Zhang, J. J. Xu and Q. J. Zhang, "Efficient harmonic balance simulation of nonlinear microwave Circuits with dynamic neural models," *IEEE MTT-S Int. Microwave Symp. Dig.*, , pp. 1423–1426, June 2006.

[19] Q. J. Zhang, *NeuroModelerPlus*, Department of Electronics, Carleton University, K1S 5B6, Canada.

[20] Advanced Design System (ADS) ver. 2006A, Agilent Technologies, Inc., 2006.

High-Frequency Analysis of Scattering from Complex Targets in Half Space

Xiao Feng Li , Yong Jun Xie , Rui Yang , and Yuan Yuan Wang

National Key Laboratory of Antennas and Microwave Technology,
Xidian University, Xi'an 710071, China
lxf.xidian@yahoo.com.cn , yjxie@xidian.edu.cn , mattomato811118@yahoo.com.cn ,
wylpforever@163.com

***Abstract*—** The high-frequency method for solving the scattering from electrically large conductive targets in half space is presented in this paper. The high-frequency method is deduced by introducing the half-space Green's function into the conventional method of physical optics, method of equivalent currents. Combined with the graphical-electromagnetic computing method and ray tracing technique that account for shadowing and multiple scattering in half space, one may calculate the radar cross-section of a conductive target object in a half space. The numerical results show that this method is efficient and accurate.

***Index Terms*—** Half-space physical optics (HFPO), half-space Equivalent Edge Currents (HFEEC), graphical-electromagnetic computing, radar cross section (RCS).

I. INTRODUCTION

With the development of electromagnetics, researchers have directed significant attention toward targets in half space, especially the electrically large PEC targets above the earth or the sea, such as geophysical, remote sensing, wave propagation. A variety of RCS prediction softwares have been widely used for interactive modeling, design, and analysis of aircraft with RCS specifications in free space [1], which are based on the high-frequency techniques [2-7] and provide an efficient tool to obtain real-time results. However, how fast and accurate it is to calculate the radar cross section of half-space targets is still a challenging problem, in particular, the objectives of great size.

Numerous authors have derived a variety of methods which are used for computing the radar cross section (RCS) of complex radar targets in half space. The scattering fields of the targets in half space could be computed by using the Finite element method (FEM) [8], Finite-difference time-domain methods (FDTD) [9], but they cause some difficulties in the solution procedure such as the discrete space need for a huge number of grids in the solution procedure [10]. Some researchers try to combine the half-space Green's function with the Method of moment (MOM), or fast multipole method (FMM) to consider the electrically large targets in half space [11], but this also requires more mass storage memory in general personal computer, which results in lower processing speed and more computing time.

In addition, Johnson and others clarify an accuracy of a "four-path" model which includes single scattering effects only [12]. The results show that the four-path model provides reasonable predictions. The above methods have provided us with a better idea to solve the targets in half space.

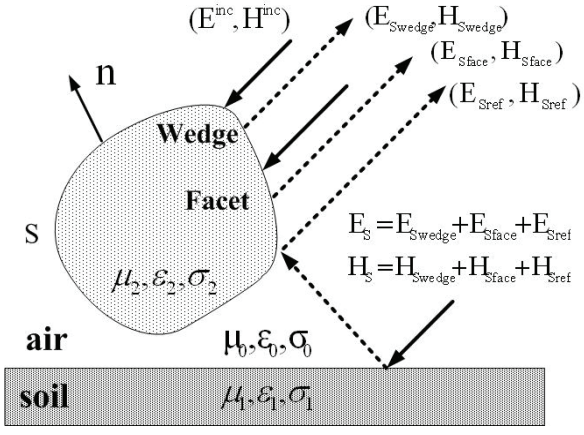

Fig. 1. a plane wave illuminating an arbitrarily shaped 3-D object located above a lossy half space.

In this paper, an improved high-frequency method is presented for analysis of scattering from

electrically large targets in a half space. Based on the analysis of the scattered field due to the facet's surface in half space [13-14], we have further introduced the high-frequency method into the wedges of conductive targets with electrically large size in half space. Furthermore, the facets illuminated by the ground reflected wave were also added to the contributions from the firstly illuminated facets. Therefore, inclusion of returns from these in the overall return is an important process, and one should be aware of their magnitude.

II. THEORY

As shown in Fig. 1, consider an arbitrarily shaped object illuminated by a plane wave in a half space, and surface *S* is assumed to represent a closed surface of a target.

This paper deals with RCS analysis where it is implicitly assumed that the radar frequency is high enough such that the corresponding wavelength is small compared to the physical dimensions of the scattering body. Therefore we use the term complex body to imply also a body with large electric dimensions. Thus the scattering calculations are in the high-frequency region. Due to the poor rate of convergence of the moment method when applied to electrically large bodies (in addition to its requirement for a large computer), it is logical to use the high-frequency method.

The classical high-frequency techniques for RCS prediction are based on a target model in terms of facets and wedges [1]. Besides we included the correction in our calculations by accounting for the currents that are induced on a target that was illuminated by the ground reflected wave. Thus, the term for the overall scattered field from a complex body may be written as:

Total scattered field E_s = scattered fields from facets E_{sface} + scattered fields from wedges E_{swedge} + scattered fields from ground reflected wave E_{sref}

When calculating these fields, one may precede by using magnetic or electric field integral equation formulations. The following calculations are presented in terms of electric field formulations.

A. Graphical Processing in Half-Space

The GRECO method was introduced by Rius in 1993 [3]. It can be integrated with CAD geometric modeling packages and high-frequency theory for RCS predictions. Using the hardware graphics accelerator, hidden surfaces of the image have been previously removed.

To the fixed screen, the calculation complexity is not varied with the complexity and dimension of targets. The targets are rebuilt by displaying lists technology of OpenGL and hidden surfaces of the image have been previously removed by the hardware graphics accelerator. Then we make use of the resolution to disperse the curve face into pixels that satisfy the requirement of the electromagnetic calculation, meanwhile, the scene is rendered using the Phong local illumination model [3].

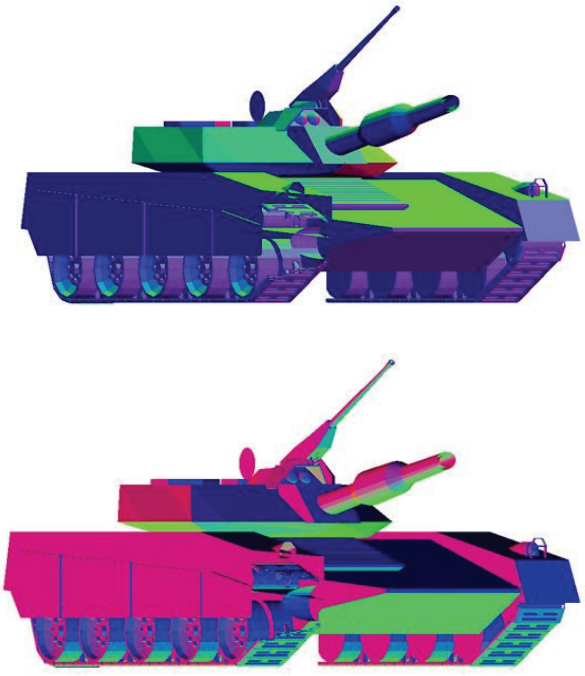

Fig. 2. Rendered image of tank in half space at the workstation screen. Six red, blue, and green light sources are located on positive and negative axis. The blending of the three colors at each pixel of the two images is equal to the positive and negative components of the unit normal.

For three light sources of purely green, red and blue colors, respectively, located over each one of the three coordinate axes, the three color components for this pixel are equal to the

(n_x, n_y, n_z) components of the unit normal to surface.

As shown in Fig. 3, in order to show that this method is efficient and accurate, we have returned to the calculated unit normal on the surface and have a good agreement with actual results. Meanwhile, the depths of each pixel are obtained in the same way. The depth of each pixel is equal to the distance between the observer and each surface element.

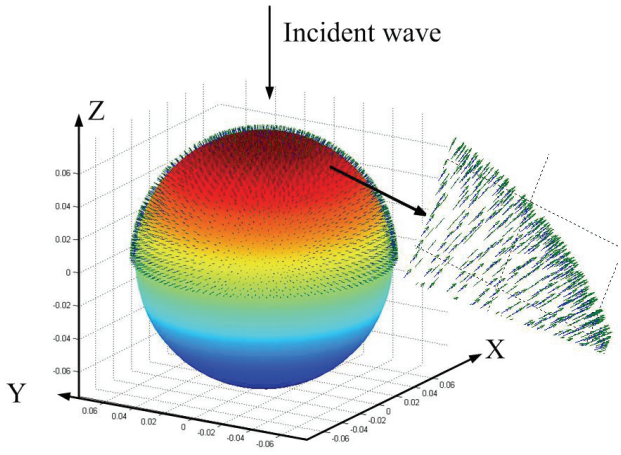

Fig. 3. Calculated unit normal distribution of the sphere in half space. The incident wave direction is $\theta_{inc} = 0, \varphi_{inc} = 0$.

Edges are detected on the target image as discontinuities of the unit normal to the surface when the z coordinates remain continuous. It must be noted that eclipsed surfaces may also produce discontinuities in the normal to the surface, but in that case the z coordinate would be discontinuous.

Obtaining the unit normal and edge parameters of each illuminated pixel of the target, the radar cross section of conductive targets can be exactly calculated with the half-space high frequency method.

B. Facet Scattering in Half-Space

The scattered electric field $\mathbf{E}_{sf}$ from an arbitrary facet is based on the following form for the electric field integral equation.

$$\mathrm{E}_{sf}(r) = -\mathbf{j}\omega \mathrm{A}(r) - \nabla V_e, , r \in S\,, \qquad (1)$$

where A and V_e represent electric vector and scalar potentials.

According to the high-frequency theory, we can get the accurate surface current by applying physical optics approximations over illuminated surface in half space. Through the proper boundary conditions, the surface current can be represented as:

$$\mathbf{J}(\mathbf{\bar{r}'}) \approx 2\hat{\mathbf{n}} \times \mathbf{H_i}\,, \qquad (2)$$

where $\hat{n}$ is the inward surface unit normal and $\mathbf{H_i}$ is the polarization unit vectors for incident magnetic field.

In order to solve the scattering fields of the electrically large PEC targets in half space, the half-space Green's function was introduced into the high-frequency method. The half-space Green's function can be impressed by the vector and scalar potentials, and the vector potential is not uniquely specified. In this paper, we express it as follows [15]:

$$\overline{\mathbf{G}}_A = (\hat{\mathbf{x}}\hat{\mathbf{x}} + \hat{\mathbf{y}}\hat{\mathbf{y}})G_A^{xx} + \hat{\mathbf{z}}\hat{\mathbf{x}}G_A^{zx} + \hat{\mathbf{z}}\hat{\mathbf{y}}G_A^{zy} + \hat{\mathbf{z}}\hat{\mathbf{z}}G_A^{zz} \qquad (3)$$

with

$$G_A^{xx} = G_A^{yy}\,,\ G_x^{qe} = G_y^{qe}\,. \qquad (4)$$

Here, G_A^{xx}, G_A^{zx}, G_A^{zy} and G_A^{zz} denote the spatial domain half-space Green's function for the electric vector potentials; G_x^{qe}, G_y^{qe} and G_z^{qe} denote the spatial domain half-space Green's function for the electric scalar potentials.

In order to obtain the half-space Green's function, we compute the vector and the scalar potentials by the discrete complex image method. Through the Sommerfeld identity, a closed-form spatial Green's function of a few terms is found from the quasi-dynamic images, the complex images, and the surface waves [15-16].

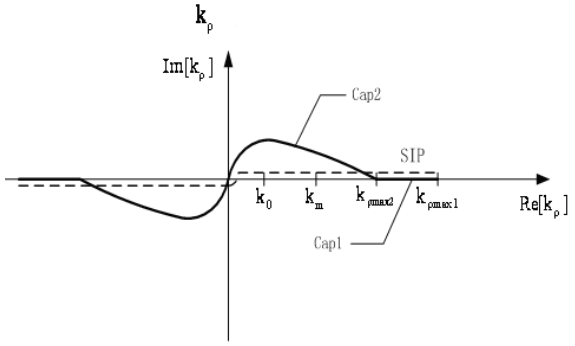

Fig. 4. The paths *Cap*1 and *Cap*2 used in two-level approximation.

To obtain the spatial-domain Green's functions in closed forms, it would be useful to give the definition of the spatial-domain Green's function

$$G = \frac{1}{4\pi}\int_{SIP} \widetilde{G}(k_\rho) H_0^{(2)}(k_\rho) k_\rho dk_\rho , \qquad (5)$$

where, G and $\widetilde{G}$ are the Green's function in the spatial and spectral domains, respectively. $H_0^{(2)}$ is the Hankel function of the second kind and *SIP* is the Sommerfeld integration path.

To alleviate the necessity of investigating the spectral-domain Green's functions in advance and the difficulties caused by the trade-off between the sampling range and the sampling period, the approximation is performed in two levels. The first part of approximation is performed along the path *Cap*1 while the second part is done along the path *Cap*2 as shown in Fig.4. The main formulations may refer to [17-18].

It is permissible to express the vector and the scalar potentials as follows:

$$A(r) = \mu_0 \int_S \overline{G}_A(r,r') \cdot J(r') dS' \qquad (6)$$

$$V_e(r) = \frac{-1}{j\omega\omega_0}\int_S [G_x^{qe}(r,r')\frac{\partial J_x}{\partial x'} + G_y^{qe}(r,r')\frac{\partial J_y}{\partial y'} + G_z^{qe}(r,r')\frac{\partial J_z}{\partial z'}] dS' , \qquad (7)$$

where r and r' represent the position vectors for the observation point and the increment area dS', respectively, and u_0 and ε_0 denote the free-space permeability and permittivity, respectively.

The half-space Green's function has been introduced into the physical optics method to consider the scattering of electrically large conductive targets in half space. Combined with the graphical-electromagnetic computing (GRECO) method, the shadow regions have been previously removed by the hardware graphics accelerator, and the geometry information is obtained by reading the color and depths of each pixel.

To apply the far-field approximation, that is, the observation point is located far enough from the scattering object, we could substitute (2), (3) into the scattered field $\mathbf{E}_{sf}$ due to the facet's surface, which leads to the equation:

$$E_{sf}(\bar{r}) = -j\omega\int_s \bar{G}_A \cdot J(\bar{r}')ds' + \frac{k\cdot\hat{s}}{\omega}\int_s [G_x^{qe}\frac{\partial}{\partial x}J(\bar{r}') + G_y^{qe}\frac{\partial}{\partial y}J(\bar{r}') + G_z^{qe}\frac{\partial}{\partial z}J(\bar{r}')]ds' . \qquad (8)$$

Equation (8) is then calculated for every illuminated facet and the complex RCS due to scattering from every illuminated facet is calculated as [19]:

$$\sqrt{\sigma} = \lim_{R\to\infty} 2\sqrt{\pi}R\frac{E_{sf}\cdot\hat{e}_r}{E_o}\exp(jkR) , \qquad (9)$$

where $\exp(jkR)$ is a phase term that has been introduced into the equation in order to account for the facet location with respect to the global coordinate system. Here, R is the position vector for the facet's reference vertex with respect to the global coordinate system.

C. Wedge Scattering in Half-Space

According to the high-frequency method, the far field scattered from a wedge can be assumed as radiated by an equivalent line current located on the edge. This equivalent current depends on both the directions of incidence and observation relative to orientation of the edge, so that its value is not constant along the edge. F and V_m represent magnetic vector and scalar potentials.

The MEC (Method of Equivalent Currents) is an integrative technique dealing with radiation integrals. The source of the diffracted field is now ascribed to fictitious equivalent currents, both electric and magnetic currents flowing along the edge. This approach has been investigated by many authors. Here, the main formulations are presented. For detailed derivations, the interested reader may refer to [20-21]. The electric and magnetic equivalent currents can be represented as:

$$I_e = \frac{j2(\hat{t}\cdot E_{inc})D_e}{kZ_0\sin\beta_i\sin\beta_s} , \qquad (10)$$

$$I_m = \frac{j2(\hat{t}\cdot H_{inc})D_m}{kY_0\sin\beta_i\sin\beta_s} , \qquad (11)$$

where Y=1/Z is the admittance of the medium, and D_e, D_m is the soft, hard scalar diffraction coefficient [3].

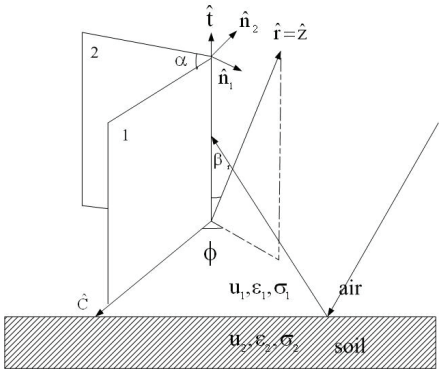

Fig. 5. The reflected field of the ground and wedge in half space.

The HFEEC (high-frequency equivalent electric current) depend on the angles α, ϕ, β_r, defined in Fig. 5. These angles were computed from the knowledge of the unit normal to both faces of the edge as follows:

$$\alpha = \cos^{-1}(-n_1.n_2) \ , \tag{12}$$

$$\sin\beta_r = \sqrt{t_x^2 + t_y^2} \ , \tag{13}$$

$$\cos\phi = \frac{n_{1x}t_y - n_{1y}t_x}{\sqrt{t_x^2 + t_y^2}} , \tag{14}$$

where t is the unit vector along the edge direction.

$$\hat{t} = \frac{n_1 \times n_2}{|n_1 \times n_2|} . \tag{15}$$

But it is not appropriate to calculate the scattering field from the ground by three-dimensional Green's function. In order to solve the scattering fields in half space, the half-space Green's function is introduced to calculate the contributions of scattering between the target and the ground plane.

As shown in Fig. 5, on the basis of the electric vector potentials, we consider the impact of the spatial domain half-space Green's function for the magnetic vector potentials.

$$\overline{\mathbf{G}}_{\mathbf{F}} = (\hat{\mathbf{x}}\hat{\mathbf{x}} + \hat{\mathbf{y}}\hat{\mathbf{y}})\mathbf{G}_{\mathbf{F}}^{\mathbf{xx}} + \hat{\mathbf{z}}\hat{\mathbf{x}}\mathbf{G}_{\mathbf{F}}^{\mathbf{zx}} + \hat{\mathbf{z}}\hat{\mathbf{y}}\mathbf{G}_{\mathbf{F}}^{\mathbf{zy}} + \hat{\mathbf{z}}\hat{\mathbf{z}}\mathbf{G}_{\mathbf{F}}^{\mathbf{zz}} \tag{16}$$

with

$$G_F^{xx} = G_F^{yy} , \tag{17}$$

where G_F^{xx}, G_F^{zx}, G_F^{zy} and G_F^{zz} denote the spatial domain half-space Green's function for the magnetic vector potentials;

It is permissible to express the vector and the scalar potentials as follows:

$$A_1(r) = \int_L \overline{G}_{A1}(r,r') \cdot I_e \hat{t} dL' \tag{18}$$

$$V_e(r) = \frac{-1}{j\omega\omega_0} \int_L [G_x^{qe}(r,r') I_e \frac{\partial t_x}{\partial x'} + G_y^{qe}(r,r') I_e \frac{\partial t_y}{\partial y'} + G_z^{qe}(r,r') I_e \frac{\partial t_z}{\partial z'}] dL' , \tag{19}$$

$$F_1(r) = \int_L \overline{G}_{F1}(r,r') \cdot I_m \hat{t} dL' \ , \tag{20}$$

and substitute (17), (18), (19) into the wedge scattered field E_{sw}.

$$E_{sw}(r) = -j\omega A(r) - \nabla V_e - \frac{1}{\varepsilon_0} \nabla \times F, r \in L . \tag{21}$$

Here, A and V_e represent electric vector and scalar potentials, F represents the magnetic vector potential, which leads to the equation:

$$\nabla \times \overline{\mathbf{G}}_F = \begin{bmatrix} \frac{\partial}{\partial \mathbf{y}} \mathbf{G}_F^{\mathbf{zx}} & \frac{\partial}{\partial \mathbf{y}} \mathbf{G}_F^{\mathbf{zx}} - \frac{\partial}{\partial \mathbf{z}} \mathbf{G}_F^{\mathbf{yy}} & \frac{\partial}{\partial \mathbf{y}} \mathbf{G}_F^{\mathbf{zz}} \\ \frac{\partial}{\partial \mathbf{z}} \mathbf{G}_F^{\mathbf{xx}} - \frac{\partial}{\partial \mathbf{x}} \mathbf{G}_F^{\mathbf{zx}} & -\frac{\partial}{\partial \mathbf{x}} \mathbf{G}_F^{\mathbf{zy}} & -\frac{\partial}{\partial \mathbf{x}} \mathbf{G}_F^{\mathbf{zz}} \\ -\frac{\partial}{\partial \mathbf{y}} \mathbf{G}_F^{\mathbf{xx}} & \frac{\partial}{\partial \mathbf{x}} \mathbf{G}_F^{\mathbf{yy}} & \mathbf{0} \end{bmatrix} . \tag{22}$$

The scattered electric field for the M illuminated wedge is defined as Equation (23) and the complex RCS due to scattering from every illuminated wedges is calculated as Equation (9).

$$\mathbf{E}_{sw}(\vec{\mathbf{r}}) = -j\omega\boldsymbol{\mu}_0 \int_L \overline{\mathbf{G}}_A(\mathbf{r},\mathbf{r}') \cdot I_e \hat{t} dL' + \frac{k \cdot \hat{s}}{\omega \cdot \varepsilon_0} \int_L [G_x^{qe} \frac{\partial}{\partial x} I_e \hat{t} + G_y^{qe} \frac{\partial}{\partial y} I_e \hat{t} + G_z^{qe} \frac{\partial}{\partial z} I_e \hat{t}] dL' - j\omega\varepsilon_0 \int_L \nabla \times \overline{\mathbf{G}}_F(\mathbf{r},\mathbf{r}') \cdot I_m \hat{t} dL'. \tag{23}$$

Therefore, the overall RCS for the complex body, assuming only first-order terms, is

$$\sigma = 4\pi \lim_{R\to\infty} R^2 \frac{\left| \sum_{n=1}^{N} (E_{sw} \cdot \hat{e}_r)_n + \sum_{m=1}^{M} (E_{sf} \cdot \hat{e}_r)_m \right|^2}{|E_o|^2} . \tag{24}$$

D. Multiple Scattering in Half-Space

Calculating the contributions of multiple scattering in half space is a formidable task. However, describing the complex geometry in terms of facets significantly reduces the problem. The multiple scattering contributions between the land and the targets are primarily expressed in terms of facet-facet interactions.

Multiple interactions between the target and the half-space interface are important when the target is near the interface. In the past, this issue is often ignored.

The field previously considered only incident is not enough, so the reflected field and the impact of multiple interactions must be taken into account. Consider a plane wave:

$$\vec{\mathbf{E}}_{\mathbf{i}}(\vec{r}) = \hat{\mathbf{q}} E_0 e^{-jk_0 \hat{\mathbf{i}}\cdot\vec{\mathbf{r}}}, \quad \hat{\mathbf{q}} = \hat{\mathbf{v}}_{\mathbf{i}}, \hat{\mathbf{h}}_{\mathbf{i}}, \tag{25}$$

where E_0 is the amplitude of incident field, $\hat{i}$ is the incident direction, and $\hat{v}_i, \hat{h}_i$ are the polarization vectors for incident electric and magnetic fields.

With

$$\hat{i} = \sin(\hat{x}\cos\varphi_i + \hat{y}\sin\varphi_i) - \hat{z}\cos\theta_i \quad , \tag{26}$$

$$\hat{h}_i = \frac{\hat{z}\times\hat{i}}{\left|\hat{z}\times\hat{i}\right|} = \hat{y}\cos\varphi_i - \hat{x}\sin\varphi_i \quad , \tag{27}$$

$$\hat{v}_i = \hat{h}_i \times \hat{i} = -\cos\theta_i(\hat{x}\cos\varphi_i + \hat{y}\sin\varphi_i) - \hat{z}\sin\theta_i . \tag{28}$$

The field can be calculated for orientation that is needed to study electromagnetic wave interaction with interface. The algorithm for this case is composed of two major steps.

1) Ray-tracing technique.

In order to apply the planar reflection coefficients reflection coefficients for the transverse electric (TE) Γ and the transverse magnetic (TM) case $\overline{\Gamma}$, the incident field needs to be decomposed into its TE and TM components. Using subscript c to denote local coordinates (see Fig. 6), the incident field can be written as:

$$E_1^i = (\vec{E}^i \cdot \hat{\phi}_c^i)\hat{\phi}_c^i + (\vec{E}^i \cdot \hat{\theta}_c^i)\hat{\theta}_c^i . \tag{29}$$

The reflected field is then given by

$$E_1^s = \Gamma(\vec{E}^i \cdot \hat{\phi}_c^i)\hat{\phi}_c^i + \overline{\Gamma}(\vec{E}^i \cdot \hat{\theta}_c^i)\hat{\theta}_c^i . \tag{30}$$

The reflected field is easily found once $\hat{\phi}_c^i$ and $\hat{\theta}_c^i$ are determined in terms of the global xyz coordinate in region I.

Once the ray paths from region I to region II are found, the field amplitude along the ray can be determined by geometrical optics [22]. Then, a ray-tracing technique is applied to the selected facet to compute the phase delay due to multiple bounce between the facets of the pair.

2) Physical Optical.

The multiple scattering contributions for selected facet in region II are computed by using a generalized form of Knott's calculations for an obtuse rectangular dihedral corner reflector [23]. His calculations were extended to account for the general case, in which the shape of the facet of the pair is quadrilateral or triangular. Computed contributions are then added to the overall fields in Equation (24).

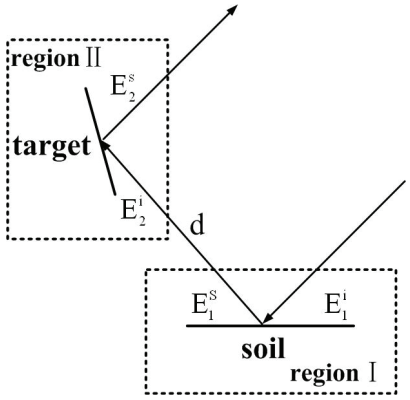

Fig. 6. The multiple scattering between the ground and target in half space.

III. RESULTS

When the object is calculated with the high-frequency method from the simple targets to the complex ones in half space, the CPU time for the RCS prediction is spent only on the electromagnetic part of the computation while the more time-consuming geometric model manipulations are left to the graphics hardware. Regardless of whether the targets are simple or complex ones, the scattering field of each illuminated pixel is calculated in the same way. Combined with the half-space Green's function, the high-frequency approximations to RCS prediction is easily computed from the knowledge of the unit normal at the illuminated targets in half space.

If we consider the simulation of complex electrically large size ($l >> \lambda$) targets with HFSS software, it is very easy to exceed the existing computer memory space, so we first compare with the results of the calculation and the simulation of the simple electrically large size targets in half space, and apply this algorithm to the complex ones in half space.

To ensure correlation with computations, special attention was given to the accuracy of model construction. Illustrations of the verification work are presented in the following sections.

A. Half Space and Free Space

Figure 7 shows a perfectly conducting pyramid ($5\lambda \times 5\lambda \times \lambda$) is placed $\lambda/4$ above the soil. Here, λ represents the wavelength in the vacuum. The soil has a relative dielectric permittivity $\varepsilon_r = 4.0$, relative magnetic permeability $\mu_r = 1.0$. The agreement is excellent.

There is good fit between the prediction of the derivation equation and the simulation of HFSS software, but there are slight discrepancies in some places. The major reason is the phase term that has been introduced into the equation to account for the facet location with respect to the global coordinate system.

Figure 8 shows a perfectly conducting ellipsoid is placed $\lambda/4$ above the soil. Here, the soil has a relative dielectric permittivity $\varepsilon_r = 4.0$, relative magnetic permeability $\mu_r = 1.0$.

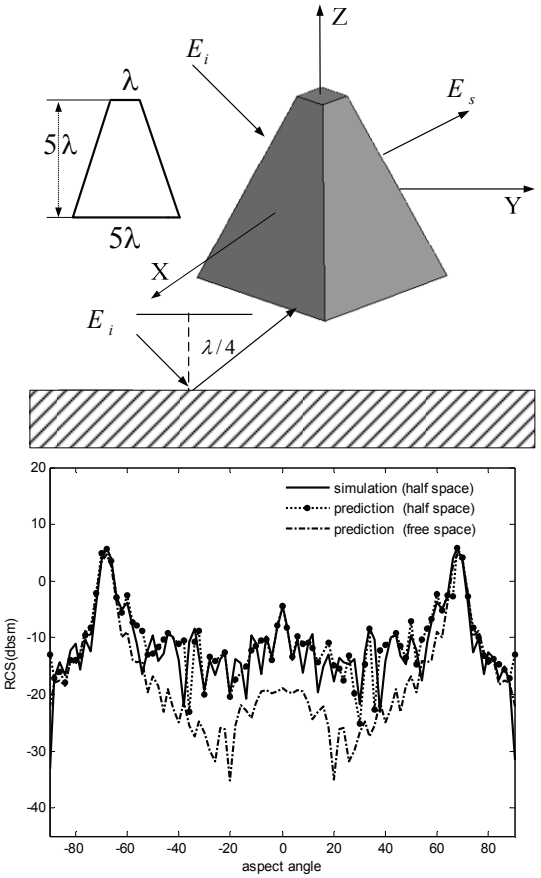

Fig. 7. 5 λ *5 λ *1 λ pyramid comparison of prediction and simulation of software in half space, frequency 10 GHZ, vertical polarization.

We can conclude that it is necessary to consider the effect of the half space environment. The results show that the RCS calculated with half-space Green's function are greater than that calculated with free-space Green's function. Compared with the actual results, it is efficient and accurate to introduce the half-space Green's function into the conventional the high-frequency method.

B. Wedge Scattering

Figure 8 shows a perfectly conducting wedge placed $\lambda/4$ above the soil. Here, the soil has a relative dielectric permittivity $\varepsilon_r = 4.0$, relative magnetic permeability $\mu_r = 1.0$.

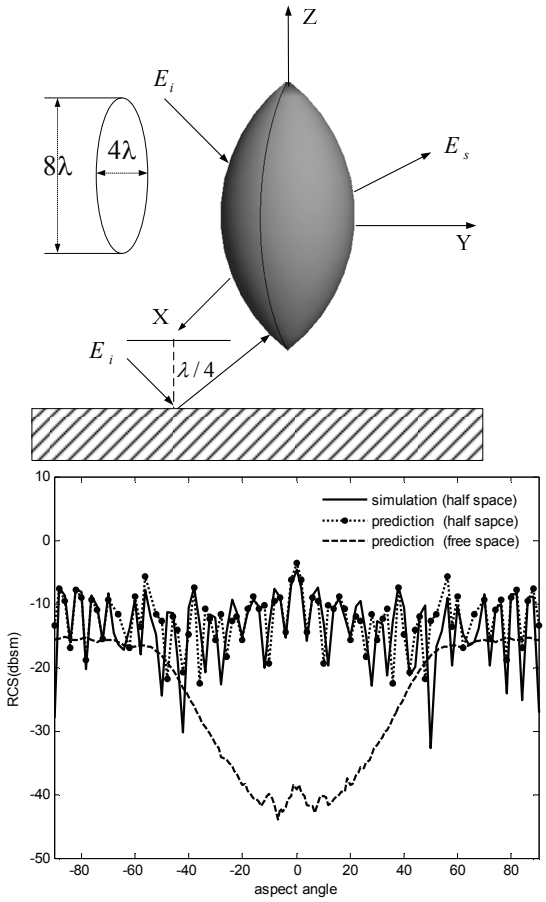

Fig. 8. 8 λ *4 λ ellipsoid comparison of prediction and simulation of software in half space, frequency 10 GHZ, vertical polarization.

It indicates the predictions are in good agreement with the simulation of software, which proves that the half-space Green's function applied the wedge is accuracy for the targets with large electric

dimensions in half space. In Fig. 9, We could see that, for these backscatter RCS, inclusion of returns from these wedges in the overall return is an important process.

C. Multiple Scattering

Figure 9 shows a perfectly conducting ellipsoid placed $\lambda/4$ above the soil. Here, the soil has a relative dielectric permittivity $\varepsilon_r = 4.0$, relative magnetic permeability $\mu_r = 1.0$.

It is important to notice that in Fig. 10, the multiple scattering in half space (HFMUL) is correct for aspect angles between -30^0 to -10^0 and 10^0 to 30^0. In order to improve the high-frequency result, the method of HFMUL is added to HFPO + HFEEC, the numerical solution agrees very well with the simulation results.

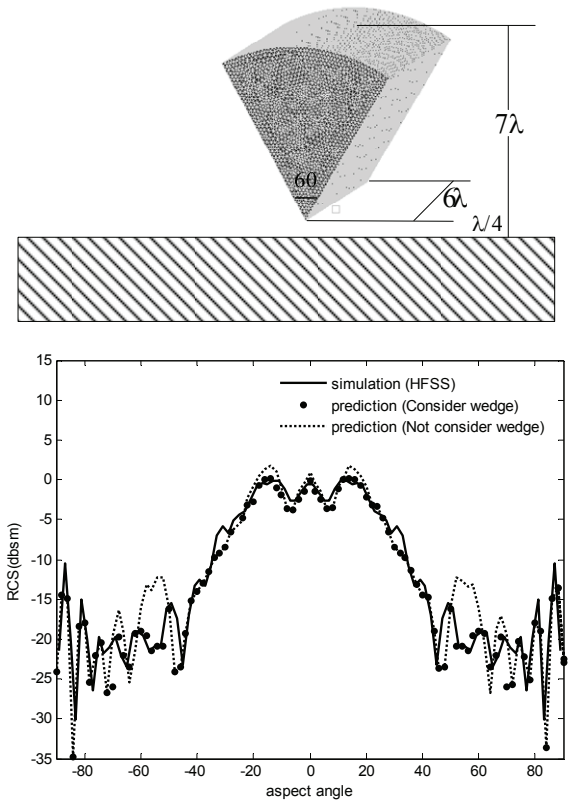

Fig. 9. Wedge comparison of prediction and simulation of software in half space, frequency 10 GHZ, vertical polarization.

D. Complex Targets

Various complex bodies have been used for verifications. The following presents an illustration for a generic missile model. Figure 11 shows the missile is placed 5m above the soil. The soil has a relative dielectric permittivity $\varepsilon_r = 4.0$, relative magnetic permeability $\mu_r = 1.0$.

Figure 12 shows that the contributions of scattering between the target and the ground plane have a great effect upon the predictions in half space. The prime reason for that is the phase discrepancy caused by the reflected waves with different wave distance from the ground and the scatters. In fact, the scattering fields in half space may be easily found for a set of source, if the half space dyadic Green's function of the environment are available [15].

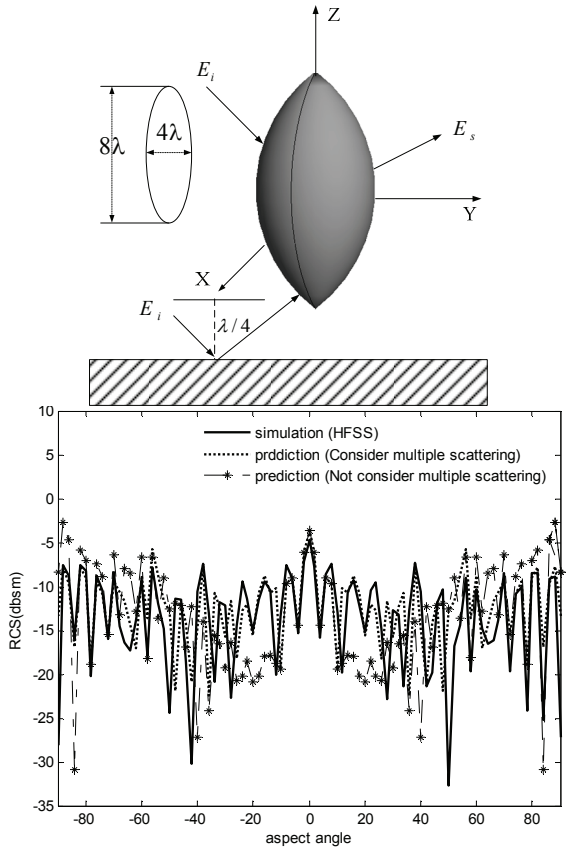

Fig. 10. The ellipsoid is placed $\lambda/4$ m in half space, frequency 10 GHZ, and vertical polarization.

IV. CONCLUSION

In this paper, we have presented an accurate and efficient approach for calculating the electrically large PEC targets in half space. In order to consider the electrically large PEC targets in half space, the half-space high-frequency method has been deduced by introducing the half-space Green's function into the conventional physical optics method (PO), method of equivalent currents (MEC). Combined with the graphical-electromagnetic computing (GRECO) method, the shadow regions are eliminated by displaying lists technology of OpenGL to rebuild the target and the geometry information is obtained by reading the color and depths of each pixel. Finally, we included the correction in our calculations by accounting for the currents on facets that were illuminated by the ground reflected wave. Then one may calculate the radar cross-section of a conductive target object in a half space. The numerical results have shown that this method is efficient and accurate.

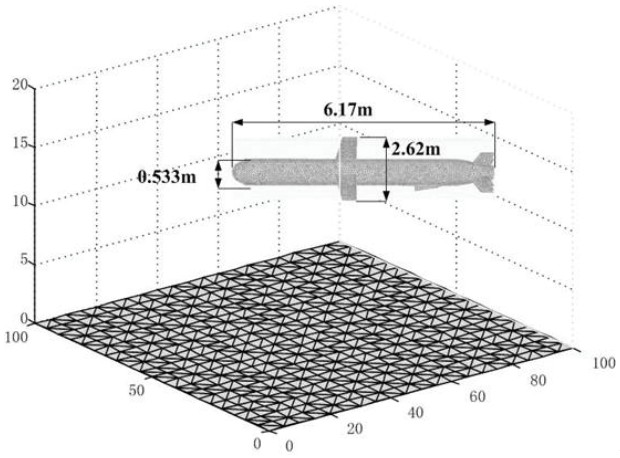

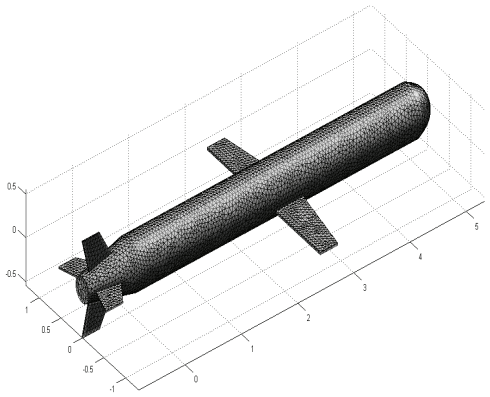

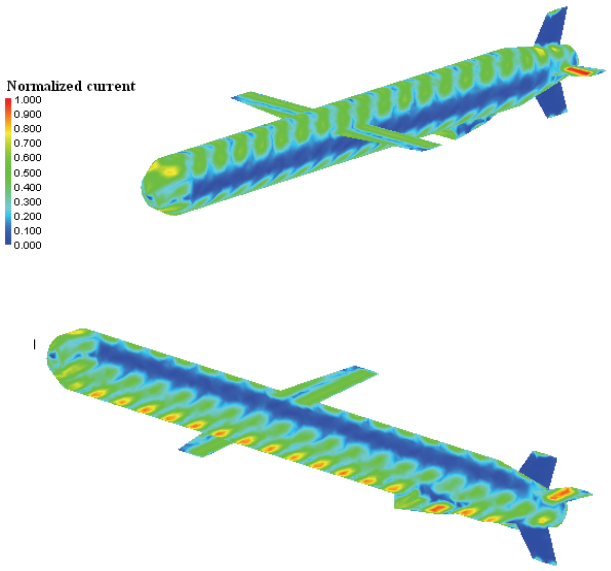

Fig. 11. Induced electric current on the surface of the missile in half space, frequency 1 GHZ, vertical polarization, at a incident angle of $\theta_i = 30, \varphi_i = 0$.

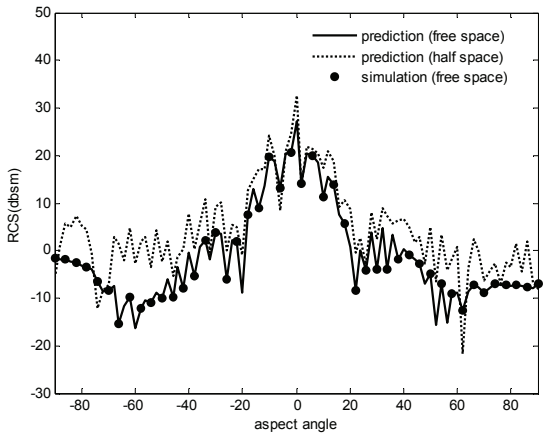

Fig. 12. The missile is placed 5m above the soil in half space, frequency 1 GHZ, and vertical polarization.

REFERENCES

[1] N. Yousee, "Radar Cross Section of Complex Targets," *Proc. IEEE*, vol. 77, no. 5, pp. 722-734, 1989.

[2] D. M. Elking, J. M. Roedder, D. D. Car and S. D. Alspach, "A review of high-frequency radar cross section analysis capabilities at McDonnell Douglas aerospace," *IEEE Antennas and Propag*, vol. 37, no. 5, pp. 33-43, 1995.

[3] J. M. Rius, M. Ferrando and L. Jofre, "High-Frequency RCS of complex radar targets in real-time," *IEEE Antennas and Propag,* vol. 41, no. 9, pp. 1308-1460, 1993.

[4] E. F. Knott, "A Progression of high-frequency RCS prediction techniques," *Proc. IEEE,* vol. 73, pp. 252-264, 1985.

[5] C. Long Yu and S. W. Lee, "Radar Cross Section Computation and Visualization by Shooting and Bouncing rays (SBR) Technique," *IEEE Antennas Propag,* vol. 37, pp. 194-205, Feb. 1989.

[6] S. M. Rao, D. R. Wilton, A. W. Glisson, "Electromagnetic scattering by surfaces of arbitrary shape," *IEEE Trans. Antennas Propag*, vol. 30, pp. 409-418, 1982.

[7] M. Domingo, F. Rivas, J. Perez, R. P. Torres, and M. F. Catedra, "Computation of the RCS of complex bodies modeled using NURBS surfaces," *IEEE Antennas Propag*, vol. 37, no. 1, pp. 36-47, 1995.

[8] D. H. Han and A. C. Polycarpou, "Ground Effects for VHF/HF antennas on helicopter air frames," *IEEE Trans Antennas Propag*, vol. 49, no. 3, pp. 402-412, 2001.

[9] Q. L. Li, D. B. Ge, S. Y. Shi, and Y. B. Yan, "An Approach for Solving Ground Wave Scattering from Objects," *J. MICROW,* vol. 14, no. 3, pp. 23-28, 1998.

[10] X. L. Ming, N. Z. Ping, and W. Jun, "Electric-Field-Type Dyadic Green's Functions for Half-Spaces and its Evaluation," *J.UEST China,* vol. 33, no. 5, pp. 485-4881, 2004.

[11] Z. Liu, J. He, Y. Xie, A. Sullivan, and L. Carin, "Multilevel Fast Multiple Algorithm for General Targets on a Half-Space Interface," *IEEE Trans. Antennas Propag,* vol. 50, no. 12, pp. 1838-1849, 2002.

[12] J. T. Johnson, "A study of the four-path model for scattering from an object above a half space," *Microwave and Optical Technology Letters*, vol. 30, no. 2, pp. 130-134, 2001.

[13] X. F. Li, Y. J. Xie, P. Wang, and T. M. Yang, "High-Frequency Method for Scattering From Electrically Large Conductive Targets in Half-Space," *IEEE Antennas and Wireless Propagation Letters*, vol. 6, pp. 259-262, 2007.

[14] X. F. Li, Y. J. Xie, and R. Yang, "High-frequency method analysis on scattering from homogenous dielectric objects with electrically large size in half space." *Progress in Electromagnetic Research B,* vol. 1, pp. 177-188, 2008.

[15] J. J. Yang, Y. L. Chow and D. G. Fang. "Discrete complex images of a three-dimensional dipole above and within a lossy ground," *Proc. Inst. Elect. Eng. H*, vol. 138, no. 4, pp. 319-326, 1991.

[16] Y. L. Chow, "A closed-form spatial Green's function for the thick microstrip substrate," *IEEE Trans. Microwave Theory Tech*, vol. 39, no. 3, pp. 588-592, 1991.

[17] G. Dural and M. I. Aksum, "Closed-Form Green's Function for General Sources and Stratified Media," *IEEE Transaction on Microwave Theory and Techniques*, vol. 43, no. 7, July 1995.

[18] M. I. Aksum, "A Robust Approach for the Derivation of Closed-Form Green's Function," *IEEE Transaction on Microwave Theory and Techniques*, vol. 44, no. 5, May 1996.

[19] Y. Z. Ruan, *Radar Cross Section and Stealth Technology,* National Defense Industry Press, 1998.

[20] A. Michaeli, "Equivalent edge currents for arbitrary aspects of observation," *IEEE Trans. Antennas Propag*, vol. 32, pp. 252-258, 1984.

[21] A. Michaeli, "Elimination of infinities in equivalent edge currents, part I: Fringe current components," *IEEE Trans. Antennas Propag*, vol. 34, pp. 912-918, 1986.

[22] H. Ling, R. C. Chou, and S. W. Lee, "Shooting and Bouncing Rays: Calculating the RCS of an Arbitrarily Shaped Cavity," *IEEE Trans. Antennas Propag*, vol. 37, pp.194-205, 1989.

[23] E. F. Knott, "RCS reduction of dihedral corners," *IEEE Trans. Antennas Propag*, vol. 25, pp. 406-409, May 1977.

Xiao Feng Li received the Bachelor degree in electronic engineering from Xidian University, Xi'an, Shannxi, China, in 2005. Since 2006, he has taken a combined master-doctor program and worked

for Ph.D. in Xidian University. He has been engaged in the development of the high-frequency RCS predictions. His current research interests involve both high frequency techniques and numerical methods for electromagnetic scattering analysis.

Yong Jun Xie received the B.S., M.S., and Ph.D. degrees in electronic engineering from the Xidian University, Xi'an, Shannxi, China, in 1990, 1993 and 1996, respectively. From 1998 to 1999 he worked at the University of Texas at Dallas as a postdoctoral research associate. Then he worked at Duke University as a postdoctoral research associate from 1999 to 2001. Currently he is a professor at Xidian University. His research interests include electromagnetic theory, microwave technology, and mobile telecommunications.

Rui Yang received the Bachelor degree in electronic engineering from Xidian University, Xi'an, Shannxi, China, in 2004. Since 2005, he has taken a combined master-doctor program and worked for Ph.D. in Xidian University. His current research interests involve metamaterials and antenna design.

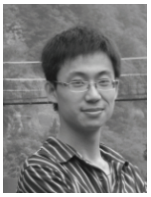

Yuan Yuan Wang received the Bachelor degree in electronic engineering from Xidian University, Xi'an, Shannxi, China, in 2005. Since 2006, he has taken a combined master-doctor program and worked for Ph.D. in Xidian University. His current research interests involve metamaterials and antenna design.

EM Scattering by a Lossy Dielectric-Coated Nihility Elliptic Cylinder

A-K. Hamid

Department of Electrical and Computer Engineering
University of Sharjah, Box 27272, Sharjah, UAE
akhamid@sharjah.ac.ae

***Abstract*—** The problem of electromagnetic wave scattering by a lossy dielectric coated nihility elliptic cylinder is analyzed by solving the analogous problem of scattering by two lossy dielectric layers elliptic cylinder using the method of separation of variables. The incident, scattered, and transmitted fields are expressed in terms of complex Mathieu functions. Numerical results are obtained for the scattered fields of lossy and lossless dielectric coated nihility circular and elliptic cylinders to show their effect on the backscattering widths.

***Index Terms*—** Nihility, lossy dielectric, elliptic cylinder, Mathieu functions.

I. INTRODUCTION

Analytical solution to the problem of a plane electromagnetic wave scattering by a lossless dielectric coated PEC elliptic cylinder has been investigated by many authors [1-2], and the solution was later extended to the nonconfocal dielectric case [3]. Axial slot antenna on a dielectric-coated elliptic cylinder was solved by [4]. Sebak obtained a solution to the problem of scattering from dielectric-coated impedance elliptic cylinder [5]. The scattering by mutilayered dielectric elliptic cylinders has been studied by many authors [6-12]. Recently, scattering by nihility circular cylinders and spheres were studied by many authors by letting the refractive index of the dielectric medium approach zero [13-16].

In this paper, the solution of the electromagnetic wave scattering by a lossy dielectric coated nihility elliptic is obtained by solving the problem of scattering by two lossy dielectric layered elliptic cylinders and letting the refractive index of the inner dielectric layer approach zero (relative permittivity and relative permeability of the inner cylinder are approximately null-valued, i.e., the electromagntic waves cannot propagate in that region). Nihility is unachievable, but it may be approximately simulated in some narrow frequency range [13]. The analysis and the software used for obtaining the numerical results have been validated by calculating the normalized backscattering widths for dielectric coated nihility elliptic cylinder of axial ratios approximately 1, and showing that these results are in full agreement with the same obtained for a lossless dielectric coated nihility circular cylinder analyzed using cylindrical wave functions.

II. FORMULATION OF THE SCATTERING PROBLEM

Consider the case of a linearly polarized electromagnetic plane wave incident on a two lossy dielectric layered elliptic cylinder at an angle ϕ_i with respect to the positive x axis, as shown in Fig. 1.

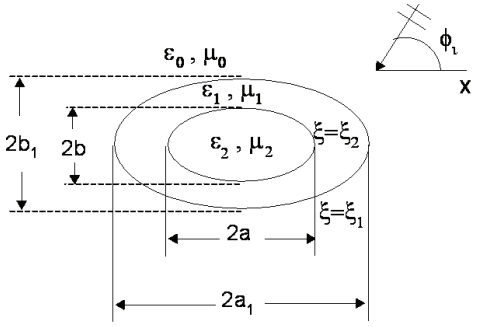

Fig. 1. Geometry of the scattering problem.

The outer dielectric layer has permittivity ε_1 and permeability μ_1 while the inner layer has permittivity ε_2 and permeability μ_2 .The semi-major and semi-minor axes for the inner dielectric

layer are a and b and for the outer dielectric layer are a_1 and b_1.

It is convenient to define the x and y coordinates of the Cartesian coordinate system in terms of the u and v coordinates of an elliptical coordinate system also located at the centre of the cylinder in the form of $x = F\cosh u\cos v$ and $y = F\sinh u\sin v$. A time dependence of e^{jwt} is assumed throughout the analysis, but suppressed for convenience.

The electric field component of the TM polarized plane wave of amplitude E_0 is given by

$$E_z^i = E_0 e^{jk_0\rho\cos(\varphi-\varphi_i)} \tag{1}$$

where k_0 is the wave number in free space and $j=\sqrt{-1}$. The incident electric field may be expressed in terms of complex angular and radial Mathieu functions as follows

$$E_z^i = \sum_{m=0}^{\infty} A_{em} R_{em}^{(1)}(c_0,\xi) S_{em}(c_0,\eta) + \sum_{m=1}^{\infty} A_{om} R_{om}^{(1)}(c_0,\xi) S_{om}(c_0,\eta) \tag{2}$$

where,

$$\begin{matrix} A_{em} \\ om \end{matrix} = E_0 j^m \frac{\sqrt{8\pi}}{\begin{matrix} N_{em} \\ om \end{matrix}(c_0)} \begin{matrix} S_{em} \\ om \end{matrix}(c_0,\cos\phi_i) \tag{3}$$

$$\begin{matrix} N_{em} \\ om \end{matrix}(c) = \int_0^{2\pi} \left[\begin{matrix} S_{em} \\ om \end{matrix}(c,\eta)\right]^2 dv \tag{4}$$

while $c_0 = k_0 F$, F is the semifocal length of the elliptical cross section, $\xi = \cosh u$, $\eta = \cos v$, S_{em} and S_{om} are the even and odd angular Mathieu functions of order m, respectively, $R_{em}^{(1)}$ and $R_{om}^{(1)}$ are the even and odd radial Mathieu functions of the first kind, and N_{em} and N_{om} are the even and odd normalized functions.

The scattered electric field outside the two dielectric layered elliptic cylinder ($\xi > \xi_1$) may be expressed in terms of Mathieu functions as follows

$$E_z^s = \sum_{m=0}^{\infty} B_{em} R_{em}^{(4)}(c_0,\xi) S_{em}(c_0,\eta) + \sum_{m=1}^{\infty} B_{om} R_{om}^{(4)}(c_0,\xi) S_{om}(c_0,\eta) \tag{5}$$

where B_{em} and B_{om} are the unknown scattered field expansion coefficients, $R_{em}^{(4)}$ and $R_{om}^{(4)}$ are the even and odd Mathieu functions of the fourth kind. The transmitted electric field into the outer dielectric layer ($\xi_2 < \xi < \xi_1$) may be written as

$$E_z^I = \sum_{m=0}^{\infty} \left[C_{em} R_{em}^{(1)}(c_1,\xi) + D_{em} R_{em}^{(2)}(c_1,\xi) \right] S_{em}(c_1,\eta) + \sum_{m=1}^{\infty} \left[C_{om} R_{om}^{(1)}(c_1,\xi) + D_{om} R_{om}^{(2)}(c_1,\xi) \right] S_{om}(c_1,\eta) \tag{6}$$

where $c_1 = k_1 F$, $k_1 = \omega\sqrt{\mu_1\varepsilon_1}$, $\varepsilon_1 = \varepsilon_1' - j\varepsilon_1''$, C_{em}, C_{om}, D_{em}, D_{em} are the unknown transmitted field expansion coefficients, and $R_{em}^{(2)}$ and $R_{om}^{(2)}$ are the radial Mathieu functions of the second type.

Similarly, the transmitted electric field into the inner dielectric layer ($\xi < \xi_2$) may be written as

$$E_z^{II} = \sum_{m=0}^{\infty} F_{em} R_{em}^{(1)}(c_2,\xi) S_{em}(c_2,\eta) + \sum_{m=1}^{\infty} F_{om} R_{om}^{(1)}(c_2,\xi) S_{om}(c_2,\eta) \tag{7}$$

where $c_2 = k_2 F$, $k_2 = \omega\sqrt{\mu_2\varepsilon_2}$, $\varepsilon_2 = \varepsilon_2' - j\varepsilon_2''$, and F_{em}, F_{om} are the unknown transmitted field expansion coefficients.

The magnetic field components inside and outside the elliptic cylinder can be obtained using Maxwell's equation, i.e.,

$$H_u = \frac{-j}{\omega\mu h}\frac{\partial E_z}{\partial v} \tag{8}$$

$$H_v = \frac{-j}{\omega\mu h}\frac{\partial E_z}{\partial u} \tag{9}$$

where $h = F\sqrt{\cosh^2 u - \cos^2 v}$. The unknown expansion coefficients in equation (5) can be obtained by imposing the boundary conditions at the various interfaces. Continuity of the tangential field components at $\xi = \xi_1$ and $\xi = \xi_2$ require that

$$E_z^i + E_z^s = E_z^I \qquad \xi = \xi_1 \qquad (10)$$

$$H_v^i + H_v^s = H_v^I \qquad \xi = \xi_1 \qquad (11)$$

$$E_z^I = E_z^{II} \qquad \xi = \xi_2 \qquad (12)$$

$$H_v^I = H_v^{II} \qquad \xi = \xi_2. \qquad (13)$$

Substituting equations (2), (5)-(7), into equations (10)-(13) and applying the orthogonality property will lead to a system of equations which may be solved numerically for the unknown scattered field coefficients B_{em} and B_{om}.

The expressions for the incident, scattered and transmitted electromagnetic fields for TE case can be obtained using the duality principle of the TM case.

III. NUMERICAL RESULTS

The obtained numerical results are presented as normalized echo pattern widths for lossy dielectric coated nihility circular and elliptic cylinders of different sizes, axial ratios, incident angles and permittivities, for both TM and TE polarizations of the incident wave. To validate the analysis and the software used for calculating the results, we have computed the normalized echo pattern widths for lossy $(\varepsilon_1 = 9.8 - j\,0.5)$ and lossless $(\varepsilon_1 = 9.8 - j\,0.0)$ dielectric coated nihility elliptic cylinders of axial ratio 1.001, $k_o a = 1.05$, $k_o a_1 = 2.1$, $\varepsilon_1 = 9.8 - j\,0.0$, and $\varphi_i = 180^o$. The numerical results have been shown in Fig. 2, and they are in full agreement for lossless case, verifying the accuracy of the analysis as well as the software used for obtaining the results [15].

Figure 3 shows the echo width pattern for a lossy dielectric coated nihility elliptic cylinder for both TM and TE cases with an incident angle of $\varphi_i = 180^o$. The numerical results are plotted for $\varepsilon_1 = 4.0 - j\,0.0$ and $\varepsilon_1 = 4.0 - j\,0.5$. The electrical dimensions of the scatterer are $k_o a = 2.50, k_o a_1 = 3.51$, $k_o b = 1.25$, and $k_o b_1 = 2.76$. It can be seen that the TM nihility lossless case has higher echo width values in the backward directions compared to the TE case. The lossy TM and TE cases have lower values compared to the losseless case in the forward and backscattering directions. Figure 4 shows a similar case with an incident $\phi_i = 90^o$.

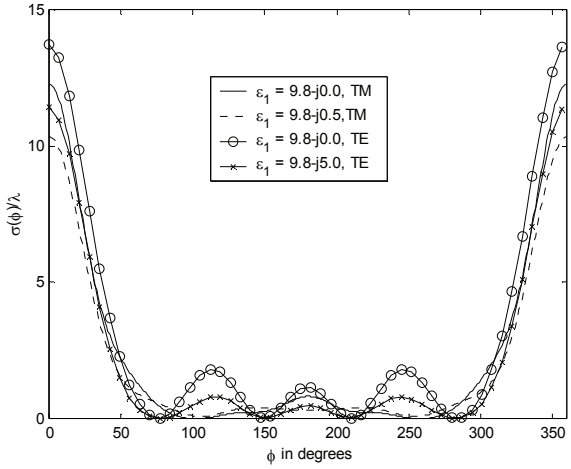

Fig. 2. Echo width pattern against the scattering angle ϕ of a lossy dielectric coated nihility circular cylinder with $k_o a = 1.05$, $k_o a_1 = 2.1$ and $\varphi_i = 180^o$.

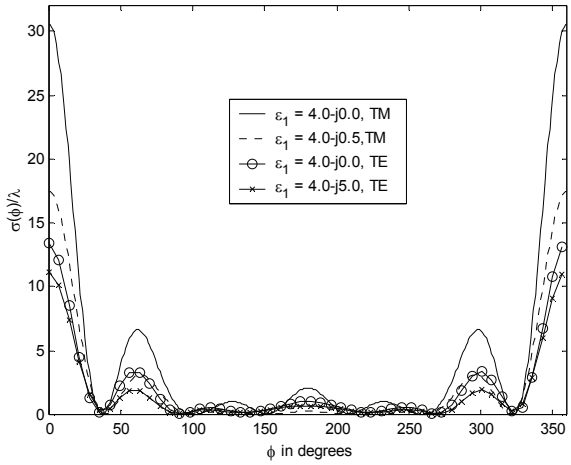

Fig. 3. Echo width pattern against the scattering angle ϕ of a lossy dielectric coated nihility elliptic cylinder with $k_o a = 2.50$, $k_o a_1 = 3.51$, $k_o b = 1.25$, and $k_o b_1 = 2.76$, and $\varphi_i = 180^o$.

Figure 5 shows the backscattering echo width pattern against ε_1' of a lossy and lossless dielectric coated nihility elliptic cylinder. The electrical dimensions are $k_o a = 1.25$, $k_o a_1 = 2.18$, $k_o b = 0.62$, and $k_o b_1 = 1.88$, and the incident

angle is $\phi_i = 0^o$. It can be seen that the backscattering echo width for nihility coated lossless case is higher than the coated lossless PEC case for higher values of $\varepsilon_1^{'}$, namely more than 8.

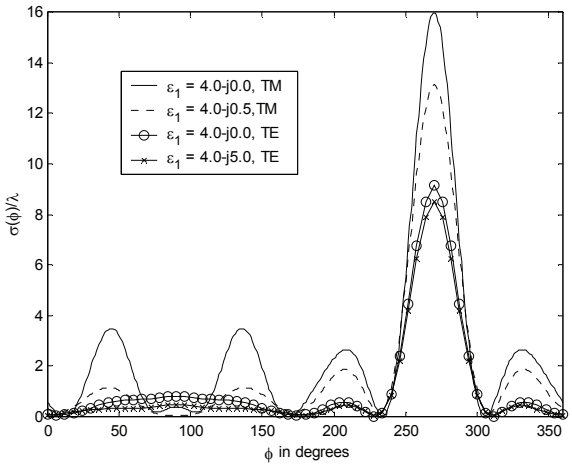

Fig. 4. Echo width pattern against the scattering angle ϕ of a lossy dielectric coated nihility elliptic cylinder with $k_o a = 2.50$, $k_o a_1 = 3.51$, $k_o b = 1.25$, and $k_o b_1 = 2.76$, and $\varphi_i = 90^o$.

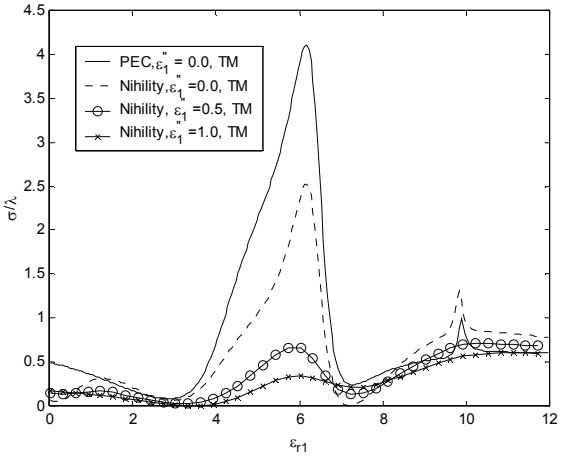

Fig. 5. Backscattering echo width pattern against $\varepsilon_1^{'}$ of a lossy dielectric coated nihility elliptic cylinder with $k_o a = 1.25$, $k_o a_1 = 2.18$, $k_o b = 0.62$, and $k_o b_1 = 1.88$, and $\phi_i = 0^o$.

Figure 6 shows the backscattering echo width pattern against $k_o a_1$ of a lossy and lossless dielectric coated nihility elliptic cylinder. The electrical dimensions are $k_o a = 0.6$, $k_o a_1 = 2.18$, $k_o b = 0.5$, and $k_o b_1$ changes simultaneously with $k_o a_1$ for incident angle $\phi_i = 0^o$. It can be seen that the backscattering echo width for nihility coated lossless case is lower than the coated lossless PEC case for $k_o a_1$ greater than 2.5.

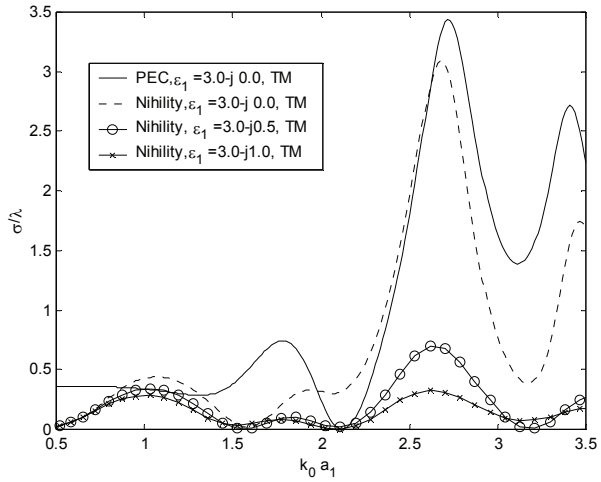

Fig. 6 Backscattering echo width pattern against $k_o a_1$ of a lossy dielectric coated nihility elliptic cylinder with $k_o a = 0.6$, $k_o b = 0.5$ and $\phi_i = 0^o$.

IV. CONCLUSIONS

Analytical solution of the electromagnetic wave scattering by lossy and lossless dielectric coated nihility circular and elliptic cylinders is obtained for TM and TE polarizations. The validity and accuracy of the obtained numerical results were verified against the case of lossless dielectric coated nihility circular cylinder using cylindrical wave functions and the agreement was excellent. Numerical results were presented as a function of the geometrical parameters of the cylinder and can be used to design scatterers with reduced or enhanced backscattering echo widths. Further, the solution is general where the special case of coated nihility circular cylinder may be obtained by letting the axial ratios approximately equal to 1.0 while the special case of coated nihility strip may be obtained by letting the thickness of the inner cylinder vanishes (letting the minor axis of the inner cylinder approaches zero). The nihility medium as well as different loss tangents considered in the numerical results showed a significant change in echo width patterns, i.e.

reduced at some geometrical parameters while enhance at others. It is worth mentioning that nihility material may be released from metamaterial where the refractive index approaches zero, i.e., metamaerial is made of mixture of helices and resonant dipoles [17], and nihility could happen at frequencies higher than optical frequencies.

ACKNOWLEDGMENT

The author wishes to acknowledge the support provided by the University of Sharjah, U.A.E.

REFERENCES

[1] H. A. Ragheb and L. Shafai, "Electromagnetic scattering from a dieletric coated elliptic cylinder," *Can. J. Phys.,* vol. 66, pp. 1115-1122, 1988.

[2] J. H. Richmond, "Scattering by a dielectric conducting elliptic cylinder with dielectric coating," *Radio Sci,* vol. 23, pp. 1061-1066, 1988.

[3] H. A. Ragheb, L. Shafai, and M. Hamid, "Plane wave scattering by a conducting elliptic cylinder coated by a nonconfocal dielectric," *IEEE Trans. Antenna and Propag.,* vol. 39, pp. 218-223, 1991.

[4] J. H. Richmond, "Axial slot antenna on dielectric coated elliptic cylinder," *IEEE Trans. Antenna and Propag.,* vol. 37, pp. 1235-1241, 1989.

[5] A-R. Sebak, "Scattering from dielectric coated impedance elliptic cylinder," *IEEE Trans. On Antenna and Propag.,* vol. 48, pp. 1574-1580, 2000.

[6] R. Holand and V. P. Cable, "Mathieu functions and their applications to scattering by a coated strip," *IEEE Trans. On Elect. Compt.,* vol. 34, no. 1, pp. 9-16, 1992.

[7] S. Caorsi, M. Pastorino, and M. Raffetto, "Electromagnetic scattering by a multilayer elliptic cylinder under transverse-magnetic illumination: series solution in terms of Mathieu function," *IEEE Trans. On Antenna and Propag.,* vol. 45, no. 6, pp. 926-935, 1997.

[8] E. S. Caorsi, M. Pastorino, and M. Raffetto, "Electromagnetic scattering by weakly lossy multilayer elliptic cylinders," *IEEE Trans. On Antenna and Propag.,* vol. 46, no. 11, pp. 1750-1751, 1998.

[9] A. Sebak, L. Shafai, and H. Ragheb, "Electromagnetic scattering by a two layered piecewise homogeneous confocal elliptic cylinder," *Radio Science*, vol. 26, pp. 111-119, 1991.

[10] A-K. Hamid, **"**Multi-Dielectric Loaded Axially Slotted Antenna on Circular or Elliptic Cylinder," *J. of Electromagnetic Waves and Applications,* vol. 20, no. 9, pp. 1259-1271, 2006.

[11] A-K. Hamid**, "**Scattering from a Semi-Elliptic Channel in a Ground Plane Loaded by a Lossy or Lossless Dielectric Elliptic Shell", *Applied Computational Electromagnetics Society Journal,* vol. 22, no. 3, pp. 414-419, 2007.

[12] A-K. Hamid and M. I. Hussein, "Electromagnetic Scattering by a Lossy Dielectric Coated Elliptic Cylinder," *Canadian Journal of Physics,* vol. 81, no. 5, pp. 771-778, 2003.

[13] A. Lakhtakia and J. B. Geddes, "Scattering by a nihility cylinder," *AEÜ International Journal of Electronic and Communications (AEÜ),* vol. 61, pp. 62-67, 2007.

[14] A. Lakhtakia, "Scattering by a nihility sphere," *Microwave and Optical Technology Letters,* vol 48, pp. 895- 896, 2006.

[15] S. Ahmed and Q. A. Naqvi, "Scattering of Electromagnetic Waves by a Coated Nihility Cylinder", *Journal of Infrared, Millimeter and Terahertz Waves,* vol. 30, no. 10, pp. 1044-1052, 2009.

[16] S. Ahmed and Q. A. Naqvi, "Directive EM Radiation of a Line Source in the Presence of a Coated Nihility Cylinder", *Journal of Electromagnetic Waves and Applications,* vol. 23, no. 5-6, 2009 , vol. 11, pp. 761-771, 2009.

[17] S. Tretyakov, A. Sihvola, and L. Jyla, "Backward wave region and negative refraction in chiral composites", *Photonics and Nanostructures- Fundemantes and Applications,* vol . 3, pp. 107-115, 2005.

A-K. Hamid was born in Tulkarm, WestBank, on Sept. 9, 1963. He received the B.Sc. degree in Electrical Engineering from West Virginia Institute of Technology and University, West Virginia, U.S.A. in 1985. He received the M.Sc. and Ph.D. degrees from the University of Manitoba, Winnipeg, Manitoba, Canada in 1988 and 1991, respectively, both in Electrical Engineering. From 1991-1993, he was with Quantic Laboratories Inc., Winnipeg, Manitoba, Canada, developing two and three dimensional electromagnetic field solvers using boundary integral method. From 1994-2000 he was with the faculty of electrical engineering at King Fahd University of Petroleum and Minerals, Dhahran, Saudi Arabia. Since Sept. 2000 he is with the electrical and computer engineering at the University of Sharjah, Sharjah, United Arab Emirates. His research interest includes EM wave scattering from two and three dimensional bodies, propagation along waveguides with discontinuities, FDTD simulation of cellular phones, and inverse scattering using neural networks.

FDTD Investigation on Electromagnetic Scattering from Two-Dimensional Layered Rough Surfaces

Juan Li, Li Xin Guo, and Hao Zeng

School of Science
Xidian University,No. 2, Taibai Road, Xi'an, Shaanxi, China
lijuan029@yeah.net, lxguo@mail.xidian.edu.cn, tsanghao@foxmail.com

***Abstract*—** This paper presents an investigation into the electromagnetic scattering characteristic of two-dimensional (2-D) layered rough surfaces by using a finite-difference time-domain (FDTD) algorithm, which constitutes a three-dimensional scattering problem. The uniaxial perfectly matched layer medium is adopted for truncation of FDTD lattices, in which the finite-difference equations can be used for the total computation domain by properly choosing the uniaxial parameters. The upper and down rough surfaces are characterized with Gaussian statistics for the height and the autocorrelation function. The angular distribution of bistatic scattering coefficent from a 2-D single-layered rough surface is calculated, and it shows good agreement with the numerical result through the Kirchhoff Approximation except for with large scattering angles. Finally, the bistatic scattering coefficents versus scattered and azimuthal angle for different conditions are analyzed in detail.

***Index Terms*—** Finite difference time domain (FDTD), electromagnetic scattering, rough surface.

I. INTRODUCTION

The electromagnetic scattering from a randomly rough surface has attracted considerable interest in the fields of radar surveillance, surface physics, and remote sensing of the ocean and soil. The analytical technique [1] and numerical techniques [2-3] have been developed for the efficient analysis of scattering by a single-layered rough surface. However, when the electromagnetic wave is incident on stratified soil, sand cover of arid regions, or ice and oil on the sea surface, it is necessary to investigate the scattering from multilayered rough surfaces. There have been some studies on the scattering from layered rough surfaces in recent years. Tabatabaeenejad, et al. [4] analyzed the bistatic scattering from two-dimensional (2-D) stratified rough surfaces by using the small perturbation method (SPM). Some numerical methods are also used to solve the scattering characteristic from 1-D or 2-D layered medium, such as the forward-backward method with spectral acceleration [5], the extended boundary condition method (EBCM) [6], and the steepest descent fast multipole method (SDFMM) [7]. In this paper, the finite-difference time-domain (FDTD) algorithm is utilized to analyze the electromagnetic scattering from 2-D layered rough surfaces. As for the FDTD algorithm applying to rough surface scattering is concerned, Hastings *et al*. analyzed the scattering from 1-D rough surface using the FDTD method with PML absorbing boundary [8]. Kuang et al. adopted the FDTD method to study the composite scattering from a target above the 2-D periodic rough surface [9]. In our previous work, this method with Mur and UPML absorbing boundary was utilized to solve the composite scattering from a target above 1-D randomly rough surface [10, 11]. Comparing the FDTD algorithm with other numerical methods, there are some advantages: the rough surface may be PEC and dielectric, which is due to the reason that any other change need not be done in the origina1 FDTD code except the part where the material constants are set in each cell. In addition, the results obtained by this method are in the time domain, and can indicate both the transient behavior as well as the steady state.

In the paper, the uniaxial perfectly matched layer (UPML) medium is adopted for truncation of FDTD lattices . In the uniaxial medium the finite-difference equations are suitable for the whole computation domain due to the field satisfy Maxwell's equations, which makes the problem simple. The paper is organized as follows: the theoretical formulae of calculating scattering fields

by FDTD are developed in Section II. The bistatic scattering coefficent versus scattered and azimuthal angle are presented and discussed in Section III for different conditions. Section IV ends with the conclusions of the paper and proposes further investigations in this topic.

II. BISTATIC SCATTERING FROM 2-D LAYERED ROUGH SURFACES

The geometry for 2-D layered rough surfaces is shown in Fig. 1, where the scattering model is composed of three homogeneous layers: the air, the upper medium layer with the finite thickness H, and the lower medium layer with infinite depth. The upper interface $f_1(x,y)$ and lower interface $f_2(x,y)$ are characterized with Gaussian statistics for the height and the autocorrelation function. The parameters ε_1, ε_2 represent the relative dielectric constants of the upper medium layer and the lower medium layer, respectively.

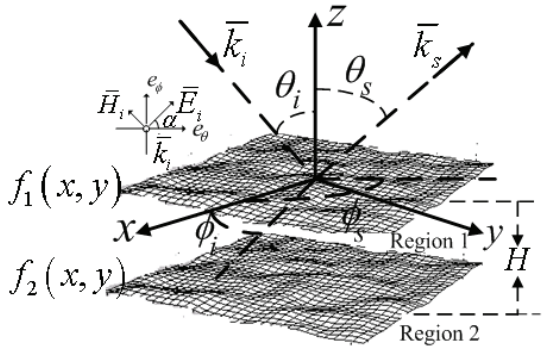

Fig. 1. Geometry of 2-D layered rough surfaces.

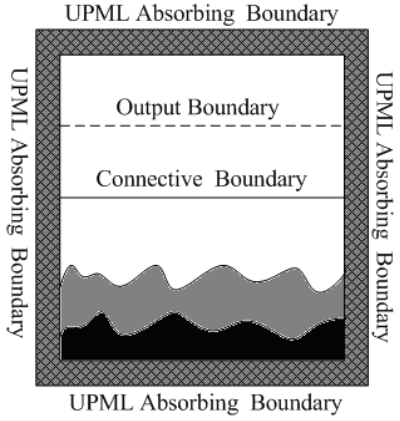

Fig. 2. Division model of computation region for the FDTD algorithm.

A. Simulation of Rough Surface and FDTD Model

In this section, a two-dimensional Gaussian randomly rough interface is simulated by Monte Carlo method [12]. It is assumed that the size of the rough surface is $S = L \times L$, and N is the number of the points discretized in the x- and y-directions. The rough surface profile $f(x,y)$ is expressed as:

$$f(x,y) = \frac{1}{L \times L} \sum_{m=-\frac{N}{2}}^{\frac{N}{2}-1} \sum_{n=-\frac{N}{2}}^{\frac{N}{2}-1} F\left(K_{xm}, K_{yn}\right) \exp(iK_{xm}x + iK_{yn}y) \tag{1}$$

$$F\left(K_{xm}, K_{yn}\right) = 2\pi L \sqrt{W(K_{xm}, K_{yn})} \begin{cases} \dfrac{N(0,1) + j_0 N(0,1)}{\sqrt{2}}, & m,n \neq 0, \dfrac{N}{2} \\ N(0,1) \quad m \text{ or } n = 0, \dfrac{N}{2} \end{cases} \tag{2}$$

where $j_0 = \sqrt{-1}$, $K_{xm} = \dfrac{2\pi m}{L}$ and $K_{y,n} = \dfrac{2\pi n}{L}$ are the discrete set of spatial frequencies. To generate a real sequence, the requirement for $F\left(K_{xm}, K_{yn}\right)$ is as follows

$$F\left(K_{xm}, K_{yn}\right) = F^*\left(-K_{xm}, -K_{yn}\right) \tag{3a}$$

$$F\left(K_{xm}, -K_{yn}\right) = F^*\left(-K_{xm}, K_{yn}\right) \tag{3b}$$

$W(K_{xm}, K_{yn})$ is the power spectral density function of Gaussian rough surface [12] given by:

$$W(K_{xm}, K_{yn}) = \frac{l_x l_y h^2}{4\pi} \exp\left(-\frac{K_{xm}^2 l_x^2}{4} - \frac{K_{yn}^2 l_y^2}{4}\right), \tag{4}$$

where, h is the root mean square (rms) of random surface height. l_x and l_y are the correlation lengths along the x- and y-directions.

It is important for us to know the division of the computation region with FDTD algorithm in calculating electromagnetic scattering from 2-D layered rough surfaces. Figure 2 shows the section plane along the x direction of the FDTD computation region. The incident wave is generated on the connective boundary, and the UPML absorbing medium is the outer boundary of FDTD region. In addition, the output boundary must be set to do a near-to-far transformation to obtain the far fields.

B. UPML Absorbing Boundary

In theory, the computational domain should be unbounded due to the scattered field existing in the infinite free space, but no computer can store an unlimited amount of data. To deal with the conflict, a virtual absorbing boundary must be built, and the outgoing waves have to propagate outward without non-physical reflection from the boundary. There have been many absorbing boundary conditions developed to implement this in the FDTD algorithm. Where, the UPML absorbing medium [13] is used to terminate the FDTD lattices, in which the finite-difference equations can be used for the total computation domain due to the fields satisfying Maxwell's equations (Ampere's law and Faraday's law). This makes the algorithm efficient since one does not have to take special care of the interface plane between the boundary and the interior regions. In addition, the uniaxial medium can be perfectly matched to an interior lossy medium without any modification except for properly choosing the uniaxial parameters. In the uniaxial medium, Ampere's law and Faraday's law in the *xyz* coordinate are expressed as

$$\begin{cases} \dfrac{\partial H_z}{\partial y}-\dfrac{\partial H_y}{\partial z}=(j_0 w\varepsilon_1+\sigma_1)\dfrac{s_y s_z}{s_x}E_x \\ \dfrac{\partial H_x}{\partial z}-\dfrac{\partial H_z}{\partial x}=(j_0 w\varepsilon_1+\sigma_1)\dfrac{s_x s_z}{s_y}E_y \\ \dfrac{\partial H_y}{\partial x}-\dfrac{\partial H_x}{\partial y}=(j_0 w\varepsilon_1+\sigma_1)\dfrac{s_x s_y}{s_z}E_z \end{cases} \tag{5a}$$

$$\begin{cases} \dfrac{\partial E_z}{\partial y}-\dfrac{\partial E_y}{\partial z}=-j_0 w\mu_1\dfrac{s_y s_z}{s_x}H_x \\ \dfrac{\partial E_x}{\partial z}-\dfrac{\partial E_z}{\partial x}=-j_0 w\mu_1\dfrac{s_x s_z}{s_y}H_y \\ \dfrac{\partial E_y}{\partial x}-\dfrac{\partial E_x}{\partial y}=-j_0 w\mu_1\dfrac{s_x s_y}{s_z}H_z \end{cases} \tag{5b}$$

where, ε_1 , μ_1 , σ_1 represent the electrical permittivity, the magnetic permeability, and the electric conductivity in the interior medium. s_x , s_y and s_z are only spatially variant along the x , y , and z directions, $s_x = k_x + \sigma_x / j_0 w\varepsilon_0$, $s_y = k_y + \sigma_y / j_0 w\varepsilon_0$, and $s_z = k_z + \sigma_z / j_0 w\varepsilon_0$, referring to [13]. In equation(5), for Ampere's law the intermediate variables P_x' , P_y' , P_z' and P_x , P_y , P_z are introduced as

$$P_x' = \frac{s_y s_z}{s_x}E_x,\quad P_y' = \frac{s_x s_z}{s_y}E_y,\quad P_z' = \frac{s_y s_x}{s_z}E_z \tag{6}$$

$$P_x = P_x' / s_y,\quad P_y = P_y' / s_z,\quad P_z = P_z' / s_x \tag{7}$$

and for Faraday's law, the intermediate variables B_x , B_y , and B_z are inserted

$$B_x = \mu_1\frac{s_z}{s_x}H_x,\quad B_y = \mu_1\frac{s_x}{s_y}H_y,\quad B_z = \mu_1\frac{s_y}{s_z}H_z \ . \tag{8}$$

Using a Fourier transform where $j_0 w \to \partial/\partial t$, the equations above can be transformed into the time domain. Thus, in Ampere's law the electric fields in the constant x plane are obtained by the following relations $H_y, H_z \to P_x' \to P_x \to E_x$, i.e.,

$$\frac{\partial H_z}{\partial y}-\frac{\partial H_y}{\partial z}=\varepsilon_1\frac{\partial P_x'}{\partial t}+\sigma_1 P_x' \tag{9a}$$

$$\frac{\partial P_x'}{\partial t}=k_y\frac{\partial P_x}{\partial t}+\frac{\sigma_y}{\varepsilon_0}P_x \tag{9b}$$

$$k_x\frac{\partial P_x}{\partial t}+\frac{\sigma_x}{\varepsilon_0}P_x=k_z\frac{\partial E_x}{\partial t}+\frac{\sigma_z}{\varepsilon_0}E_x \ . \tag{9c}$$

Similarly, in Faraday's law the magnetic field in the constant x plane is deduced by the relations $E_y, E_z \to B_x \to H_x$

$$\frac{\partial E_z}{\partial y}-\frac{\partial E_y}{\partial z}=-k_y\frac{\partial B_x}{\partial t}-\frac{\sigma_y}{\varepsilon_0}B_x \tag{10a}$$

$$k_x\frac{\partial B_x}{\partial t}+\frac{\sigma_x}{\varepsilon_0}B_x=\mu_1 k_z\frac{\partial H_x}{\partial t}+\frac{\mu_1}{\varepsilon_0}\sigma_z H_x \ . \tag{10b}$$

For planes of constant y or constant z the uniaxial parameters are simply permuted and similar expressions can easily be derived.

C. Connective Boundary

The connective boundary divides the computation region into the total field region and the scattered field region. The total field region contains the incident field and the scattered field, but the scattered field region only includes the scattered field [14]. It will be shown how the incident wave is generated on the connective boundary and limited in total field region.

In Fig. 1, a plane wave $\bar{E}_i = \hat{E}_0 \exp\left(-j_0 \bar{k}_i \cdot \bar{r} + j_0 wt\right)$ propagates in the direction of $\bar{k}_i$. The incidence direction $\bar{k}_i$ makes angles θ_i relative to the z -axis, and ϕ_i relative to the x-axis. The unit vector $\hat{E}_0$ is the unit polarization direction. The

polarization direction is rotated counter clockwise by the angle α (i.e. the polarization angle) from e_θ within the incidence plane. The incident wave is computed using the 1-D FDTD method [14] with the same spatial step $\Delta x = \Delta y = \Delta z = \delta$ and temporal step Δt as the 3-D FDTD method mentioned above. Where, Δx , Δy , Δz are the spatial increments in the x -, y - and z -directions. To ensure the stability and accuracy of the FDTD algorithm, $\Delta t = 0.5 \times \delta / c$ is presented to satisfy the Courant stability criterion in [15] and c is the light speed propagation in the vacuum.

Let $E_{x,i}^n$, $E_{y,i}^n$, $H_{x,i}^n$ and $H_{y,i}^n$ be the incident electrical and magnetic fields at the connective boundary. The finite- difference equations on the connective boundary should then be updated as:

$$E_x^{n+1}\left(i, j+\frac{1}{2}, k\right) = E_x^n\left(i, j+\frac{1}{2}, k\right) + \frac{\Delta t}{\varepsilon}\left[\nabla \times \bar{H}\right]_x^{n+1/2} - \frac{\Delta t}{\varepsilon}\frac{H_{y,i}^{n+1/2}\left(i+\frac{1}{2}, j, k+\frac{1}{2}\right)}{\Delta z} \tag{11}$$

$$E_y^{n+1}\left(i, j+\frac{1}{2}, k\right) = E_y^n\left(i, j+\frac{1}{2}, k\right) + \frac{\Delta t}{\varepsilon}\left[\nabla \times \bar{H}\right]_y^{n+1/2} + \frac{\Delta t}{\varepsilon}\frac{H_{x,i}^{n+1/2}\left(i, j+\frac{1}{2}, k+\frac{1}{2}\right)}{\Delta z} \tag{12}$$

$$H_x^{n+\frac{1}{2}}\left(i, j+\frac{1}{2}, k+\frac{1}{2}\right) = H_x^{n-\frac{1}{2}}\left(i, j+\frac{1}{2}, k+\frac{1}{2}\right) - \frac{\Delta t}{\varepsilon}\left[\nabla \times \bar{H}\right]_x^n + \frac{\Delta t}{\mu}\frac{E_{y,i}^n\left(i, j+\frac{1}{2}, k\right)}{\Delta z} \tag{13}$$

$$H_y^{n+\frac{1}{2}}\left(i+\frac{1}{2}, j, k+\frac{1}{2}\right) = H_y^{n-\frac{1}{2}}\left(i+\frac{1}{2}, j, k+\frac{1}{2}\right) - \frac{\Delta t}{\varepsilon}\left[\nabla \times \bar{E}\right]_y^n - \frac{\Delta t}{\mu}\frac{E_{x,i}^n\left(i+\frac{1}{2}, j, k\right)}{\Delta z}. \tag{14}$$

In numerical simulations, a finite-length rough surface must be used to model scattering from the infinite surface. When a plane wave strikes the finite-length rough surface, boundary reflection occurs. One way of minimizing reflection is to construct an incident wave that tapers to very small values at the surface edges. Reflection still occurs and cannot be completely eliminated, but it makes negligible contributions to the scattered field. To solve this problem, Fung et al. put forward the Gaussian window function [16] to guard against the truncation effect, and the Gaussian window function is written as

$$G(x, y) = \exp\left\{-\left[(x-x_0)^2 + (y-y_0)^2\right]\left(\frac{\cos\theta_i}{T}\right)^2\right\} \tag{15}$$

where x_0 and y_0 are the spatial coordinates at the center of the connective boundary, T is a constant which determines the width of the window function, $\cos\theta_i / T = 2.6/\rho_m$ and ρ_m is the minimum distance from the center (x_0, y_0) to the edge surface.

D. Output Boundary

The near fields for the rough surface can be obtained on the basis of theory described above. As indicated in [14], a way to obtain the far field is to do a near-to-far field transformation, which is based on the surface equivalence theorem. The transform formula for the output boundary is expressed as

$$\bar{E}_\theta = \hat{\theta}(-j_0 k_0 \frac{\exp(-jk_0 r)}{4\pi r})\left[z_0 f_x \cos\theta_s \cos\phi_s + z_0 f_y \cos\theta_s \sin\phi_s + (-f_{mx}\sin\phi_s + f_{my}\cos\phi_s)\right] \tag{16}$$

$$\bar{E}_\phi = \hat{\phi}\, j_0 k_0 \frac{\exp(-j_0 k_0 r)}{4\pi r}\left[z_0 f_x \sin\phi_s - z_0 f_y \cos\phi_s + f_{mx}\cos\theta_s \cos\phi_s + f_{my}\cos\theta_s \sin\phi_s\right] \tag{17}$$

where k_0 is the incident wave number (i.e., $k_0 = |\bar{k}_i|$). r is the distance from the origin of the $xyz-$ coordinate to any point at infinity and z_0 is the wave impedance in free space. ϕ_s represents the scattered azimuthal angle, and θ_s is the scattered angle. The terms f_x , f_y , f_{mx} , and f_{my} are related to equivalent surface electric and magnetic currents [14]. In the paper, we choose the incident plane xoz (see Fig. 1)as the reference plane. Thus, the horizontal polarization wave is incidence on a 2-D rough surface when the incident electric field $\bar{E}_i$ is in the plane xoz (i.e. $\alpha = 0^o$). Otherwise, the vertical polarization wave is considered (i.e.

$\alpha = 90^{\circ}$). The bistatic scattering coefficient [17] in the far zone is shown as

$$\sigma_{\mathrm{HH}} = \lim_{r\to\infty} \frac{4\pi r^2}{S} \frac{\left|\bar{E}_{\theta}\right|^2}{\left|\bar{E}_i\right|^2}, \sigma_{\mathrm{VH}} = \lim_{r\to\infty} \frac{4\pi r^2}{S} \frac{\left|\bar{E}_{\phi}\right|^2}{\left|\bar{E}_i\right|^2} \quad (\alpha = 0^{\circ}) \tag{18a}$$

$$\sigma_{\mathrm{HV}} = \lim_{r\to\infty} \frac{4\pi r^2}{S} \frac{\left|\bar{E}_{\theta}\right|^2}{\left|\bar{E}_i\right|^2}, \sigma_{\mathrm{VV}} = \lim_{r\to\infty} \frac{4\pi r^2}{S} \frac{\left|\bar{E}_{\phi}\right|^2}{\left|\bar{E}_i\right|^2} \quad (\alpha = 90^{\circ}) \ . \tag{18b}$$

III. NUMERICAL RESULTS AND DISCUSSIONS

In this section, the numerical results of basic scattering from a 2-D two-layered rough surface for different conditions are discussed in detail. For convenience, some parameters describing the rough surface are measured in wave length λ, and $S = 25.6\lambda \times 25.6\lambda$. The spatial increment is taken as $\Delta x = \Delta y = \Delta z = \delta = \lambda/10$. The PML

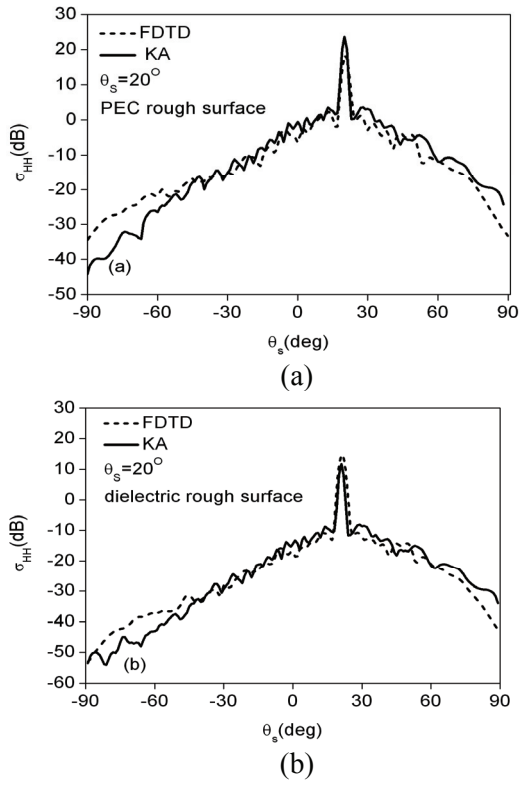

Fig. 3. Comparison of the two different methods for the bistatic scattering from 2-D single-layered rough surface, $\theta_i = 20^{\circ}$ (a) PEC (b) dielectric. thickness is 5δ.

The randomly rough surface is created by 10 Monte Carlo realizations and it is assumed that the horizontal incident wave is considered (i.e., $\alpha = 0^{\circ}$). The incident azimuthal angle is $\phi_i = 180^{\circ}$, and incident frequency is 0.3GHz in the following results.

In order to ensure the validity of FDTD algorithm presented in the paper, in Fig. 3 we first compute the angular distribution of bistatic scattering coefficient from 2-D PEC and dielectric single-layered rough surface using the Kirchhoff Approximation (KA) and FDTD, respectively. The incident angle is 20° and the bistatic HH polarized scattering is considered. The rms height and correlation length of rough surface is given by $h = 0.1\lambda$ and $l_x = l_y = 1.0\lambda$. The relative dielectric constant of dielectric rough surface is $\varepsilon_r = (2.5, 0.18)$ .The results from KA are obtained by introducing the 2-D tapered incident wave [18] instead of the plane wave into the classical Kirchhoff approximation [19].

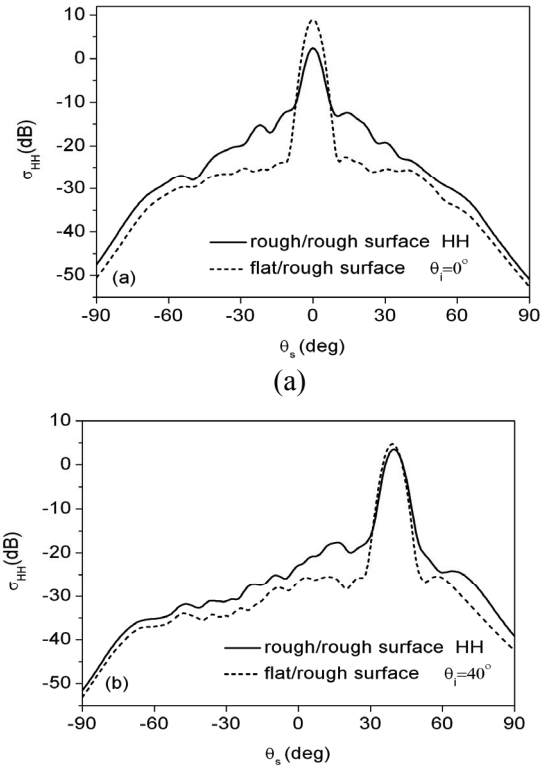

Fig. 4. The angular distribution of bistatic scattering coefficient for the different roughness of upper interface (a) $\theta_i = 0^{\circ}$, (b) $\theta_i = 40^{\circ}$.

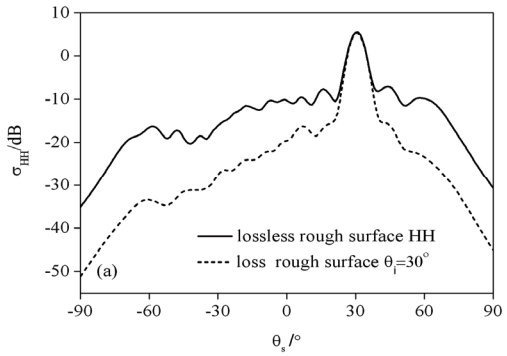

(a)

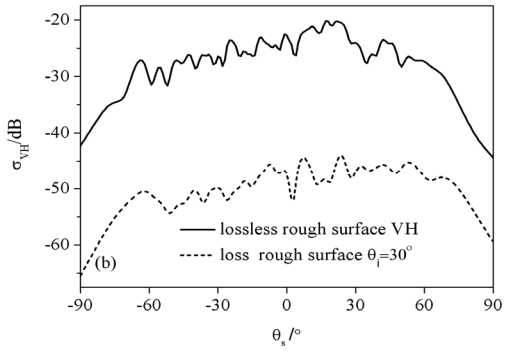

(b)

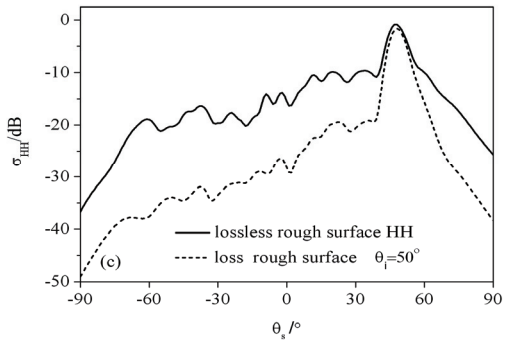

(c)

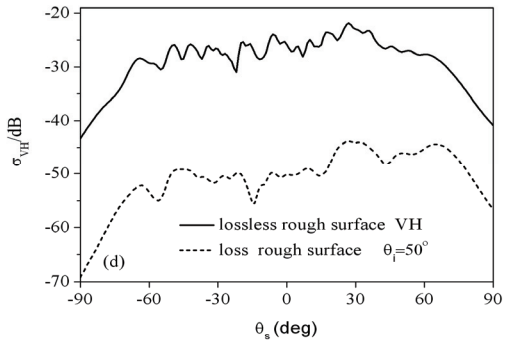

(d)

Fig. 5. Bistatic scattering coefficient from the two-layered lossless/ loss rough surface(a)HH $\theta_i = 30^o$ (b)VH $\theta_i = 30^o$ (a)HH $\theta_i = 50^o$ (b)VH $\theta_i = 50^o$.

It is obvious that the angular distribution of scattering coefficient for both the PEC (Fig. 3(a)) and dielectric (Fig. 3(b)) rough surface by FDTD is in good agreement with that obtained by KA except for the large scattering angles, which demonstrates the feasibility and applicability of FDTD algorithm.

Figure 4 presents the angular distribution of bistatic scattering coefficient for the case of the upper interface is flat but the lower interface is rough (i.e., flat/rough, $h_2 = 0.2\lambda$, $l_{2x} = l_{2y} = 1.3\lambda$), and for the case of both the two interfaces are rough (i.e., rough/rough, $h_1 = 0.1\lambda$, $l_{1x} = l_{1y} = 1.0\lambda$, $h_2 = 0.2\lambda$, $l_{2x} = l_{2y} = 1.3\lambda$). The thickness of upper medium layer is $H = 2\lambda$ where the results for HH polarization are given for both the incident angle 0^o (Fig. 4 (a)) and 40^o (Fig. (b)). The relative dielectric constant of upper medium layer is $\varepsilon_1 = (3.7, 0.13)$, and that of the lower medium layer is $\varepsilon_2 = (16.16, 1.15)$ [20]. It is shown that the bistatic scattering from a rough/rough surface is stronger than that of a flat/rough surface for all the scattering angles except for the specular direction. In the large scattered direction, the latter is relatively approach to the former.

In Fig. 5, co-polarized (HH) and cross-polarized (VH) bistatic scattering coefficients from two-layered lossless/loss rough surfaces ($h_1 = 0.1\lambda$, $l_{1x} = l_{1y} = 1.0\lambda$, $h_2 = 0.2\lambda$, $l_{2x} = l_{2y} = 1.3\lambda$, $H = 2\lambda$) are investigated for the different incident angles, where the dielectric constant of lossless rough surfaces is $\varepsilon_1 = 3.7$, $\varepsilon_2 = 16.16$, and that of loss rough surfaces is $\varepsilon_1 = (3.7, 0.13)$, $\varepsilon_2 = (16.16, 1.15)$. As the HH polarization (Fig. 5(a) and Fig. 5(c)) is concerned, it is easily observed that the bistatic scattering coefficient from two-layered lossless rough surfaces is much greater than the result of two-layered loss rough surfaces for the scattered angles except for the specular direction. But for VH polarization (Fig.5 (b) and Fig. 5 (d)), the scattering from lossless layered rough surfaces is larger than that of loss rough surfaces over the whole scattered angles range.

To further explore the important scattering characteristics of 2-D layered rough surfaces, the azimuthal variation of bistatic HH- and VH-polarized scattering coefficients are investigated for different scattered angles in Fig. 6. The

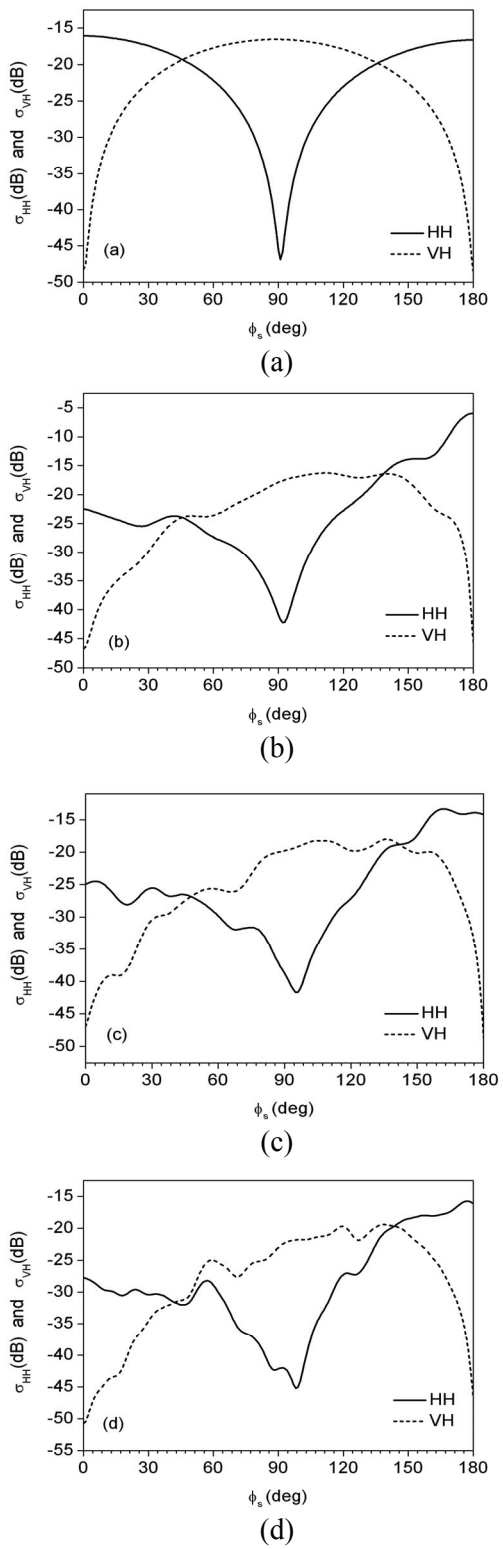

Fig. 6. The azimuthal distribution of bistatic scattering coefficient from two-layered rough surfaces $\theta_i = 20^o$ (a) $\theta_s = 5^o$ (b) $\theta_s = 15^o$ (c) $\theta_s = 30^o$ (d) $\theta_s = 45^o$.

parameters of rough surface are identical to the data in Fig. 5. The incident angle 20^o is considered. It is shown that the angular distribution from HH-polarized scattering coefficients reaches a maximum in the neighborhood where the VH polarization is a minimum and vice versa in Fig.6. In addition, it is observed that the azimuthal angular pattern of the scattered angle 0^o is nearly symmetric for both HH polarization and VH polarization, but the minimum of HH polarization and the maximum of VH polarization begin to shift towards the forward direction ($\phi_s = 180^o$) for the other scattering angles.

IV. CONCLUSIONS

This paper presents a study of electromagnetic scattering from 2-D layered rough surfaces by using FDTD algorithm. At first, the basic theory of FDTD method for calculating the scattered field is developed, including the generation of incident wave, the UPML absorbing boundary conditions, and a transform from near- to far- field on the output boundary. Then the numerical results of bistatic scattering coefficent versus scattered and azimuthal angle for different conditions are shown and analyzed in detail. Future investigation will include the electromagnetic scattering from 2-D layered rough surfaces with a large-scale rough surface and a large incident angle.

ACKNOWLEDGEMENT

This work was supported by the National Natural Science Foundation of China (Grant No. 60571058) and the Specialized Research Fund for the Doctoral Program of Higher Education, China (20070701010).

REFERENCES

[1] T. M. Elfouhaily and J. T. Johnson, "A New Model for Rough Surface Scattering," *IEEE Trans. Geosci. Remote Sensing*, vol. 45, no.7, pp. 2300-2308, 2007.

[2] R. L. Wagner, J. M. Song, and W. C. Chew, "Monte Carlo Simulation of Electromarrnetic Scattering from Two-Dimensional Random Rough Surfaces," *IEEE Trans. Antennas Propag*., vol. 45, no. 2, pp. 235-245,1997.

[3] S. Q. Li , C. H. Chan, M. Y. Xia, B. Zhang, and L. T. Sang, "Multilevel expansion of the

sparse-matrix canonical grid method for two-dimensional random rough surfaces," *IEEE Trans. Antennas Propag*., vol. 49, no. 11, pp. 1579-1589, 2001.

[4] A. Tabatabaeenejad and M. Moghaddam, "Bistatic scattering from three-dimensional layered rough surfaces," *IEEE Trans. Geosci. Remote Sensing*, vol. 44, no. 8, pp. 2102-2114, 2006.

[5] C. D. Moss, T. M. Grzegorczyk, H. C. Han, and J. A. Kong, "Forward-backward method with spectral acceleration for scattering from layered rough surfaces," *IEEE Trans. Antennas Propag*., vol. 54, no. 3, pp. 1006-1016, 2006.

[6] C. H. Kuo and M. Moghaddam, "Scattering from multilayer rough surfaces based on the extended boundary condition method and truncated singular value decomposition," *IEEE Trans. Antennas Propag*., vol. 54, no. 10, pp.2917-2929, 2006.

[7] M. E. Shenawee, "Polarimetric scattering from two-layered two-dimensional random rough surfaces with and without buried objects," *IEEE Trans. Geosci. Remote Sensing*, vol. 52, no. 1, pp. 67-76, 2005.

[8] F. D. Hastings, J. B. Schneider, and S. L. Broschat, "A Monte-Carlo FDTD technique for rough surface scattering," *IEEE Trans. Antennas Propagat.*, vol. 43, no. 11, pp. 1183-1191, 1995.

[9] L. Kuang and Y. Q. Jin, "Bistatic scattering from a three-dimensional object over a randomly rough surface using the FDTD algorithm," *IEEE Trans. Antennas Propagat.*, vol. 55, no. 8, pp. 2302-2312, 2007.

[10] J. Li, L. X. Guo and H. Zeng, "FDTD investigation on the electromagnetic scattering from a target above a randomly rough sea surface," *Waves in Random and Complex Media*, vol. 18, no. 4, pp. 641-650, 2008.

[11] J. Li, L. X. Guo, and H. Zeng, "FDTD investigation on bistatic scattering from a target above two-layered rough surfaces using UPML absorbing condition," *Progress In Electromagnetics Research,* vol. 88, pp. 197-211, 2008.

[12] Y. Kuga and P. Phu, "Experimental studies of millimeter wave scattering in discrete random media and from rough surfaces," *Progress In Electromagnetics Research*, vol. 14, pp. 37–88, 1996.

[13] S. D. Gedney, "An anisotropic perfectly matched layer-absorbing medium for the tr uncation of FDTD lattices," *IEEE Trans. Antennas Propagat.*, vol. 44, no. 12, pp.1630-1639, 1996.

[14] A. Taflove and S. C. Hagness, *Computational Electrodynamics: The Finite-Difference Time- Domain Method*, Artech House, 1995.

[15] J. S. Juntunen, T. D. Tsiboukis, "Reduction of numerical dispersion in FDTD method through artificial anisotropy,"*IEEE Trans. on Microwave Theory Tech.*, vol. 58, pp. 582-588,2000.

[16] A. K. Fung, M. R. Shah, and S. Tjuatja, "Numerical simulation of scattering from three- dimensional randomly rough surfaces," *IEEE Trans. Geosci. Remote Sensing*, vol. 32, no. 5, pp. 986-995, 1995.

[17] G. Ruck, D. E. Barrick, W. D. Stuart, and C. K. Krichbaum, *Radar Cross Section Handbook*, vol. 1, Plenum Press, 1970.

[18] L. Tsang, J. A. Kong and K. H. Ding. *Scattering of Electromagnetic Waves*, John Wiley & Sons. Inc, 2001.

[19] J. A. Ogilvy, *Theory of wave scattering from random rough surface,* IOP Publishing, 1991.

[20] J. R. Wang and T. J. Schmugge, "An empirical model for the complex dielectric permittivity of soils as function of water content," *IEEE Trans. Geosci. Remote Sensing*, vol. GRS-18, pp. 288–295, 1980.

Electrical Performance Estimations for Shaped Dielectric Lens Antenna with Array Feed

Yosuke Tajima, Shinji Kamada, Naobumi Michishita and Yoshihide Yamada

Department of Electrical and Electronic Engineering
National Defense Academy
1-10-20 Hashirimizu, Yokosuka-shi, 239-8686 JAPAN
yyamada@nda.ac.jp

***Abstract*—**A shaped dielectric lens antenna with simple array feeds was developed to realize wide-angle beam scanning in car-mounted radar systems. The electrical performance of the dielectric lens antenna has been previously studied through electromagnetic simulations. The authors fabricated a practical dielectric lens antenna operating at 20 GHz and measured its performance. A convenient patch antenna configuration was developed for the array feed. A power divider comprising eight branched microstrip lines was designed in order to achieve precise excitation coefficients for the array feed. Design accuracy of the array feed was confirmed from measured and calculated results for the excitation coefficients and radiated electric field. To determine the wide-angle beam scanning characteristics, the aperture amplitude and phase distributions were estimated numerically using the obtained array radiated electric field. Excellent flat-phase characteristics were confirmed. The commercial electromagnetic simulator FEKO was employed for the numerical simulations. The radiation patterns at a 30° beam scanning angle were measured. Very good agreements between the measured and calculated results were found. Moreover, sufficient antenna gain was confirmed through experiments.

***Index Terms*—** Shaped dielectric lens antenna, array feed, wide-angle beam scanning, electromagnetic simulation.

I. INTRODUCTION

Communication and car safety systems are under development as part of the Intelligent Transportation Systems (ITS) operating in the millimeter-wave frequency bands [1, 2]. For collision avoidance, car radar systems that can scan 15° have been developed. However, in order to expand the system for local street use, wide-angle beam scanning ability of over 30° is necessary. For this, a dielectric lens antenna is considered one of the promising candidates [3]. The authors have been studying shaped dielectric lens antennas. Lens shaping based on Abbe's sine condition [4] was proven to have excellent wide-angle beam scanning capability [5]. Moreover, the wide-angle beam scanning capability can be further improved by employing simple array feeds [6]. Previously, the electrical performance of the array-feed dielectric lens antenna was studied through electromagnetic simulations [7]. In the simulations, rectangular horn antennas were considered as elements of the array feed. By employing both a shaped dielectric lens and array feed, an almost flat aperture phase distribution was achieved. As a result, the radiated beam at the 30° direction could maintain the same beam shape at the 0° direction [7].

In this study, the realization of a shaped lens and array feed is pursued, and the appropriate simulation tool for this rather complicated configuration is identified. As an array element antenna, a patch antenna configuration is developed in place of the rectangular horn. In order to achieve proper excitation coefficients for the array feed, a power divider consisting of a microstrip circuit is designed. The shaped dielectric lens is fabricated by adequately forming a polycarbonate material. In order to confirm the design accuracies, electromagnetic simulation results and measured results are compared. As a simulator, the FEKO suite (ver. 5.3) is employed. The electric field distributions of the array feed and dielectric lens are obtained and achievement of design concepts is confirmed. Finally, the wide-angle beam scanning characteristics—radiation patterns and antenna gains—are confirmed. As a result, the realization of a wide-angle beam scanning antenna is confirmed.

II. CONCEPT OF ARRAY-FEED SHAPED LENS ANTENNA

The antenna configuration is shown in Fig. 1. The dielectric lens antenna has an axisymmetrical structure around the Z axis. The lens surfaces were shaped based on Abbe's sine condition [4, 5]. Beam scanning is achieved by replacing the feed positions. The on-focus feed is placed at the origin of the XYZ axes. The off-focus feed for beam scanning is placed in the XZ plane. Here, the beam scanning is achieved in the XZ plane. In the off-focus feed, a linear array antenna arranged in the Y axis direction is employed.

The roles of the lens antenna and the array feed cooperate in this configuration. The shaped lens antenna can achieve a constant wave front in the scanning plane. As a result, a sharp beam is obtained in the scanning plane. The array feed is designed to achieve a constant wave front in the transverse plane. Thus, a sharp beam is obtained in the transverse plane. With the assistance of these two parts, a sharp pencil beam is achieved in the wide-angle beam direction.

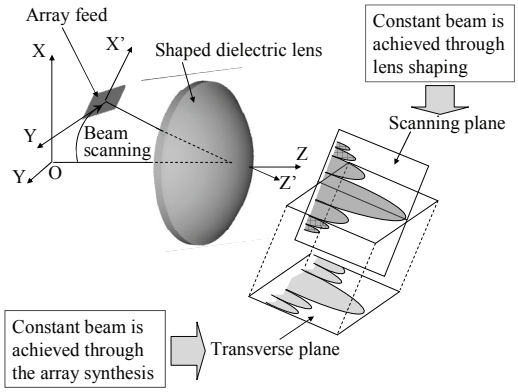

Fig. 1. Configuration of array feed and shaped lens antenna.

III. DESIGN RESULTS OF THE ARRAY FEED LENS ANTENNA

A. Shaped Dielectric Lens for Wide-Angle Scanning

The abilities of the shaped lens in 30° beam scanning are shown in Fig. 2. The effects of the lens are studied through ray tracings. The ideal condition is that all rays refracted by the lens become parallel. In the scanning directions of Fig. 2 (a), refracted rays become parallel and arranged in a straight line. However, in the transverse direction, refracted rays become curved and form a U-shaped line. The ray tracing results are converted to the antenna aperture phase distribution (ϕ_{ap}), as shown in Fig. 2 (b). In the scanning plane, constant phases are achieved. However, in the transverse plane, large phase delays occurred. These phase delays produce radiation pattern degradation in the transverse plane. Thus, compensation of this phase delay is necessary to achieve excellent scanning characteristics. We employed an array feed configuration for this purpose.

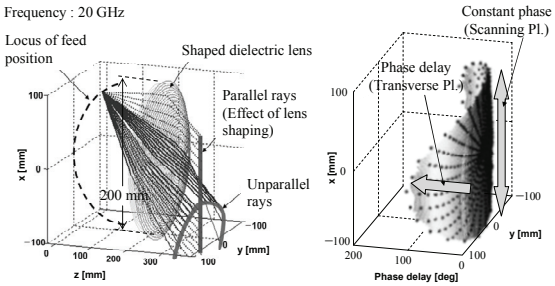

Fig. 2. Abilities of the shaped dielectric lens, (a) ray tracing result, and (b) aperture phase distribution (ϕ_{ap}).

B. Array Feed

A configuration of the array feed is shown in Fig. 3. The array feed is directed to the lens direction, as indicated by the Z' axis. Array elements are arranged in the Y axis that correspond to the transverse direction. The radiation patterns of array elements in the scanning plane and the transverse plane are indicated by $El_s(\theta_s)$ and $El_t(\theta_t)$, respectively. $El_s(\theta_s)$ has a rather narrow beam so as to illuminate the lens efficiently. Hence, the array element length in the X' axis direction is about 1.5 wavelengths. On the other hand, $El_t(\theta_t)$ has a wide beam width so as to ease the radiation pattern synthesis in the transverse plane. The array element length in the Y axis direction is 0.5 wavelengths. Array elements are excited with excitation coefficients V_i.

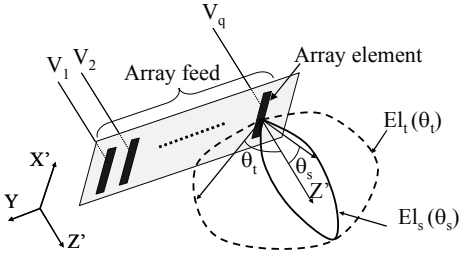

Fig. 3. Configuration of the array feed.

Figure 4 shows the geometry of the radiation pattern synthesis. L is the length between the lens and a feed horn. The array elements are located

along the Y axis. El_j (j = 1,2,・・・, q) indicates array elements and y_j represents their positions. $F(y_{Di})$ (I = 1,2,・・・, p) is objective radiation patterns on the lens surface that have p components, which are represented by Eq(1).

$$[F] = [B][V]. \quad (1)$$

Here, [F] components are expressed by complex numbers that have amplitude and phase values. Amplitude values are composed of the projected values of $El_s(\theta_s)$ in Fig. 7 (b) on the lens surface sampled at p points (y_{Di}). Phase values are composed of p sampling points of the objective pattern of Fig. 6. [V] is excitation coefficients of array elements. [B] is a p×q matrix which expresses contributions of [V] to each lens position of y_{Di} (i=1,2,・・・, p).

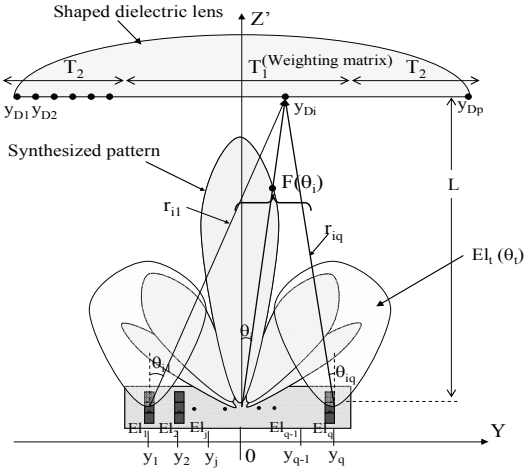

Fig. 4. Geometry of radiation pattern synthesis.

Equation (1) can be solved using the Leased Mean Square method. [V] is expressed by the next equation [8].

$$[V] = ([B]^H[T]^H[T][B])^{-1}[B]^H[T]^H[T][F]. \quad (2)$$

Here, H indicates complex conjugate and transpose of a matrix. [T] is a weighting matrix used to emphasize certain angular regions. [T] has only diagonal components (t_{ii}). By imposing large weights on the lens region, both amplitude and phase radiation patterns are designed adequately. The most suitable value of [T] is determined by trial and error [6].

Excitation coefficients (V_i) of Eq.(2) are shown in Figs. 5 (a) and (b). Eight array elements are employed. As for the array element, a rectangular aperture of 1.5 × 0.5 wavelengths is considered. The radiation patterns ($El_s(\theta_s)$ and $El_t(\theta_t)$) are expressed by the following equation.

$$E(\theta_s,\theta_t) = \frac{je^{-jkR}}{\lambda R}\frac{\sin(ku1.5\lambda/2)}{(ku1.5\lambda/2)}\frac{\sin(kv0.5\lambda/2)}{(kv0.5\lambda/2)}.$$
$$u = \sin\theta_s\cos\theta_t, \quad v = \sin\theta_s\sin\theta_t \quad (3)$$

In Fig. 5 (a), amplitude taper is formed to the edge elements. In Fig. 5 (b), large phase delay is formed to the edge elements. By applying V_i to Eq.(1), the radiated electric fields (amplitude and phase) of the array feed are calculated. These radiated electric fields are refracted by the lens and perform the antenna aperture distribution. The calculated antenna aperture phase distributions are shown in Fig. 6. The data in Fig. 6 corresponds to that of Fig. 2 (b). The objective pattern indicates the opposite phase ($-\phi_{ap}$) of Fig. 2 (b). It is recognized that excellent $-\phi_{ap}$ is achieved in the designed pattern. Thus, it is certain that sufficient phase delay compensation can be achieved using the array feed.

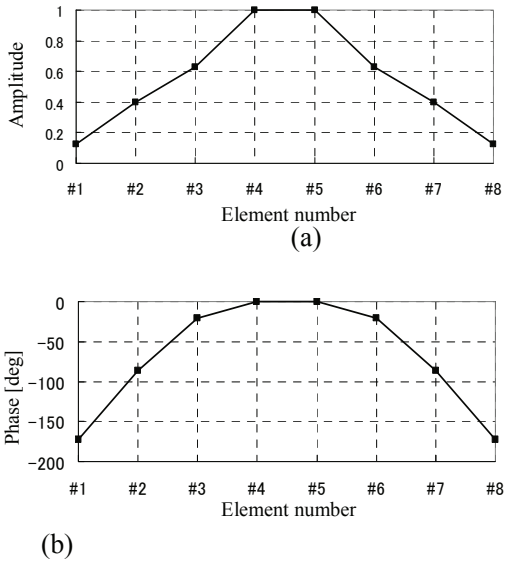

Fig. 5. Excitation coefficients (V) for 30° beam scanning, (a) amplitude of V, and (b) phase of V.

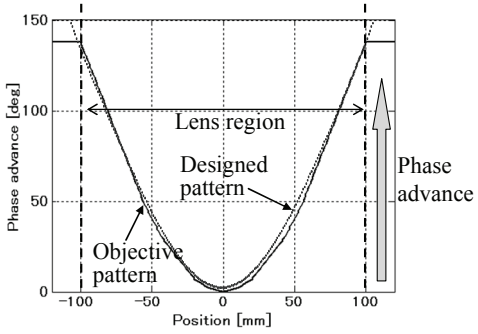

Fig. 6. Aperture phase distribution from array feed ($-\phi_{ap}$).

IV. SIMULATION OF THE ARRAY FEED LENS ANTENNA

A. Simulation Condition

The simulation methods and simulation details are summarized in Table 1. It is assumed that a very large memory is needed for calculation of the array feed and the dielectric lens. Utilization of the MLFMM becomes inevitable. In order to apply MLFMM, the surface equivalent principle is employed for the dielectric substrate of the array feed and the dielectric lens body. Mesh sizes and the number of meshes in the simulation objects are given in Table 1. More than 10,000 meshes are used in simulating each object. The total memory size of 5.1 GB and the calculation time of 20 hours are required.

Table 1: Simulation parameters.

Computer specification		CPU		Xeon 3.2 GHz×2
		Software		FEKO (Suite 5.3) with MLFMM
Frequency				20 GHz
Simulation models of dielectric material				Surface equivalence principle (SEP)
Array feed	Dielectric substrate	Finite plane		
		Mesh size		λ/20
	Patch	Mesh size	Edge	λ/40
			Face	λ/20
	Number of meshes			25,086
Shaped dielectric lens	Mesh size			λ/3.5
	Number of meshes			17,068
Used memory				5.1 GBytes
Calculation time				20 H

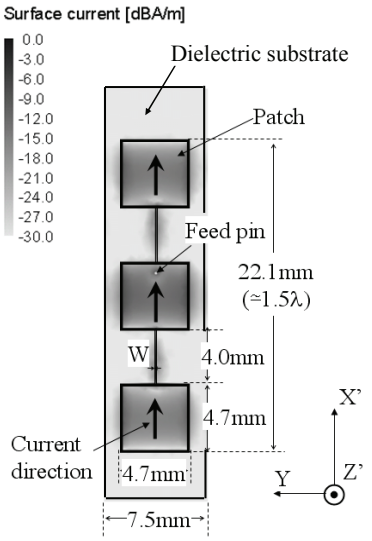

(a)

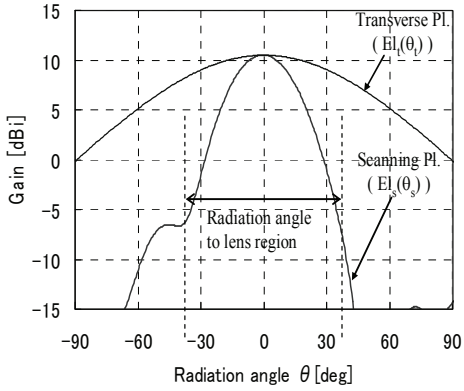

(b)

Fig. 7. Configuration of array element, (a) structure, and (b) radiation pattern.

B. Simulation Results of the Array Element

The actual structure of the fabricated array element is shown in Fig. 7 (a). The array element is composed of three square patch antennas [7]. The center patch is fed by the feed pin. Square patches are connected by thin connecting lines in order to be excited in phase. All the metallic parts are conformed on the dielectric substrate of $\varepsilon_r = 2.2$.

The square patch size becomes the half wavelength in the dielectric substrate. The connecting line length is determined so as to excite three patches in phase. Simulated results are shown in Fig. 7(b). In the $El_s(\theta_s)$, a rather sharp beam antenna is achieved. The edge level becomes less than -15 dB. In the $El_t(\theta_t)$ plane, the broad beam is achieved.

C. Simulation Results of the Array Feed

Electrical field distributions of the array feed are shown in Fig. 8. In the scanning plane of Fig. 8 (a), many curved regions are observed. These regions correspond to wave fronts. It is recognized that wave fronts coincide with the spherical wave fronts. Thus, in the scanning plane, spherical waves are produced. In the transverse plane of Fig. 8 (b), the synthesized wave front becomes flatter than the spherical wave front. This wave front change is considered the result of the phase advance. Consequently, it is anticipated through this wave front shape that the phase advance design has been successfully achieved.

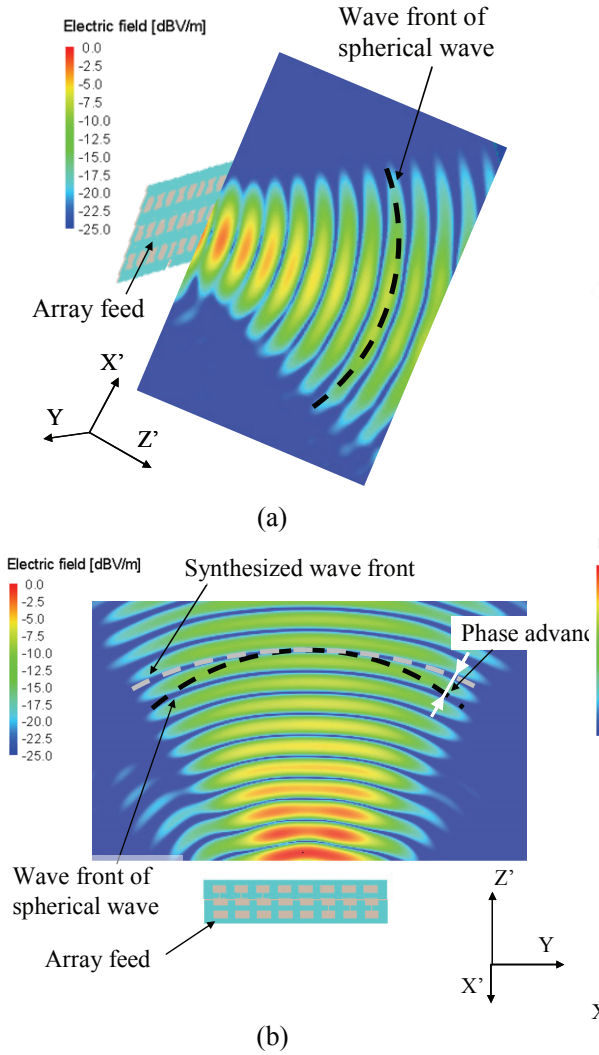

Fig. 8. Electric field distribution of the array feed, (a) scanning plane, and (b) transverse plane.

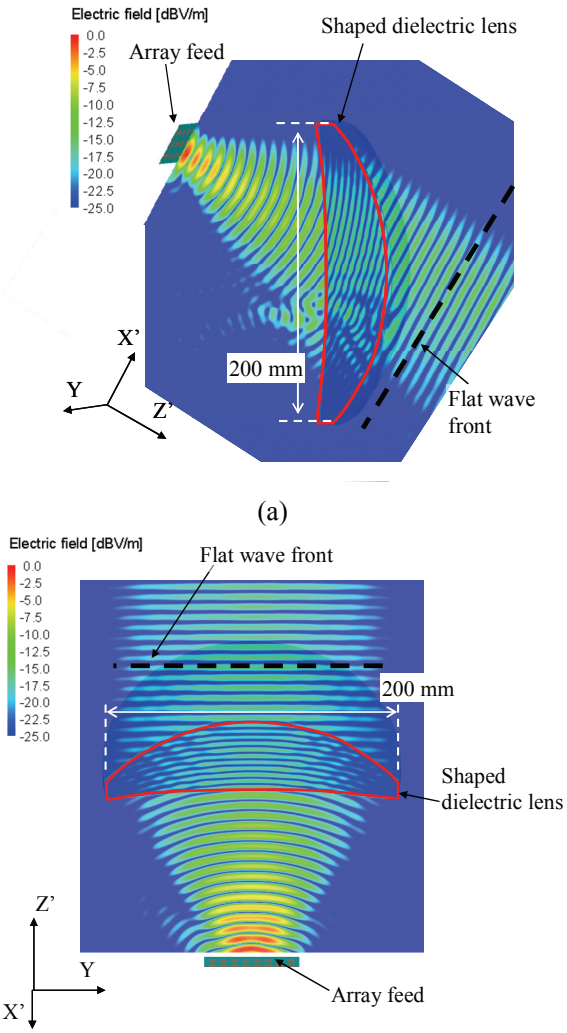

Fig. 9. Electric field distribution of 30° scanning beam, (a) scanning plane, and (b) transverse plane.

D. Simulation Results of Array and Shaped Lens Antenna

Electrical field distributions of the dielectric lens are shown in Fig. 9. In the scanning plane of Fig. 9 (a), it is recognized that the flat wave front is achieved in front of the lens. In the transverse plane of Fig. 9 (b), the flat wave front is also achieved. Consequently, desired constant phase distributions are expected in the antenna aperture plane.

Antenna aperture distributions are shown in Fig. 10. In the illumination distribution of Fig. 10 (a), the high intensity region is shifted to the upper part of the aperture plane. This reason is clearly recognized from the electrical field distribution of Fig. 9 (a). Electrical fields on the lower part of the antenna aperture become weak. In order to achieve symmetrical illumination distribution, the tilt angle of the array feed should be larger than 30°. In the phase distribution of Fig.10 (b), excellent constant phase characteristic is achieved. The effects of dielectric lens shaping and the array feed are confirmed.

E. Radiation Pattern

Radiation beam shapes are shown in Fig. 11. In the bore site beam of Fig. 11 (a), an axisymmetrical beam shape is achieved. In this case, two array elements are arranged side by side, as shown in Fig. 14 (b). Three dB beam widths in the scanning (θ) and transverse (ϕ) planes both become 4.5°. In the 30° scanning beam of Fig. 11 (b), an almost axisymmetrical beam is achieved. Three dB beam widths in the scanning and transverse plane become 4.5° and

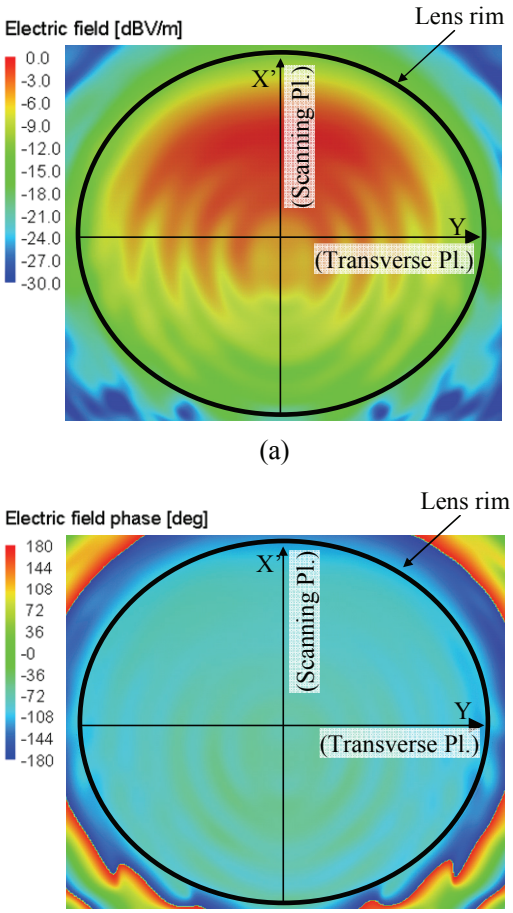

Fig. 10. Aperture distribution of 30° scanning beam, (a) field intensity, and (b) phase.

5.0°, respectively. The reason for the broadened beam width of 5.0° on the scanning plane is recognized from the intensity distribution on the scanning of Fig. 10 (a).

V. MEASURED RESULTS

A. Measurement Setting

Measurement set up of the radiation patterns is shown in Fig. 12. The off-focus feed is placed at 30° offset from the dielectric lens axis (Z). The feed position adjustment is very important. The alignment accuracy of about 1 mm is achieved. During the measurements, the supporting metal frames and the antenna back area are covered by the electromagnetic absorbing sheet. Measured planes include the scanning and the transverse planes, as shown in Fig. 12. The dielectric lens antenna is composed of the polycarbonate whose electric constants are $\varepsilon_r = 2.64$ and $\tan\delta = 0.0075$.

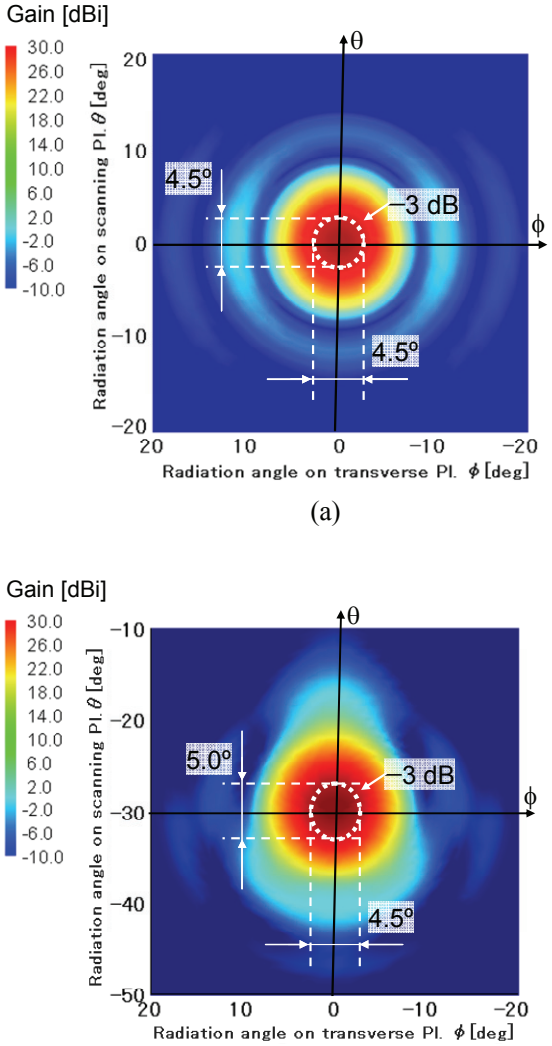

Fig. 11. 2D radiation beam shapes of the bore site and 30° scanning beams, (a) bore site beam, and (b) 30° scanning beam.

The antenna diameter is 200 mm and thickness is 57 mm. The antenna weight is 1.3 Kg.

B. Array feed

First of all, the fabricated array element is shown in Fig. 13 (a). Three square patches are excited in phase through connecting lines. Measured and simulated radiation patterns are shown in Fig. 13 (b). In $El_s(\theta_s)$ and $El_t(\theta_t)$ patterns, simulated and measured results agree very well. Thus, it is shown that the fabrication of the array element has been successfully performed. The band width characteristics of the array feed is determined by the input impedance

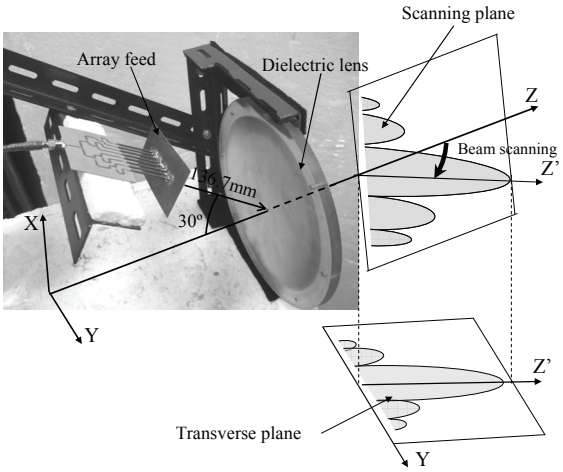

Fig. 12. Antenna structure for radiation pattern measurement.

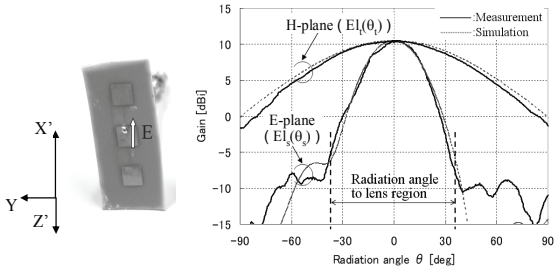

(a) (b)

Fig. 13. Array element, (a) fabricated, and (b) radiation pattern.

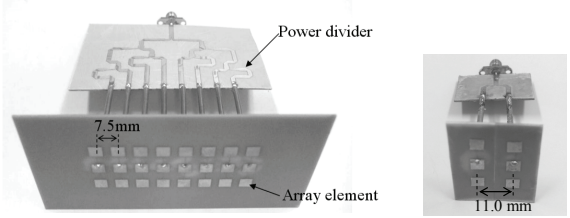

(a) (b)

Fig. 14. Array feed, (a) 30° scanning beam, and (b) Bore site beam.

bandwidth of the patch antenna [9]. About 20% bandwidth in VSWR<2 was reported.

Next, configurations of array feed are shown in Fig. 14. The array feed for a 30° scanning beam, as shown in Fig. 14 (a), is composed of eight array elements.

The array feed for the bore site is composed of two array elements. In this feed, an almost axisymmetrical beam is achieved. Array elements of both the array feeds are excited through the power divider.

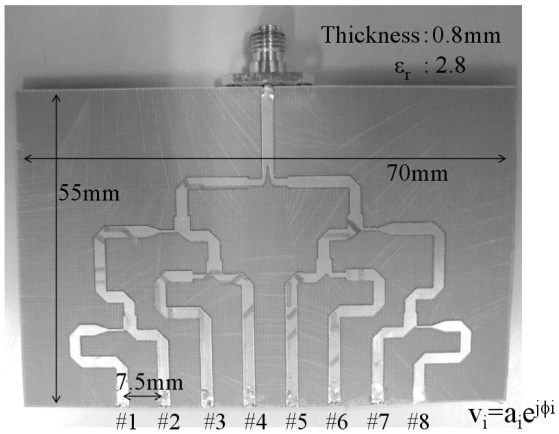

Fig. 15. Power divider for the 30° scanning beam.

C. Power Divider

Configuration of the power divider for the 30° scanning beam is shown in Fig. 15. Branching circuits are composed on the dielectric substrate of ε_r = 2.8 and tanδ = 0.0018. The circuit line lengths determine the phase values of terminals. The circuit line widths at the branching points determine the dividing power values of the terminals. As the result, excitation coefficients (V_i) are designed. In order to confirm the achievement of this power divider, measured amplitude and phase characteristics of all terminals are obtained.

Measured frequency characteristics are shown in Figs. 16 (a) and (b). At the amplitude characteristics of Fig. 16 (a), frequency dependences are divided into two groups. The first one consists of terminals a_2, a_7 and a_1, a_8. The other group consists of terminals a_3, a_6 and a_4, a_5. Within each group, frequency dependence becomes similar. However, frequency dependence becomes opposite between different groups. Hence, at the branching point dividing #1,#2 terminals and #3,#4 terminals, opposite frequency dependence is produced. By refining these branching points, all the curves can become parallel. The insertion loss of this power divide can be estimated by summing up the square values of a_i. The estimated insertion loss is about 6.5 dB. The insertion loss is divided into the strip line loss of 2 dB and radiation loss of 4.5 dB. Because the purpose of this paper is to achieve the accurate excitation coefficient, reduction of this large insertion loss is considered as the future subject. At the phase characteristics of Fig. 16 (b), frequency dependences become almost similar in all terminals. At 20 GHz points, measured and design objects agree very well.

Excitation coefficients of the power divider are summarized in Fig.17. The target values are the designed results of Fig.5. In the amplitude and phase characteristics, target values are accurately achieved with the fabricated power divider.

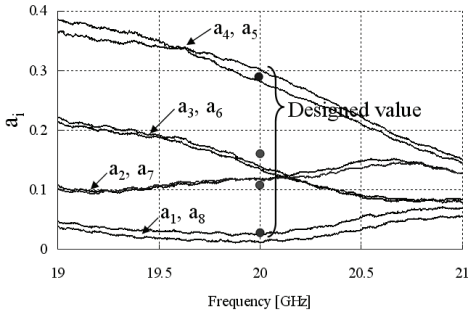

(a)

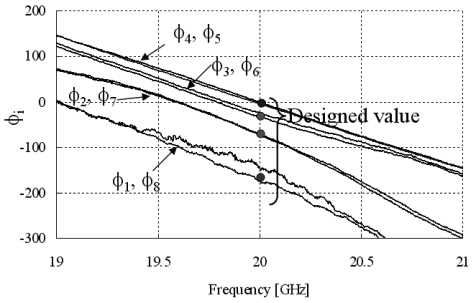

(b)

Fig. 16. Amplitude and phase characteristics of the power divider, (a) amplitude, and (b) phase.

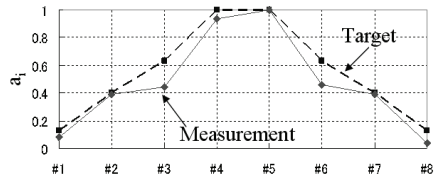

(a)

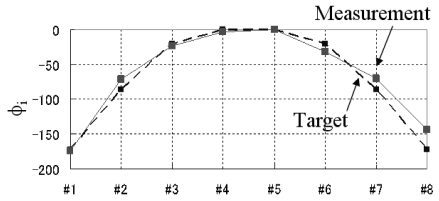

(b)

Fig. 17. Excitation coefficients, (a) amplitude of V, and (b) phase of V.

D. Radiation Pattern

Measured and simulated beam scanning characteristics are shown in Fig.18. In the scanning plane of Fig.18 (a), measured and simulated results agree very well. The beam width in the 30° scanning beam becomes slightly broader than the bore site beam. This result is anticipated from the beam shape of Fig.11 (b). The antenna gain decrease at the 30° scanning angle is 1.7 dB. A rather small gain decrease is achieved. In the transverse plane of Fig.18 (b), measured and simulated results agree very well. Almost identical beam widths are achieved in the bore site and at the 30° scanning beams. As a result, realization of the wide-angle beam scanning antenna is confirmed.

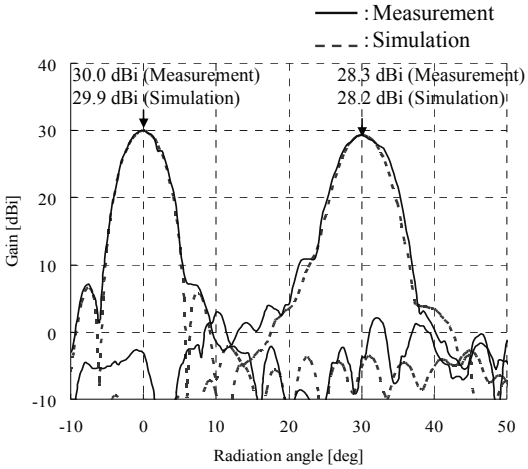

(a)

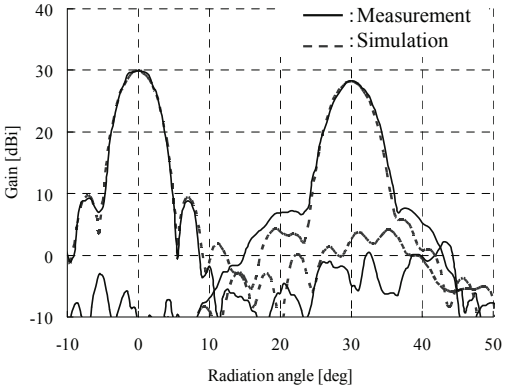

(b)

Fig. 18. Radiation patterns of the array feed lens antenna, (a) scanning plane, and (b) transverse plane.

In order to confirm the antenna gain, antenna measurement is conducted. The configuration of the gain reference antenna is shown in Fig.19. In this case, as the gain reference, a half wave dipole antenna is attached at the #5 output terminal. The others are terminated by 50 Ω resistances. The power ratio of each port

Table 2: Power ration of power divider.

Port number	#1	#2	#3	#4	#5	#6	#7	#8
Power ratio	0.002	0.059	0.076	0.347	0.384	0.082	0.059	0.001

obtained from Fig. 17 is shown in Table 2. The power ratio of the #5 port becomes 0.384. The purpose of this configuration is to avoid the affect of large insertion loss of the power divider.

The radiation patterns of the gain reference antenna and 30° scanning beams are shown in Fig. 20. These values are measured using radiation power. At the gain reference antenna, a measured power of −68.0 dBm is obtained, which corresponds to −2.0 dBi by the following equation.

$$-68.0\ [\text{dBm}] = 2.15\ [\text{dBi}] \times 0.384$$
$$= -2.0\ [\text{dBi}] \quad (4)$$

The measured power of the 30° scanning beams becomes −37.7 dBm. Thus, the antenna gain is estimated to be 28.3 dBi, as shown in Fig. 20. This value is consistent with the simulated value of 28.2 dBi.

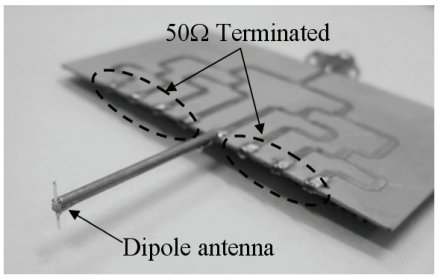

Fig. 19. Structure of gain reference antenna of the off-focus feed.

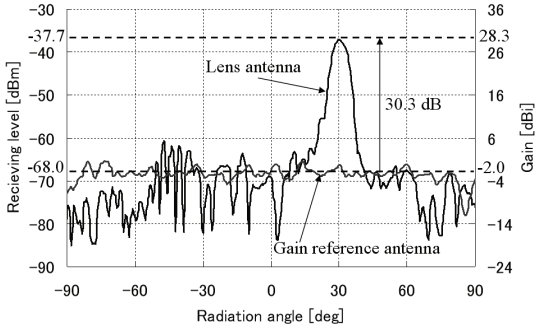

Fig. 20. Gain calculation from measurement.

The measured gain of the bore site beam is obtained through the same method. In this case, the dipole antenna is attached at the one terminal of Fig. 14 (b) and the other is terminated by 50 Ω resistance. The measured and simulated gains of the bore site beam also agree very well, as shown in Fig. 18 (a). In conclusion, this study has ensured that antenna gains can be successfully achieved.

VI. CONCLUSIONS

Realization of the shaped dielectric lens antenna with array feed is ensured through measurement and electromagnetic simulations. Important technical results developed are summarized as follows.

(1) As an array element, a convenient patch antenna configuration is developed that replaces the previous rectangular horn antenna.

(2) For the 30° beam scanning, an eight-branch power divider is fabricated. Accurate excitation coefficients are confirmed through the measured results.

(3) The achievements of design concepts of the array feed and the shaped lens are confirmed through electromagnetic simulations of the electric field distributions.

(4) Antenna radiation characteristics at 30° beam scanning are ensured through the radiation pattern measurements. Beam shapes that are almost identical to the on-focus feed are confirmed.

(5) Excellent antenna gains coinciding with simulated values are ensured through measurement.

REFERENCES

[1] Research and Innovative Technology Administration, http://www.its.dot.gov/index.htm.

[2] Japanese Ministry of Land, Infrastructure, Transport and Tourism, Road Bureau ITS Homepage, http://www.mlit.go.jp/road/ITS/.

[3] T. Kato, T. Tanizaki, T. Ishii, H. Tanaka, and Y. Takimoto, “76 GHz high preference radar sensor featuring fine stem scanning mechanism utilizing NRD technology,”

IEEE Intelligent Vehicles Symposium, pp. 163-170, May 2001.

[4] Y. T. Lo and S. W. Lee, *Antenna Handbook,* Van Nostrand Rainhold Company, vol. 2, pp. 16-23, 1988.

[5] Y. Tajima and Y. Yamada, "Design of Shaped Dielectric Lens Antenna for Wide Angle Beam Steering," *Electron. and Comm. in Japan Part Ⅲ,* vol. 89, no.2, pp. 1-12, February 2006.

[6] Y. Tajima and Y. Yamada, "Improvement of Beam Scanning Characteristics of a Dielectric Lens Antenna by Array Feed," *IEICE Trans. Fundamentals,* vol. E91-A, no. 7, pp. 1616-1624, July 2008.

[7] Y. Tajima, N. Michishita and Y.Yamada, "FEKO Simulation of the Shaped Dielectric Lens Antenna Capable of Wide Angle Beam Scanning," *25th International Review of Progress in Applied Computational Electromagnetics,* March 2009.

[8] S. Takubo and Y. Yamada, "Low Sidelobe and Asymmetrical Pattern Synthesis of an Unequally Spaced Array Antenna," *IEICE ISAP' 00,* vol. 3, pp. 1195-1198, Aug. 2000.

[9] Y. Tajima and Y. Yamada, "Design of a Patch Array Feed for the Dielectric Lens Antenna Achieving Wide Angle Beam Scanning," *IEEE International Conference on Communication Systems*, p. 46, Nov. 2008.

Yosuke Tajima received the B.S., M.S. and Dr. degrees in Electronics Engineering from National Defense Academy, Kanagawa, in 2000, 2005 and 2009. He enlisted in Japan Air Self Defense Force in 2000. He was engaged in tests and developments of radar and avionics equipments. His current research interests include lens and phased array antennas. Now he is a Captain.

Shinji Kamada graduated from Akita University and received the B.S. degree in Electrical and Electronic Engineering in 2004. He enlisted in Japan-Air-Self-Defense-Force in 2004. Now he is a technical official. He was engaged in tests of electronic equipments. He entered the Master course of Electrical and Electronic Engineering of National Defense Academy in 2008. His current research interests include lens antennas and metamaterial antennas.

Naobumi Michishita received the B.E., M.E., and D.E. degrees in Electrical and Computer Engineering from Yokohama National University in 1999, 2001, and 2004, respectively. He joined the Department of Electrical and Electronic Engineering, National Defense Academy, as a research associate in 2004. He was a visiting scholar at the University of California, Los Angeles from 2006 to 2007. He received the Young Engineer Award from the IEEE AP-S Japan Chapter and IEICE in 2004 and 2005, respectively. His current research interests include metamaterial antennas and electromagnetic analysis. He is a member of IEEE.

Yoshihide Yamada graduated from the Nagoya Institute of Technology and received the BS and

MS degrees in electronics in 1971 and 1973, respectively. He received the DE degree from the Tokyo Institute of Technology in 1989. In 1973, he joined the Electrical Communication Laboratories of the Nippon Telegraph and Telephone Corporation (NTT). Until 1984, he was engaged in research and development related to reflector antennas for terrestrial and satellite communications. Beginning in 1985, he engaged in R&D for base station antennas for mobile radio systems. In 1993, he moved to the NTT Mobile Communications Network Inc. (NTT DoCoMo). In 1995, he was temporarily transferred to the YRP Mobile Telecommunications Key Technology Research Laboratories Co., Ltd. At the same time, he was a guest professor at the cooperative research center of Niigata University, and a lecturer at the Science University of Tokyo, both from 1996. In 1998, he took a position as a professor at the National Defense Academy. At present, he is interested in very small RFID antennas, shaped dielectric lens antennas, and electromagnetic simulations of large objects. He is a member of the IEICE and JSST of Japan and an IEEE society member of AP, VT, and COMM.

Calculation of the Magnetic Forces Between Planar Spiral Coils using Concentric Rings

Abbas Shiri and Abbas Shoulaie

Department of Electrical Engineering
Iran University of Science and Technology, Tehran, Iran
abbas_shiri@iust.ac.ir, shoulaie@iust.ac.ir

***Abstract*—** In this paper, the forces between current carrying planar spiral coils are calculated. In order to facilitate the calculation process, the coils have been replaced by concentric rings and using first and second order complete elliptic integrals, the forces between them have been calculated. The comparison of the calculations resulting from the replaced rings method and the direct method shows that the former is more effective in both simplicity and calculation time. To evaluate the precision of the calculations, planar spiral coils have been constructed and tested. The experimental results validate the results of the calculations.

***Index Terms*—** Planar spiral coils, magnetic force, vector magnetic potential, concentric rings.

I. INTRODUCTION

Planar spiral coils are used extensively in different applications such as communications, power electronics, and casting industries [1-3]. In these systems, to have a high inductance and flat configuration, spiral windings are employed. In DC/DC converters, because of flatness and special configuration, planar spiral coils are a better replacement for the ordinary inductances in order to reduce the volume of the converter. To calculate the magnetic force between these coils, some methods have been reported in literature. In [2] these forces are obtained just by test. In [3] the finite difference method is employed to calculate the force between them; furthermore, in this reference to calculate the magnetic force, spiral coils are replaced by concentric rings, but there is no study and discussion on the precision of the method. In [4] the force between circular coaxial coils has been investigated. Recently, the above authors employed mesh-matrix method in order to calculate the force between spiral coils [5]. In this paper, using concentric rings instead of spiral coils, an effective and simple procedure is developed to calculate the magnetic force between these coils. Using the results obtained from the numerical solution of the direct calculation method, the precision of the proposed method is investigated and finally compared with experimental results.

II. DIRECT CALCULATION METHOD

Consider a system of two spiral coils as shown in Fig. 1. To calculate the magnetic force between them, we should first calculate the vector magnetic potential resulting from one of the coils in any given point like P (see Fig. 2).

Vector magnetic potential of spiral coil 1 in any given point P is obtained by the following equation [6]:

$$A = \frac{\mu_0 I_1}{4\pi} \oint \frac{dl'}{R_1} \tag{1}$$

where I_1 is the current of the coil, dl' is the longitudinal differential component, and R_1 is the distance between this differential component and point P.

The coordinates marked by prime are related to the source. With suitable substitutions for dl', the following equation for vector magnetic potential is obtained:

$$A = \frac{\mu_0 I_1}{4\pi} \oint \frac{[-a_x \sin\phi' + a_y \cos\phi']r'd\phi' + [a_x \cos\phi' + a_y \sin\phi']dr'}{R_1}. \tag{2}$$

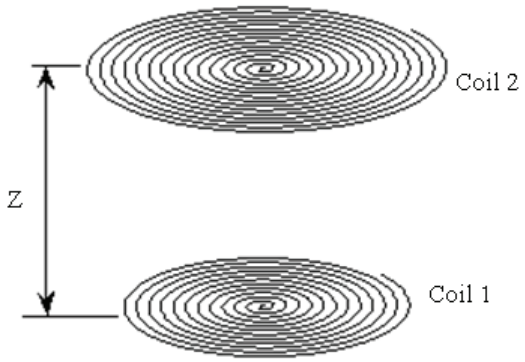

Fig. 1. The two spiral coils in z distance of each other.

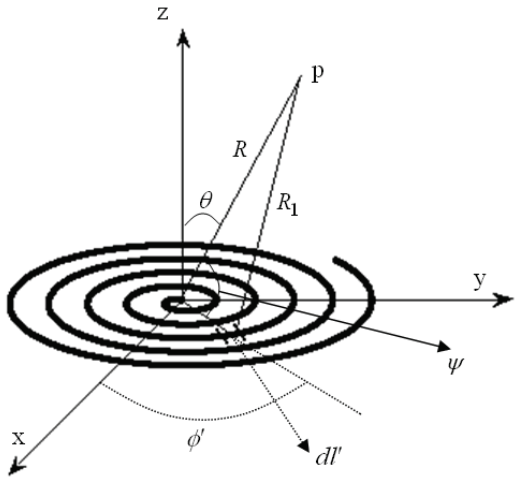

Fig. 2. Calculation of the vector magnetic potential of spiral coils in any given point like P.

To calculate the integral in (2), one of the integral variables must be replaced by another one according to the relations between them. The variables ϕ' and r' have a linear relation; consequently, we can write [7, 8]:

$$\phi' = K_1 r' \tag{3}$$

where K_1 is a constant coefficient that is called "compression factor" of coil 1. This factor depends on the diameter of the wire used and the structure of the coil and determines its compression. Having the vector magnetic potential, the magnetic field is calculated using the following equation [6]:

$$B = \nabla \times A \tag{4}$$

The force acted on the coil 2 is [9]:

$$F_{21} = I_2 \oint_{C_2} dl_2 \times B \tag{5}$$

In the above equation, dl_2 is longitudinal differential component on coil 2. Substituting proper expression for dl_2 and employing (4) in (5) and doing some mathematical calculations, we get:

$$F_{21} = a_x f_x + a_y f_y + a_z f_z \tag{6}$$

where f_x, f_y and f_z are the components of the force in directions x, y and z, respectively, and are equal to (7)-(9) at the bottom of the page.

In equations (7)-(9), the parameters r_1' and r_1 are the inner radii of coil 1 and 2, respectively, and r_2' and r_2 are the outer radii of coils 1 and 2, respectively. Also, the following equation has been used [7, 8]:

$$\phi = K_2 r \tag{10}$$

where K_2 is compression factor of coil 2 determined with regard to the compression of the coil and the diameter of the wire used in it.

III. CONCENTRIC RINGS METHOD

In the previous section, it was observed that to obtain the force between spiral coils, using the analytical method is slightly complex and time-consuming. Furthermore, the obtained integrands are not smooth functions, and we have some difficulties in the calculation of their integrals. Especially when the coils are compressively wounded, the problem is more acute.

$$f_x = \frac{\mu_0 I_1 I_2}{4\pi} \int_{r_1}^{r_2} \int_{r_1'}^{r_2'} \frac{[r\sin(K_2 r - K_1 r') - K_1 r r'\cos(K_2 r - K_1 r') + K_1 r'^2][\sin(K_2 r) + K_2 r\cos(K_2 r)]}{[(r\cos(K_2 r) - r'\cos(K_1 r'))^2 + (r\sin(K_2 r) - r'\sin(K_1 r'))^2 + z^2]^{3/2}} dr' dr \tag{7}$$

$$f_y = -\frac{\mu_0 I_1 I_2}{4\pi} \int_{r_1}^{r_2} \int_{r_1'}^{r_2'} \frac{[r\sin(K_2 r - K_1 r') - K_1 r r'\cos(K_2 r - K_1 r') + K_1 r'^2][\cos(K_2 r) + K_2 r\sin(K_2 r)]}{[(r\cos(K_2 r) - r'\cos(K_1 r'))^2 + (r\sin(K_2 r) - r'\sin(K_1 r'))^2 + z^2]^{3/2}} dr' dr \tag{8}$$

$$f_z = -\frac{\mu_0 I_1 I_2}{4\pi} z \int_{r_1}^{r_2} \int_{r_1'}^{r_2'} \frac{(1 + K_1 K_2 r r')\cos(K_2 r - K_1 r') - (K_2 r - K_1 r')\sin(K_2 r - K_1 r')}{[(r\cos(K_2 r) - r'\cos(K_1 r'))^2 + (r\sin(K_2 r) - r'\sin(K_1 r'))^2 + z^2]^{3/2}} dr' dr \tag{9}$$

To overcome this problem, accepting some errors, we can replace the spiral coils with concentric rings and then calculate the forces between them [7]. For this purpose, we first calculate the force between two concentric current carrying rings. Suppose rings 1 and 2 with radiuses a and b while carrying currents I_1 and I_2, respectively (see Fig. 3). To obtain the force exerted on the upper ring from the lower ring, we first calculate the magnetic field of lower ring in any given point P. To calculate the magnetic field, we use the vector magnetic potential concept. The vector magnetic potential of ring 1 in any point P on ring 2, using (1), is equal to (Fig. 4):

$$A = a_\phi \, f(R,\theta) \tag{11}$$

in which the function $f(R,\theta)$ is as follows:

$$f(R,\theta) = \frac{\mu_0 I_1}{4\pi}\int_0^{2\pi} \frac{a\sin\phi'}{\sqrt{R^2+a^2-2aR\sin\theta\sin\phi'}}d\phi'. \tag{12}$$

In the above equation, a is the radius of ring 1, μ_0 is the permeability of vacuum, I_1 is the current of ring 1, and R is the distance between the origin and the field point P (Fig. 4). By obtaining the vector magnetic potential, magnetic field is calculated using (4). Substituting (11) and (12) in (4) and doing some mathematical calculations, we get:

$$B = a_R \, g_1(R,\theta) + a_\theta \, g_2(R,\theta) \tag{13}$$

where g_1 and g_2 are:

$$g_1(R,\theta) = \frac{1}{R\sin\theta}[\cos\theta \; f(R,\theta) + \sin\theta \frac{\partial}{\partial\theta} f(R,\theta)] \tag{14}$$

$$g_2(R,\theta) = -\frac{1}{R}[f(R,\theta) + R\frac{\partial}{\partial R} \; f(R,\theta)]. \tag{15}$$

The force exerted on ring 2 from ring 1 is calculated using (5). Applying (13)-(15) to (5) and also substituting an appropriate expression for dl_2 and doing some simple mathematical calculations, the following equation for the force is obtained:

$$F_{21} = -a_z \frac{\mu_0 ab I_1 I_2 z}{2} \int_0^{2\pi} \frac{\sin\phi'}{[z^2+a^2+b^2-2ab\sin\phi']^{3/2}}d\phi'. \tag{16}$$

In the above equation, b is the radius of ring 2 and z is the axial distance between the two rings.

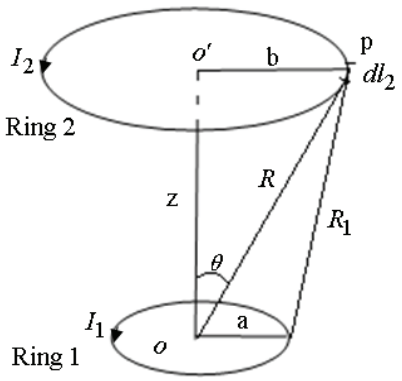

Fig. 3. Two concentric current carrying rings.

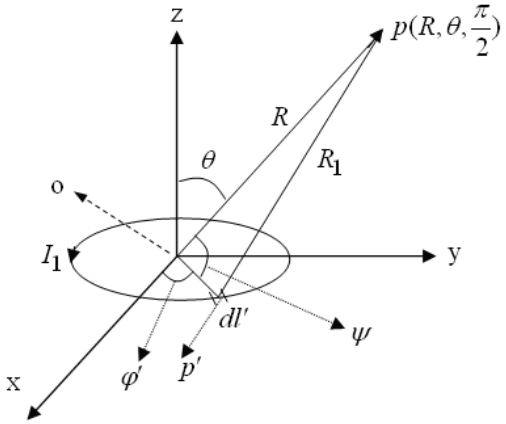

Fig. 4. Determination of vector potential of a current carrying ring with radius a in any given point P.

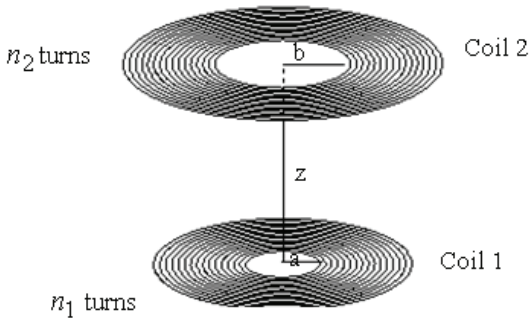

Fig. 5. Two coils with concentric rings.

The force obtained in (16) has no analytical solution, so we can use numerical integration methods to solve it. Changing the integral variable as $\phi' = (3\pi/2) + 2\theta$ in (16), the following equation for the force is obtained:

$$F_{21} = a_z \left(\frac{\mu_0 \; I_1 I_2 \;\; z \;\; k}{2\sqrt{ab} \;\; (1-k^2)}\right) \left[(1-k^2)K(k) - (1-\frac{1}{2}k^2)E(k)\right] \tag{17}$$

where k is a constant parameter and is equal to:

$$k = \sqrt{\frac{4ab}{(a+b)^2 + z^2}} \tag{18}$$

and $K(k)$ and $E(k)$ are the first and the second order elliptic integrals, respectively, with the following definitions:

$$K(k) = \int_0^{\frac{\pi}{2}} \frac{d\theta}{(1-k^2 \sin^2 \theta)^{1/2}} \tag{19}$$

$$E(k) = \int_0^{\frac{\pi}{2}} (1-k^2 \sin^2 \theta)^{1/2} \quad d\theta. \tag{20}$$

Now, having the force between the two rings, we can calculate the force between the two spiral coils after replacing them by concentric rings (Fig. 5). The magnetic force between the two coils (the force exerted on coil 2 from coil 1 in Fig. 5) will be as follows:

$$F_{21} = I_1 I_2 \sum_{j=0}^{n_2-1} \sum_{i=0}^{n_1-1} f_{21}(j,i) \tag{21}$$

where n_1 and n_2 are the number of turns of coil 1 and 2, respectively, and $f_{21}(j,i)$ is equal to:

$$f_{21}(j,i) = a_z \left(\frac{\mu_0 \, z k'}{2\sqrt{a_i \, b_j} \;\; (1-k'^2)}\right) \left[(1-k'^2)K(k') - (1-\frac{1}{2}k'^2)E(k')\right] . \tag{22}$$

In the above equation, z is the distance between the two coils, and the parameters a_i, b_j and k' are defined as:

$$a_i = a_0 + (\frac{1}{2} + i)\, s_1 \tag{23}$$

$$b_j = b_0 + (\frac{1}{2} + j)\, s_2 \tag{24}$$

$$k' = \sqrt{\frac{4a_i b_j}{(a_i + b_j)^2 + z^2}} \tag{25}$$

where a_0 and b_0 are the inner radius of coils 1 and 2 and s_1 and s_2 are the distance between two neighboring turns in coils 1 and 2, respectively. If the coils are wound compressively, then s_1 and s_2 must be replaced by the diameter of the wires used in coils 1 and 2, respectively.

IV. CALCULATION RESULTS

In Section II, the force between two spiral coils was analytically obtained (equation (6)). Suppose that the compression factors of the coils are high. In this case, the force values in the x and y directions are almost zero, and the component of the force in the z direction is non- zero [7] which is given by equation (9). The force in this relation is the force exerted on coil 2 from coil 1 as it is shown in Fig. 1. Although we use precise analytical relations to obtain the force in (9), its integral has no analytical solution, and numerical integration techniques must be used to solve it. The integrand of the equation (9) has some "semi-poles" which depend on the value of the compression factors K_1 and K_2. The curve of the integrand versus variables r and r' is shown in Fig. 6 for different values of r and r' from 0 to 1. As seen in the figure, by increasing the values of r and r' from zero, the value of the integrand produces some sharp peaks (the semi-poles points). It is clear that integration of these surfaces is much more difficult because in order to obtain higher precisions, one needs to increase the number of iterations of numerical integration intensively which, in turn, requires much longer computational time to solve such a problem.

Now we compare the results of direct calculation of the force using equation (9) with that of the replaced concentric rings method. To calculate the integral in equation (9), we used recursive adaptive Simpson Quadrature method. In the replaced concentric rings method, the radius of each ring is assumed to be the average of the inner and the outer radii of each turn of spiral coils. In Tables 1 and 2 the results of calculation of the force using two methods for different values of turn number and different center to center distance of coils are compared. In these tables, the current in both coils is 20 Amperes, the diameter of the wires is 2 mm, and the compression factor for both coils is assumed to be $2\pi/d$, where d is the diameter of the wires in both coils; meaning that for each turn of coils or for change of 2π Radians in the value of variable ϕ in cylindrical coordinates, the change in the value of variable r

(the radial growth of coils) is equal to diameter of the wires used in the coils. In Table 1, it is assumed that the coils start to grow from point (0, 0). Comparing the results of the two methods in this table, it is seen that for the fewer number of

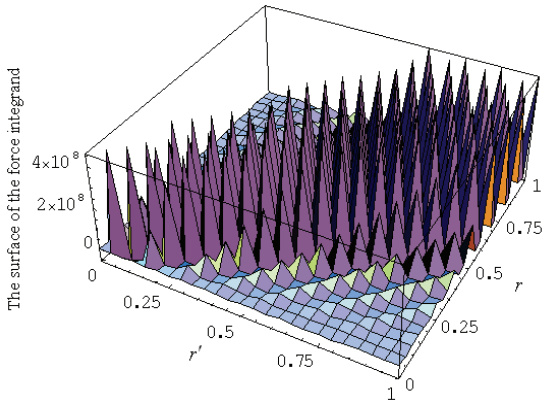

Fig. 6. The integrand in force equation for 500 turns in each coil.

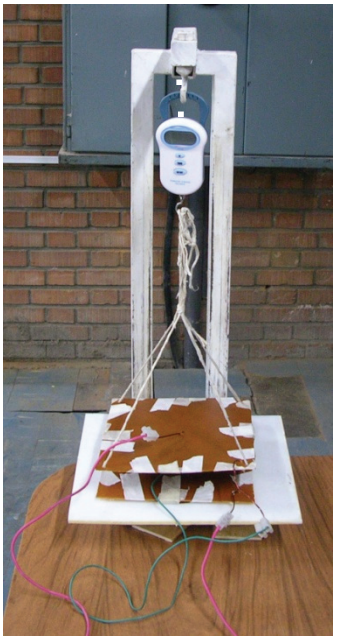

Fig. 7. Measurement of the magnetic force between the two spiral coils.

turns the error is high, but by increasing the number of turns, the error gradually decreases, and when the turn number approaches to 100, the error becomes zero. In Tables 1 and 2 the precision of the calculations is adjusted according to the numerical value of the results. For instance, for the first column of Table 1 the calculated numbers are in the range of 10^{-13} (their minimum value). To compare the calculation time in the two approaches, it suffices to mention that the required calculation time using the adaptive Simpson method for 100 turns in Table 1 for precision of 10^{-4} is 28000 times more than that of using replaced concentric rings method. As seen in the table, the results precisely coincide with each other. Another interesting point about Table 1 is that by increasing the distance between the two coils, the calculation error increases showing that in large distances, the replaced concentric rings method does not present a proper approximation of the force.

In Table 2, the comparison between the two methods is made for the case in which the inner radius of the two coils are equal to 2.5cm; in other words, the coils start to wind from $r = 2.5cm$. As seen from the results of the table, the errors in this case are less than the corresponding errors in Table 1. For example, the force error for 2 turn coils in distance of 8 cm reduced from 94.6% in Table 1 to 0.12% in Table 2. These fewer errors for lower turn numbers decrease expeditiously to zero by increasing the turn numbers.

According to the results of Tables 1 and 2, generally for turn numbers higher than 10 turns in each coil, using the replaced concentric rings presents good approximations while having much simpler and faster calculations compared with that of the direct method and using (9).

Now, suppose the case in which there is a smaller compression factor for the coils compared with the previous one, i.e. for each turn of coils or for change of 2π Radians in the value of variable ϕ in cylindrical coordinate, the change in the value of variable r is more than the diameter of the wires used in the coils. For example, suppose that the growth of r is equal to 6 mm; in this case, the compression factor for both coils will be:

$$K_1 = K_2 = \frac{2\pi}{0.006}.$$

The results of the calculations of the force with the above mentioned conditions using the methods of direct and replaced rings are presented in Table 3. In this table, like the previous cases, the current of the coils is 20 Amperes.

It is interesting to compare the results of Tables 1 and 3. In Table 3, the trend of increasing and decreasing of error with the increase of the distance between the two coils and the number of turns is the same as Table 1; but in this case, the

Table 1. Comparison of the force calculation methods between two spiral coils (inner radii and compression factor of the coils are 0 and $2\pi/0.002$, respectively).

	Number of Turns or Rings Per Coil	2	5	10	20	50	100
Z=2cm	Direct Method (N)	2.9854×10^{-6}	2.3725×10^{-4}	5.6356×10^{-3}	7.1760×10^{-2}	1.0079	5.4610
	Replaced Rings Method (N)	1.3416×10^{-6}	2.2745×10^{-4}	5.6091×10^{-3}	7.1713×10^{-2}	1.0078	5.4610
	Error (%)	55.1	4.1	0.47	0.07	0.01	0
Z=4cm	Direct Method (N)	4.9389×10^{-7}	2.3834×10^{-5}	9.2665×10^{-4}	2.2472×10^{-2}	5.8029×10^{-1}	4.0310
	Replaced Rings Method (N)	9.0210×10^{-8}	2.1251×10^{-5}	9.1686×10^{-4}	2.2445×10^{-2}	5.8024×10^{-1}	4.0310
	Error (%)	81.7	10.8	1.1	0.12	0.01	0
Z=8 cm	Direct Method (N)	1.0599×10^{-7}	2.1389×10^{-6}	8.8644×10^{-5}	3.6843×10^{-3}	2.1795×10^{-1}	2.3208
	Replaced Rings Method (N)	5.7461×10^{-9}	1.5053×10^{-6}	8.6061×10^{-5}	3.6745×10^{-3}	2.1791×10^{-1}	2.3208
	Error (%)	94.6	29.6	2.9	0.27	0.02	0

* Precision of the calculations in numerical integration for rings of 2 to 100 turns are $0.5\times10^{-13}, 0.5\times10^{-10}, 0.5\times10^{-9}, 0.5\times10^{-7}, 0.5\times10^{-5}$ and 0.5×10^{-4}, respectively.

Table 2. Comparison of the force calculation methods between two spiral coils (inner radii and compression factor of the coils are 2.5cm and $2\pi/0.002$, respectively).

	Number of Turns or Rings Per Coil	2	5	10	20	50	100
Z=2cm	Direct Method (N)	1.8844×10^{-3}	1.3230×10^{-2}	5.8839×10^{-2}	2.5524×10^{-1}	1.7033	7.0917
	Replaced Rings Method (N)	1.8851×10^{-3}	1.3234×10^{-2}	5.8849×10^{-2}	2.5526×10^{-1}	1.7033	7.0917
	Error (%)	-0.04	-0.03	-0.02	-0.01	0	0
Z=4cm	Direct Method (N)	5.1474×10^{-4}	4.0012×10^{-3}	2.0961×10^{-2}	1.1654×10^{-1}	1.0846	5.4020
	Replaced Rings Method (N)	5.1465×10^{-4}	4.0009×10^{-3}	2.0961×10^{-2}	1.1654×10^{-1}	1.0846	5.4020
	Error (%)	+0.02	+0.01	0.0	0.0	0	0
Z=8 cm	Direct Method (N)	7.6578×10^{-5}	6.6545×10^{-4}	4.1678×10^{-3}	3.1257×10^{-2}	4.8080×10^{-1}	3.2851
	Replaced Rings Method (N)	7.6487×10^{-5}	6.6492×10^{-4}	4.1660×10^{-3}	3.1252×10^{-2}	4.8079×10^{-1}	3.2851
	Error (%)	+0.12	+0.08	+0.04	+0.02	+0.002	0

* Precision of the calculations in numerical integration for rings of 2 to 100 turns are $0.5\times10^{-9}, 0.5\times10^{-8}, 0.5\times10^{-7}, 0.5\times10^{-6}, 0.5\times10^{-5}$ and 0.5×10^{-4}, respectively.

Table 3. Comparison of the force calculation methods between two spiral coils (inner radii and compression factor of the coils are 0 and $2\pi/0.006$, respectively).

	Number of Turns or Rings Per Coil	2	5	10	20	50	100
Z=2cm	Direct Method (N)	7.3291×10^{-5}	3.0192×10^{-3}	2.7852×10^{-2}	1.7814×10^{-1}	1.5234	6.8511
	Replaced Rings Method (N)	5.9885×10^{-5}	2.9807×10^{-3}	2.7794×10^{-2}	1.7806×10^{-1}	1.5234	6.8511
	Error (%)	18.3	1.3	0.2	0.05	0.0	0
Z=4cm	Direct Method (N)	9.7945×10^{-6}	7.3240×10^{-4}	1.1940×10^{-2}	1.1105×10^{-1}	1.2302	6.0918
	Replaced Rings Method (N)	6.0653×10^{-6}	7.1382×10^{-4}	1.1902×10^{-2}	1.1100×10^{-1}	1.2301	6.0918
	Error (%)	38.1	2.5	0.3	0.05	0.01	0
Z=8 cm	Direct Method (N)	1.3593×10^{-6}	9.5316×10^{-5}	2.8855×10^{-3}	4.7627×10^{-2}	8.3326×10^{-1}	4.9196
	Replaced Rings Method (N)	4.4275×10^{-7}	8.9553×10^{-5}	2.8669×10^{-3}	4.7589×10^{-2}	8.3320×10^{-1}	4.9196
	Error (%)	67.4	6.1	0.65	0.08	0.01	0

* Precision of the calculations in numerical integration for rings of 2 to 100 turns are $0.5\times10^{-11}, 0.5\times10^{-9}, 0.5\times10^{-7}, 0.5\times10^{-6}, 0.5\times10^{-5}$ and 0.5×10^{-4}, respectively.

Table 4. Characteristics of the constructed spiral coils

	Number of turns	Inner radius(cm)	Diameter of wire used (mm)
Coil 1	54	2.15	1.6
Coil 2	55	2.0	1.6

Table 5. Experimental results and their comparison with calculation results of the replaced rings method

	Current of Coils (A)	4.8	5.4	7.3	10.6	14.1
Z=2 cm	Measured Force (N)	0.1079	0.1373	0.2453	0.5199	0.9123
	Calculated Force (N)	0.1067	0.1351	0.2469	0.5206	0.9211
Z=4 cm	Measured Force (N)	0.0687	0.0785	0.1472	0.3139	0.5592
	Calculated Force (N)	0.0640	0.0810	0.1480	0.3119	0.5520
Z=8 cm	Measured Force (N)	0.0196	0.0294	0.0589	0.1275	0.2158
	Calculated Force (N)	0.0256	0.0324	0.0592	0.1248	0.2208

calculated percentage of relative error of the force is lower than the corresponding values in Table 1. At first, it seemed that by decreasing the compression factor the calculation error increases, but this assumption is not true because by decreasing the compression factor, the relative error of calculations with replaced rings method decreases. This is also true for smaller compression factors [10].

V. THE EXPERIMENTAL RESULTS

In order to evaluate the precision of the replaced concentric rings method in calculating the force between coils, two coils with different radii were precisely constructed in the laboratory with the characteristics presented in Table 4.

To precisely measure the repelling and attracting forces between the coils, a test as illustrated in Fig. 7, is arranged. In this figure, one of the coils is placed on a fiber board isolator whose permeability is the same as air, and the other coil is connected to a digital force meter via four pieces of string and a fiber board isolator. So, by applying current to the circuit of the two coils, the force exerted on the higher coil, which is equal to the force on the lower coil, is precisely measured.

In Table 5, the calculation and experimental results for different distances are presented. To

obtain the calculation results of this table, due to the large number of turns and inner radii for the coils, the replaced concentric rings method is employed. Regarding the results and the explanations of the previous section, using this method in this case causes no significant error. As Table 5 shows, the results of the force measurement are in good accordance with the results of the calculations, validating the precision of the proposed method.

VI. CONCLUSION

In this paper, the force between spiral coils is calculated using two methods: direct method and replaced concentric rings method. In the direct method, we face integrals with no analytical solutions. The numerical solution of these integrals, due to the fact that the integrands are not smooth, is difficult and time-consuming. To overcome this problem, we employed replaced concentric rings method which has simpler calculations and reduces the calculation time. Due to the obtained results, the calculation error of the replaced rings method for number of turns more than 10 is negligible, and the method is effective. These errors are reduced by increasing the inner radius of spiral coils, which is the case of many practical applications, and are acceptable values in lower turn numbers, too. According to the measurements done on the constructed coils, the calculation results are in good agreement with the experimental results, validating the effectiveness of the replaced rings method.

REFERENCES

[1] S. Atluri and M. Ghovanloo, "A wideband power-efficient inductive wireless link for implantable microelectronic devices using multiple carriers", *IEEE International Symp. On Circuits and Systems (ISCAS)*, pp. 1131-1134, 2006.

[2] Y. Fukuda, T. Inoue, T. Mizoguchi, S. Yatabe, and Y. Tachi, "Planar inductor with ferrite layers for DC-DC converter", *IEEE Trans. on Mag.,* vol. 39, pp. 2057-2061, 2003.

[3] A. Meriched, M. Feliachi, and H. Mohellebi, "Electromagnetic forming of thin metal sheets", *IEEE Trans. on Mag.,* vol. 36, pp. 1808-1811, 2000.

[4] A. Shiri, M. R. Alizadeh Pahlavani, and A. Shoulaie, "A new and fast procedure for calculation of the magnetic forces between cylindrical coils", *International Review of Electrical Engineering,* vol. 4, no. 5, September/October 2009.

[5] A. Shiri and A. Shoulaie, "A new methodology for magnetic force calculations between planar spiral coils", *Progress in Electromagnetics Research,* vol. 95, pp. 39-57, 2009.

[6] D. K. Cheng, *Field and Wave Electromagnetics,* Second Edition, Addison Wesley, 1989.

[7] A. Shiri, "Calculation of magnetic forces between current carrying coils in two plates", *Master of Science Thesis,* Iran University of Science & Technology, 2006.

[8] M. R. Spiegel, *Schaum's outline series: Mathematical Handbook of Formulas and Tables*, McGraw-Hill, 1968.

Abbas Shiri was born in Hashtrood, Iran in 1980. He received the B.Sc. and M.Sc. degrees both in electrical engineering in 2004 and 2006, respectively, and is currently working toward a Ph.D. degree in electrical engineering at Iran University of Science and Technology (IUST).

His areas of research interests include electromagnetic systems and actuators, power electronics and drives, electrical machine design and modeling and linear electric machines.

Abbas Shoulaie was born in Isfahan, Iran in 1949. He received the B.Sc. degree from Iran University of Science and Technology (IUST), Tehran, Iran, in 1973, and the M.Sc. and Ph.D. degrees in electrical engineering from U.S.T.L, Montpellier, France, in 1981 and 1984, respectively.

He is a Professor at the department of Electrical Engineering, IUST. He is the author of more than 100 journal and conference papers in the field of power electronics, electromagnetic systems, electrical machine, linear machine and HVDC.

A New Method for Estimating the Direction-of-Arrival Waves by an Iterative Subspace-Based Method

Hatem Changuel [1], Adel Changuel [2], Ali Gharsallah [1]

[1] Laboratoire de physique de la matière molle, Unité de recherche:
Circuits et Système Electronique Haute Fréquence
Faculté des Sciences de Tunis, Campus Universitaire Tunis El-manar, 2092, Tunisie
Hatem.Changuel@fsg.rnu.tn, ali.gharsallah@fst.rnu.tn

[2] Ecole Préparatoire aux Académies Militaires (EPAM),
Av. Maréchal Tito 4000 Sousse, Tunisie.
changuel@topnet.net

***Abstract*—** In this paper, a new subspace-based method for high-resolution direction-of-arrival (DOA) estimation of multiple plane waves in a noisy environment is proposed. This method called Iterative-Subspace-Decomposition (ISD) involves an iterative decomposition into two blocks of the matrices corresponding to the noise and the source subspaces. The proposed algorithm provides enhanced estimation performance of the DOA. It also significantly improves the resolution capability with respect to existing algorithms. The method can be applied to low signal-to-noise ratio (SNR) environment and is suitable for arrays with arbitrary sensor geometries, including linear arrays. Several numerical simulations are presented to assess the proposed method enhanced performance in comparison to that obtained by some classical algorithms. This comparative study has shown that the ISD leads to a significant reduction in the Root Mean Square Errors (RMSE) and resolution rate capabilities of the DOA estimates. As though, it is shown that the ISD method is superior in resolving closely spaced signals with a small number of snapshots and at low SNR.

***Index Terms*—** Subspace-based methods, DOA estimation, iterative decomposition, high-resolution capability, estimation performance, arbitrary sensor geometries, linear arrays.

I. INTRODUCTION

Direction of Arrival (DOA) estimation of narrowband wave fronts impinging on an array of sensors has long been of great interest in several applications [1]. Numerous techniques have been developed to determine the angle of arrival of signals incident on an antenna array [2]. These methods typically are based on the phase difference of the signal at adjacent elements in the antenna array since this phase difference is proportional to the angle of arrival of the incoming signal.

In the literature, the classical subspace based methods have been investigates extensively [3]. Super-resolution techniques have also been developed that take advantage of the structure of the input data model. These methods, including MUSIC [4], ESPRIT [5] and SUMWE [6], fall into a class of algorithms known as subspace-based techniques [7]. Nevertheless, the existing linear operation based methods, e.g., Propagator [8], find the signal or noise subspace from the array data by partitioning the array response matrix or exploiting the array geometry and its shift invariance property, and then estimate the directions of arrival (DOAs) of incident signals by the way similar to the classical MUSIC estimator. However, it is shown in [6] that the estimation accuracy of the linear operation based methods is generally poorer than the classical subspace based methods (e.g., MUSIC) from the statistical viewpoint. That's why MUltiple SIgnal Classification (MUSIC) is a popular high-resolution technique for estimating the DOA of

multiple plane waves in a noisy environment, using an array of M sensors [9]. The method involves eigendecomposition of the spectral covariance matrix Γ of the M-dimensional data vector to determine the noise and the source subspace. The matrix Γ is estimated from a finite number of samples of the data vector. For a given data size K, reduction of the signal-to-noise ratio (SNR) at the sensor array output causes an increase in the covariance matrix estimation error and a corresponding increase in the DOA estimation error [10]. The estimation errors may be reduced by increasing K, but requirements of temporal coherence and speed impose an upper limit on the permissible value of K.

Inevitably, the performance of the MUSIC estimator suffers a progressive degradation as the SNR is reduced. In the case of finite data samples, it cannot resolve adjacent sources with large power level differences between them. In this work, the possibility of using an Iterative-Subspace-Decomposition (ISD) technique is explored to improve the performance of the MUSIC in low SNR environment. The ISD method is based on the invariance property of noise and source subspace after an iterative decomposition into two blocks. This method not only has a higher resolution than the MUSIC but also can resolve very weak sources in the vicinity of strong ones. The proposed algorithm can handle all array configurations and like the MUSIC method its DOA estimates are asymptotically exact, i.e., exact estimates are obtained asymptotically as the number of measurements goes to infinity irrespective of the SNR and angular separations of the sources [11].

The paper is organized as follows. First, the signal and noise model is presented and DOA estimation problem is formulated. Next, the new method is presented and its iterative process is investigated. Simulation results for comparison between the proposed algorithm and the MUSIC method are given in Section 4, followed by a summary of the main conclusions arising from this work.

II. DATA MODEL AND MUSIC ALGORITHM

Consider a Uniform Linear Array (ULA) of M sensors with intersensor spacing d. If plane waves from N narrowband far field sources, with the same known center frequency f_0, arrive at the array at angles $\theta_1, \theta_2, \ldots, \theta_N$, with respect to the array normal, the complex received signal of the mth sensor at time t, can be written as

$$\begin{aligned} r_m(t) &= \sum_{i=1}^{N} a_m(\theta_i) s_i(t - \tau_m(\theta_i)) + b_m(t) \\ &= \sum_{i=1}^{N} a_m(\theta_i) s_i(t) exp(-j2\pi f_0 \tau_m(\theta_i)) + b_m(t) \end{aligned} \quad (1)$$

where $\tau_m(\theta_i)$ is the propagation delay between a reference point and the mth sensor for the ith wavefront impinging on the array from direction θ_i as shown in Fig. 1, $a_m(\theta_i)$ is the corresponding sensor element complex response (gain and phase) at frequency f_0, and $b_m(t)$ is additive noise at the mth sensor element.

With the narrow band assumption, $s_i(t)$ is the ith signal complex envelop representation which can be shown as

$$s_i(t) = u_i(t) exp(j(2\pi f_0 t + \varphi_i(t))), \quad i = 1,\ldots,N \quad (2)$$

where $u_i(t)$ and $\varphi_i(t)$ are slowly varying functions of time that define the amplitude and phase of ith signal, respectively. Slowly varying means $u_i(t) \approx u_i(t-\tau)$ and $\varphi_i(t) \approx \varphi_i(t-\tau)$ for all possible propagation delays τ between array sensors, and as a result of this, the effect of a time delay on received waveforms is simply a phase shift, i.e.,

$$s_i(t-\tau) \approx s_i(t) exp(-j2\pi f_0 \tau) \quad (3)$$

Using vector notation for the received signals of M sensors, the data model can be presented as

$$\underline{r}(t) = \sum_{i=1}^{N} \underline{a}(\theta_i) s_i(t) + \underline{b}(t) \quad (4)$$

where

$$\begin{aligned} &\underline{r}(t) = [r_1(t),\ldots,r_M(t)]^T, \ \underline{b}(t) = [b_1(t),\ldots,b_M(t)]^T, \\ &\underline{a}(\theta_i) = [a_1(\theta_i) exp(-j2\pi f_0 \tau_1(\theta_i)),\ldots, \\ &\qquad a_M(\theta_i) exp(-j2\pi f_0 \tau_M(\theta_i))]^T \end{aligned} \quad (5)$$

$i = 1,\ldots,N$.

and superscript T denotes transpose of a matrix. The $M \times 1$ vector $\underline{a}(\theta_i)$ is known as array response or array steering vector for direction θ_i. With defining the $M \times N$ matrix $A = [\underline{a}(\theta_1),...,\underline{a}(\theta_N)]$ and $N \times 1$ vector $\underline{s}(t) = [s_1(t),...,s_N(t)]^{\mathrm{T}}$, relation (4), can be written as

$$\underline{r}(t) = A\underline{s}(t) + \underline{b}(t). \quad (6)$$

The problem of determining the DOAs can now be reduced to the problem of estimating the vector parameter $\theta = [\theta_1,...,\theta_N]^{\mathrm{T}}$ given K observations or *snapshots* $\{x(t)\}_{t=1}^{K}$. In order to make the estimation problem tractable, some assumptions have to be made about the model (6). The following assumptions are common in the literature on DOA estimation:

A1) The number of sensors M is larger than the number of emitting sources N, i.e., $M > N$. The number of sources N is assumed to be known.

A2) The steering vectors $\underline{a}(\theta)$ is known for all θ and the array is configured in such a way that the matrix A has full column rank, i.e., rank $(A) = N$. This also implies the source directions to be different in space, i.e., $\theta_i \neq \theta_j$.

A3) The additive noise at each sensor is a zero-mean stationary complex Gaussian random vector which is both temporally and spatially white. The noise processes of different sensors are uncorrelated and with the covariance matrix

$$\Gamma_b = E\{\underline{b}(t)\underline{b}(t)^{\mathrm{H}}\} = \sigma_b^2 I_M, \quad (7)$$

where σ_b^2 is the noise power at each sensor and I_M is an $M \times M$ identity matrix.

It is further assumed that the noise is uncorrelated with the N source signals.

A4) the sources are uncorrelated zero mean stationary processes with the $N \times N$ diagonal covariance matrix

$$P_S = E\{\underline{s}(t)\underline{s}(t)^{\mathrm{H}}\} = diag\{\eta_1^2, \eta_2^2, ..., \eta_N^2\}, \quad (8)$$

where $\eta_i^2 = E\{|s_i(t)|^2\}$ denote the power (variance) of the ith source.

From the above assumptions and (6), the $M \times M$ covariance matrix of received data can be expressed as

$$\Gamma = E\{\underline{r}(t)\underline{r}(t)^{\mathrm{H}}\} = AP_S A^{\mathrm{H}} + \sigma_b^2 I_M = \Gamma_s + \Gamma_b \quad (9)$$

where $\Gamma_s = AP_S A^{\mathrm{H}}$ denote the signal covariance matrix.

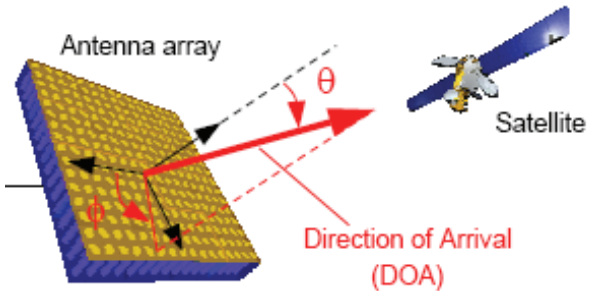

Fig. 1. Geometry of the array for DOA estimation.

Let Γ be eigen decomposed as

$$\begin{aligned}\Gamma &= [\mathrm{U_s V_b}]\, diag\{P_S, 0\}[\mathrm{U_s V_b}]^{\mathrm{H}} + \sigma_b^2 I_M \\ &= [\mathrm{U_s V_b}]\, diag\{P_S + \sigma_b^2 I_N, \sigma_b^2 I_{M-N}\}[\mathrm{U_s V_b}]^{\mathrm{H}} \quad (10) \\ &= [\mathrm{U_s V_b}]\begin{bmatrix}\Lambda & 0 \\ 0 & \sigma_b^2 I_{M-N}\end{bmatrix}\begin{bmatrix}\mathrm{U_s^H} \\ \mathrm{V_b^H}\end{bmatrix}\end{aligned}$$

where $\Lambda = diag\{\eta_1^2 + \sigma_b^2, \eta_2^2 + \sigma_b^2, ..., \eta_N^2 + \sigma_b^2\}$,

$\mathrm{U_s}$ and $\mathrm{V_b}$ are the signal subspace and noise subspace eigen vector matrices, respectively. It can be shown that $A^{\mathrm{H}}\mathrm{V_b}$=0. Or equivalently,

$$\underline{a}^{\mathrm{H}}(\theta)\mathrm{V_b}\mathrm{V_b^H}\underline{a}(\theta) = 0 \quad (11)$$

at the true DOAs.

In practice, the data covariance matrix Γ is not available but a maximum likelihood estimate $\hat{\Gamma}$ based on a finite number (K) of data samples can be obtained as

$$\hat{\Gamma} = \frac{1}{K}\sum_{k=1}^{K}\underline{r}(t_k)\underline{r}(t_k)^{\mathrm{H}} \quad 12)$$

where $t_k = kT_s$, T_s is the sampling period and estimation of DOA of sources is based on this sample covariance matrix.

If $\hat{\Gamma}$ is eigen decomposed as in (10), one would arrive at the estimate of the noise subspace eigen vector matrix as $\hat{\mathrm{V}}_\mathrm{b}$. Since $\hat{\mathrm{V}}_\mathrm{b}$ is only an estimate, the left-hand side of (11), would be minimum, and not zero, at the true DOAs if V_b is replaced by $\hat{\mathrm{V}}_\mathrm{b}$. Spectral MUSIC utilizes this fact, so that the ambiguity function,

$$F_{MUSIC}(\theta)=\left(\frac{1}{\underline{a}^{\mathrm{H}}(\theta)\hat{\mathrm{V}}_\mathrm{b}\hat{\mathrm{V}}_\mathrm{b}^{\mathrm{H}}\underline{a}(\theta)}\right) \tag{13}$$

peaks at the true DOA, whereas Root MUSIC simply roots the polynomial $\underline{a}^{\mathrm{H}}(\theta)\hat{\mathrm{V}}_\mathrm{b}\hat{\mathrm{V}}_\mathrm{b}^{\mathrm{H}}\underline{a}(\theta)$ to find the DOA.

III. PROPOSED DOA ESTIMATION ALGORITHM: Iterative-Subspace-Decomposition (ISD) Method

A set of basis vectors that span the signal subspace S are the eigenvectors corresponding to the N largest eigenvalues of the measurement covariance matrix Γ. This follows from the definition of the eigenvalues and eigenvectors of Γ given by

$$\Gamma\underline{v}_m=\lambda_m\underline{v}_m,\qquad m=1,2,...,M, \tag{14}$$

where $\lambda_1\geq\lambda_2\geq...\geq\lambda_M$ are the eigenvalues (in decreasing order) of Γ and $\underline{v}_i$ are the corresponding eigenvectors. Inserting for Γ into (14), gives

$$\Gamma_s\underline{v}_m=\left(\lambda_m-\sigma_b^2\right)\underline{v}_m, \tag{15}$$

which is the definition of the eigenvalues and the eigenvectors of the signal covariance matrix $\Gamma_s=APA^{\mathrm{H}}$, where $\left(\lambda_m-\sigma_b^2\right)$ is the mth eigenvalue and $\underline{v}_m$ is the mth eigenvector.

The $M\times M$ matrix Γ_s is by construction positive semidefinite with rank equal to N (under the assumption that the signals are not fully correlated). This means that Γ_s has N positive, nonzero eigenvalues and M-N eigenvalues that are equal to zero. The eigenvalues of Γ are then $\lambda_1\geq\lambda_2\geq...\geq\lambda_N>\lambda_{N+1}=...=\lambda_M=\sigma_b^2$ and the eigenvectors of Γ corresponding to the N largest eigenvalues are the same as the eigenvectors of Γ_s that correspond to the only nonzero eigenvalues. These eigenvectors span the same subspace as Γ_s and hence also A. The signal subspace can then be written as:

$$S=span\{A\}=span\{\mathrm{U}_\mathrm{s}\}, \tag{16}$$

where $\mathrm{U}_\mathrm{s}=\left[\underline{v}_1,\underline{v}_2,...,\underline{v}_N\right]$. Similarly, the noise subspace is

$$S^{\perp}=span\{\mathrm{V}_\mathrm{b}\}, \tag{17}$$

where $\mathrm{V}_\mathrm{b}=\left[\underline{v}_{N+1},\underline{v}_{N+2},...,\underline{v}_M\right]$. For an infinite number of snapshots K, the sample covariance matrix is equal to the measurement covariance matrix, that is, $\lim_{\mathrm{M}\to\infty}\hat{\Gamma}=\Gamma$, and the signal subspace can be found as described above.

In practice, however, there is a finite amount of data available, which implies that $\hat{\Gamma}\neq\Gamma$. This means that the exact signal subspace cannot be found. Instead, estimates of the signal and noise subspaces can be made from the eigenvectors of $\hat{\Gamma}$, i.e., $\hat{S}=span\{\hat{\mathrm{U}}_\mathrm{s}\}$ and $\hat{S}^{\perp}=span\{\hat{\mathrm{V}}_\mathrm{b}\}$, where $\hat{\mathrm{U}}_\mathrm{s}=\left[\underline{\hat{v}}_1,\underline{\hat{v}}_2,...,\underline{\hat{v}}_N\right]$, $\hat{\mathrm{V}}_\mathrm{b}=\left[\underline{\hat{v}}_{N+1},\underline{\hat{v}}_{N+2},...,\underline{\hat{v}}_M\right]$, and $\underline{\hat{v}}_m$, $m=1,2,...,M$ are the eigenvectors corresponding to the eigenvalues of $\hat{\Gamma}$, which are $\hat{\lambda}_1\geq\hat{\lambda}_2\geq...\geq\hat{\lambda}_M$.

A. Signal and Noise Subspace

The $M\times M$ sample covariance matrix $\hat{\Gamma}$ given in (12), is a positive definite matrix. We denote its eigenvalues (in decreasing order) and their corresponding eigenvectors by $\hat{\lambda}_m$ and $\underline{\hat{v}}_m$, i.e.,

$$\hat{\Gamma}=\mathrm{VDV}^{\mathrm{H}}=\sum_{m=1}^{M}\hat{\lambda}_m\underline{\hat{v}}_m\underline{\hat{v}}_m^{H} \tag{18}$$

where $\mathrm{V}=\left[\underline{\hat{v}}_1,\underline{\hat{v}}_2,...,\underline{\hat{v}}_M\right]$ and $\mathrm{D}=diag\left\{\hat{\lambda}_1,\hat{\lambda}_2,...,\hat{\lambda}_M\right\}$

Establishing of the signal and noise subspace is obtained using the following observations; Because it is assumed that $M>N$, the $M\times M$ eigenvalues matrix D and the $M\times M$ eigenvectors matrix V can divided into four parts as follows:

$$\mathrm{V} = \begin{bmatrix} \mathrm{V}_{11} & \mathrm{V}_{12} \\ \underbrace{\mathrm{V}_{21}}_{N} & \underbrace{\mathrm{V}_{22}}_{M-N} \end{bmatrix} \begin{matrix} \} & N \\ \} & M-N \end{matrix} \tag{19}$$

and

$$\mathrm{D} = \begin{bmatrix} \mathrm{D}_1 & \mathrm{D}_2 \\ \underbrace{\mathrm{D}_3}_{N} & \underbrace{\mathrm{D}_4}_{M-N} \end{bmatrix} \begin{matrix} \} & N \\ \} & M-N \end{matrix}. \tag{20}$$

The submatrices V_{11} and V_{21} define the signal subspace matrix V_S. The submatrices V_{12} and V_{22} define the noise subspace matrix V_B. V_S and V_B are the same signal and noise subspace defined by the MUSIC method. The two blocks D_2 and D_3 for the diagonal matrix D are two null matrices.

Assume first that there is no noise present. The spectral covariance matrix Γ can then be written

$$\begin{aligned} \Gamma = \Gamma_s = \mathrm{VEV}^{\mathrm{H}} &= \begin{bmatrix} \mathrm{V_S} & \mathrm{V_B} \end{bmatrix} \begin{bmatrix} \mathrm{E} & 0 \\ 0 & 0 \end{bmatrix} \begin{bmatrix} \mathrm{V_S^H} \\ \mathrm{V_B^H} \end{bmatrix} \\ &= \mathrm{V_S E V_S^H} \end{aligned} \tag{21}$$

where E is the $N \times N$ diagonal matrix which contain the eigenvalues (in decreasing order) of the signal covariance matrix Γ_s.

Now assume that noise is included in the model. The spectral covariance matrix Γ can then be written

$$\begin{aligned} \Gamma &= \Gamma_s + \Gamma_b = \mathrm{V_S E V_S^H} + \sigma_b^2 I_M \\ &= \mathrm{V_S E V_S^H} + \mathrm{V_S}\left(\sigma_b^2 I_N\right)\mathrm{V_S^H} + \mathrm{V_B}\left(\sigma_b^2 I_{M-N}\right)\mathrm{V_B^H}. \\ &= \begin{bmatrix} \mathrm{V_S} & \mathrm{V_B} \end{bmatrix} diag\left\{\mathrm{E} + \sigma_b^2 I_N, \sigma_b^2 I_{M-N}\right\} \begin{bmatrix} \mathrm{V_S} & \mathrm{V_B} \end{bmatrix}^{\mathrm{H}} \end{aligned} \tag{22}$$

Thus, the $M-N$ dimensional subspace spanned by the $M-N$ noise eigenvectors may be justifiably referred to as the noise subspace. The N dimensional subspace spanned by the incident signal mode vectors may also be referred to as the signal subspace. Both subspaces are disjoint.

By including the partitioning of the matrix V and D, a new covariance matrix Γ is defined as

$$\begin{aligned} \Gamma &= \begin{bmatrix} \mathrm{V_{11}D_1V_{11}^H} & \mathrm{V_{11}D_1V_{21}^H} \\ \mathrm{V_{21}D_1V_{11}^H} & \mathrm{V_{21}D_1V_{21}^H} \end{bmatrix} + \begin{bmatrix} \mathrm{V_{12}D_4V_{12}^H} & \mathrm{V_{12}D_4V_{22}^H} \\ \mathrm{V_{22}D_4V_{12}^H} & \mathrm{V_{22}D_4V_{22}^H} \end{bmatrix} \\ &= \begin{bmatrix} \mathrm{V_S} & \mathrm{V_B} \end{bmatrix} diag\left\{\mathrm{D_1}, \mathrm{D_4}\right\} \begin{bmatrix} \mathrm{V_S} & \mathrm{V_B} \end{bmatrix}^{\mathrm{H}}. \end{aligned} \tag{23}$$

Add and leave out the noise covariance matrix Γ_b, relation (23), can be written as

$$\Gamma = \mathrm{V_S}\left(\mathrm{D_1} - \sigma_b^2 I_N\right)\mathrm{V_S^H} + \mathrm{V_S}\left(\sigma_b^2 I_N\right)\mathrm{V_S^H} + \mathrm{V_B D_4 V_B^H} \tag{24}$$

By identification with (22), the signal covariance matrix can be written as:

$$\Gamma_s = \begin{bmatrix} \mathrm{V_{11}D_1'V_{11}^H} & \mathrm{V_{11}D_1'V_{21}^H} \\ \mathrm{V_{21}D_1'V_{11}^H} & \mathrm{V_{21}D_1'V_{21}^H} \end{bmatrix} = \begin{bmatrix} \mathrm{Q_{S1}} & \mathrm{Q_{S2}} \\ \mathrm{Q_{S3}} & \mathrm{Q_{S4}} \end{bmatrix}, \tag{25}$$

and the noise covariance matrix can be written as

$$\begin{aligned} \Gamma_b &= \begin{bmatrix} \mathrm{V_S} & \mathrm{V_B} \end{bmatrix} diag\left\{\sigma_b^2 I_N, \mathrm{D_4}\right\} \begin{bmatrix} \mathrm{V_S} & \mathrm{V_B} \end{bmatrix}^{\mathrm{H}}, \\ &= \mathrm{V_S}\left(\sigma_b^2 I_N\right)\mathrm{V_S^H} + \Gamma_{bb} \end{aligned} \tag{26}$$

where

$$\Gamma_{bb} = \begin{bmatrix} \mathrm{V_{12}D_4'V_{12}^H} & \mathrm{V_{12}D_4'V_{22}^H} \\ \mathrm{V_{22}D_4'V_{12}^H} & \mathrm{V_{22}D_4'V_{22}^H} \end{bmatrix} = \begin{bmatrix} \mathrm{Q_{B1}} & \mathrm{Q_{B2}} \\ \mathrm{Q_{B3}} & \mathrm{Q_{B4}} \end{bmatrix}, \tag{27}$$

$$\mathrm{D_1'} = \mathrm{D_1} - \sigma_b^2 I_N = \mathrm{E} \quad \text{and} \quad \mathrm{D_4'} = \mathrm{D_4} = \sigma_b^2 I_{M-N}.$$

The parameters $\mathrm{Q_{S1}}$, $\mathrm{Q_{S2}}$, $\mathrm{Q_{S3}}$ and $\mathrm{Q_{S4}}$ are, respectively, $N \times N$, $N \times (M-N)$, $(M-N) \times N$ and $(M-N) \times (M-N)$ dimensional submatrices. $\mathrm{Q_{B1}}$, $\mathrm{Q_{B2}}$, $\mathrm{Q_{B3}}$ and $\mathrm{Q_{B4}}$ are, respectively, $N \times N$, $N \times (M-N)$, $(M-N) \times N$ and $(M-N) \times (M-N)$ dimensional submatrices.

Lastly, the noise subspace $\mathrm{R_B}$ and the signal subspace $\mathrm{R_S}$ is obtained by a linear operation of the matrix formed from the noise and signal covariance matrix:

B. Iterative Subspace-Decomposition-Signal (ISDS) Method

From the signal covariance matrix (25), $\mathrm{G_S}$ is defined to be the $N \times (M-N)$ linear operator source. The rows of $\mathrm{Q_{S3}}$ can be expressed as a linear combination of linearly independents rows of $\mathrm{Q_{S1}}$; equivalently, there is a $N \times (M-N)$ linear operator $\mathrm{G_S}$ between $\mathrm{Q_{S1}}$ and $\mathrm{Q_{S3}}$

$$\mathrm{Q_{S3}} = \mathrm{G_S^H Q_{S1}} \Rightarrow \mathrm{V_{21}} = \mathrm{G_S^H V_{11}}. \tag{28}$$

Then it follows from (28), that

$$\mathrm{R_{Bs}^H} A(\theta) = 0_{(M-N)\times N} \quad \text{or} \quad span\{\mathrm{R_{Bs}}\} \perp span\{A\}$$

and

$$span\{\mathrm{R}_{\mathrm{Ss}}\} = span\{A\}, \tag{29}$$

where $\mathrm{R}_{\mathrm{Bs}} = \begin{bmatrix} \mathrm{G}_{\mathrm{S}} \\ -I_{M-N} \end{bmatrix}$ and $\mathrm{R}_{\mathrm{Ss}} = \begin{bmatrix} I_N \\ \mathrm{G}_{\mathrm{S}}^{\mathrm{H}} \end{bmatrix}$ are the noise and signal subspace matrices, respectively. Because the $M \times (M-N)$ matrix R_{Bs} has a full rank of $(M-N)$, the columns of R_{Bs} form the basis for the null space $\aleph\left(A^H(\theta)\right)$ of $A^H(\theta)$, and clearly, the orthogonal projector onto this noise subspace is given by

$\Pi_{\mathrm{R}_{\mathrm{Bs}}} = \mathrm{R}_{\mathrm{Bs}}\left(\mathrm{R}_{\mathrm{Bs}}^{\mathrm{H}}\mathrm{R}_{\mathrm{Bs}}\right)^{-1}\mathrm{R}_{\mathrm{Bs}}^{\mathrm{H}}$, which implies that

$$\begin{aligned} &\Pi_{\mathrm{R}_{\mathrm{Bs}}}\underline{a}(\theta) = 0_{M\times 1} \quad \text{for} \quad \theta = \theta_i \\ &i = 1,\ldots,N \end{aligned} \tag{30}$$

where

$$\underline{a}(\theta) = \left[1, exp\left(-j2\pi f_0 \tau(\theta)\right), \ldots, exp\left(-j2\pi f_0 (M-1)\tau(\theta)\right)\right]^{\mathrm{T}}$$

and $0_{M\times 1}$ is an $M \times 1$ null vector. Evidently, the directions can be estimated based on the orthogonal property (30).

C. Iterative Process

The common assumption used for the following iterations is that the noise subspace matrix R_{B} (i.e., R_{Bs} or R_{Bb}) has a full rank of $(M-N)$. Because it is assumed that $M > N$, the $M \times (M-N)$ noise subspace matrix R_{BI} can be divided, at the *I*th iteration, into two parts as follows:

$$\mathrm{R}_{\mathrm{B_I}} = \begin{bmatrix} \mathrm{W}_{\mathrm{I}} \\ \mathrm{Z}_{\mathrm{I}} \end{bmatrix} \begin{matrix} \} M-N \\ \} \quad N \end{matrix} \tag{31}$$

where R_{BI} and W_{I} are two submatrices with full rank, the row of Z_{I} can be expressed as a linear combination of linearly independent rows of W_{I}; equivalently there is a $N \times (M-N)$ linear operator $\mathrm{G}_{\mathrm{I+1}}$ at the (I+1)th iteration, between W_{I} and Z_{I}

$$\mathrm{G}_{\mathrm{I+1}}\mathrm{W}_{\mathrm{I}} = \mathrm{Z}_{\mathrm{I}}. \tag{32}$$

Then it follows from (34), that

$$\mathrm{R}_{\mathrm{B_{I+1}}}^{\mathrm{H}} A(\theta) = 0_{(M-N)\times N} \quad \text{or} \quad span\left\{\mathrm{R}_{\mathrm{B_{I+1}}}\right\} \perp span\{A\}$$

and

$$span\left\{\mathrm{R}_{\mathrm{S_{I+1}}}\right\} = span\{A\} \tag{33}$$

where

$\mathrm{R}_{\mathrm{B_{I+1}}} = \begin{bmatrix} \mathrm{G}_{\mathrm{I+1}} \\ I_{M-N} \end{bmatrix}$ and $\mathrm{R}_{\mathrm{S_{I+1}}} = \begin{bmatrix} -I_N \\ \mathrm{G}_{\mathrm{I+1}}^{\mathrm{H}} \end{bmatrix}$ are the noise and signal subspace matrices at the (I+1)th iteration, respectively.

Thus, a continuation of iterative decomposition of the new noise subspace matrix enables us to reduce the contribution of the noise and consequently to increase the signal-to-noise ratio, by keeping the information useful of the signal to be detected. The ISD spectrum, at the *I*th iteration, can be expressed as:

$$F_{ISD}^{I}(\theta) = \frac{1}{\underline{a}^{H}(\theta)\mathrm{R}_{\mathrm{B_I}}\mathrm{R}_{\mathrm{B_I}}^{\mathrm{H}}\underline{a}(\theta)} \tag{34}$$

where

$$\mathrm{R}_{\mathrm{B_I}} = \begin{bmatrix} \mathrm{G}_{\mathrm{I}} \\ I_{M-N} \end{bmatrix}. \tag{35}$$

The matrix $\mathrm{R}_{\mathrm{B_I}}\mathrm{R}_{\mathrm{B_I}}^{\mathrm{H}}$ is a projection matrix onto the noise subspace. For steering vectors that are orthogonal to the noise subspace, the denominator of (34), will become very small, and thus the peaks will occur in $F_{ISD}^{I}(\theta)$ corresponding to the angle of arrival of the signal.

IV. SIMULATION RESULT

In this section, the estimation accuracies of the proposed method and the classical MUSIC technique are compared for the problem of DOA estimation. Some numerical examples are investigated to illustrate the performance of the proposed method more explicitly. The array herein is assumed to be a ULA composed of 5 isotropic sensors, whose spacing equal half-wavelength. The number of signals is assumed to be known *a priori*. The simulation results include probabilities rate of resolving the two sources and root mean squared errors (RMSE's) of estimated DOAs. In all the simulations of this paper successful simulations are those that show two distinct peaks.

A. RMSE of Estimated DOA

Suppose that the ULA receives two uncorrelated narrowband signals with equal power. We make 200 Monte Carlo (Realizations) runs for

each experiment to compute the Root-Mean-Squared Errors (RMSE's) of estimated DOAs. The true DOAs are given by {88°, 93°}. The background noise is assumed to be a stationary Gaussian white random process with zero mean. The RMSE's of estimated DOAs versus SNR are shown in Fig. 2, where the number of sensors is 5 and the number of snapshots is 100. The Propagator method is also plotted for comparison.

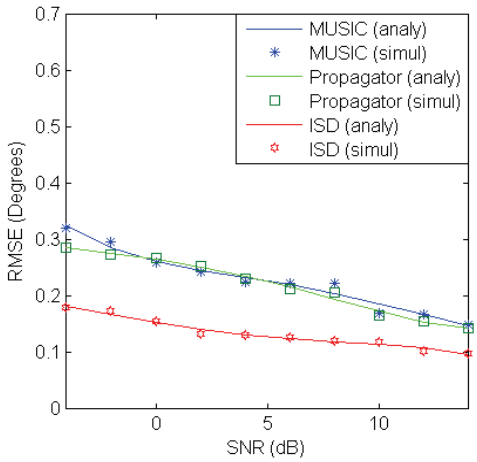

Fig. 2. RMSE's of estimated DOAs versus SNR. DOAs of signal 1 to 2 are 88° and 93°. The number of snapshots and the number of sensors are equal to 100 and 5, respectively.

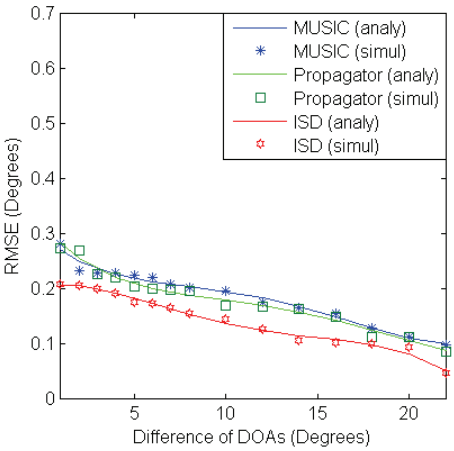

Fig. 3. RMSE's of estimated DOAs versus difference of DOAs between the two sources. The number of snapshots, SNR and the number of sensors are equal to 100, 12 dB and 5, respectively.

It is demonstrated in Fig. 2 that the ISD estimator provides the comparable estimation accuracy with the MUSIC and Propagator methods when SNR is greater than 10dB, and yields the more estimation accuracy than the latter as SNR ≤ 10 dB. It should be noted that the RMSE for the proposed method is higher than the classical MUSIC and Propagator methods over the range of SNR that we simulated, especially in the case of low SNR (SNR < 5 dB), the proposed method surpasses the MUSIC estimator. The RMSE's of the two estimators (MUSIC and Propagator) approach to the ISD as SNR becomes high.

The RMSE of the DOA estimation error obtained by ISD, MUSIC and Propagator methods is plotted versus difference of DOAs between the two sources in Fig. 3. Another example is to demonstrate the superiority of the ISD method over the other method.

It is clearly seen that the ISD method has high-resolution capability.

B. Resolution Rate Capabilities

Let us assume that the number N of mobile users is 2 and each sample covariance matrix is estimated from 100 snapshots in the simulation.

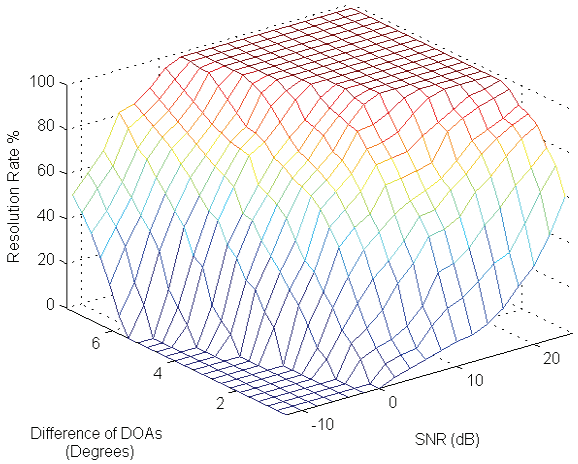

Fig. 4. Resolution rate capabilities versus SNR and difference of DOAs between the two sources. The number of snapshots and the number of sensors are equal to 100 and 5, respectively.

The two sources are considered resolved if the differences between the estimates and their respective true locations are both less than the separation between the sources, i.e., if $83° \le \hat{\theta}_1 < 93°$ and $88° \le \hat{\theta}_2 < 98°$. Throughout simulations, the powers of the sources are assumed equal.

The resolving rate capabilities obtained by the proposed ISD method versus SNR and difference of DOAs between the two sources are plotted in Fig. 4, where the number of snapshots and the number of sensors are equal to 100 and 5, respectively.

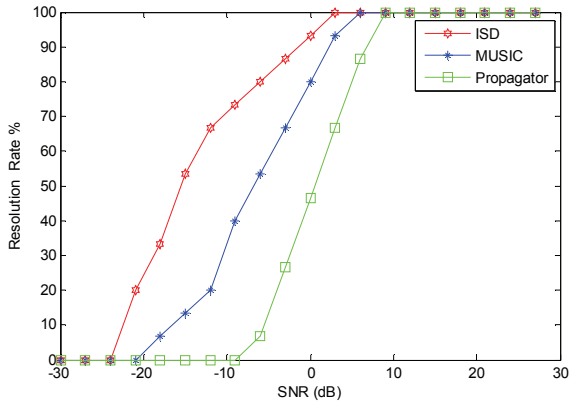

(a)

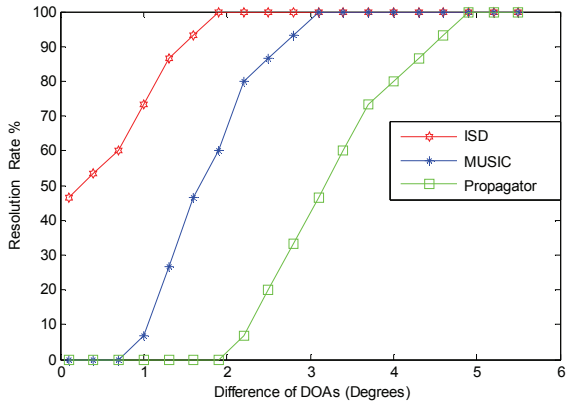

(b)

Fig. 5. Resolution rate capabilities, performance comparisons of the proposed and classical methods, (a) Resolution rate capabilities versus SNR. DOAs of signal 1 to 2 are 88° and 93°. The number of snapshots and the number of sensors are 100 and 5, respectively, (b) Resolution rate capabilities versus difference of DOAs between the two sources. The number of snapshots, SNR and the number of sensors are equal to 100, 12 dB and 5 respectively.

When the two sources are uncorrelated, the results are displayed in Fig. 5. Figure 5(a) shows that the resolution capabilities of the proposed and the classical MUSIC methods are practically the same. The resolution performance of the Propagator method is also included for comparison. It can be verified from Fig. 5(a) that to have a resolution rate more than 90 %, the SNR of ISD, MUSIC and Propagator method must be higher than -5 dB, 0 dB and 5 dB, respectively.

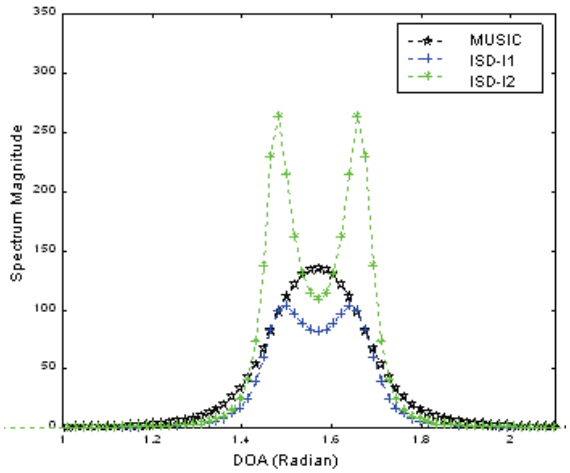

(a)

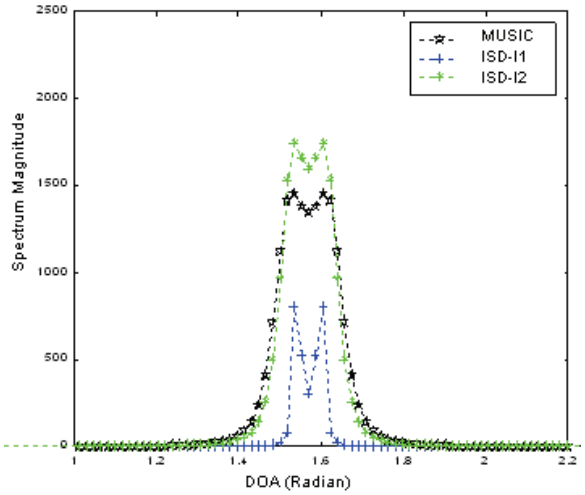

(b)

Fig. 6. Spectrum magnitude of proposed method and MUSIC versus DOA of sources, (a) Spectrum magnitude of proposed ISD method (for Iteration: I=1 and I=2) and MUSIC. DOAs of signal 1 to 2 are 88° and 93°. The number of snapshots, SNR and the number of sensors are equal to 100, -5 dB and 5, respectively, (b) Spectrum magnitude of proposed ISD method (for Iteration: I=1 and I=2) and MUSIC. DOAs of signal 1 to 2 are 88° and 93°, respectively. The number of snapshots, SNR and the number of sensors are equal to 100, 5 dB and 5 respectively.

As illustrated by Fig. 5(b) that though the classical MUSIC and Propagator are unable to resolve the sources when the difference of DOAs between the sources becomes less then 3° and 5°

respectively. The proposed ISD method can, however, estimate the DOAs of the sources more accurately when the difference of DOAs between the sources becomes less then 2°.

Figures 5 and 4 shows higher resolution capabilities of proposed method in resolving closely spaced sources with large power differences at low SNR condition compared to MUSIC and Propagator. The same as the first experiment in all successful simulations of MUSIC method the proposed algorithm has also been successful with a much distinct peaks.

To evaluate the dependence of the estimation accuracy of the proposed method on the number of iterations, the spectrum magnitude of estimated DOAs for the proposed ISD method for two different levels of iteration (I =1 and I = 2), is plotted in Fig. 6. The number of snapshots is 100, SNR changes at -5 dB in Fig. 6(a) and 5 dB in Fig. 6(b), and the number of sensor is 5. MUSIC method is also included for comparison.

The observation indicates that the proposed method can resolve the two DOAs at low SNR condition, unlike MUSIC method. This guarantees that the ISD approach can preserve high accuracy in the case of low-SNR.

V. CONCLUSION

The approach presented here for iterative subspace decomposition is very general and can be applied to all array configurations. The ISD method is interpretable in terms of the geometry of complex M spaces where in the eigen structure of the measured Γ matrix plays the central role. ISD method provides asymptotically unbiased estimates of a general set of signal parameters and its superiority over MUSIC accuracy bound. In geometric terms, ISD minimizes the distance from the steering vectors $\underline{a}(\theta)$ continuum to the signal subspace whereas maximum likelihood minimizes a weighted combination all component distances.

The effect of ISD on the performance of MUSIC is analyzed by numerically evaluating and comparing: (1) the RMSE in the spectral covariance estimates obtained using finite data, and (2) the resolution rate capabilities of the DOA estimates. It is shown that ISD leads to a significant improvement in the performance of the MUSIC estimator.

The array elements may be arranged in a regular or irregular pattern and may differ or be identical in directional characteristics (amplitude/phase) provided their polarization characteristics are all identical. The extension to include general polarizationally diverse antenna arrays will be more completely described in a future work.

ACKNOWLEDGMENT

The authors would like to thank the anonymous reviewers for their valuable comments that significantly improved the presentation of this paper.

REFERENCES

[1] H. Krim and M. Viberg, “Two decades of array signal processing research,” *IEEE Signal Processing Mag*., vol. 13, pp. 67-94, Jul. 1996.

[2] D. F. Breslin, “Adaptive Antenna Arrays Applied to Position Location,” *MASTER OF SCIENCE in the Bradley Department of Electrical and Computer Engineering*, August 1997.

[3] M. Viberg, B. Otterstem, and T. Kailath, “Detection and estimation in sensor array using weighted subspace fitting,” *IEEE Trans. Signal Process*., vol. 39, no. 11, pp. 2436-2449, November 1991.

[4] O. R. Schmit, “Multiple Emitter Location and Signal Parameters Estimation,” *IEEE Trans. on Antennas and Propagation*, vol. 34, pp. 276-280, March 1986.

[5] R. Roy and T. Kailath, “ESPRIT—Estimation of signal parameters via rotational invariance technique,” *IEEE Trans. Acoust., Speech Signal Process*, vol. 37, no. 7, pp. 984-995, July 1989.

[6] J. Xin and A. Sano, “Computationally Efficient Subspace-Based Method for Direction-of-Arrival Estimation Without Eigendecomposition,” *IEEE, Trans. on Signal Processing*, vol. 52, no. 4, April 2004.

[7] F. Castanie, “Estimateurs fondés sur les sous-espaces,” chapitre du livre, *Analyse spectrale*, *Traité IC2*, *Editions HERMES*, 2003.

[8] S. Marcos, A. Marsal, and M. Benidir, “The propagator method for source bearing

estimation," *Signal Process*., vol. 42, no. 2, pp. 121-138, 1995.
[9] P. Stoica and R. Moses, "Introduction to spectral analysis," *Prentice Hall Inc*., 1997.
[10] B. D. Rao and K. V. S. Hari, "Performance analysis of Root-MUSIC," *IEEE Trans. Signal Processing*, vol. 37, pp. 1939-1949, 1989.
[11] A. Olfat and S. N-Esfahani, "A new signal subspace processing for DOA estimation," *ELSEVIER Signal Processing*, vol. 84, pp. 721-728, November 2003.

Hatem Changuel received the M.S. degree in electronic devices from the Faculty of Sciences of Monastir, Tunisia, in 1997 and the Ph.D. degree in electrical engineering from the Ecole Nationale d'Ingénieurs de Tunis, in 2008. His main research interests are in the area of communication aspects of array antennas such as DOA, array processing techniques and ambiguity issues in direction finding.

Adel Changuel received the M. S. degree in Microelectronic devices from the Université Joseph Fourier de Grenoble (UJF), France, in 1993 and the Ph.D. degree in micro-electronics engineering with the TIMA Laboratory, System-level Synthesis Group from the Institut Nationale Polytechnique of Grenoble (INPG) France, in 1996. Since 2004, he was with the department of computer science at the EPAM, Sousse, Tunisia. His current research interests include robotics, design, and prototyping hardware-software embedded systems using microcontrollers.

Ali Gharsallah received the M.S. degree in radio-electrical engineering from the Ecole Supérieur de Télécomm-unication de Tunis in 1986 and the Ph.D. degree in 1994 from the Ecole Nationale d'Ingénieurs de Tunis. Since 1991, he has been with the Department of Physics at the Faculty of Science of Tunisia. His current research interests include antennas, array signal processing, multilayered structures, and microwave integrated circuits.

2010 INSTITUTIONAL MEMBERS

DTIC-OCP LIBRARY
8725 John J. Kingman Rd, Ste 0944
Fort Belvoir, VA 22060-6218

AUSTRALIAN DEFENCE LIBRARY
Northcott Drive
Canberra, A.C.T. 2600 Australia

BEIJING BOOK CO, INC
701 E Linden Avenue
Linden, NJ 07036-2495

BUCKNELL UNIVERSITY
69 Coleman Hall Road
Lewisburg, PA 17837

ROBERT J. BURKHOLDER
OHIO STATE UNIVERSITY
1320 Kinnear Road
Columbus, OH 43212

DARTMOUTH COLLEGE
6025 Baker/Berry Library
Hanover, NH 03755-3560

DSTO EDINBURGH
AU/33851-AP, PO Box 830470
Birmingham, AL 35283

SIMEON J. EARL – BAE SYSTEMS
W432A, Warton Aerodome
Preston, Lancs., UK PR4 1AX

ELLEDIEMME
Libri Dal Mondo
PO Box 69/Poste S. Silvestro
Rome, Italy 00187

ENGINEERING INFORMATION, INC
PO Box 543
Amsterdam, Netherlands 1000 Am

ETSE TELECOMUNICACION
Biblioteca, Campus Lagoas
Vigo, 36200 Spain

OLA FORSLUND
SAAB MICROWAVE SYSTEMS
Nettovagen 6
Jarfalla, Sweden SE-17588

GEORGIA TECH LIBRARY
225 North Avenue, NW
Atlanta, GA 30332-0001

HRL LABS, RESEARCH LIBRARY
3011 Malibu Canyon
Malibu, CA 90265

IEE INSPEC
Michael Faraday House
6 Hills Way
Stevenage, Herts UK SG1 2AY

IND CANTABRIA
PO Box 830470
Birmingham, AL 35283

INSTITUTE FOR SCIENTIFIC INFO.
Publication Processing Dept.
3501 Market St.
Philadelphia, PA 19104-3302

KUWAIT UNIVERSITY
Postfach/po box 432
Basel, Switzerland 4900

LIBRARY – DRDC OTTAWA
3701 Carling Avenue
Ottawa, Ontario, Canada K1A OZ4

LIBRARY of CONGRESS
Reg. Of Copyrights
Attn: 407 Deposits
Washington DC, 20559

LINDA HALL LIBRARY
5109 Cherry Street
Kansas City, MO 64110-2498

RAY MCKENZIE – TELESTRA
13/242 Exhibition Street
Melbourne, Vic, Australia 3000

MISSISSIPPI STATE UNIV LIBRARY
PO Box 9570
Mississippi State, MS 39762

MISSOURI S&T
400 W 14th Street
Rolla, MO 56409

MIT LINCOLN LABORATORY
Periodicals Library
244 Wood Street
Lexington, MA 02420

OSAMA MOHAMMED
FLORIDA INTERNATIONAL UNIV
10555 W Flagler Street
Miami, FL 33174

NAVAL POSTGRADUATE SCHOOL
Attn:J. Rozdal/411 Dyer Rd./ Rm 111
Monterey, CA 93943-5101

NDL KAGAKU
C/0 KWE-ACCESS
PO Box 300613 (JFK A/P)
Jamaica, NY 11430-0613

OVIEDO LIBRARY
PO BOX 830679
Birmingham, AL 35283

PENN STATE UNIVERSITY
126 Paterno Library
University Park, PA 16802-1808

DAVID J. PINION
1122 E PIKE STREET #1217
SEATTLE, WA 98122

KATHERINE SIAKAVARA-
ARISTOTLE UNIV OF
THESSALONIKI
Gymnasiou 8
Thessaloniki, Greece 55236

SWETS INFORMATION SERVICES
160 Ninth Avenue, Suite A
Runnemede, NJ 08078

TIB & UNIV. BIB. HANNOVER
DE/5100/G1/0001
Welfengarten 1B
Hannover, Germany 30167

UNIV OF CENTRAL FLORIDA
4000 Central Florida Boulevard
Orlando, FL 32816-8005

UNIVERSITY OF COLORADO
1720 Pleasant Street, 184 UCB
Boulder, CO 80309-0184

UNIVERSITY OF KANSAS –
WATSON
1425 Jayhawk Blvd 210S
Lawrence, KS 66045-7594

UNIVERSITY OF MISSISSIPPI
JD Williams Library
University, MS 38677-1848

UNIVERSITY LIBRARY/HKUST
CLEAR WATER BAY ROAD
KOWLOON, HONG KONG

UNIV POLIT CARTAGENA
Serv Btca Univ,
Paseo Alfonso XIII, 48
Cartagena, Spain 30203

THOMAS WEILAND
TU DARMSTADT
Schlossgartenstrasse 8
Darmstadt, Hessen, Germany 64289

STEVEN WEISS
US ARMY RESEARCH LAB
2800 Powder Mill Road
Adelphi, MD 20783

YOSHIHIDE YAMADA
NATIONAL DEFENSE ACADEMY
1-10-20 Hashirimizu
Yokosuka, Kanagawa,
Japan 239-8686

ACES COPYRIGHT FORM

This form is intended for original, previously unpublished manuscripts submitted to ACES periodicals and conference publications. The signed form, appropriately completed, MUST ACCOMPANY any paper in order to be published by ACES. PLEASE READ REVERSE SIDE OF THIS FORM FOR FURTHER DETAILS.

TITLE OF PAPER:

AUTHORS(S)

PUBLICATION TITLE/DATE:

RETURN FORM TO:

Dr. Atef Z. Elsherbeni
University of Mississippi
Dept. of Electrical Engineering
Anderson Hall Box 13
University, MS 38677 USA

PART A - COPYRIGHT TRANSFER FORM

(NOTE: Company or other forms may not be substituted for this form. U.S. Government employees whose work is not subject to copyright may so certify by signing Part B below. Authors whose work is subject to Crown Copyright may sign Part C overleaf).

The undersigned, desiring to publish the above paper in a publication of ACES, hereby transfer their copyrights in the above paper to The Applied Computational Electromagnetics Society (ACES). The undersigned hereby represents and warrants that the paper is original and that he/she is the author of the paper or otherwise has the power and authority to make and execute this assignment.

Returned Rights: In return for these rights, ACES hereby grants to the above authors, and the employers for whom the work was performed, royalty-free permission to:

1. Retain all proprietary rights other than copyright, such as patent rights.
2. Reuse all or portions of the above paper in other works.
3. Reproduce, or have reproduced, the above paper for the author's personal use or for internal company use provided that (a) the source and ACES copyright are indicated, (b) the copies are not used in a way that implies ACES endorsement of a product or service of an employer, and (c) the copies per se are not offered for sale.
4. Make limited distribution of all or portions of the above paper prior to publication.
5. In the case of work performed under U.S. Government contract, ACES grants the U.S. Government royalty-free permission to reproduce all or portions of the above paper, and to authorize others to do so, for U.S. Government purposes only.

ACES Obligations: In exercising its rights under copyright, ACES will make all reasonable efforts to act in the interests of the authors and employers as well as in its own interest. In particular, ACES REQUIRES that:

1. The consent of the first-named author be sought as a condition in granting re-publication permission to others.
2. The consent of the undersigned employer be obtained as a condition in granting permission to others to reuse all or portions of the paper for promotion or marketing purposes.

In the event the above paper is not accepted and published by ACES or is withdrawn by the author(s) before acceptance by ACES, this agreement becomes null and void.

AUTHORIZED SIGNATURE — TITLE (IF NOT AUTHOR)

EMPLOYER FOR WHOM WORK WAS PERFORMED — DATE FORM SIGNED

Part B - U.S. GOVERNMENT EMPLOYEE CERTIFICATION

(NOTE: if your work was performed under Government contract but you are not a Government employee, sign transfer form above and see item 5 under Returned Rights).

This certifies that all authors of the above paper are employees of the U.S. Government and performed this work as part of their employment and that the paper is therefor not subject to U.S. copyright protection.

AUTHORIZED SIGNATURE — TITLE (IF NOT AUTHOR)

NAME OF GOVERNMENT ORGANIZATION — DATE FORM SIGNED

PART C - CROWN COPYRIGHT

(NOTE: ACES recognizes and will honor Crown Copyright as it does U.S. Copyright. It is understood that, in asserting Crown Copyright, ACES in no way diminishes its rights as publisher. Sign only if *ALL* authors are subject to Crown Copyright).

This certifies that all authors of the above Paper are subject to Crown Copyright. (Appropriate documentation and instructions regarding form of Crown Copyright notice may be attached).

AUTHORIZED SIGNATURE TITLE OF SIGNEE

NAME OF GOVERNMENT BRANCH DATE FORM SIGNED

Information to Authors

ACES POLICY

ACES distributes its technical publications throughout the world, and it may be necessary to translate and abstract its publications, and articles contained therein, for inclusion in various compendiums and similar publications, etc. When an article is submitted for publication by ACES, acceptance of the article implies that ACES has the rights to do all of the things it normally does with such an article.

In connection with its publishing activities, it is the policy of ACES to own the copyrights in its technical publications, and to the contributions contained therein, in order to protect the interests of ACES, its authors and their employers, and at the same time to facilitate the appropriate re-use of this material by others.

The new United States copyright law requires that the transfer of copyrights in each contribution from the author to ACES be confirmed in writing. It is therefore necessary that you execute either Part A-Copyright Transfer Form or Part B-U.S. Government Employee Certification or Part C-Crown Copyright on this sheet and return it to the Managing Editor (or person who supplied this sheet) as promptly as possible.

CLEARANCE OF PAPERS

ACES must of necessity assume that materials presented at its meetings or submitted to its publications is properly available for general dissemination to the audiences these activities are organized to serve. It is the responsibility of the authors, not ACES, to determine whether disclosure of their material requires the prior consent of other parties and if so, to obtain it. Furthermore, ACES must assume that, if an author uses within his/her article previously published and/or copyrighted material that permission has been obtained for such use and that any required credit lines, copyright notices, etc. are duly noted.

AUTHOR/COMPANY RIGHTS

If you are employed and you prepared your paper as a part of your job, the rights to your paper initially rest with your employer. In that case, when you sign the copyright form, we assume you are authorized to do so by your employer and that your employer has consented to all of the terms and conditions of this form. If not, it should be signed by someone so authorized.

NOTE RE RETURNED RIGHTS: Just as ACES now requires a signed copyright transfer form in order to do "business as usual", it is the intent of this form to return rights to the author and employer so that they too may do "business as usual". If further clarification is required, please contact: The Managing Editor, R. W. Adler, Naval Postgraduate School, Code EC/AB, Monterey, CA, 93943, USA (408)656-2352.

Please note that, although authors are permitted to re-use all or portions of their ACES copyrighted material in other works, this does not include granting third party requests for reprinting, republishing, or other types of re-use.

JOINT AUTHORSHIP

For jointly authored papers, only one signature is required, but we assume all authors have been advised and have consented to the terms of this form.

U.S. GOVERNMENT EMPLOYEES

Authors who are U.S. Government employees are not required to sign the Copyright Transfer Form (Part A), but any co-authors outside the Government are.

Part B of the form is to be used instead of Part A only if all authors are U.S. Government employees and prepared the paper as part of their job.

NOTE RE GOVERNMENT CONTRACT WORK: Authors whose work was performed under a U.S. Government contract but who are not Government employees are required so sign Part A-Copyright Transfer Form. However, item 5 of the form returns reproduction rights to the U. S. Government when required, even though ACES copyright policy is in effect with respect to the reuse of material by the general public.

APPLIED COMPUTATIONAL ELECTROMAGNETICS SOCIETY JOURNAL
http://aces.ee.olemiss.edu

INFORMATION FOR AUTHORS

PUBLICATION CRITERIA

Each paper is required to manifest some relation to applied computational electromagnetics. **Papers may address general issues in applied computational electromagnetics, or they may focus on specific applications, techniques, codes, or computational issues.** While the following list is not exhaustive, each paper will generally relate to at least one of these areas:

1. **Code validation.** This is done using internal checks or experimental, analytical or other computational data. Measured data of potential utility to code validation efforts will also be considered for publication.

2. **Code performance analysis.** This usually involves identification of numerical accuracy or other limitations, solution convergence, numerical and physical modeling error, and parameter tradeoffs. However, it is also permissible to address issues such as ease-of-use, set-up time, run time, special outputs, or other special features.

3. **Computational studies of basic physics.** This involves using a code, algorithm, or computational technique to simulate reality in such a way that better, or new physical insight or understanding, is achieved.

4. **New computational techniques** or new applications for existing computational techniques or codes.

5. **"Tricks of the trade"** in selecting and applying codes and techniques.

6. **New codes, algorithms, code enhancement, and code fixes.** This category is self-explanatory, but includes significant changes to existing codes, such as applicability extensions, algorithm optimization, problem correction, limitation removal, or other performance improvement. **Note: Code (or algorithm) capability descriptions are not acceptable, unless they contain sufficient technical material to justify consideration.**

7. **Code input/output issues.** This normally involves innovations in input (such as input geometry standardization, automatic mesh generation, or computer-aided design) or in output (whether it be tabular, graphical, statistical, Fourier-transformed, or otherwise signal-processed). Material dealing with input/output database management, output interpretation, or other input/output issues will also be considered for publication.

8. **Computer hardware issues.** This is the category for analysis of hardware capabilities and limitations of various types of electromagnetics computational requirements. Vector and parallel computational techniques and implementation are of particular interest.

Applications of interest include, but are not limited to, antennas (and their electromagnetic environments), networks, static fields, radar cross section, inverse scattering, shielding, radiation hazards, biological effects, biomedical applications, electromagnetic pulse (EMP), electromagnetic interference (EMI), electromagnetic compatibility (EMC), power transmission, charge transport, dielectric, magnetic and nonlinear materials, microwave components, MEMS, RFID, and MMIC technologies, remote sensing and geometrical and physical optics, radar and communications systems, sensors, fiber optics, plasmas, particle accelerators, generators and motors, electromagnetic wave propagation, non-destructive evaluation, eddy currents, and inverse scattering.

Techniques of interest include but not limited to frequency-domain and time-domain techniques, integral equation and differential equation techniques, diffraction theories, physical and geometrical optics, method of moments, finite differences and finite element techniques, transmission line method, modal expansions, perturbation methods, and hybrid methods.

Where possible and appropriate, authors are required to provide statements of quantitative accuracy for measured and/or computed data. This issue is discussed in "Accuracy & Publication: Requiring, quantitative accuracy statements to accompany data," by E. K. Miller, *ACES Newsletter,* Vol. 9, No. 3, pp. 23-29, 1994, ISBN 1056-9170.

SUBMITTAL PROCEDURE

All submissions should be uploaded to ACES server through ACES web site (http://aces.ee.olemiss.edu) by using the upload button, journal section. Only pdf files are accepted for submission. The file size should not be larger than 5MB, otherwise permission from the Editor-in-Chief should be obtained first. Automated acknowledgment of the electronic submission, after the upload process is successfully completed, will be sent to the corresponding author only. It is the responsibility of the corresponding author to keep the remaining authors, if applicable, informed. Email submission is not accepted and will not be processed.

PAPER FORMAT (INITIAL SUBMISSION)

The preferred format for initial submission manuscripts is 12 point Times Roman font, single line spacing and single column format, with 1 inch for top, bottom, left, and right margins. Manuscripts should be prepared for standard 8.5x11 inch paper.

EDITORIAL REVIEW

In order to ensure an appropriate level of quality control, papers are peer reviewed. They are reviewed both for

technical correctness and for adherence to the listed guidelines regarding information content and format.

PAPER FORMAT (FINAL SUBMISSION)

Only camera-ready electronic files are accepted for publication. The term **"camera-ready" means that the material is neat, legible, reproducible, and in accordance with the final version format listed below.**

The following requirements are in effect for the final version of an ACES Journal paper:

1. The paper title should not be placed on a separate page. The title, author(s), abstract, and (space permitting) beginning of the paper itself should all be on the first page. The title, author(s), and author affiliations should be centered (center-justified) on the first page. The title should be of font size 16 and bolded, the author names should be of font size 12 and bolded, and the author affiliation should be of font size 12 (regular font, neither italic nor bolded).

2. An abstract is required. The abstract should be a brief summary of the work described in the paper. It should state the computer codes, computational techniques, and applications discussed in the paper (as applicable) and should otherwise be usable by technical abstracting and indexing services. The word "Abstract" has to be placed at the left margin of the paper, and should be bolded and italic. It also should be followed by a hyphen (—) with the main text of the abstract starting on the same line.

3. All section titles have to be centered and all the title letters should be written in caps. The section titles need to be numbered using roman numbering (I. II. ….)

4. Either British English or American English spellings may be used, provided that each word is spelled consistently throughout the paper.

5. Internal consistency of references format should be maintained. As a guideline for authors, we recommend that references be given using numerical numbering in the body of the paper (with numerical listing of all references at the end of the paper). The first letter of the authors' first name should be listed followed by a period, which in turn, followed by the authors' complete last name. Use a coma (,) to separate between the authors' names. Titles of papers or articles should be in quotation marks (" "), followed by the title of journal, which should be in italic font. The journal volume (vol.), issue number (no.), page numbering (pp.), month and year of publication should come after the journal title in the sequence listed here.

6. Internal consistency shall also be maintained for other elements of style, such as equation numbering. As a guideline for authors who have no other preference, we suggest that equation numbers be placed in parentheses at the right column margin.

7. The intent and meaning of all text must be clear. For authors who are not masters of the English language, the ACES Editorial Staff will provide assistance with grammar (subject to clarity of intent and meaning). However, this may delay the scheduled publication date.

8. Unused space should be minimized. Sections and subsections should not normally begin on a new page.

ACES reserves the right to edit any uploaded material, however, this is not generally done. It is the author(s) responsibility to provide acceptable camera-ready pdf files. Incompatible or incomplete pdf files will not be processed for publication, and authors will be requested to re-upload a revised acceptable version.

COPYRIGHTS AND RELEASES

Each primary author must sign a copyright form and obtain a release from his/her organization vesting the copyright with ACES. Copyright forms are available at ACES, web site (http://aces.ee.olemiss.edu). To shorten the review process time, the executed copyright form should be forwarded to the Editor-in-Chief immediately after the completion of the upload (electronic submission) process. Both the author and his/her organization are allowed to use the copyrighted material freely for their own private purposes.

Permission is granted to quote short passages and reproduce figures and tables from and ACES Journal issue provided the source is cited. Copies of ACES Journal articles may be made in accordance with usage permitted by Sections 107 or 108 of the U.S. Copyright Law. This consent does not extend to other kinds of copying, such as for general distribution, for advertising or promotional purposes, for creating new collective works, or for resale. The reproduction of multiple copies and the use of articles or extracts for commercial purposes require the consent of the author and specific permission from ACES. Institutional members are allowed to copy any ACES Journal issue for their internal distribution only.

PUBLICATION CHARGES

All authors are allowed for 8 printed pages per paper without charge. Mandatory page charges of $75 a page apply to all pages in excess of 8 printed pages. Authors are entitled to one, free of charge, copy of the journal issue in which their paper was published. Additional reprints are available for a nominal fee by submitting a request to the managing editor or ACES Secretary.

Authors are subject to fill out a one page over-page charge form and submit it online along with the copyright form before publication of their manuscript.

ACES Journal is abstracted in INSPEC, in Engineering Index, DTIC, Science Citation Index Expanded, the Research Alert, and to Current Contents/Engineering, Computing & Technology.